COLD ION-NEUTRAL REACTIONS

Inauguraldissertation

zur
Erlangung der Würde eines Doktors der Philosophie
vorgelegt der
Philosophisch-Naturwissenschaftlichen Fakultät
der Universität Basel

von

Felix Henry Joynson Hall

aus Truro, Cornwall, United Kingdom

Basel, 2013

Genehmigt von der Philosophisch-Naturwissenschaftlichen Fakultät

auf Antrag von

Prof. Dr. Stefan Willitsch und Prof. Dr. John P. Maier

Basel, den 26.03.2013

Prof. Dr. Jörg Schibler

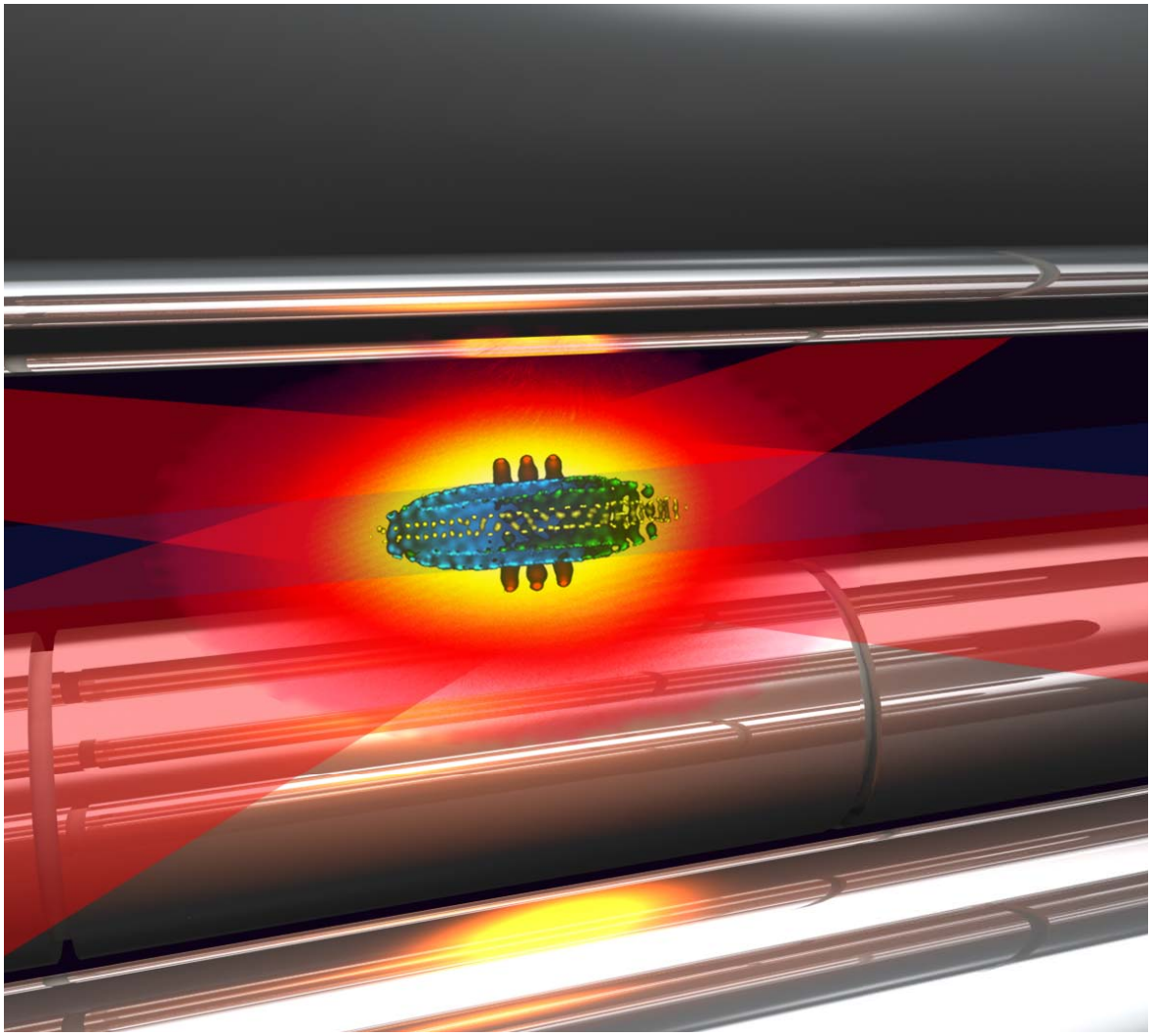

Abstract

Cold ion-neutral reactive processes were studied in an hybrid trap down to average collision energies $\langle E_{coll} \rangle / k_{\mathrm{B}} \geq 20$ mK. The atomic ion-neutral systems $Ca^+ + Rb$ and $Ba^+ + Rb$ were studied, and the results interpreted with high-level quantum chemical and quantum scattering calculations. Three reactive processes were found to be in competition, namely non-radiative charge transfer induced by non-adiabatic couplings between potential energy surfaces, radiative charge transfer, and radiative association of molecular ions, which were observed using mass spectrometry. The role of light in these processes was investigated. Enhancement of reaction rate constants from electronically excited entrance channels was observed and rationalized using computed potential energy curves. The collision-energy dependence of the reaction rate constants was investigated, and was found to be in line with predictions of both classical and quantum models uncovering general effects in cold ion-neutral systems. Cold reactions in the molecular ion-neutral system $N_2^+ + Rb$ were also investigated with average collision energies two orders of magnitude lower than previously realized. The reaction rate constant in this system was found to depend strongly on the Rb $^2P_{3/2}$ population, with the rate constant from the corresponding excited entrance channel being significantly faster than the collision rate predicted by Langevin theory. A classical capture model was developed taking into account the charge permanent-quadrupole intermolecular force and was found to reproduce the observed rate. The implied near unit reaction probability was rationalized by a near electronic resonance of entrance and product channels. A detailed description of the implementation of the ion-neutral hybrid trap is given. A thorough comparison of the results from state-of-the-art experiments and theory reveals general features of light assisted cold ion-neutral reactions.

Acknowledgements

I would first like to acknowledge Stefan Willitsch for the opportunity to be part of such an exciting research program. His guidance and advice were exceptional, and his openness to discussion and debate crucial in making this work the success that it is.

I would like to acknowledge Xin Tong for his patient demonstration of some of the key techniques used in this work, for his kind and ceaseless openness to discussion, and for the pleasant and productive working environment that he helped to maintain.

I would like to acknowledge the work and help of the Master and project students which were involved in this project: Andreas Bünzli for the simulation of the experiment, Sarina Zürcher for help with the characterization of the magneto-optical trap, Andreas Buck for work on the hybrid trap, Gregor Hegi for simulation of the mass spectra, and Pascal Eberle for help in characterizing reactions in the hybrid trap. Their input has helped immensely, and the working relationships maintained during their time in the group were a pleasure.

I would like to acknowledge the help and support of other members of the group for creating an interesting and pleasant working atmosphere, and for being open to useful discussions, in particular Matthias Germann for help with computer programming.

I would like to acknowledge the mechanical workshop for their ceaseless enthusiasm and the quality of work they produced, on which the success of the experiment was critically based: Dieter Wild, Grischa Martin, Franz Haefeli, and Volkan Demir.

I would like to acknowledge assistance with electronics from Andreas Tonin and Georg Holderied, and assistance with lasers and programming from Anatoly Johnson.

I would like to gratefully acknowledge the enjoyable and fruitful collaboration with the theory group of Olivier Dulieu at Laboratoire Aimé Cotton, CNRS, Bâtiment 505, Université Paris-Sud XI, 91405 Orsay Cedex, France. The Potential energy curve calculations performed with Nadia Bouloufa-Maafa and Mireille Aymar were key in rationalizing observed rate constants, and the quantum scattering calculations performed with Maurice Raoult were key in rationalizing observed product branching ratios, and uncovering the mechanisms behind general features of cold ion-atom reactions. The fruitful and animated discussions enjoyed between myself, Stefan, Olivier and Maurice

are acknowledged, which were also very insightful and important for furthering the fundamental understanding of the processes occurring in cold ion-neutral reactions, and for which I am extremely grateful. The various contributions of the Paris group are also acknowledged specifically in figure captions and in the text where appropriate.

I would like to thank John Maier for kindly agreeing to co-examine this work.

I would like to gratefully acknowledge funding for this project from Swiss National Science Foundation grant numbers PP0022-118921 and PP002P-140834 and the University of Basel.

Finally, I would like to thank my family, especially and wholeheartedly my partner Annika, for providing me with endless support, and a happy and relaxed home environment, allowing me to give as much as I have to this work.

Contents

List of Figures

Chapter 1

Introduction and concepts

This work presents an investigation into cold, light assisted ion-neutral reactive collisions. The main aim of the project was to construct and characterize an ion-neutral hybrid trap and to investigate reactive collisions of various species down to unprecedentedly low collision energies. This goal was motivated by the opportunity to observe unique reactive behavior expected to present itself at low ion-neutral collision energies and provide a test for the various theoretical descriptions which exist for this energy regime. The resulting work, of which this thesis provides a detailed account, was successful in realizing these aims. First, purely atomic ion-neutral systems were prepared and studied in the hybrid trap, where for the first time radiative association of the reaction partners to form molecular ions was observed in such a sub-Kelvin environment. As a result of the laser cooling schemes in the hybrid trap, reactions between various excited states of the reaction partners were studied, and state-to-state reaction rates spanning two orders of magnitude were determined. The experimental observations in these systems were compared to and rationalized in part using calculations performed by the theory group at Laboratoire Aimé Cotton in Orsay, with which a strong collaboration was initiated and maintained. The detailed and thorough comparison of experiment and theory enabled new insights on the general behavior of cold ion-neutral reactions to be uncovered. Second, a molecular-ion neutral reaction system was investigated with collision energies two orders of magnitude lower than previously realized. Distinctly molecular effects were observed in the resulting reactions, with the rates being well described by a classical model developed as part of this work.

Like the city of Basel sits at the border of Switzerland, Germany and France, the research presented in this work sits at the border between atomic and molecular physics, chemical physics, and reaction dynamics, and as such involves concepts and techniques form all three disciplines. In this introduction, cold species and collisions are introduced, and the types of ion-neutral reactive processes as well as quantum effects are described. The concepts behind the interaction of light with matter, including laser cooling, are described in detail, before the theory of the ion and neutral traps used are introduced. The subsequent chapter then describes the technical implementation

of these traps, followed by a description of the experimental and analytical techniques used in the experiments. The results of the experiments and the comparison to theory are then provided and discussed followed by conclusions and an outlook.

Some figures in the results chapters were produced, and resulted from the calculations performed by, the theory group of Olivier Dulieu (as described in the acknowledgments). Permission was courteously given to reproduce these figures, and the contributors in each case are acknowledged in the figure caption.

1.1 Cold species

First of all, it is important to define what is meant by cold. Formally, temperature is defined as a parameter of the state of a closed system in thermal equilibrium with its surroundings, and for an ideal gas serves as a parameter of the Maxwell-Boltzmann distribution [1]. In this case temperature T can be related to the root-mean-squared velocity of the distribution v, and the average Kinetic energy $\langle E_{K.E.} \rangle$ through $\frac{n}{2} k_B T = \langle E_{K.E.} \rangle = \frac{1}{2} m v^2$ where n is the number of degrees of freedom in the system, k_B is Boltzmann's constant, and m is the mass of the species [2]. A consequence of the laser cooling and trapping methods employed in this work, however, is that the species are not in thermal equilibrium with their environment, and indeed, especially in the case of ions in an ion trap, their velocities do not follow a Maxwell-Boltzmann distribution. In this case the assignment of a thermodynamic temperature is not appropriate. It is customary in the field, however, to present average kinetic energy in units of Kelvin with $\langle E_{K.E.} \rangle / k_B$ (K). Although this is in units of K, it is not a temperature. "Cold" in the context of this work therefore refers to a low average kinetic energy of the species with 1 mK $\lesssim \langle E_{K.E.} \rangle / k_B \lesssim$ 1 K. "Ultracold" then refers to species with $\langle E_{K.E.} \rangle / k_B \lesssim$ 1 mK. For collision systems, an average collision energy can be defined as described later, which can be expressed in units of Kelvin by dividing by Boltzmann's constant: $\langle E_{coll} \rangle / k_B$ (K). "Cold collisions" in the context of this work therefore refers to a low average collision energy of the colliding species, with 1 mK $\lesssim \langle E_{coll} \rangle / k_B \lesssim$ 1 K, and "ultracold collisions" with $\langle E_{coll} \rangle / k_B \lesssim$ 1 mK.

Pioneering work to generate trapped cold ensembles of species in the gas phase was motivated primarily by high resolution spectroscopy (where small Doppler broadening and long interrogation times are needed) including the development of more accurate optical clocks for time frequency standards, and the study of processes of astrophysical importance (where experimental conditions ideally resemble those of space where $T \geq$ 2.7 K). To this end, such techniques as molecular beams [3], and storage in ion traps [4] were employed. Over three decades ago, the first experiments using light to cool ions [5, 6] and subsequently to cool and trap atoms to sub-millikelvin temperatures [7] were achieved, opening up new research avenues in physics and chemistry such as atom interferometry [8], Bose-Einstein Condensation [9], quantum information processing [10], and, more recently, controlling ultracold reactive collisions [11].

Cold trapped ensembles of atoms and ions, or even single species, have both practically useful, and under the right conditions, distinctly unique properties. They can be highly localized for long periods, allowing specific and extended interrogation with fields or other particles. Pure ground or other specific quantum state ensembles can be generated and sustained, allowing state specific effects to be investigated and controlled [12]. The key feature of cold trapped species which has sparked the most interest, however, is their increasingly quantum behavior at kinetic energies approaching zero.

The origin of most of the observed and predicted quantum behavior in cold trapped systems is the increasing wave nature of particles at lower energies. The wave nature of the species is quantified by the de Broglie wavelength $\lambda = h/mv$, where h is Planck's constant, and gives a measure of the extent of the particle wave-function. At temperatures associated with Doppler laser cooling of ^{87}Rb for example (146 μK), the de Broglie wavelength is 27 nm, which is far beyond typical bond lengths. In the ultracold environments achieved after the evaporative cooling of ^{87}Rb in magnetic traps ($\approx$ 10 nK), the de Broglie wavelength becomes macroscopic ($\approx$ 10 μm), and comparable to the dimensions of the potential in which they are confined, and as a result (given sufficient density), can form a Bose-Einstein Condensate [9], where all the particles can be described with a single wave-function.

At room temperature, a near continuum of collisional angular momenta are available to colliding species, and the individual contribution of each is intractable. At lower collision energies however, only a few quanta are available, and, as will be seen in section 1.2, the contribution of each quantum to scattering can be observed [13]. At ultralow collision energies, no quanta are available, and only head-on, or "s-wave" collisions are possible, which can be utilized to precisely and dramatically control reactivity [11].

This work was partly motivated by the possibility of observing quantum behavior in cold ion-neutral hybrid systems. In this work, Rb atoms are trapped and laser cooled to $\approx$ 100 μK (λ = 30 nm), and ions are trapped and cooled to $\approx$ 10 mK ($\lambda \approx$ 3 nm), reducing the available quanta of collisional angular momentum to a few tens, and hence making available a regime where quantum behavior plays a significant role.

1.2 Cold ion-neutral collisions and reactions

As discussed in section 1.1, cold trapped species can display a range of useful and interesting properties, including distinctly quantum behavior at the lowest energies. In low energy reaction dynamics, classical [14] as well as quantum [15, 16] models are commonly used to quantify collisional and reactive processes, and it is important to compare their predictions against experiment, particularly in energy regions where they may both be applicable in principle. In this section the universality of cold ion-neutral reactions will be discussed, followed by a description of classical capture models involving different classes of inter-molecular force. Types of long-range quantum mechanical effects that can occur at low collision energies are then briefly described. Finally, the types of reaction processes occurring at short-range in cold ion-neutral

systems are discussed.

1.2.1 Universal behavior of cold ion-neutral reactions

An important theme in the study of cold ion-neutral collisions and reactions is the extent to which they can be described by "universal" behavior, that is to what extent the dynamics can be described solely by the long-range part of the ion-neutral interaction potential. Classical capture models [14] for barrierless processes, such as most ion neutral reactions (as discussed in the next subsection) assume that the short-range part of the potential is unimportant, and that the reaction rate can described by the rate of complex formation, i.e., the capture of the partners by one another at long-range, by assuming that every collision leads to a reaction.

A classical capture model has been compared to a fully quantum treatment [16] in cold ground state collisions of Na^+ + Na. The quantum treatment relies on the ab initio calculation of relevant potential energy curves (PECs) and then performing quantum scattering calculations from these curves [17] (see also section 3.7.2). It was found that in a certain range of collision energies ($k_B\cdot$ 10 nK to $k_B\cdot$ 100 K for Na^+ + Na [16]) a classical capture model was sufficient to describe the dynamics up to a scaling factor. The classical capture model, however, only depends on the reduced mass of the collision system and the polarisability of the neutral partner (see section 1.2.2), and so the possibility becomes apparent that the dynamics of all cold ion-neutral reactions may be sufficiently described by a universal behavior that only changes between systems by scaling factors.

To avoid relying on the calculation of accurate PEC's, and to highlight the possible universal nature of cold ion-neutral collisions, a quantum defect theory for $-1/r^4$ type potentials (i.e., the long-range charge induced-dipole interaction between ions and atomic neutrals in their ground electronic state) was developed [18, 19], whereby a universal scattering spectrum was produced based solely on length scales relating to the reduced mass and long-range interaction potentials of the ion-neutral collision partners. It was shown [18] that the characteristic length scale for scattering for the studied alkali-atom alkali-ion systems is hundreds of times larger than the short-range region where the potential starts to deviate from its long-range form. It was therefore proposed that the entire collision energy dependence and shape resonance spectrum (see section 1.2.4 for a discussion of shape resonances) in cold ion-neutral systems is universal, i.e., that they are essentially the same for any ground state atomic-ion atomic-neutral cold collision system up to scaling factors.

A further "quantum Langevin" model based on multichannel quantum-defect theory [15] was developed which addressed long-range potentials of the general form $-1/r^n$, and also specifically for resonant charge exchange [20]. A form of the rate constant was given as the product of a "rate scale" (depending on the reduced mass and long-range interaction form of the potential) and a universal function of the scaled collision energy [15]. It was found that within the quantum Langevin model [15], while the absolute value of the reaction rate constant may depend on the short-range interaction

of the PECs, its energy dependence and resonance spectrum can be parametrized using the same universal transmission probabilities. That is to say that all cold ion-neutral reactions should have an energy dependence of the reaction rate constant that is governed solely by the long-range interaction potential, but whose magnitude may be altered by the short-range interactions of the PECs, i.e. all demonstrate a universal behavior.

An important part of the experiments of this work is to provide a test for these theoretical predictions, and to address experimentally the questions of whether cold ion-neutral reactions are indeed universal (i.e., the rate constants have the same collision energy dependence for a given-long-range interaction potential up to scaling factors), and to what extent reaction rate constants deviate from the predictions of classical capture models (which assume unit reaction probability) based on the specific details of the interactions of different PECs at short-range. As it will be seen in subsequent sections, the experiments of this work are well suited to addressing these questions, since the long-range part of the potential can be modified experimentally by changing the electronic state of the neutral reaction partner or by changing the chemical identity of the ionic reaction partner, but also the effect of the short-range interactions of the PECs can be probed whilst leaving the form of the long-range potential unchanged by changing the electronic state of the ion. By investigating the behavior of reaction rate constants from different entrance channels of the same atomic-ion neutral system, by comparing the behavior of chemically different atomic-ion neutral systems, and by comparing to behaviors observed in molecular-ion neutral systems, it is the aim that the experiments of this work will provide an insight into the accuracy and applicability of this universal cold ion-neutral reaction picture.

1.2.2 Classical capture model for structureless particles

It is often useful to picture two-body chemical reactions as structureless particles colliding unperturbed by their environment in free space. A dilute, gas-phase mixture of cold (< 100 K) atomic reactants (similar to the environment for reactions studied in this work) is among the experimentally achievable systems for which this picture is most relevant. In the majority of this work, classical capture models are employed to quantify the theoretical collision rate constants, which are then compared to experimentally determined reaction rate constants in order to gain insight into the reaction mechanisms, and to provide a test for the accuracy of the universal reaction behavior predicted by such models.

A classical capture model will now be developed. Consider two structureless particles as presented in Fig. 1.1 (a), approaching one another with a relative velocity $\mathbf{v}$, connected by vector $\mathbf{R}$, where the separation of the particles perpendicular to the velocity vector is denoted b and is known as the "impact parameter" [21].

In the absence of a force between the two particles, $\mathbf{v}$ will remain constant with time t (except for the case of a head on collision), and hence by the Pythagorean theorem

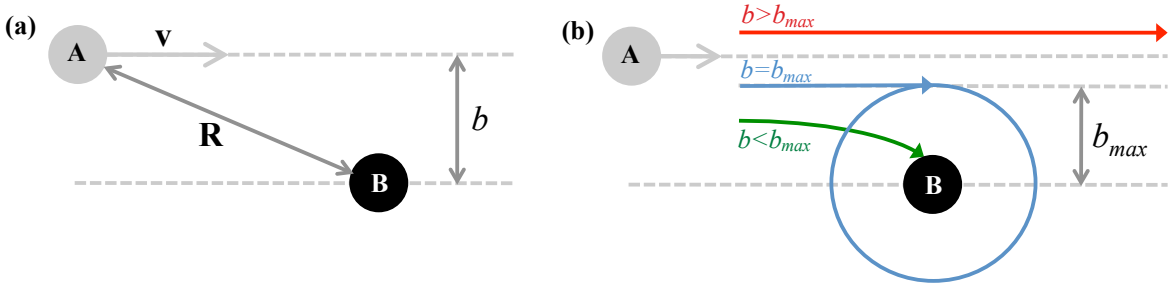

Figure 1.1: (a) Two structureless particles A and B approaching with relative velocity **v**, connected by vector **R** and with impact parameter b. (b) Possible classes of trajectory as A and B approach: no (or glancing) collision when $b > b_{max}$ (red), orbiting trajectory at the critical impact parameter b_{max} (blue), trajectories initially with $b < b_{max}$ leading to a collision (green).

the distance R can be written

$$R^2 = (vt)^2 + b^2. \tag{1.1}$$

For structureless particles, the total energy E_T of the system is just the kinetic energy E_K of the partners, and hence before the collision

$$E_T \equiv E_{K,R\to\infty} = \frac{\mu v^2}{2}, \tag{1.2}$$

where μ is the reduced mass of the collision partners, and v is the magnitude of the relative velocity of the two particles. The kinetic energy can also be expressed however in terms of the rate of change of **R**

$$E_K = \frac{\mu}{2}\left(\frac{d\mathbf{R}}{dt}\right)^2, \tag{1.3}$$

where both the rate of change of magnitude, and of direction of **R** contribute to the kinetic energy. If the kinetic energy along the line of centers is considered, then by the chain rule $(dR^2/dt) = (dR^2/dR)\cdot(dR/dt) = 2R(dR/dt)$, and hence $(dR/dt)^2 = (dR^2/dt)^2 \cdot (1/4R^2)$. But from equation 1.1 it can be seen that $(dR^2/dt) = 2v^2t$, and hence that $(dR/dt)^2 = (v^4t^2/R^2)$. Inserting this into equation 1.3 gives

$$E_K = \frac{v^4t^2\mu}{2R^2}. \tag{1.4}$$

Rearrangement of equation 1.1, however, gives that $(vt)^2 = R^2 - b^2$, which can be substituted into equation 1.4, and hence during the collision

$$E_K = \frac{\mu v^2}{2}\left(1 - \frac{b^2}{R^2}\right) \tag{1.5}$$

and since $E_T = (\mu v^2/2)$, equation 1.5 can be rewritten as

$$E_T = E_K + \frac{E_T b^2}{R^2} \tag{1.6}$$

which is purely a statement of the conservation of energy. Note that equation 1.6 shows that the total energy has two parts: the long-range kinetic energy of the particles, and the "centrifugal" energy which corresponds to the work done in rotating the vector $\mathbf{R}$, which is largest for small inter-particle distances.

Real particles have forces acting between them, and so experience an additional potential $V(R)$, which by conservation of energy must be added to equation 1.6

$$E_T = E_K + \frac{E_T b^2}{R^2} + V(R). \tag{1.7}$$

For convenience the centrifugal and potential terms are grouped into an effective potential $V_{eff}(R) = V(R) + (E_T b^2/R^2)$. As long as the long-range part of the potential $V(R)$ is of the form R^{-s} where $s > 2$, then $V_{eff}(R)$ will have a maximum, known as the "centrifugal barrier". This phenomenon is shown schematically in Fig. 1.2 which plots V_{eff} against R.

The maximum in the effective potential can be found by setting

$$\frac{d}{dR}[V_{eff}(R)]\bigg|_{R=R_{max}} = 0. \tag{1.8}$$

A criterion for the system making it to short internuclear distances where reactions can happen, is that the particles must have enough kinetic energy to overcome the centrifugal barrier. From equation 1.7, this criterion can be stated mathematically with

$$E_K\ |_{R=R_{max}} = \left[E_T - \frac{E_T b^2}{R^2} - V(R)\right]\bigg|_{R=R_{max}} \geq 0. \tag{1.9}$$

As b increases, the height of the barrier increases, and $E_K|_{R=Rmax}$ decreases. At some value of b, $E_K|_{R=Rmax}$ will be exactly zero, and this value of b is known as the critical impact parameter b_{max}. The trajectory in this case corresponds to the blue trace in Fig. 1.1 (b) where the particles are in a stable orbit of one another. For $b > b_{max}$ (shown in red in Fig. 1.1 (b)), the particles do not make it to short internuclear distances, and for $b < b_{max}$ (shown in green in Fig. 1.1 (b)), they do. In this case b_{max} is formulated

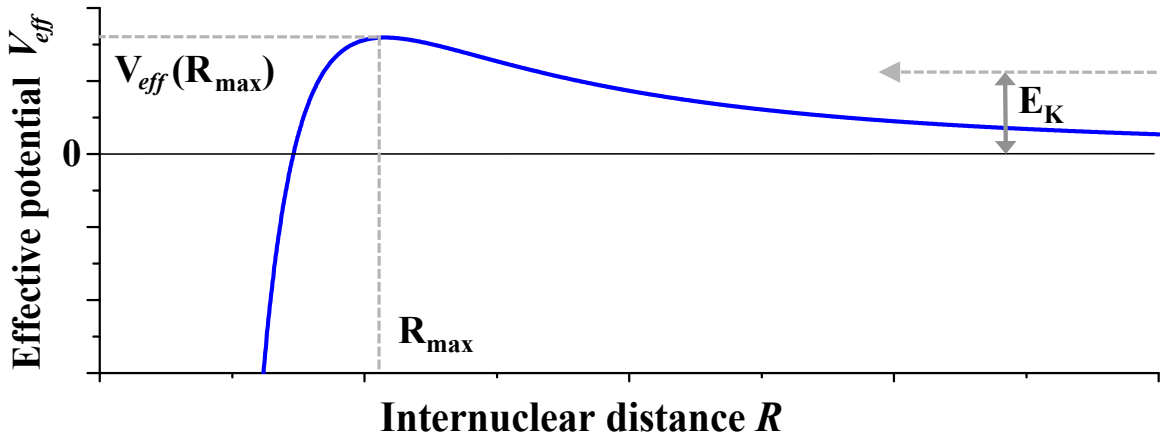

Figure 1.2: A schematic plot of V_{eff} against R for an inter-particle potential V that scales asymptotically with R^{-s} where $s > 2$. The maximum in the potential is known as the "centrifugal barrier", and occurs at R_{max} with a height of $V_{eff}(R_{max})$. Also indicated is the asymptotic kinetic energy E_K of an incoming system. A criterion for access to short-range is that $E_K|_{R=R_{max}} \geq 0$, or equivalently, $E_K \geq V_{eff}(R_{max})$.

with

$$\left[E_T - V(R_{max}) - \frac{E_T b^2}{R_{max}^2}\right]\Bigg|_{b=b_{max}} = 0. \tag{1.10}$$

For a given long-range collision energy, and a given interaction potential, equation 1.8 is used to find R_{max}. R_{max} is then inserted into $V(R)$ to find $V(R_{max})$. All these quantities are then used in equation 1.10 to find b_{max}.

The calculated b_{max} can be thought of as the maximum passing distance for which a collision will occur. In this case b_{max} defines the radius of the circle drawn around, say, particle A, perpendicular to the relative velocity vector, where if any B particles come within the area of the circle, they will collide with A. The area of this circle defines the cross section $\sigma = \pi b_{max}^2$.

The rate of collisions on average is the rate at which the collision volume is swept out by the collision circle. This rate is given by the magnitude of the velocity vector, such that the collision rate constant k_{coll} is given simply by $k_{coll} = \sigma \cdot v$.

As described above, for a particular entrance channel, the *reaction* rate may be some value below the *collision* rate, except for the case when every collision leads to a reaction, where they are equal. For reactions with an energy threshold, the energy dependence of the short-range processes must be included explicitly in the capture model. For barrierless reactions, such as the cold ion-neutral reactions studied in this work, it is postulated (see section 1.2.1) that the energy dependence of the reaction rate constant is governed solely by the long-range interaction potential, and so can be described by classical capture models such as the one derived above, although the

magnitude of the rate constants may be altered by the specific interactions of the PECs at short-range.

1.2.3 The effect of different interaction potentials $V(R)$ on the collision rate

The interaction potential between reactants A and B is dependent on the nature of the species. The long-range part of the interaction potential $V(R)$ may be formulated as

$$V(R) = \sum_{n=1}^{\infty} \frac{C_n}{R^n} \tag{1.11}$$

where C_n are long-range coefficients which can be derived from the multipole expansion of the interspecies interaction operator [22, 23]. Table 1.1 displays the mathematical expressions for some of the different classes of interaction which can play a role in ion atomic-neutral collisions.

Table 1.1: Long-range interaction coefficients in atomic units [23]

Symbol	Interaction type	Formula (a.u.)
C_3^{elst}	charge permanent-quadrupole	$(-1)^{(l+\Lambda)} \begin{pmatrix} l & 2 & l \\ -\Lambda & 0 & \Lambda \end{pmatrix} \langle l \| Q_2 \| l \rangle$
C_4^{ind}	charge induced-dipole	$-\frac{1}{2}\left(\alpha_0 + \frac{3\Lambda^2-6}{6}\alpha_2\right)$
C_5^{elst}	charge permanent-hexadecapole	$(-1)^{(l+\Lambda)} \begin{pmatrix} l & 4 & l \\ -\Lambda & 0 & \Lambda \end{pmatrix} \langle l \| Q_4 \| l \rangle$
C_6^{ind}	charge induced-quadrupole	$-\frac{1}{2}C_{zz,zz}$
C_6^{disp}	dispersion	$-\frac{1}{2\pi}\int_0^{\infty} \alpha_0^+(i\omega)\left(6\alpha_0(i\omega) + 3\frac{3\Lambda^2-6}{6}\alpha_2(i\omega)\right) d\omega$

In the formulas for C_n given in Table 1.1, l and Λ are the orbital angular momentum associated with the electronic state of the neutral reaction partner, and its projection on the collision axis respectively. The bracketed arrays are Wigner $3j$ symbols, and $\langle l \| Q_m \| l \rangle$ ($m = 2$ or 4) symbolize the reduced matrix element of the quadrupole and hexadecapole moment of the neutral, respectively. α_0 and α_2 are the scalar and tensor components of the electric dipole polarisability of the relevant quantum state of the neutral. $C_{zz,zz}$ is the z component of the quadrupole polarisability of the neutral. Lastly α_0^+ is the polarisability of the ionic reaction partner.

As can be seen from equation 1.11, the potential arising from progressively higher n falls off increasingly rapidly with distance, so that it can be expected that at long-range, terms with lower n have a larger effect on the form of the potential. It is usually sufficient to truncate equation 1.11 to include only the dominant terms. For collisions between ions with neutrals in an electronic state with $l = 0$, there is no charge permanent-quadrupole interaction, and the leading term in equation 1.11 is due to the charge induced-dipole interaction. In the case of $l = 0$, α_2 is negligibly small, so that the form of the potential may be approximated with

$$V(R) = \frac{-\alpha_0}{2R^4}. \tag{1.12}$$

Inserting this potential into equation 1.8 leads to $R_{max}^2 = (\alpha_0/E_T b^2)$. Inserting these result into equation 1.10 then gives that $b_{max} = (2\alpha_0/E_T)^{(1/4)}$, and hence the cross section

$$\sigma_L = \pi \left(\frac{2\alpha_0}{E_T}\right)^{1/2}. \tag{1.13}$$

This is known as the Langevin form of the cross section after the pioneering work on ion-neutral collisions conducted by P. Langevin in the 1900's [14], and is widely used to describe the dynamics of ground-state ion-neutral collisions. Formulating E_T in terms of velocity gives $E_T = \frac{1}{2}\mu v^2$. Inserting this into equation 1.13, and multiplying the result by v gives the Langevin rate constant k_L as

$$k_L = 2\pi \left(\frac{\alpha_0}{\mu}\right)^{\frac{1}{2}} \tag{1.14}$$

which is independent of the collision energy. Note that for evaluation in SI units, $V(R)$ of equation 1.12 should be multiplied by $e^2/(4\pi\epsilon_0)^2$, where e is the elementary charge, and ϵ_0 is the permittivity of vacuum.

If the neutral reaction partner is in an electronic state with $l = 1$, for example the Rb (5p) $^2P_{3/2}$ state, then both charge induced-dipole, and charge permanent-quadrupole interactions would be expected to be significant at long-range. The potential can again be truncated after $n = 4$, and now has the form $V(R) = (C_3^{elst}/R^3) + (C_4^{ind}/R^4)$. As can be seen in table 1.1, the form of C_3^{elst} contains a reduced matrix element. This can be reformulated for a single electron atom, neglecting spin-orbit interaction, in terms of modified spherical harmonics $C_{lm} = (4\pi/2l+1)^{(1/2)} \cdot Y_{lm}$, (where Y_{lm} are spherical harmonics) [24] to give

$$\langle l \| Q_2 \| l \rangle = \left\langle l \| - er^2 C_2 \| l \right\rangle = -e \left\langle r^2 \right\rangle \langle l \| C_2 \| l \rangle \tag{1.15}$$

which, after application of the Wigner-Eckart theorem [25], gives

$$\langle l \| Q_2 \| l \rangle = -e \left\langle r^2 \right\rangle (-1)^l (2l+1) \begin{pmatrix} l & 2 & l \\ 0 & 0 & 0 \end{pmatrix} \tag{1.16}$$

where e is the elementary charge, and $\langle r^2 \rangle$ is the square of the mean radius of the valence electron. If equation 1.16 is now inserted into the expression for C_3^{elst}, then

$$C_3^{elst} = -e \left\langle r^2 \right\rangle (-1)^{l+\Lambda} \begin{pmatrix} l & 2 & l \\ -\Lambda & 0 & \Lambda \end{pmatrix} (2l+1) \begin{pmatrix} l & 2 & l \\ 0 & 0 & 0 \end{pmatrix}. \tag{1.17}$$

For the Rb (5p) $^2P_{3/2}$ level, $l = 1$ and hence $\Lambda = 0, 1$. These projections relate to the two symmetries with which a p orbital can approach the ion, namely Σ and Π respectively. Evaluating the 3j symbols of equation 1.17 for the two symmetries gives

$$\Lambda = 0 \ (\Sigma): \quad C_3^{elst} = -e\frac{2}{5} \left\langle r^2 \right\rangle \tag{1.18}$$

$$\Lambda = 1 \ (\Pi): \quad C_3^{elst} = e\frac{1}{5} \left\langle r^2 \right\rangle \tag{1.19}$$

Since $\langle r^2 \rangle$ must be positive, it can be seen from the above equations that the Σ symmetry leads to an attractive interaction, whereas the Π leads to a repulsive interaction, a good illustration of which can be found in ref. [26]. Hence, if an atom approaches an ion with Σ symmetry, the centrifugal barrier will be lowered and occur at larger R, and hence for a given energy, the collision rate constant will be higher. If an atom approaches with Π symmetry however, the barrier will be higher and at smaller R, reducing the collision rate constant. For the calculation of the total collision rate constant, these two cases must be treated separately, and the resulting collision rate constants summed with their statistical weighting factor p, which for a P orbital is $p = 1/3$ for Σ and $p = 2/3$ for Π. The same separation should be considered when including the tensor polarisability in the C_4^{ind} term, which for $l > 0$ may no longer be negligibly small.

To evaluate the C_3^{elst} of equations 1.18 and 1.19 above, the quantity $\langle r^2 \rangle$ must be determined. This can be done within the single electron approximation using the quantum defect method, where the standard expression for mean orbital radius [27] can be altered by replacing quantum number n and atomic number Z with effective versions $n^*(l)$ and $\tilde{Z}$, found by their relation to the level energy E_{nl} [28] such that

$$E_{nl} = -\frac{\tilde{Z}^2}{2n^{*2}(l)} \quad \tilde{Z} = Z - N + 1 \tag{1.20}$$

where N is the number of electrons in the atom. In this case

$$\left\langle r^2 \right\rangle = \frac{a_0^2}{\tilde{Z}^2} \left(\tfrac{1}{2}n^{*2}\right) \left[5n^{*2} + 1 - 3l(l+1)\right] \tag{1.21}$$

where a_0 is the Bohr radius. Note that for evaluation in SI units, the C_3^{elst} coefficients of equations 1.18 and 1.19 must be multiplied by $(e/4\pi\epsilon_0)$.

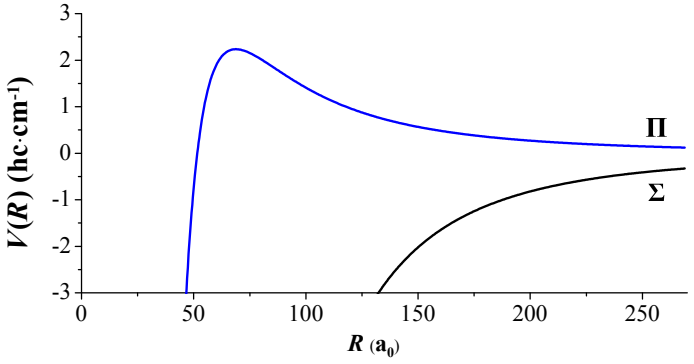

Figure 1.3: A plot of the potentials in equations 1.22 and 1.23 for the example of a singly charged ion colliding with a Rb (5p) $^2P_{3/2}$ atom showing the effect of the repulsive nature of the interactions in the Π symmetry, and the attractive nature in the Σ symmetry.

The form of the interaction potential for working out the collision rate constant for an ion-neutral collision where the neutral is in a P (i.e. $l = 1$) state is then

$$\Lambda = 0\ (\Sigma), p = \frac{1}{3}: \quad V(R) = \frac{-e\frac{2}{5}\langle r^2\rangle}{R^3} - \frac{\frac{1}{2}(\alpha_0 - \alpha_2)}{R^4} \tag{1.22}$$

$$\Lambda = 1\ (\Pi), p = \frac{2}{3}: \quad V(R) = \frac{e\frac{1}{5}\langle r^2\rangle}{R^3} - \frac{\frac{1}{2}(\alpha_0 - \frac{1}{2}\alpha_2)}{R^4}, \tag{1.23}$$

which are plotted for the example of a singly charged ion colliding with a Rb (5p) $^2P_{3/2}$ atom in Fig. 1.3.

Note that in the Σ symmetry, all interactions are attractive (since α_2 is a negative quantity), resulting in an enhanced collision rate compared to an S state neutral. In the Π symmetry however, the dominant charge permanent-quadrupole interaction is repulsive, leading to a reduced collision rate. Indeed, as shown in Fig. 1.3, for a Rb (5p) $^2P_{3/2}$ atom colliding with a singly charged ion, the barrier in $V(R)$ in the Π symmetry amounts to some 2.2 cm^{-1} (or 3.2 K), which in experiments with collision energies lower than this, precludes any collisions in the Π symmetry. (As mentioned above, for calculation in SI units, the first terms in equations 1.22 and 1.23 should be multiplied by $e/(4\pi\epsilon_0)$ and the second terms by $e^2/(4\pi\epsilon_0)^2$.)

While the form of the collision rate constant for this "extended" potential is not analytic, it can be calculated numerically. A script helping the calculation as a function of energy is given in appendix B.1. The Langevin and the "extended" collision rate constants are plotted as a function of energy for the N_2^+ + Rb $^2P_{3/2}$ system in chapter 7 in Fig. 7.5. The energy dependence of the collision rate constant which results from the use of this "extended" potential is $E^{-1/6}$. This can be shown analytically since all of the energy dependence comes from the charge permanent-quadrupole interaction. It can

be shown [21] that for a potential with long-range behavior $V(R) = -C/R^s$ (s > 2), the rate constant has the energy dependence $k \propto E^{\frac{-2}{s}+\frac{1}{2}}$, and so for the charge permanent quadrupole interaction with $s = 3$, then $k \propto E^{-1/6}$. While possible in principle, the inclusion of the higher order terms in the extended potential is not necessary in this work, since the experimental accuracy doesn't allow for the observation of the small changes in the calculated rate constant that would result. Indeed, it will be seen that this extended model is sufficient to describe the dynamics in the N_2^+ + Rb $^2P_{3/2}$ system with average collision energies $\langle E_{coll} \rangle / k_B$ down to 20 mK, the lowest energy test of molecular-ion neutral classical capture models to date.

1.2.4 Quantum mechanical effects in cold collisions

The previous subsection outlined a classical approach to ion-neutral collisions. At low collision energies, distinctly quantum behavior is expected to be important [16, 20, 23, 29–32]. Quantum effects can play a key role at large internuclear distances (specifically in the region of the centrifugal barrier), and allow the quantisation of collisional angular momentum to become observable in the reaction cross section. To explain this effect, consider the long-range effective potential $V_{eff}(R)$ as plotted schematically in Fig. 1.2, which shows a centrifugal barrier above the asymptotic energy. If a wave-function is incoming at an energy matching a quasi-bound state trapped behind the barrier, then the wave-function will be dynamically trapped in the potential, and the amplitude of the scattering wave-function increased at short internuclear distances where reactions occur. As a result there will be an enhancement of the cross section at this specific energy, known as a "shape" or "orbiting" resonance, whose position is in general independent of the subsequent reactive process. Note that this process can result from both tunneling through, and quantum reflection above the centrifugal barrier [13].

For a "head on" collision with collisional angular momentum $J = 0$, (also known as an "s-wave" collision), there is no centrifugal barrier, and so no trapping can result. As the collision energy is increased, higher values of J become accessible, and the wave function is able to be trapped behind successively higher centrifugal barriers. Hence successively larger values of J are each associated with a resonance in the cross section occurring at successively higher collision energies. This effect can be seen for example in the quantum scattering calculations for radiative processes in the Ba^+ + Rb system presented in Fig. 6.5. It is interesting to note that for increasing J, the shape resonances become increasingly thin, as the energy window for dynamical trapping becomes narrower. The phenomenon of shape resonances in ion-neutral collisions has also been seen, and beautifully explained, in calculations of non-radiative charge transfer in the Ca^+ + Rb system [29].

Shape resonances have recently been observed in merged beam experiments studying the Penning ionisation of H_2 and Ar by meta-stable He atoms [13]. It is instructive to note that the due to the light masses in this system, $J = 5$ occurs at $\approx$ 200 mK, whereas for collisions in the lightest system of this work (N_2^+ + Rb), already at the lowest average collision energies reached in the experiments ($\langle E_{coll}/k_B \rangle$ = 20 mK),

there are up to $J = 23$ quanta of collisional angular momentum (also known as "partial waves") available. This fact, coupled with a ≥ 20 mK collision energy resolution unfortunately precludes the observation of such resonances in the experiments of this work. Further experiments are currently under development to address these issues.

1.2.5 Types of ion-neutral reactive processes

A wealth of collisional and reactive processes have been predicted and observed in cold ion-neutral systems [33–42]. In purely atomic ion-neutral systems, only two chemical changes are possible, namely charge transfer ($A^+ + B \rightarrow A + B^+$), and association ($A^+ + B \rightarrow AB^+$). Charge transfer may be either through non-adiabatic or radiative couplings of potential energy curves (PECs). Association may be stabilized by a third body ($A^+ + B + M \rightarrow AB^+ + M$) or by radiative means ($A^+ + B \rightarrow AB^+ + h\nu$). Three body processes have been shown to become important at high neutral reactant densities ($\approx 10^{12}$ cm^{-3}) [40], but at the low densities used in the experiments of this work ($\approx 10^9$ cm^{-3}), three body rates are negligibly small, such that all association observed is assumed to be radiative. More complex systems can lead to more complex reactions, for example reactions of velocity selected neutral beams of CH_3F with laser cooled Ca^+ leading to CaF^+ formation [43]. The most chemically complex reaction studied in this work is the dissociative charge transfer of N_2^+ with Rb, forming 2N and Rb^+.

Resonant charge transfer has been observed in the $Yb^+ + Yb$ system [33] with a rate constant which was half of the Langevin collision rate constant, explained by the 50% probability of charge transfer in a collision of otherwise identical species. In purely ground state collisions in the mixed systems $Yb^+ + Rb$ [34] and $Ba^+ + Rb$ [35], a rate constant smaller than Langevin by a factor of $\approx 10^4$ was observed, and attributed in the latter to radiative and nonradiative processes. Electronic excitation of the reactants has led to the observation of enhanced rate constants [36, 39, 41, 44, 45], explained by enhanced opportunities for non-adiabatic interactions due to enhanced density of charge transfer states at higher energies, and also for radiative processes based on the cubic dependence of the efficiency on the emitted photon energy [42].

Fig. 1.4 illustrates the main types of two body reactive processes available in atomic ion-neutral collisions, in terms of schematic molecular PECs for a hypothetical $A^+ + B$ collision system. The system enters as $A^+ + B$ on a $^1\Sigma^+$ curve (iii) which corresponds to the lowest collision channel in an experiment. This entrance curve interacts first with a charge transfer state asymptotically connecting to ($A + B^+$) (iv), which has the same spin multiplicity and symmetry and so undergoes an avoided crossing. Passage across this avoided crossing may be adiabatic (the system stays on the same adiabatic curve and hence its form changes to that of the state with which it is crossing) or non-adiabatic (the system jumps over the avoided crossing onto the other adiabatic curve and hence keeps the form correlating with the incoming state). The probability of adiabatic or non-adiabatic passage is a function of the rate of crossing, with slow crossing rates more likely to result in adiabatic passage, and fast in non-adiabatic

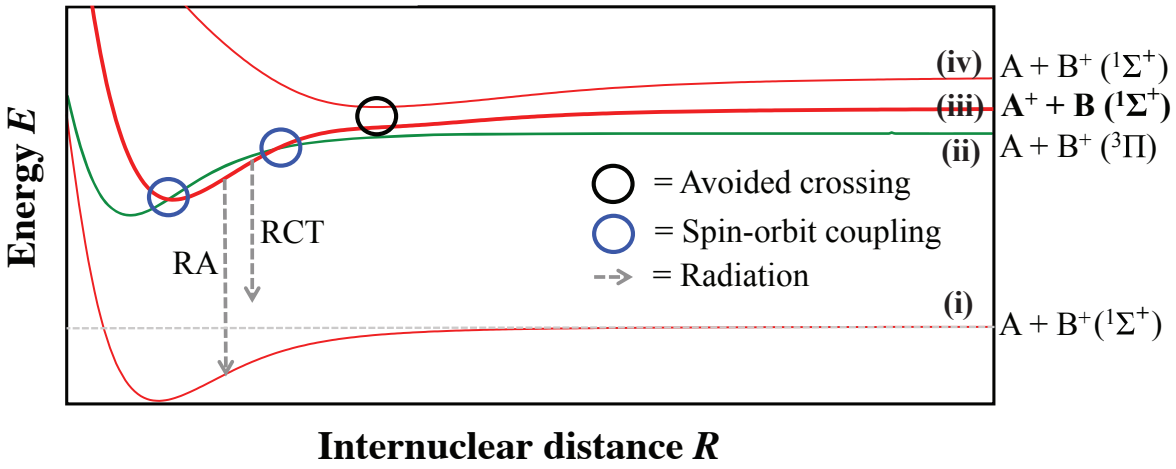

Figure 1.4: A schematic plot of some non-relativistic potential energy curves for a hypothetical $A^+ + B$ collision system entering along curve (iii), illustrating important types of PEC interactions which may lead to chemical change when exiting on (i), (ii), or (iv). RCT stands for radiative charge transfer, and RA for radiative association. Also shown are hypothetical molecular term symbols for each channel. Red curves are $^1\Sigma^+$, and green $^3\Pi$. See text for details.

passage. Indeed, the probability of non-adiabatic passage P_{na} may be calculated within the Landau-Zener approximation with

$$P_{na} = \exp(-2\pi\omega_{12}\tau_d) \tag{1.24}$$

where ω_{12} is the Rabi frequency at the crossing point, and τ_d is a measure of the interaction time [46]. Note that in Fig. 1.4, due to the energy ordering of the curves (iii) and (iv), if the available collision energy is less than their asymptotic energy separation, no flux can exit on the charge transfer curve (iv), and so this channel to charge transfer will be closed.

At smaller internuclear distances, the entrance curve crosses twice with a charge transfer curve with symmetry $^3\Pi$ (shown in green) corresponding to the situation in $Ca^+ + Rb$ (see chapter 5). In a non-relativistic treatment (as is displayed in Fig. 1.4), the two curves don't interact. Spin-orbit coupling however (which derives from the interaction between the spin and orbital magnetic moments of an electron) can mix states of differing multiplicity. Spin-orbit coupling is strongest when increasingly heavy atoms are present in the molecule. Due to their large mass, for the atomic ion-neutral systems of this work ($CaRb^+$ and $BaRb^+$), spin-orbit coupling is significant [47]. Given significant coupling, curves (ii) and (iii) will also undergo an avoided crossing (at the positions of the blue circles in Fig. 1.4), and hence the incoming system will have a probability for adiabatic passage onto curve (ii), and hence a probability to exit on the charge-transfer asymptote. This process will be referred to in the majority of

this work as non-radiative charge transfer (NRCT). Note that for crossings at large internuclear distances, where the collision energies are dominated by the asymptotic kinetic energies of the reactants, lower collision energies result in lower crossing rates, and hence higher adiabatic passage probability. For crossings at short internuclear distances where well depths dominate the asymptotic collision energy, however, the collision energy dependence of the crossing rate is expected to become negligible.

As depicted in Fig. 1.4, if the entrance channel is not the ground state of the system, then radiation to lower molecular curves is possible. Curve (i) corresponds to the lowest A + B^+ asymptote, and has the same symmetry as the entrance channel (iii), and hence dipole allowed transitions are possible. Radiative transitions to the continuum above the asymptotic energy of curve (i) (indicated dashed line RCT) will result in dissociation of the molecule along curve (i) and hence in charge transfer, referred to as radiative charge transfer (RCT). Radiative transition to a bound rovibrational state within the potential energy well of curve (i) will result in the formation of the AB^+ molecular ion, referred to as radiative association (RA). As discussed in section 3.7.2, apart from transition selection rules, the efficiency of these radiative processes depend on two dominant factors, namely the cube of the frequency of the emitted photon, and the specific Frank-Condon factors (FCFs) (i.e. the degree of overlap of the wave-functions in the states of the upper and lower curves, given a vertical transition (i.e instantaneous on the timescale of nuclear motion)). The FCFs, and hence the relative efficiencies of RCT and RA, depend very sensitively on the form of the potential energy curves, and so experimental measurement of their ratio, such as those in this work, can give information about the relevant PECs.

Radiative processes at low collision energy have a significant importance in astrophysical and atmospheric environments. RA has been studied in some theoretical detail by Dalgarno et al in systems including the removal of protons in He gas clouds (H^+ + He $\rightarrow$ HeH^+ + $h\nu$) [48], the discrepancy of the predicted and observed abundance of HeH^+ (formed from He^+ + H $\rightarrow$ HeH^+ + $h\nu$) in planetary nebulae [49], and the effect of He^+ removal (He^+ +He $\rightarrow$ He_2^+ +$h\nu$) on the abundance of CO in the ejecta of supernovae (since He^+ + CO $\rightarrow$ He + C^+ +O) [50]. Charge transfer (CT) in the H^+ + He system has also been studied theoretically [48] (where RA was found to dominate over CT only at low T), as well as radiative charge transfer in systems such as C^{++} + H [51]. Radiative quenching of He(2S) by collisions with He(1S) has also been studied, where different computational methods to determine the quenching cross-section were compared [17]. Beyond H and He, the RA of several biological precursor molecular ions which have been observed in the interstellar medium have also been studied, e.g. for CO^+ [52] and CH^+ [53]. Experimentally, RA between acetylene ions and hydrogen ($C_2H_2^+$ +H_2 $\rightarrow$ $C_2H_4^+$ + $h\nu$) has been investigated using an 80 K ring-electrode ion trap, and rate constants as high as $\approx 10^{-13}$ cm^3 s^{-1} measured [54]. Other experimental apparatus has been used, such as penning traps [55], and the selected-ion flow tube (SIFT) apparatus [56] to study for example associative reactions of CH_3^+ + H_2. At present, experiment still lags theory in the chemical breadth and energy range with

which investigations of RA, and indeed RCT and NRCT of ion-neutral systems can be undertaken. The recent development of hybrid trapping technologies such as those described in this work, provide new opportunities to extend the range of ion-neutral collision energies, and increase the accuracy with which rate constants and branching ratios of these processes can be experimentally determined. These results can then provide a test for the theory, inform astrophysical and astrochemical models, and in such a way provide a better understanding of the scientific observations made in these environments.

The three processes NRCT, RCT, and RA, form the majority of observed reactive processes in this work. It is quite possible that all three reactive processes, as well as nonreactive elastic scattering, compete from a single entrance channel. It will be seen that this is indeed the case in ground state collisions of Ca^+ + Rb.

1.3 Interaction of light with matter

Section 1.1 described the importance of light in the development of the cooling and trapping of species down to low temperatures, and the resulting benefits for studies of cold collisions. The interaction of coherent light with atoms and atomic ions forms a key topic in this work, not only in the generation of cold reaction partners, but also in the ability to investigate state-specific reactions. This section describes in detail the theoretical concepts behind laser cooling, sub-Doppler laser cooling, and magneto-optical trapping, and in doing so introduces the concepts of sublevels of electronic states, polarization of light, transition selection rules, and the determination of state population under different conditions, all of which are indispensable for the implementation and interpretation of the experiments of this work.

1.3.1 Semiclassical theory of light-matter interaction

The starting point for the treatment of the interaction of light and matter in this work is semiclassical theory, whereby the matter, or in this case atom, is treated quantum mechanically, and the light is treated as a classical electromagnetic wave. This semiclassical description is a good approximation in the case of relatively strong coherent light fields, but does not include any description of effects like spontaneous emission, or the lamb shift, and hence is not suitable for situations where only a few photons are involved. Fig. 1.5 shows a schematic of the system at hand.

The energy E_n of the n^{th} eigenstate $|\Psi_n\rangle$ of the valence electron of an atom with an Hamiltonian $\hat{H}_A$, is calculated using the Schrödinger equation

$$\hat{H}_A|\Psi_n\rangle = E_n|\Psi_n\rangle \tag{1.25}$$

and has the value $\hbar\omega_n$, where ω_n is the angular frequency of the electron, and $\hbar$ is Planck's constant divided by 2π. The light field $\mathbf{E}$ (in this case a laser field), is

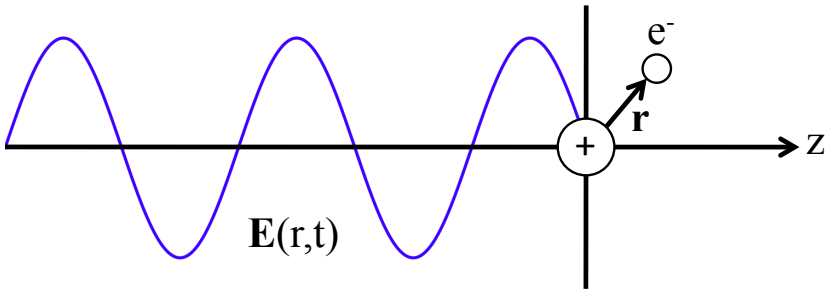

Figure 1.5: Interaction of a classical light field **E** with an atom consisting of a valence electron, and a core of single positive charge separated by **r**.

treated as a classical electromagnetic wave, with wave vector k, angular frequency ω, propagating along z with time t

$$\mathbf{E}(r,t) = \mathbf{E}_0 \cos(kz - \omega t) \tag{1.26}$$

The total Hamiltonian for the system is then the sum of the Hamiltonians describing the atom $\hat{H}_A$, the light field $\hat{H}_F$, and the interaction between them $\hat{H}_I$. In the semiclassical approach, the Hamiltonian of the light field is neglected, since it is treated as and external classical field. The total Hamiltonian is then

$$\hat{H} = \hat{H}_A + \hat{H}_I \tag{1.27}$$

where

$$\hat{H}_I = -\hat{\mu} \cdot \mathbf{E}(\mathbf{r} = 0, t) + \ldots \tag{1.28}$$

where $\hat{\mu} = -\mathrm{e}\hat{r}$ is the electric dipole moment operator of the atom, where e is the elementary charge. In the dipole approximation, the higher order terms denoted by the three dots in equation 1.28 are neglected. This is a good approximation if the field does not vary significantly over the extent of the atom. Typical atomic extensions are on the order of 10^{-10} m, and the typical wavelength of light used in this work is on the order of 10^{-6} m, and hence the dipole approximation is reasonable in this case. The interaction Hamiltonian becomes

$$\hat{H}_I(t) = -\mathrm{e} \cdot \hat{r} \cdot \mathbf{E}_0 \cos(\omega t) \tag{1.29}$$

The total Hamiltonian is now applied in the time-dependent Schrodinger equation

$$i\hbar \frac{\partial}{\partial t} |\Psi(t)\rangle = (\hat{H}_A + \hat{H}_I(t)) |\Psi(t)\rangle \tag{1.30}$$

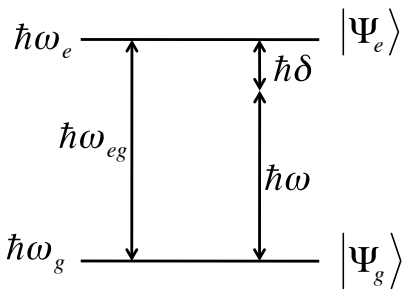

Figure 1.6: Schematic of a two level system with a ground (g) and excited (e) state. The quantities attributed to the diagram are defined in the text.

where $|\Psi(t)\rangle$ can be written as sum of the products of time independent wave functions $|\Psi_n\rangle$ and time dependent coefficients $c_n(t)$

$$|\Psi(t)\rangle = \sum_n c_n(t) e^{-i\omega_n t} |\Psi_n\rangle \tag{1.31}$$

where $i = \sqrt{-1}$. Combining equations 1.30 and 1.31, multiplying from the left by $\langle\Psi_m|$, using the properties of orthonormality ($\langle\Psi_n|\Psi_m\rangle = \delta_{nm}$), and rearranging, the Schrödinger equation becomes

$$i\hbar\dot{c}_m = \sum_n c_n(t) e^{-i(\omega_n - \omega_m)t} \langle\Psi_m|\hat{H}_I(t)|\Psi_n\rangle \tag{1.32}$$

where

$$\langle\Psi_m|\hat{H}_I(t)|\Psi_n\rangle = -\mathrm{e} \cdot \mathbf{E}_0 \cdot \langle\Psi_m|\hat{r}|\Psi_n\rangle \cdot \cos(\omega t) \tag{1.33}$$

and can be solved numerically.

1.3.2 The two-level system

Equation 1.32 can be solved numerically. In order to continue analytically it is useful to make the approximation that the electron can only exist in a limited number of eigenstates. It is useful in the case of the applications of this work to approximate to a two level system, since the scattering of light needed for laser cooling of a species is most efficient in a two-level type system. Figure 1.6 shows a schematic of such a system, and contains quantities defined by the following: laser frequency ω, atomic transition frequency $\omega_{eg} = \omega_e - \omega_g > 0$, and detuning of the laser frequency from the atomic transition frequency $\delta = \omega - \omega_{eg}$. Let the following definitions also be made; firstly that the dipole matrix element in the notation of the two level system becomes

$$\mu_{eg} = \mathrm{e}\langle\Psi_e|\hat{r}|\Psi_g\rangle, \tag{1.34}$$

secondly that the following factors can be combined in such a way as to define the Rabi frequency Ω_R,

$$\Omega_R = \frac{\mu_{eg} \cdot \mathbf{E}_0}{\hbar}, \tag{1.35}$$

and lastly that the interaction matrix elements can be denoted by the following convention

$$H_{Inm} = \langle \Psi_n | \hat{H}_I(t) | \Psi_m \rangle. \tag{1.36}$$

Due to parity considerations, i.e. that the integral over all space of an odd function is zero, the matrix elements H_{Igg} and H_{Iee} are zero. The dipole matrix element for the coupling of ground and excited states can be written

$$H_{Ieg} = \hbar\Omega_R \cos(\omega t) \tag{1.37}$$

which by Euler's relations can be written

$$H_{Ieg} = \frac{1}{2}\hbar\Omega_R(e^{i\omega t} + e^{-i\omega t}) \tag{1.38}$$

If the sum of equation 1.31 is reduced to the two level system, the general state of the atom can now be written

$$|\Psi(t)\rangle = c_g(t)e^{-i\omega_g t}|\Psi_g\rangle + c_e(t)e^{-i\omega_e t}|\Psi_e\rangle \tag{1.39}$$

Applying this to equation 1.32 in the case of the two level system, and using the fact that the matrix elements H_{Ieg} and H_{Ige} are complex conjugates, such that $\mathrm{H}_{Ieg} = \mathrm{H}^*_{Ige}$ and vice versa, the Schrödinger equation now becomes

$$i\hbar\dot{c}_g(t) = c_e(t)\frac{1}{2}\hbar\Omega^*_R(e^{i(\omega-\omega_{eg})t} + e^{-i(\omega+\omega_{eg})t}) \tag{1.40}$$

and

$$i\hbar\dot{c}_e(t) = c_g(t)\frac{1}{2}\hbar\Omega_R(e^{i(\omega+\omega_{eg})t} + e^{-i(\omega-\omega_{eg})t}) \tag{1.41}$$

1.3.3 The Rabi equations for a two-level system

In order to proceed analytically, it is useful to make the rotating wave approximation. This approximation makes use of the fact that for the applications under consideration, the detuning of the laser frequency from the atomic transition is relatively small, such that $(\omega - \omega_{eg})$ is a relatively small quantity, and so the oscillations of the functions in equations 1.40 and 1.41 attributed to this exponent will be relatively slow. The quantity $(\omega + \omega_{eg})$ in comparison is relatively large, and so the functions attributed to this exponent will oscillate rapidly (typically $\omega \approx \omega_{eg} \approx 10^{15}$ Hz), and hence average to zero on the timescales considered in the applications of this work. Removing such

terms from equations 1.40 and 1.41 leads to

$$i\dot{c}_g(t) = c_e(t)\frac{1}{2}\Omega_R^* e^{i\delta t} \tag{1.42}$$

and

$$i\dot{c}_e(t) = c_g(t)\frac{1}{2}\Omega_R e^{-i\delta t} \tag{1.43}$$

where $\delta = \omega - \omega_{eg}$. The coefficients of equations 1.42 and 1.43 can be made time independent by defining a_g and a_e such that

$$c_g(t) = a_g e^{i\frac{\delta}{2}t} \tag{1.44}$$

and

$$c_e(t) = a_e e^{-i\frac{\delta}{2}t}. \tag{1.45}$$

By applying these definitions to equations 1.42 and 1.43, performing the time derivatives, and canceling through the resulting exponential factors, the following pair of linear differential equations with constant coefficients is realized

$$\dot{a}_g = -\frac{i}{2}\Omega_R^* a_e - \frac{i}{2}\delta a_g \tag{1.46}$$

$$\dot{a}_e = -\frac{i}{2}\Omega_R a_e + \frac{i}{2}\delta a_e \tag{1.47}$$

which written in matrix notation becomes

$$i\hbar\frac{d}{dt}\begin{pmatrix} a_e \\ a_g \end{pmatrix} = \frac{\hbar}{2}\begin{pmatrix} -\delta & \Omega_R \\ \Omega_R^* & \delta \end{pmatrix} \cdot \begin{pmatrix} a_e \\ a_g \end{pmatrix} \tag{1.48}$$

where the 2×2 matrix is referred to as the Hamiltonian matrix. This system of linear differential equations with constant coefficients has a general analytic solution, which form the Rabi equations

$$a_g(t) = a_g(0)\left[\cos\left(\frac{\Omega t}{2}\right) - \frac{i\delta}{\Omega}\sin\left(\frac{\Omega t}{2}\right)\right] + i\frac{\Omega_R^*}{\Omega}a_e(0)\sin\left(\frac{\Omega t}{2}\right) \tag{1.49}$$

$$a_e(t) = a_e(0)\left[\cos\left(\frac{\Omega t}{2}\right) + \frac{i\delta}{\Omega}\sin\left(\frac{\Omega t}{2}\right)\right] + i\frac{\Omega_R}{\Omega}a_g(0)\sin\left(\frac{\Omega t}{2}\right) \tag{1.50}$$

where the effective Rabi frequency has been defined by

$$\Omega = \sqrt{|\Omega_R|^2 + \delta^2}. \tag{1.51}$$

In order to illustrate the behavior that the above equations imply, it is useful to apply some initial conditions. The most natural set is to consider an atom (or indeed an

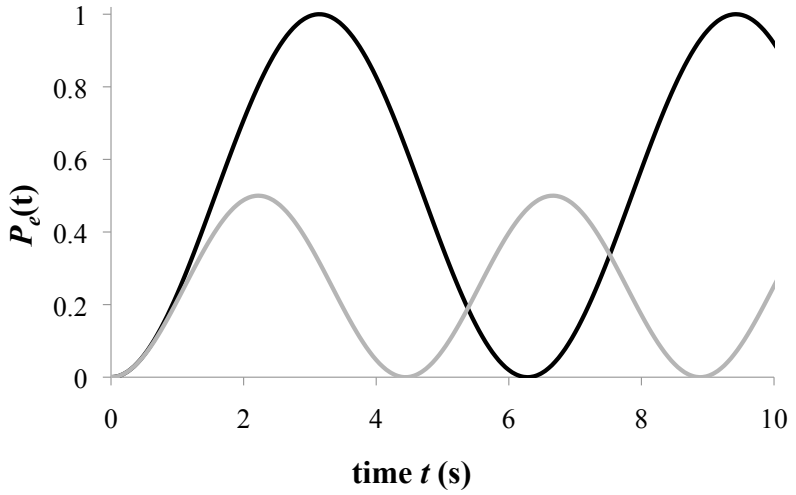

Figure 1.7: Plot of equation 1.53 showing the Rabi oscillations of excited state population as a function of time for $\Omega = \Omega_R$ with $\delta = 0$ (black trace), and with $\delta = \Omega_R$ (grey trace).

ensemble of identical atoms, whose behavior should also be reflected by these equations) in the ground state, and the light field being applied at $t = 0$, such that $a_g(0) = 1$, and $a_e(0) = 0$. If we define the population of state m to be $P_m(t) = |a_m(t)|^2$, it can be seen that the populations oscillate with a characteristic frequency determined by the effective Rabi frequency Ω:

$$P_g(t) = \frac{|\Omega_R|^2}{\Omega} \cos^2\left(\frac{\Omega t}{2}\right) + \frac{\delta^2}{\Omega^2} \tag{1.52}$$

$$P_e(t) = \frac{|\Omega_R|^2}{\Omega} \sin^2\left(\frac{\Omega t}{2}\right). \tag{1.53}$$

The oscillations of population, and the dependence on detuning is shown in Fig. 1.7, where $P_e(t)$ is plotted for the cases where $\Omega = \Omega_R$ with $\delta = 0$ (black trace), and when $\delta = \Omega_R$ (grey trace).

1.3.4 The optical Bloch equations for a two-level system

So far the effects of spontaneous emission have been completely ignored, which is not a good approximation, because the coupling of the atomic dipole to the electromagnetic vacuum modes is not negligibly weak. The picture must be altered to include the lifetime of the excited state τ, and hence a decay rate of the excited state population $\Gamma = 1/\tau$. This updated picture appears schematically in Figure 1.8. The scattering

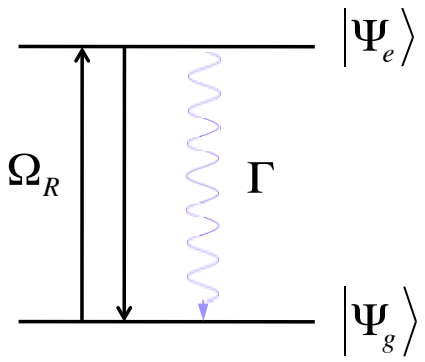

Figure 1.8: Schematic of a two level system with transfer of population by stimulated absorption and emission at a rate governed by Ω_R, and spontaneous emission at a rate governed by Γ.

rate for a two level system can be derived using Wigner-Weisskopf theory [2, 57]. The derivation is beyond the scope of this work, and just the result is presented here

$$\Gamma = \frac{\omega_{eg}^3 |\mu_{eg}|^2}{3\pi\epsilon_0 \hbar c^3}, \tag{1.54}$$

where c is the speed of light in vacuum. The picture is now of Rabi oscillations interrupted by spontaneous emission. In the case of a single atom, this would result in the population of the excited state dropping to zero after every spontaneous emission event. In the case of an ensemble of many atoms, since spontaneous emission is not correlated between the atoms, the average excited state population of all the atoms would resemble Rabi oscillation at short times; which is then damped by spontaneous emission, resulting at long times in a steady state average excited state population. In order to describe this behavior mathematically it is useful do define the density matrix ρ_{nm}, whose elements are

$$\rho_{nm} = \langle \Psi_m | \hat{\rho} | \Psi_n \rangle = a_m a_n^*, \tag{1.55}$$

where $\hat{\rho}$ is the density operator for a state $\hat{\rho} = |\Psi\rangle\langle\Psi|$. For the two level system, the density matrix can be written

$$\hat{\rho} = \begin{pmatrix} |a_e|^2 & a_e a_g^* \\ a_g a_e^* & |a_g|^2 \end{pmatrix}, \tag{1.56}$$

where the diagonal elements correspond to populations, and the off diagonal elements correspond to coherences between the levels. The dynamics can be described using the Heisenberg equation of motion

$$\frac{d}{dt}\hat{\rho} = \frac{i}{\hbar}\left[\hat{\rho}, \hat{H}\right] \tag{1.57}$$

which in matrix form can be written

$$\dot{\rho}_{mn} = \frac{i}{\hbar} \sum_k \left(\rho_{mk} H_{kn} - H_{mk} \rho_{kn} \right). \tag{1.58}$$

As was seen in equation 1.48, in the dipole and rotating wave approximations, the Hamiltonian can be written as

$$H_{ij} = \frac{\hbar}{2} \begin{pmatrix} -\delta & \Omega_R \\ \Omega_R^* & \delta \end{pmatrix}. \tag{1.59}$$

Equation 1.58 and 1.59 can be combined to give a set of differential equations. The results are the optical Bloch equations, which comprise each of a term that describes the Hamiltonian dynamics of the two level system, and a damping term describing spontaneous emission that has been added by hand. The optical Bloch equations for a two level system are presented below.

$$\dot{\rho}_{ee} = \frac{i}{2} \left(\Omega_R^* \rho_{eg} - \Omega_R \rho_{ge} \right) - \Gamma \rho_{ee} \tag{1.60}$$

$$\dot{\rho}_{gg} = -\frac{i}{2} \left(\Omega_R^* \rho_{eg} - \Omega_R \rho_{ge} \right) + \Gamma \rho_{ee} \tag{1.61}$$

$$\dot{\rho}_{eg} = \frac{i}{2} \Omega_R \left(\rho_{ee} - \rho_{gg} \right) + i\delta_{eg} - \frac{\Gamma}{2} \rho_{eg} \tag{1.62}$$

$$\rho_{ge} = \rho_{eg}^* \quad \text{(always true)}. \tag{1.63}$$

If there is no laser such that $\Omega_R = 0$, then the excited state population undergoes an exponential decay. If there is a strong laser present, then the spontaneous decay becomes unimportant at short times, and the dynamics consists of the coherent Rabi oscillations.

1.3.5 Steady state populations of a two-level system

In some applications it is useful to know the populations of the states at equilibrium, or in other words the "steady-state" populations. The expected steady state populations can be retrieved from the optical Bloch equations stated above by setting all of the time differentials, i.e. the rate of change of population and coherences, to zero. After some algebra the excited steady state population is deduced

$$\rho_{ee} = \frac{|\Omega_R|^2}{\Gamma^2 + 4\delta^2 + 2|\Omega_R|^2} \tag{1.64}$$

This equation can be written in a more intuitive form by introducing the saturation intensity of the atomic transition I_s, the intensity of the laser I, and the saturation

parameter S_0

$$I_s = \frac{\hbar\Gamma\omega_{eg}^3}{12\pi c^2} \tag{1.65}$$

$$I = \frac{c\epsilon_0}{2}|E_0|^2 \tag{1.66}$$

$$S_0 = \frac{I}{I_s} = \frac{2|\Omega_R|^2}{\Gamma^2} \tag{1.67}$$

such that the steady state solution now reads

$$\rho_{ee} = \frac{S_0/2}{1 + S_0 + \left(\frac{2\delta}{\Gamma}\right)^2}. \tag{1.68}$$

It is worth noticing that the maximum excited state population occurs when the saturation parameter approaches infinity, i.e. the laser intensity becomes infinitely large, and the population approaches 1/2. This condition is referred to as the saturation of a transition. From equation 1.68, the linewidth and lineshape of a transition can be deduced. Using that the photon scattering rate $\Gamma_P = \Gamma\rho_{ee}$, rewriting of equation 1.68 leads to

$$\Gamma_P = \Gamma\rho_{ee} = \frac{S_0}{1 + S_0} \cdot \frac{\Gamma/2}{1 + \left(\frac{2\delta}{\Gamma_L}\right)}, \tag{1.69}$$

where

$$\Gamma_L = \Gamma(1 + S_0). \tag{1.70}$$

The second factor on the right hand side of equation 1.69 has the form of a lorentzian distribution, where Γ_L is the Full Width at Half Maximum (FWHM) of the lineshape. It can be seen the larger the laser intensity, the larger the FWHM of the line. This effect is known as power broadening. It can also be seen that the minimum linewidth corresponds to the natural lifetime of the excited state. The expression for the steady state population that has been derived will be crucial in many parts of this work, since the ion-neutral reaction rates can depend strongly on the population excited electronic states.

1.3.6 Light forces

A key aspect of the use of light to manipulate and cool atomic and ionic species, is that light is able to exert a force on these species. So far the effect of light on atomic motion has been neglected. The two level system continues to be useful when exploring these effects. The field is treated as in equation 1.26, except the field is now considered to be made of photons, each with a momentum $\hbar k$, where k is related to the wavelength of the light λ by $k = 2\pi/\lambda$. Three possible processes of light-matter interaction shall be considered: absorption, stimulated emission, and spontaneous emission. There are two combinations of these processes that lead to two different kinds of light forces on

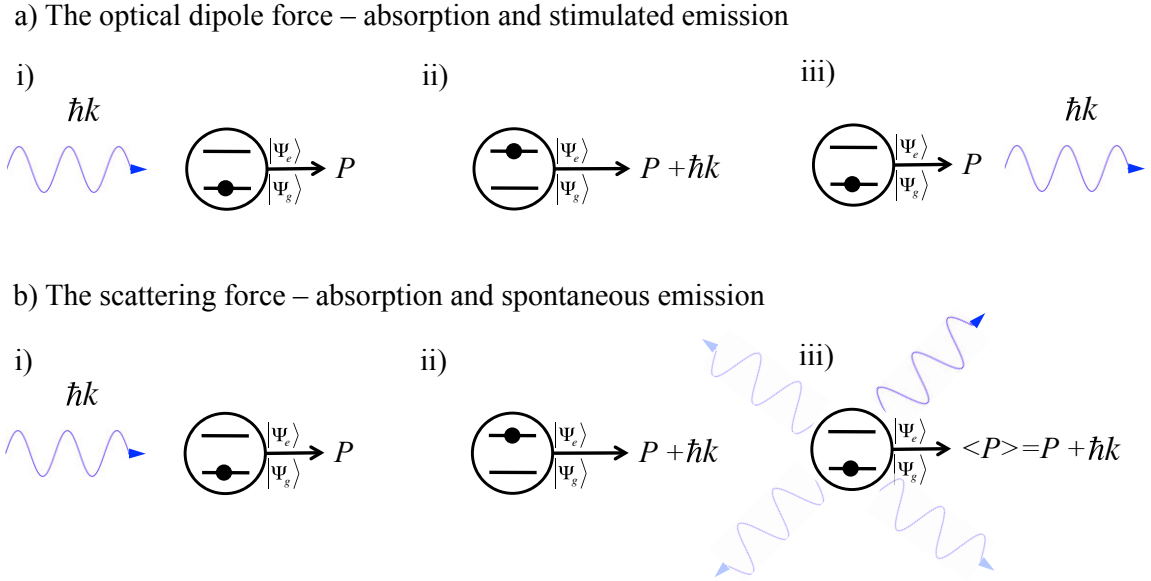

Figure 1.9: Schematic of the two different types of light force. (a) shows the optical dipole force where a photon is absorbed ((i)→(ii)), and then emitted coherently back to the light field (iii) and so there is no net change of atomic momentum P. (b) shows the scattering force where the photon is emitted in a random direction by spontaneous emission, and so there is a net change of atomic momentum over many such cycles in the direction of the laser field.

an atom. These processes are shown schematically in Fig. 1.9. In Fig. 1.9 (a) it can be seen that after absorption the photon is emitted coherently back into the laser field by stimulated emission, in which case there is no net momentum transfer to the atom. This process results in the optical dipole force. A full description of this force is beyond the scope of this work, but is briefly explained here. Although there is no net momentum transfer, there is still a force acting on the atom. When there is a detuning present in the laser frequency, a light shift is induced in the ground state. If the detuning is less than zero, then the light shift is such that the atom is attracted to intensity maxima. If two intense, far red detuned, counter propagating laser beams are present, then there is an intensity gradient, the maximum of which the atom will be attracted to. (It is worth noting that this force vanishes in a running plane wave.) This results in a conservative force, and is the working principle of optical-dipole traps. This force is relatively small, but does not saturate with intensity, so for intense beams it is possible to achieve trap depths on the order of 10^{-6} eV [58, 59].

In figure 1.9 (b) it can be seen that the photon may instead undergo spontaneous emission. The direction of the spontaneous emission is random, but the direction of absorption is always the same, and hence averaged over many cycles of absorption and

emission there is a net transfer of momentum to the atom in the direction of the laser field. This process corresponds to the scattering force. Since this process relies on spontaneous emission, this force F can be calculated as

$$F = \langle F \rangle = \hbar k \cdot \Gamma_P \tag{1.71}$$

and since Γ_P saturates at high intensities to a value of $\Gamma/2$, the maximum force on an atom is

$$F_{max} = \frac{\hbar k \Gamma}{2} \tag{1.72}$$

and hence the maximum acceleration is

$$a_{max} = \frac{F_{max}}{m} = \frac{\hbar k \Gamma}{2m} = v_r \frac{\Gamma}{2}, \tag{1.73}$$

where v_r is the recoil velocity

$$v_r = \frac{\hbar k}{m}. \tag{1.74}$$

As an example, consider ^{87}Rb, where $\lambda = 780$ nm, $\Gamma = 2\pi \times 6.1 \times 10^6$ Hz, so the recoil velocity is 5.9 mm s^{-1} and the maximum acceleration is 1.1×10^5 m s^{-1}, or 104 g. This is a large acceleration indeed, and it is worth noting that the force is maximized for species with a large natural linewidth and small wavelength of atomic transition.

1.3.7 Doppler Laser cooling

An application of the ability to apply forces on atomic or ionic species with light is to use the force such that the atoms momentum on average is reduced. Through the relation of expressions of kinetic energy $E_{\text{K.E.}} = \frac{1}{2}\frac{P^2}{m} = \frac{1}{2}mv^2$ where m is the mass of the species, v is the velocity, and P is the momentum, it can be seen that reducing the momentum is equivalent to reducing the kinetic energy. It is noticeable almost immediately that in order to apply a cooling force to a species without simultaneously heating, the force must be dissipative, and depend on the velocity of the species. A simple and effective way of doing this was first proposed by Hänsch in 1975 [60], and relies on the physics of the Doppler effect.

Consider, as before in section 1.3.6, a running wave with wave vector k and frequency ω, interacting with an atom which now has some velocity v directed opposite to that of the laser field. This scenario is presented schematically in Fig. 1.10. Given that the zero velocity detuning of the laser frequency from that of the atomic transition is $\delta_0 = \omega - \omega_{eg}$, then the detuning when the Doppler effect is considered can be written $\delta = \delta_0 - kv$. The scattering force of equation 1.71 now becomes

$$F = \hbar k \Gamma_P = \frac{\hbar k \Gamma}{2} \cdot \frac{S_0}{1 + S_0 + 2\left(\frac{\delta_0 - kv}{\Gamma}\right)^2}. \tag{1.75}$$

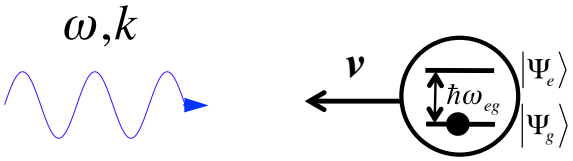

Figure 1.10: A schematic of a two level atom moving towards a traveling plane wave with velocity v.

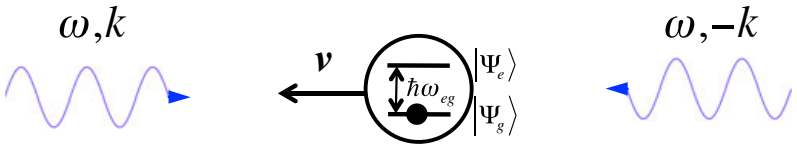

Figure 1.11: An atom in the field of two counter propagating laser beams.

For small v, a Taylor expansion of equation 1.75 can be made around $v = 0$ to the lowest order in v, i.e.

$$F \approx F(v=0) + \left.\frac{\partial F}{\partial v}\right|_{v_0} \cdot v \tag{1.76}$$

or

$$F \approx F_0 - \beta v \tag{1.77}$$

where β is the damping coefficient for a single beam

$$\beta = -\hbar k^2 \frac{4S_0\left(\frac{\delta_0}{\Gamma}\right)}{\left[1 + S_0 + \left(\frac{2\delta_0}{\Gamma}\right)^2\right]^2} \tag{1.78}$$

For $\delta_0 < 0$ (known as red detuning), $\beta > 0$, and hence damping of v, and so cooling of the species, is in effect. Also the requirement of effective laser cooling that the force is dependent on velocity is fulfilled, such that the lower velocity, the weaker the force on the atom. It is worth noting the maximum damping coefficient is achieved for $\delta_0 = -\Gamma/2$, and $S_0 = 2$, such that $\beta_{max} = \hbar k^2/4$. The term F_0 however in equation 1.77 corresponds to a constant acceleration, and hence once the atom is slowed to a stop, it will be accelerated again in the opposite direction. A single laser beam configuration like this therefore can only be used for the slowing of atomic beams, rather than stable cooling.

In order to effect a purely velocity dependent force, and hence achieve stable cooling, the use of two counter-propagating laser beams is required. This scenario is presented schematically in Fig. 1.11. Assuming a small saturation parameter, the forces of the

two beams can simply be added together, and since

$$F_{\pm} = \frac{\hbar k \Gamma}{2} \cdot \frac{S_0}{1 + S_0 + 2\left(\frac{\delta_0 \pm kv}{\Gamma}\right)^2}, \tag{1.79}$$

then the F_0 terms in the Taylor expansion to the lowest order in v of the sum cancel, and returns $F \approx -\beta v$ where

$$\beta = 8\hbar k^2 \frac{\delta_0 S_0}{\left[1 + S_0 + \left(\frac{2\delta_0}{\Gamma}\right)^2\right]^2} \tag{1.80}$$

and hence for low saturation parameters, there is a purely velocity dependent force. This configuration is known as the "one dimensional optical molasses configuration" owing to the viscous damping atoms experience within the beams. It is worth noting that atoms whose initial velocity is greater than a certain critical value v_c, will not be cooled, and for typical parameters of Doppler cooling $v_c \approx \Gamma/k$. It is also worth noting that no trapping of the atoms occurs in this scheme, since the force doesn't depend on the atoms position, but only its velocity. The extension of this one dimensional system to three orthogonal pairs of counter propagating beams is known as "optical molasses" and was first demonstrated experimentally in 1985 by S. Chu *et al* [61].

There is a limit to which this method can cool atomic or ionic species, the scale of which is set by the recoil of scattering a single photon in a random direction by spontaneous emission. By equating the rate of the random walk due to this effect, and the rate momentum is taken away from the system by laser cooling, it is possible to arrive at an expression for the Doppler limit of temperature T_D [2],

$$k_B T_D = \frac{\hbar \Gamma}{2} \tag{1.81}$$

which for example in ^{87}Rb (assuming a two level system), $T_D = 146$ μK.

1.3.8 Multilevel systems

When it is taken into consideration that no species is a two level system, and that more levels are likely to play a role in laser cooling, other cooling mechanisms become apparent which can take the minimum of kinetic energy achievable by laser cooling below the Doppler limit. In order to understand these effects, the level structure of the species must be well understood. Since laser cooling requires the scattering of many photons on a single transition, it is useful to choose the alkali metal atoms as an illustrative example, since their electronic structure is closed shell with a single valence electron. As a result they have hydrogen-like spectra, with the lifetime of the P state with respect to the S state being very short ($\approx$ a few ns), and transitions thereof in the most part lying in the visible part of the spectrum, where laser diodes are commercially

available. They are good candidates then for laser cooling, and indeed to this date all but francium of the alkalis have been successfully laser cooled experimentally. The structures of the alkali atoms are similar, and all pertain to the following discussion.

- The electrons are formed of a closed shell with zero angular momentum, and a single valence electron that possesses orbital angular momentum **L** and spin **S**.

- The spin-orbit interaction couples L and S such the total electronic angular momentum is $\mathbf{J} = \mathbf{L} + \mathbf{S}$. The resulting split energy levels are know as the fine structure, whose characteristic energy shifts are $E_{FS} = (A_{SO}/2) \cdot [J(J+1) - L(L+1) - S(S+1)]$ where A_{SO} is the spin-orbit splitting constant.

- Given the electronic quantum numbers n, l, s, and J are the principle, orbital angular momentum, spin angular momentum, and total electronic angular momentum quantum numbers respectively; each level can be assigned a term symbol in the Russel-Saunders notation $n^{2S+1}L_J$. For example the ground state of ^{87}Rb is $5\ ^2S_{1/2}$.

- For those atoms with a non-zero nuclear spin I, the total electronic angular momentum can couple with the nuclear spin such that the total angular momentum of the atom $\mathbf{F} = \mathbf{J} + \mathbf{I}$. The resulting split levels are known as the hyperfine structure, whose characteristic energy level shifts are

$$E_{HFS} = \frac{1}{2}A_{HFS}K + B_{HFS}\left(\frac{\frac{3}{2}K(K+1) - 2I(I+1)J(J+1)}{2I(I+1) - 2J(J+1)}\right) \tag{1.82}$$

  where

$$K = F(F+1) - I(I+1) - J(J+1) \tag{1.83}$$

  and A_{HFS} and B_{HFS} are experimentally determined constants associated with the species.

- Given an externally applied magnetic field, each Hyperfine level is further split into its Zeeman sublevels $m_F = F, F-1, \ldots, -F$ where the characteristic energy shift is given by $E_{Zeeman} = g_F \mu_B B m_F$ where B is the magnetic field strength, μ_B is the Bohr magneton, and g_F is the Landé g factor.

As an illustration of the above structure, Fig. 1.12 shows a schematic of the splittings of the ground state of ^{87}Rb.

Also important when considering multi-level systems as compared to the two level system, are selection rules for optical transitions, since transitions between any two levels in the complex multi-level system may not necessarily be allowed. A full derivation of all of the dipole selection rules is beyond the scope of this work, but can be found for example in reference [2]. Suffice is to say that the "allowdness" of a transition depends on the dipole matrix element

$$\mu_{eg} = e\langle n', l', S', J', I', F', m'_F | \epsilon \cdot \hat{r} | n, l, S, J, I, F, m_F \rangle \tag{1.84}$$

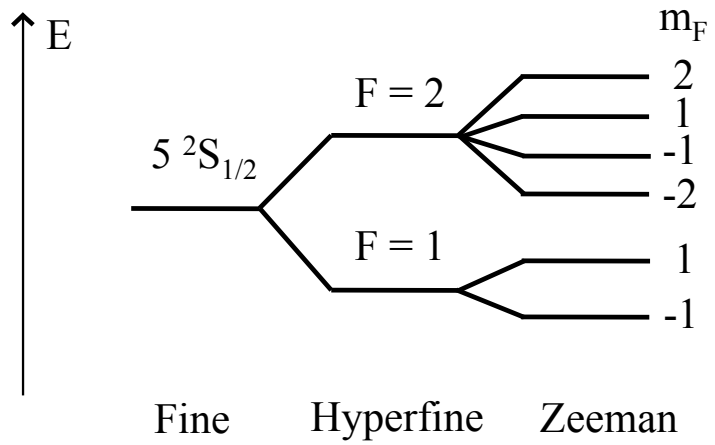

Figure 1.12: A schematic of the fine, hyperfine, and Zeeman splitting of the ground state of ^{87}Rb.

where ϵ is the polarization vector of the laser, and $\hat{r}$ is the electron position operator. Using conservation of angular momentum, and parity rules, it is possible to derive the following selection rules for a dipole transition.

- $\Delta I = \Delta S = 0$ (because the dipole operator cannot change spin)
- $\Delta L = \pm 1$
- $\Delta J = 0, \pm 1$ (but $J = 0$ to $J' = 0$ is forbidden since this would imply $\Delta L = 0$)
- $\Delta F = 0, \pm 1$ (but $F = 0$ to $F' = 0$ is forbidden since this would imply $\Delta L = 0$)
- $\Delta m_F = 0$ for linear polarization (π), +1 for right handed circularly polarized light (σ^+), and -1 for left handed circularly polarized light (σ^-).

1.3.9 Sub-Doppler laser cooling

The tools are now in place to describe the sub Doppler cooling that can be observed in such complex multilevel systems. It is now considered that the pair of counter propagating lasers, as in the case of the one dimensional optical molasses, now have polarizations such that they are both linearly polarized, but their axes of linear polarization are perpendicular. The beams produce a standing wave, whose polarization varies periodically with every whole wavelength. It can be shown that the variation of the polarization over half a period of the standing wave corresponds to that shown schematically in Fig. 1.13. It is useful to note that the coupling of the light field to the various transitions depends on the polarization. This can be determined using the selection rules listed above. Consider by way of example the case where the ground state of the system has $J = 1/2$, and the excited state has $J = 3/2$. (Note this is the

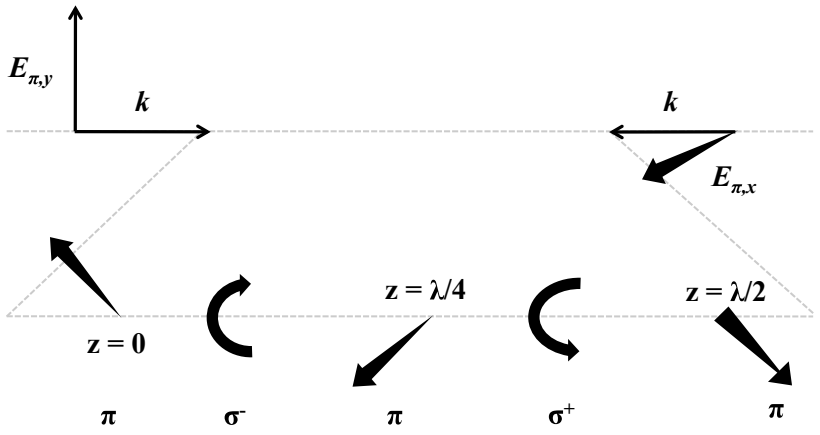

Figure 1.13: Schematic of the variation of polarization over half a wavelength of a standing wave generated by two laser beams, whose polarization axes were initially perpendicular.

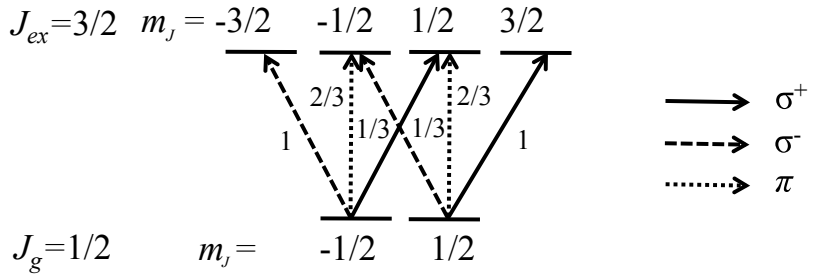

Figure 1.14: Polarizations and Clebsch-Gordon coefficients of transitions between magnetic sublevels of two hyperfine levels of an atom.

case for the cooling transition of ^{87}Rb.) The m_F sublevels can be connected by light of certain polarizations, and the relative strengths of each transition can be derived from $|c_{eg}|^2$ where c_{eg} are the Clebsch-Gordon coefficients of the transition. These transitions are illustrated in Fig. 1.14. Consider now an atom with the energy level structure as depicted in Fig. 1.14, traveling through the standing wave as depicted in Fig. 1.13. At positions along the wave where the polarization is σ^+, the atom will undergo transitions such that it ends up in $|\frac{1}{2}, \frac{1}{2}\rangle$ (where the notation $|J, m_J\rangle$ has been employed). Similarly, at positions where the polarization is σ^-, the atom undergoes transitions such that it ends up in $|\frac{1}{2}, -\frac{1}{2}\rangle$. It can be seen that a moving atom gets pumped back and forth between the two magnetic sublevels of $J = 1/2$. Now consider that there is

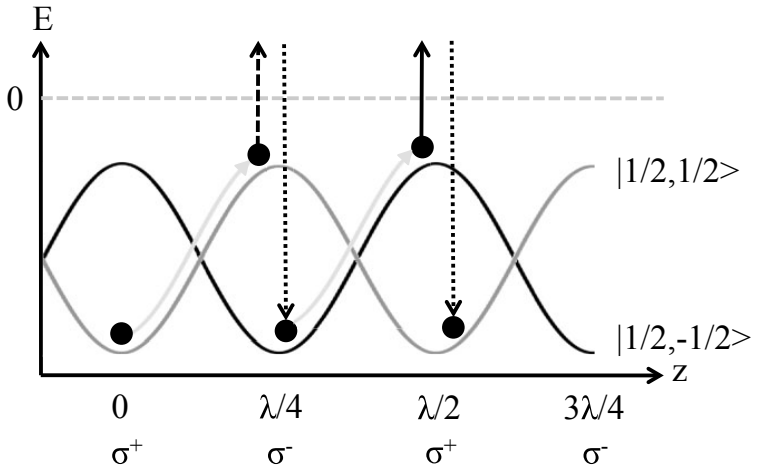

Figure 1.15: The mechanism of Sisyphus cooling for an atom with internal structure and transitions as in Fig. 1.14, traveling through a standing wave with polarizations as in Fig. 1.13. The oscillating black and grey curves represent the oscillating energies of the $|\frac{1}{2},\frac{1}{2}\rangle$ and $|\frac{1}{2},-\frac{1}{2}\rangle$ sublevels respectively, induced by the varying light shifts in regions of different light polarizations. The dashed and dotted arrows represent optical transition to and from the $J = 3/2$ excited state.

a polarization dependent light shift of the ground state, which can be written as [2]

$$\Delta E_g = \frac{\hbar\Gamma^2 S_0 |c_{eg}|^2}{4\delta}. \tag{1.85}$$

Since the light shift depends on the Clebsch-Gordon coefficients, with reference to Fig. 1.14, it can be seen for example that for σ^+, the light shift in $|\frac{1}{2},\frac{1}{2}\rangle$ is nine times stronger than for $|\frac{1}{2},-\frac{1}{2}\rangle$, and vice versa for σ^- light. So as the atom travels through the standing wave, the energy of the magnetic sublevels is oscillating, and the oscillation of the energy of the $|\frac{1}{2},\frac{1}{2}\rangle$ and $|\frac{1}{2},-\frac{1}{2}\rangle$ sublevels is 180° out of phase, such that when one is experiencing its maximum light shift, the other its experiencing its minimum. The key to the sub-Doppler cooling mechanism, is that pumping is most likely to occur from the sublevel that is least shifted, to the sublevel that is most shifted for a given polarization region. As a result, the atom is always traveling towards a region where its internal energy is higher (and hence its kinetic energy is lowered by traveling there), and when it reaches near the maximum, its is pumped to the sublevel where the internal energy is minimized, but has not gained any kinetic energy in doing so. The atom is constantly traveling up a "hill" of internal level energy, and losing kinetic energy in doing so. This cooling mechanism is referred to as "Sisyphus cooling" in reference to the Greek myth where Sisyphus is condemned to roll a boulder up a mountain, only to watch it roll down, and have to start again. A schematic of the mechanism of Sisyphus cooling is presented in figure 1.15.

The damping force on the atom, β, is increased by a factor of $2|\delta|/\Gamma > 1$ for typical Doppler cooling, and hence cooling below the Doppler limit becomes possible. The picture of Doppler and sub Doppler cooling mechanisms is extendable to three dimensions, i.e. for beams in an optical molasses configuration, and also extendable to setups which use counter propagating beams of σ^+ and σ^- polarization [62], which are however more difficult to conceptualize into simple schematic pictures.

1.3.10 The magneto-optical trap (MOT)

In the description of the interaction between light and matter so far, only light forces that damp the motion of a species have been investigated. Although optical molasses will lead to an increase of atomic density in the region of intersection of the beams above background, the atoms are free to drift out of this region. In this case the atoms are not trapped, as there is no position dependent force to create a potential in which the atoms might be held. The trapping of atoms is important for many desired applications of atomic, molecular and optical physics, and its achievement has led to many important discoveries, not least that of Bose-Einstein condensation [9], photoassociation [63], and matter wave applications [8]. In this work, the main advantages of trapped cooled atoms over just cooled atoms, are the dramatic increase of atomic density in traps, and an enhanced ability to characterize the density distribution and temperature of the atoms in the trap. The observation of just a few single reaction events requires a reasonable density of the reactants, such that the events can be monitored on a reasonable timescale. The lower bound of this timescale is set in this work by the response of the technology needed to image the reactants (≈ 100 ms), whilst the upper bound is set by the the reaction rate of the ions with background gas (≈ 1000 s). The typical rate constants associated with the processes studied in this work ($10^{-13} - 10^{-8}$ cm^3 s^{-1}) are such that for densities typical of atomic traps ($10^8 - 10^{12}$ cm^{-3}), the timescale for reactions of atoms with the ions fall within the required observation window, and hence atom traps are useful for studying these types of processes. The accurate measurement of reaction rates also requires an accurate knowledge of the density, and density distribution of the reactants. Since the characterization of these properties is a well-known and relatively straightforward procedure for atom traps, their use in reaction studies is also advantageous. A magneto-optical trap for ^{87}Rb was used in this work, whose working principles will now be described.

Following from subsection 1.3.7, a simple extension of the optical molasses configuration of orthogonal pairs of σ^+ and σ^- polarized beams to a trap effecting both cooling and trapping forces was first demonstrated in 1987 by Raab *et al* [62]. The necessary position dependence of the light force for trapping was provided by the addition of a quadrupolar magnetic field, whose magnitude was zero in the center of the trap, and increased linearly with distance from the trap center. This magnetic field was provided by two coils of wire with current passing through them in opposite directions (i.e. in an anti-Helmholtz configuration). The combination of σ^+/σ^- optical molasses with

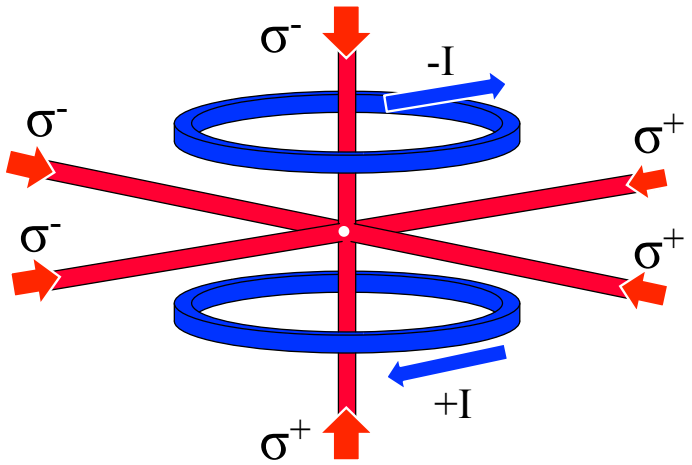

Figure 1.16: A schematic of a magneto-optical trap (MOT) consisting of three orthogonal pairs of counter propagating circularly polarized laser beams (in red), and two wire coils in an anti-Helmholtz configuration with current I (in blue).

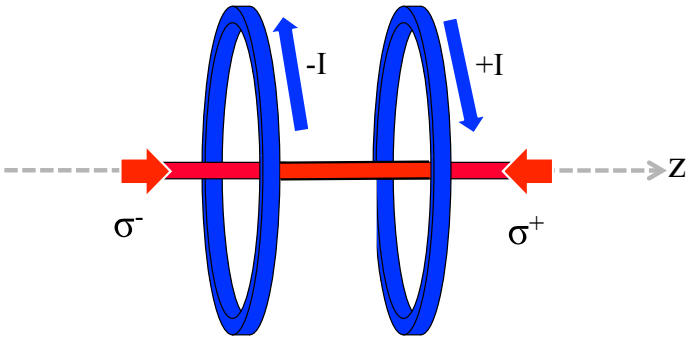

Figure 1.17: A schematic of two counter propagating circularly polarized laser beams passing through the axis of two wire coils with current I, in an anti Helmholtz configuration. $z = 0$ is the point along z equidistant from the two coils.

such a magnetic field is known a "magneto-optical trap" (MOT) and has become the workhorse of atomic laser cooling experiments, and a schematic of the configuration is presented in Fig. 1.16. To get a picture of the working principles of the MOT, it is useful to consider the situation in one dimension, a schematic of which is presented in Fig.1.17.

In Fig. 1.17, the magnetic field along the principle axis is $B(z) = A \cdot z$, where A is a constant. From the Zeeman shift formula $E_{Zeeman} = g_J \mu_B B m_J$, it can be seen that the energy of magnetic sublevels shift linearly with magnetic field strength, and hence linearly with distance from $z = 0$. Consider a species whose ground state has $J_g = 0$,

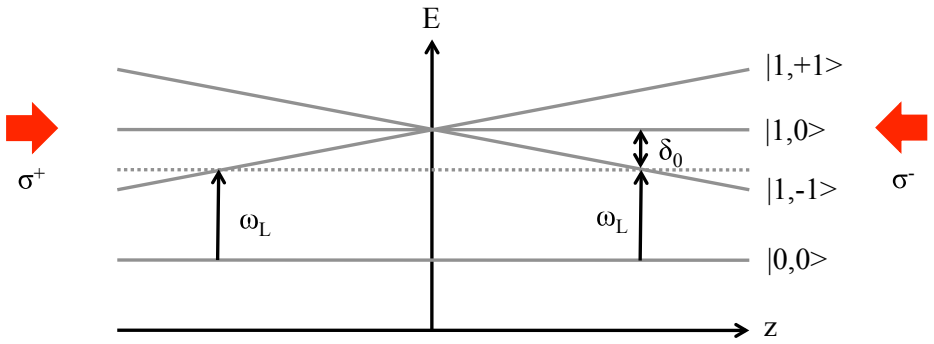

Figure 1.18: A schematic of the magnetic sublevels of an atom denoted $|J, m\rangle$, and the dependence of their energy on offset from the magnetic field zero at z=0. The dotted line is the energy of the ground sate plus that of the cooling lasers. ω_L is the frequency of the cooling lasers, which have circular polarizations σ^+ and σ^+, and which are detuned from the zero field atomic transition frequency by δ_0. The magnetic field strength along z is $B(z) = A \cdot z$ where A is a constant.

and whose excited state has $J_e = 1$. The ground state has only one magnetic sublevel where $m = 0$, but the excited state has three magnetic sublevels with $m = +1, 0, -1$. Since the energy level shift of the magnetic sublevel depends on m, the excited state sublevels all shift in a different way in response to a magnetic field. These shifts for different m can be seen schematically in Fig 1.18. The restoring force on the atom to the point $z = 0$ along z in Fig. 1.18 is described in the following. Consider an atom displaced in the $+z$ direction in state $|0, 0\rangle$. The energy of the magnetic sublevels in the excited state are shifted by the magnetic field via the Zeeman effect. In the $+z$ direction, the $|1, -1\rangle$ sublevel is brought closer into resonance with the cooling laser, which is detuned from the zero field atomic transition frequency so that Doppler cooling is in effect. The $|1, +1\rangle$ sublevel is shifted out of resonance, and the $|1, 0\rangle$ sublevel is not shifted by a magnetic field. Since the $|1, -1\rangle$ sublevel is shifted closer into resonance with the cooling laser, photons are more likely to be scattered from this state. Since the transition in this case requires $\Delta m = -1$, then from the selection rules outlined in section 1.3.8, the scattering of a photon with σ^- polarization is much more likely. The propagation direction of the laser beam with σ^- polarization is along $-z$, and so the scattering of these photons implies a net gain in momentum of the atom along $-z$, and so an atom straying into +z region will feel a restoring force towards z = 0. When that atom moves into the region of $-z$, the situation is reversed. Now scattering of σ^+ polarized photons is more likely, and so the atom is again restored towards $z = 0$. The cooling and restoring forces that an atom experiences in this one-dimensional configuration can be quantified by the following. Equation 1.75, which gave the force on an atom in the field of two counter propagating laser beams, can be

modified to include the magnetic field dependence of the detuning

$$F_{\pm} = \frac{\hbar k \Gamma}{2} \cdot \frac{S_0}{1 + S_0 + \left(\frac{2\delta_{\pm}}{\Gamma}\right)^2} \tag{1.86}$$

where

$$\delta_{\pm} = \delta_0 \mp kv \pm \frac{\mu' B}{\hbar} \tag{1.87}$$

where

$$\mu' = (g_e m_e - g_g m_g)\,\mu_B \quad \text{and} \quad B = A \cdot z \tag{1.88}$$

where the subscripts e and g pertain to the excited and ground states respectively. For small velocities and small displacements from the magnetic field zero, equation 1.86 can be expanded as in section 1.3.7 such that

$$F \approx -\beta v - \kappa z \tag{1.89}$$

where β is the same as shown in equation 1.80 for optical molasses, and κ is

$$\kappa = \frac{\mu' A}{\hbar k}\beta \tag{1.90}$$

There are now both damping and restoring forces, resulting in a trap which cools atoms automatically. The spring constant of the potential is κ, and so the trap frequency ω_{MOT} for an atom of mass m is given by $\omega_{MOT} = \sqrt{\kappa/m}$, which for typical MOT parameters is on the order of $2\pi \times 1$ kHz. This one-dimensional picture can be extended to three dimensions as long as the polarization and coil configuration of Fig 1.16 is upheld. There are then two degenerate trap frequencies along x and y, and a third along z, since the magnetic field gradient along z is typically half that along x and y. It is worth noting that the Sisyphus sub-Doppler cooling mechanism is still in effect in a magneto optical trap, since the scale over which the magnetic field varies is large compared to scale over which the polarization varies in the standing waves.

This section has derived, from a relatively fundamental starting point, the principles of operation of a magneto optical trap for Alkali atoms. The Alkali atom used in the entirety of this work is ^{87}Rb, and is the ultracold neutral reactant for all of the reactions studied. The practicalities of a MOT for ^{87}Rb, including its design, construction, implementation and characterization, are presented elsewhere in sections 2.3 and 4.

1.4 Ion trapping and cooling

In section 1.3, the cooling and trapping of atoms was discussed, in which light is used for both purposes. Due to their sensitivity to stray electric fields, and the large inter-species Coulomb forces, it is prohibitively difficult to trap more than one ion sufficiently

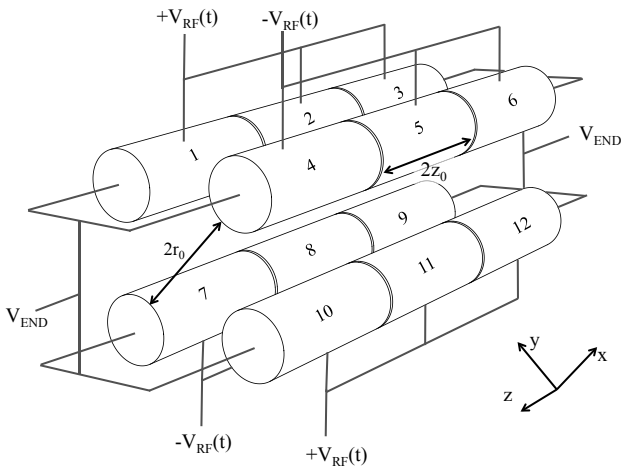

Figure 1.19: Schematic of the rods of the ion trap showing key static endcap (END) and radio frequency (RF) voltage assignments, and dimension definitions.

strongly with light alone. The ions' sensitivity to electric fields can alternatively be viewed as a distinct advantage, as it allows them to be very strongly controlled, and hence deeply trapped, by modest dynamic electric fields. This section describes the main working principles of a radio-frequency ion trap, and derives expressions which allow the theoretical characterization of such important quantities as the ion kinetic energy within the trap, trap frequencies, and trap depths for different ions in the trap. Although other ion trapping schemes are possible (see e.g. review ref. [64]), this work exclusively uses a linear-Paul trap, and so only the theoretical treatment for this type of ion trap is described below. Laser cooling of ions is similar to the case for atoms, but with subtle differences, and results in the formation of Coulomb crystals, which are also discussed.

1.4.1 Equations of motion for ions in a linear Paul trap

The equations of motion for ions in a linear-Paul trap can be determined from an understanding of the potential in which the ions are located. Ions are very sensitive to electric potentials due to their electric charge, and so an electric potential is the most convenient method to effect control, and provide deep trapping. A static quadrupole electric field can be created by aligning four rods (as in Fig 1.19) and applying opposite static voltages to adjacent rods. Early work on the focusing of molecular beams of molecules with an electric dipole moment, primarily by W. Paul et al. [65, 66], used such static fields, but it was quickly noticed that ions traveling along the z-axis (axial

direction) could only be focused in one radial direction, and were defocused in the other. Following work concerning particle optics [67], it was noticed that if the ions traveled through a series of lenses for which focusing and defocusing alternated in the respective radial directions, a net convergence of the ions could be achieved. In the frame of reference of ions with constant z velocity, the *spatial* periodic focusing and defocusing of the ions in x and y could be seen as periodicity in *time*. Instead of alternating rods with opposite static voltages, four long rods were used with oscillating radio frequency (rf) voltages, which when set to the correct frequency and amplitude, depending on the ions mass to charge ratio, effected convergence of the ions. This device was coined the Paul mass filter. This two dimensional dynamic stabilization of ion trajectories was generalized to three dimensions. Assuming such a three dimensional potential has the form

$$\Phi = \alpha x^2 + \beta y^2 + \gamma z^2 \tag{1.91}$$

and that the Lapace equation

$$\nabla^2 \Phi = 0 \tag{1.92}$$

where ∇ is the gradient operator, must be satisfied, then it follows that the coefficients must obey

$$\alpha + \beta + \gamma = 0. \tag{1.93}$$

In order to satisfy equation 1.93, the choice $\alpha = -\beta, \gamma = 0$ can be made, which corresponds to the linear mass filter discussed above [68, 69]. Alternatively, the choice $\alpha = \beta, \gamma = -2\beta$ can be made, which corresponds to a radially symmetric three-dimensional trap, initially coined the *Ionenkäfig* (i.e. an ion cage) [70].

Although the concepts of ion trapping remain basically unchanged from the first discoveries mentioned above, there have been many modifications to suit Paul-type ion traps for other purposes, for example in the advances made for the measurement of integral cross sections of reactions (see e.g. [54]), and for studies with large numbers of ions in near-harmonic linear Paul traps (see e.g. [71, 72]). There have been many other other important extensions away from the linear-Paul-type trap, including the development of Penning traps [73], and surface-electrode traps [74]. A discussion of such other traps is beyond the scope of this work, but is discussed at length for example in ref. [64].

The linear-Paul ion trap used in the experiments of this work is presented schematically in Fig. 1.19 and follows the design strategy of ref. [75]. Radial confinement of the ions was provided by a time varying electric potential with opposite sign applied to adjacent rods, labeled $\pm V_{RF}$ in fig. 1.19, as per the above discussion. The potential close to the trap axis due to this field is

$$V(x, y, t) = V_{RF,0} \left(\frac{x^2 - y^2}{r_0^2} \right) \cos(\Omega t) \tag{1.94}$$

where $V_{RF,0}$ is the zero to peak rf voltage (typically $150 - 350$ V), Ω is the angular frequency of the rf voltage ($2\pi \times 3.1$ MHz), and r_0 is the inscribed radius of the rods

(7.3 mm). The ion is confined radially in an harmonic pseudopotential (i.e. a time averaged potential) [76, 77]. Axial confinement was provided by static voltages V_{END} applied to the end segments of each rod (endcaps) (typically $0 - 20\ V$) as can be seen in Fig. 1.19. The first non-vanishing term of the Taylor expansion of the potential due to the endcaps U about the trap center can be written

$$U(x, y, z) = \frac{\kappa V_{END}}{z_0^2}[z^2 - \tfrac{1}{2}(x^2 + y^2)] \tag{1.95}$$

where κ is an experimentally determined geometrical factor (determined to be 0.346 for the ion trap of this work [78]), and z_0 is the distance between the encaps as defined in Fig. 1.19 (10.4 mm). It can be seen that the potential in the above equations is harmonic, which is a reasonable approximation for ions close to the axis. Experimentally, the "ideal" linear quadrupole where the potential is most harmonic is created by ensuring r, the radius of the rods of each electrode, is approximately equal to r_0 [79].

The equations of motion are found by applying Newton's second law ($F = ma$) involving force F, mass m and acceleration a. The force on a particle with charge Q due to an electric field $\mathbf{E}$ is $Q\mathbf{E}$, and acceleration can be written as the second-time-derivative of displacement r, and so the equation of motion becomes

$$Q\mathbf{E} = m\ddot{\mathbf{r}}. \tag{1.96}$$

Electric field is the gradient of the electric potential, so eqn. 1.96 can be written

$$\ddot{\mathbf{r}} + \frac{Q}{m}\nabla(\mathbf{U} + \mathbf{V}) = \mathbf{0} \tag{1.97}$$

Substituting equations 1.94 and 1.95 into eqn. 1.97 returns

$$\frac{\partial^2}{\partial t^2}\begin{bmatrix} x \\ y \\ z \end{bmatrix} - \frac{Q}{m}\begin{bmatrix} 2\frac{V_{0,RF}}{r_0^2}\cos(\Omega t)x - \frac{\kappa V_{END}}{z_0^2}x \\ -2\frac{V_{0,RF}}{r_0^2}\cos(\Omega t)y - \frac{\kappa V_{END}}{z_0^2}y \\ 2\frac{\kappa V_{END}}{z_0^2}z \end{bmatrix} = 0. \tag{1.98}$$

If the substitution $\tau = \frac{1}{2}\Omega t$ is made into eqn. 1.98 such that $\frac{\partial^2}{\partial t^2} = \frac{\Omega^2}{4}\frac{\partial^2}{\partial \tau^2}$ then it returns

$$\frac{\partial^2}{\partial \tau^2}\begin{bmatrix} x \\ y \\ z \end{bmatrix} + \begin{bmatrix} 2\frac{4QV_{0,RF}}{m\Omega^2 r_0^2}\cos(2\tau)x - \frac{4Q\kappa V_{END}}{m\Omega^2 z_0^2}x \\ 2\frac{-4QV_{0,RF}}{m\Omega^2 r_0^2}\cos(2\tau)y - \frac{4Q\kappa V_{END}}{m\Omega^2 z_0^2}y \\ \frac{8Q\kappa V_{END}}{m\Omega^2 z_0^2}z \end{bmatrix} = 0. \tag{1.99}$$

These represent the Mathieu equations, and can be written in a general form

$$\frac{d^2}{d\tau^2} + [a_i + 2q_i\cos(\Omega\tau)]r_i = 0, \quad i = x, y, z \tag{1.100}$$

with the Mathieu stability parameters

$$a_x \;=\; a_y \;=\; -\frac{1}{2}a_z \;=\; \frac{-4\kappa Q V_{END}}{m\Omega^2 z_0^2} \tag{1.101}$$

$$q_x \;=\; -\,q_y \;=\; \frac{4QV_{0,RF}}{m\Omega^2 r_0^2}, \quad q_z \;=\; 0. \tag{1.102}$$

In the limit that $q_i << 1$ and $a_i << 1$, the Mathieu equations can be solved analytically giving the solution [77]

$$r_i(t) = r_{1i}\cos(\omega_i t + \phi)[1 + \tfrac{q_i}{2}\cos(\Omega t)], \quad i = x, y, z \tag{1.103}$$

with

$$\omega_i = \tfrac{1}{2}\Omega\sqrt{a_i + \tfrac{1}{2}q_i^2} \tag{1.104}$$

where r_{1i} is the amplitude of motion in direction i, and ϕ is a phase determined by the conditions of the initial position and velocity of the ion. The ω_i are the harmonic (secular) trap frequencies of the trap, which are mass dependent. There are two terms on the right hand side of eqn. 1.103. The first is associated with the slow, large amplitude secular motion of the ion in the pseudopotential. The second is associated with a fast, small amplitude oscillatory motion of the ion due to the dynamic nature of the rf fields.

The secular motion in the radial direction is often approximated as motion in a time independent pseudopotential V^*, which corresponds to the average kinetic energy stored in the micromotion. Near the trap axis it is given by

$$V^*(x, y) = \tfrac{1}{2}m(\omega_x^2 x^2 + \omega_y^2 y^2) \tag{1.105}$$

1.4.2 Ion kinetic energies

The total kinetic energy of an ion averaged over one period of secular motion can be written [77]

$$E_{K.E.} = \tfrac{1}{2}m\langle\dot{r}_{1i}\rangle \cong \tfrac{1}{4}m r_{1i}^2\omega_i^2 \cdot \left(1 + \frac{q_i^2}{q_i^2 + 2a_i}\right) \tag{1.106}$$

where the first term on the right hand side is the kinetic energy due to secular motion, and the second term is that due to micromotion, and where r_{1i} corresponds to the outermost point of the trajectory of the ion. For axial motion (along z), $q_z = 0$, and so energy is purely secular. Since the secular motion is thermal, the kinetic energy along z can be expressed as

$$E_{K.E.,z} = \tfrac{1}{2}k_B T_z \cong \tfrac{1}{4}m r_{1z}^2\omega_z^2 \tag{1.107}$$

where T_z is a characteristic temperature ($T_z \approx 12$ mK for laser cooled Ca^+ ions). The radial motion and hence radial energy is dominated by that of the micromotion. In

the radial direction, typically $|a_i| << q_i^2$ for $i = x, y$ and hence

$$E_{K.E.,i} = k_B T_i \cong \tfrac{1}{2} m r_{1i}^2 \omega_i^2 \quad (i = x, y). \tag{1.108}$$

The trap depth in the radial and axial directions can be approximated within the harmonic approximation by considering that the radial potential extends from the axis to r_0, and that the axial potential extends from the trap center to z_0. In this case the depths are given simply by

$$D_i = \frac{1}{2} m \omega_i r_0^2 \qquad (i = x, y) \tag{1.109}$$

in the radial directions and

$$D_z = \frac{1}{2} m \omega_z z_0^2 \tag{1.110}$$

in the axial direction. In practice the depths are found by simulating the potential of the ion trap using finite element methods [80]. For the trap used in this work as described above with $V_{0,RF} = 250$ V, $V_{END} = 8$ V, and $\Omega = 2\pi \times 3.1$ MHz, the simulations gave $D_r = 4.6$ eV, and $D_z = 2.7$ eV [80].

1.4.3 Excess micromotion

If a static offset field $\mathbf{E}_{\mathrm{DC}}$ is applied which displaces the ions from the rf axis, the Mathieu equations are altered resulting in a solution of the lowest order in a_i and q_i of [77]

$$r_i(t) \cong \left[r_{0i} + r_{1i} \cos(\omega_i t + \phi)\right] \left[1 + \tfrac{q_i}{2} \cos(\Omega t)\right] \tag{1.111}$$

where

$$r_{0i} \cong \frac{Q \mathbf{E_{DC}} \cdot \hat{r}_i}{m \omega_i^2} \tag{1.112}$$

where the product of the first term in the first bracket, and the second term in the second bracket of equation 1.111 corresponds to the motion due to "excess micromotion". This motion is a driven motion, and is distinguished from micromotion due to the fact that it can be reduced by by the application of compensation DC voltages on the endcaps, and cannot be reduced by laser cooling. The kinetic energy resulting from this excess micromotion may be estimated by $\frac{1}{2} q_i r_{0i}$ which is significant even for small stray fields such as patch potentials [77].

1.4.4 Laser cooling of ions

The principles of Doppler laser cooling discussed at length for neutral atoms in section 1.3 hold true for ions with a simple energy level structure which enables closed optical cycling transitions. Ionic species with a single valence electron, such as the singly charged alkaline-earth cations, can fulfill this condition, of which all but Ra^+ have been successfully laser cooled. Laser cooling was first achieved with Mg^+ ions in 1978

by Wineland et al. [5], and since has become the workhorse of low energy ion physics, finding particular use in the realm of quantum-information processing [10]. David Wineland was recognized for his contribution to developing the interaction of light and single quantum particles in this direction in 2012 by being awarded the Nobel Prize in Physics.

Unlike laser cooling and trapping of atoms, the ions are trapped in an electric potential, and so it is often possible to damp the motion of the ions in the trap in all three dimensions just by the application of a single cooling (and repumper) laser beam. Although in this case momentum is being removed from the ion in only one direction, the translational degrees of freedom of the ion are coupled by the anharmonicities in the trapping potential and by the Coulomb interaction between ions if more than one is present, and hence momentum can be reduced in all three dimensions.

Laser cooling reduces the kinetic energy of the ions in the trap. If their kinetic energy is reduced such that it is sufficiently below the potential energy arising from their interaction, then the ions form ordered structures whose shape reflects the potential of the trap known as "Coulomb crystals". Simulations have shown that if the plasma-coupling parameter

$$\Gamma = \frac{E_{pot}}{E_{kin}} = \frac{Q^2}{4\pi\epsilon_0 r_w k_B T} \tag{1.113}$$

where $r_w = (3/(4\pi\rho))^{1/3}$ is the Wigner-Seitz radius giving the average distance between ions where ρ is the density of the ions, exceeds $\Gamma \approx 150$, then a phase transition from a cloud like to a crystalline state occurs [81, 82].

The ions which are laser cooled fluoresce, and spatially resolved fluorescence images can be recorded of Coulomb crystals, and indeed single ions, using a charge-coupled-device (CCD) camera. The technical implementation of trapping and cooling of ions, including images of Coulomb crystals can be found in section 2.2. The ion number and kinetic energy can be characterized by comparison of experimental images to those produced by molecular dynamics (MD) simulations, which are discussed in section 1.5. The mass-to-charge ratio of ions inside the trap can be determined by resonantly exciting their motion by the application of an additional rf electric field at their trap frequency, and observing the effect of this on the laser cooled ions, the technical implementation of which is described in section 3.4.

1.5 Molecular Dynamics simulations

Ions in an ion trap for which the motional levels are not resolved [83] move classically, and hence their motion can be simulated by molecular dynamics (MD) methods [84–86]. This involves solving Newton's equations of motion over many small time steps for ions experiencing a combination of forces which approximate to those present experimentally. In practice, this involves the use of the software *Protomol* [87], which solves the equations of motion using a leapfrog algorithm for a predefined ensemble of ions experiencing predefined forces, and which outputs the ion positions and trajectories

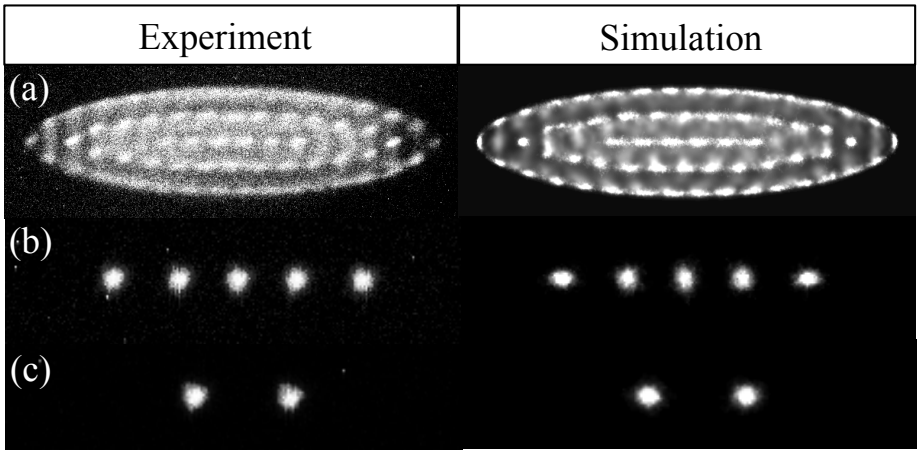

Figure 1.20: Experimental and simulated fluorescence images of (a) a Coulomb crystal of 210 Ca^+ ions with average total kinetic energy ($\langle E_{kin} \rangle / k_B$) of 3.1 K, (b) Five Ca^+ ions in a string with $\langle E_{kin} \rangle / k_B = 34$ mK, (c) Two Ca^+ ions with $\langle E_{kin} \rangle / k_B = 30$ mK.

for each time step. Through the use of *Matlab* codes, these outputs enable a reconstruction of the corresponding time averaged laser cooling images, which can then be compared to those of the experiment. Such comparisons are made in Fig. 1.20, where experimental and simulated images are presented for a crystal of Ca^+ ions (a), and for strings (b). The comparison of the images enables the inference of many important characteristics of the experimental Coulomb crystal from the simulation results, including ion number, crystal composition, secular temperature, average total kinetic energy ($\langle E_{kin} \rangle / k_B$), and ion velocity distributions, all of which are indispensable for the analysis and characterization of reactions in the hybrid trap. The procedures for the determination of these characteristics will be presented here only in brief, and for a more in depth analysis the reader is referred to Refs. [85, 88].

The total force $F_{\mathrm{i,tot}}$ acting on ion i in an ensemble of ions inside the ion trap may be formulated as

$$F_{\mathrm{i,tot}} = F_{\mathrm{i,trap}} + F_{\mathrm{i,Coulomb}} + F_{\mathrm{i,cooling}} + F_{\mathrm{i,heating}} + F_{\mathrm{i,offset}} \tag{1.114}$$

where the terms from left to right on the right hand side of this equation represent the forces due to the trapping potential, the Coulomb interaction between ions, laser cooling, heating due to background collisions and imperfections in the rf fields, and rotationally asymmetric static offset voltages in the trap. $F_{\mathrm{i,trap}} = -Q_i \nabla_i V'$ where Q is the charge of the ion, ∇ is the Nabla operator, and V' is the harmonic trapping potential $V' = V + U$, with V and U as defined in equations 1.94 and 1.95 respectively.

The Coulomb force is defined with

$$F_{\mathrm{i,Coulomb}} = -\frac{1}{4\pi\epsilon_0}\nabla_i \sum_{i\neq j} \frac{Q_i Q_j}{r_{ij}}. \tag{1.115}$$

The velocity dependent cooling force due to laser cooling is implemented along the z axis (as in the experiments) with $F_{\mathrm{i,cooling}} = -\beta\dot{z}$ where β is a damping coefficient, much the same as seen in equation 1.80, but which in practice is determined iteratively. Heating is implemented by applying a random velocity "kick" of a predefined magnitude to each ion at every timestep. Radial offset of the ions from the rf axis, corresponding to the application of equal voltages to say electrodes 7, 8, 9, 10, 11, and 12 of Fig. 1.19, is implemented with a constant force in the desired direction, which for the current example would equate to an equal constant force along x and y.

The output of a simulation are files with ion positions and velocities for each timestep. The position file is used to create a 3D histogram for many timesteps, which corresponds to a 3D intensity plot of the ions probability distribution. If the histogramming is started after the ions have formed a stable Coulomb crystal, the resulting intensity plot corresponds to the time averaged laser cooling fluorescence signal of Coulomb crystals in the experiment. The observation of crystals in the experiment is by collecting the spatially resolved laser cooling fluorescence through optics and projecting the image onto a CCD chip. To compare the simulated intensity histograms to the experimental images therefore, an additional *Matlab* program is implemented which takes into account the angle of observation, the focal depth of the imaging system, and the projection of the 3D intensity onto a 2D plane. To this end, slices in the plane of observation are taken of the 3D histogram and are blurred using a Gaussian blur function to different extents based on their distance from the focal plane, before finally being added together to form a 2D projection. An example of the result of this procedure can be seen in Fig. 1.20, where faithful reproductions are achieved.

Multicomponent Coulomb crystals can be simulated, with the advantage that ions which are non-fluorescing in the experiments can be made visible in the simulations. By observing the effect that non-laser cooled ions have on the shape of the laser cooled ion distribution in the simulations, the numbers and mass of those non-fluorescing ions in the Coulomb crystals of the experiments can be approximated. Such comparisons with multicomponent crystals can be seen for example in Figs. 6.3 and 7.1.

Once the parameters of the simulation have been adjusted such that no better reproduction of the experimental image is possible, the characteristics of the simulated crystal are assumed to be sufficiently representative of the experimental crystal.

From a comparison of successive ion positions in the simulation output, the velocity of each ion is calculated for each timestep with $v_{\mathrm{i,t}} = ((x_{\mathrm{i,t}} - x_{\mathrm{i,t}-\tau})^2 + (y_{\mathrm{i,t}} - y_{\mathrm{i,t}-\tau})^2 + (z_{\mathrm{i,t}} - z_{\mathrm{i,t}-\tau})^2)^{\frac{1}{2}}/\tau$ where τ is the duration of the timestep. These velocities are histogramed, and the resulting plot approximates the total (i.e. both the secular and micromotion) velocity distribution $\rho(v)$ of the ions in the trap. As will be seen in section 3.8, it is this $\rho(v)$ that is used to determine velocity averaged theoretical rate

constants. These plots can also be represented as ion total kinetic energy distributions $g(E)$. This $g(E)$ distribution can be obtained from a transformation of the velocity distribution $\rho(v)$, and using the relation $E = \frac{1}{2}mv^2$. Since $g(E)dE = \rho(v)dv$, then

$$g(E) = \rho\left((2E/m)^{\frac{1}{2}}\right) \cdot \frac{dv}{dE}, \tag{1.116}$$

and hence

$$g(E) = \rho\left((2E/m)^{\frac{1}{2}}\right) \cdot \left(\frac{1}{2mE}\right)^{\frac{1}{2}}. \tag{1.117}$$

Assuming collision of the ions with a stationary target (which the atomic reaction partners are assumed to be in this work due to their kinetic energy being two orders of magnitude lower than that of the ions), then the collision energy distributions are obtained using the above procedure with E replaced by $E_{coll} = \frac{1}{2}\mu v^2$, where μ is the reduced mass of the ionic and neutral collision partners. For practical purposes it is necessary that the distribution is normalized such that the area under the distribution equals unity. This can be achieved for histograms with sufficiently small bin sizes by ensuring

$$\sum_{i=0}^{\infty} P_i \; \delta E_i = 1 \tag{1.118}$$

where P_i is the probability density attributed to to the i^{th} bin with width δE_i. Alternatively, a high order polynomial fit is applied to a plot of probability density against bin center to extract an analytic functional form of the distribution, which then is normalized by integration. A plot of such collision energy distributions for different shapes, sizes and composition of Coulomb crystals is shown in Fig. 3.8 (c) and (d), and correspond to the crystals presented in (a) and (b). The resulting distributions are highly non-Maxwellian, where the bumps in the probability density correspond to different shells of the Coulomb crystal structure. For the largest crystals, tails in the distribution up to $E_{coll}/k_B = 70$ K are observed. The distribution is thinnest for a string of ions located on the rf axis. As can be seen in Fig. 3.9, radially offsetting a string from the rf axis results in a broadening of distribution to higher energies.

It is useful to characterize the kinetic energy and collision energy distributions using quantities that describe their average properties. A measure of the kinetic energy averaged over one rf period is given by the root-mean-square (RMS) velocity $(v_{i\alpha}^{rms})^2 = (1/J)\sum_{j=1}^{J} v_{i\alpha,j}^2$, where $\alpha = x, y, z$; j is the time step number, J is the total number of time steps in one rf period, and i is the ion index [85]. The time averaged total kinetic energy can then be written

$$\langle E_{K.E}\rangle = \frac{1}{2N} m \sum_{i}^{N} \left[\left\langle (v_{ix}^{rms})^2 \right\rangle + \left\langle (v_{iy}^{rms})^2 \right\rangle + \left\langle (v_{iz}^{rms})^2 \right\rangle\right], \tag{1.119}$$

where $\langle ... \rangle$ denotes an average taken over many rf periods and N is the number of ions. As discussed above, the average total collision energy $\langle E_{coll}\rangle$ for collisions of the ions

with a stationary atomic target can be obtained in the same way by replacing m (the ion mass) with μ (the reduced mass of the ion and the atom) in the above equation. This average collision energy can then be expressed in units of K with $\langle E_{coll} \rangle / k_B$. As discussed in section 1.1, while presented in units associated with temperature due to convention, this energy is not a temperature in the thermodynamic sense.

The secular energies, which correspond to the slow thermal motion of ions in the trap, are extracted form the simulations by averaging the velocities over one rf period, $v_{i\alpha}^{sec} = (1/J) \sum_{j=1}^{J} v_{i\alpha,j}$. The secular energy does not include micromotion, and so the resulting velocity distribution is quasi-thermal and can be ascribed a temperature within the Maxwell-Boltzmann definition [85]. The secular temperature T_{sec} can then be defined through

$$\frac{2}{3k_B} \langle E_{sec} \rangle = T_{sec} = \frac{1}{3Nk_B} m \sum_{i}^{N} \left[\left\langle (v_{ix}^{sec})^2 \right\rangle + \left\langle (v_{iy}^{sec})^2 \right\rangle + \left\langle (v_{iz}^{sec})^2 \right\rangle \right]. \tag{1.120}$$

Typical secular temperatures for laser cooled Coulomb crystallized ions are ≈ 10 mK.

Chapter 2

Technical implementations

The previous chapters have introduced theoretical aspects of the key concepts and components of this work. This chapter aims at describing the technical aspects of implementing these concepts experimentally, and provides an insight into the hardware and experimental techniques that are integral in achieving the results presented in this work. The entire experimental apparatus described was conceived, designed, and implemented as part of this work. Not only is the apparatus presented the first example of an ion-atom hybrid trap within the sphere of the research group, but at the time of design (autumn 2009) there had been only one published realization of an ion-atom hybrid trap globally [33]. It is therefore important to provide a detailed documentation of the methods developed to implement what has become a successful hybrid trap, which is provided by this and the following chapter. The discussion includes ultra-high vacuum techniques, sources of atoms and ions, design of the ion trap and magnetic coils for the magneto-optical trap, laser cooling hardware, inter-trap effects, and finally the hybrid experimental setup.

2.1 Ultra-high vacuum (UHV)

Ultra high vacuum (UHV) ($\approx 10^{-9}$ mbar) is required in the experiment chamber. To put UHV in context, the density of air at room temperature and pressure (RTP) is typically 10^{19} cm^{-3}, whereas the density of molecules at 10^{-10} mbar is 10^{6} cm^{-3}, meaning that in the typical ion Coulomb crystal volume there will be on average only a few ten background gas molecules at any given time.

High levels of vacuum are required for these experiments for several reasons. Ions are inherently reactive species, and reactions of ions with neutral species are often barrierless, meaning that at higher background pressures, trapped ions react with background gas on timescales comparable with the reactions of interest, vastly complicating reaction dynamics analysis. For example, it has been shown that Ca^+ reacts in excited states with H_2O [89] and H_2 [90] with rate constants of 1×10^{-11}cm^3 s^{-1} and 8×10^{-10}cm^3 s^{-1} respectively. At partial pressures of 5×10^{-8} mbar, the neutral densities

would be $\approx 1.2\times10^9$ cm^{-3}, which is comparable with the densities in a magneto-optical trap (MOT). The $1/e$ lifetime of a Ca^+ ion with respect to reactions with H_2O and H_2, with say 20 % of population in excited states, would therefore be on the order of 0.002 s^{-1} and 0.2 s^{-1} respectively, which is of the same order as the typical lifetime of a Ca^+ ion in the presence of a Rb MOT (≈ 0.02 s^{-1}). To minimize the effect of these background reactions, the background pressure is maintained below 5×10^{-10} mbar during experiments, ensuring that the background processes are typically two orders of magnitude slower than the processes of interest.

Another reason for using UHV conditions for ion trapping, is that the Coulomb crystalized ions are heated by collisions with background gas molecules, due to the exchange of momentum during a collision, and also the rf heating induced by out of phase collisions. Hence, even if the background gas present was inert with respect to reactions with the laser cooled ion, its effect could still be observed by the heating, and at high enough background pressures, melting of the Coulomb crystal. Since the analysis of the reaction dynamics relies on accurate simulation of the crystals by molecular dynamics (MD) methods, the colder, and hence the more spatially ordered the crystal, the easier it is to accurately simulate. Also the experiments of this work are concerned with the low temperature behavior of ion-neutral reactions, and so colder crystals are more suited to this end.

UHV experimental conditions were achieved by placing all the necessary equipment (i.e. traps, atom sources, alignment tools) inside a vacuum chamber, and pumping out as much of the gas inside as possible to reach pressures $\approx 10^{-10}$ mbar. The chamber is made from stainless steel, and has resealable flanges to allow access inside the chamber, and to easily change components when necessary. Each seal comprises two flanges, each with a circular stainless steel knife edge near the perimeter. The knife edges are brought together and a circular copper gasket is placed in between, such that the hard knife edges bite into the soft copper gasket from both sides. The resulting seal is tightened using a distribution of nuts and bolts around the flange perimeter, which are tightened sequentially in a star pattern such that the distribution of pressure around the gasket is even.

Once sealed, the gas is removed from the chamber by a turbo-molecular pump (*Oerlikon MAG W 600*) at 600 l s^{-1} which is backed by a rotary pump (*Oerlikon Trivac NT 10*). The pressure of the foreline (i.e the line between the rotary and the turbo pump) is measured by a Pirani gauge (*Pfeiffer Pirani Gauge TPR280*), and is typically 5×10^{-4} mbar. The pressure of the vacuum chamber is measured by a hot cathode gauge (*Pfeiffer Bayard-Alpert PBR260*) and after intial pumping is typically 1×10^{-8}mbar. The remaining gas in the chamber is analyzed by a residual gas analyzer (RGA)(*Kurt J. Lesker AccuQuad RGA*). After initial pumping, the remaining gas tends to be H_2O due to its propensity to stick to the walls of the chamber, and H_2 due to outgasing from the stainless-steel chamber walls. To eject the H_2O, the entire chamber is "baked" (i.e. heated) to 190°C, resulting in an internal temperature of 100 °C, for approximately four days, until the H_2O partial pressure has been minimized. To remove the H_2, a titanium sublimation pump (*Varian Tisub*) is used periodically releasing titanium

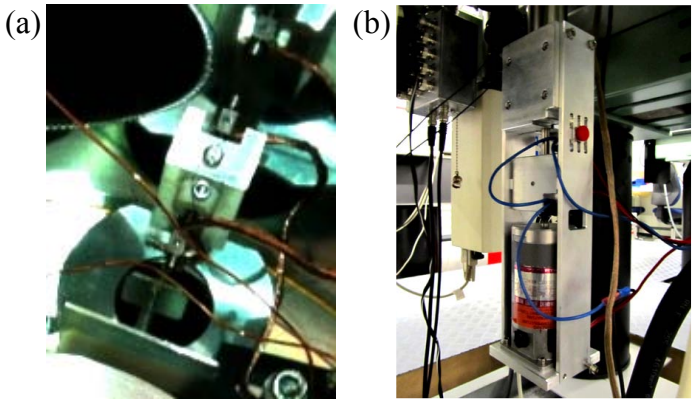

Figure 2.1: (a) A picture of one of the ovens used as the atomic source for either Ba^+ or Ca^+ generation. It consists of a resistively heated, isolated steel tube filled with Ba or Ca powder. (b) A picture of the computer controlled mechanical oven shutter mechanism. (The oven shutter that this drives can be seen near the bottom of (a).)

vapor deposited as a thin film on the chamber walls which reacts with residual gas (including H_2) to form a solid product. After this procedure, base pressures below 5×10^{-10} mbar are achieved.

2.2 Technical implementation of trapping and cooling ions.

The operational theory of the trapping and laser cooling of ions in a linear quadrupole ion trap was discussed in section 1.4. This section describes the equipment and procedures used to put these theories into practice, and includes important technical details and arrangements. Two different ions, $^{40}Ca^+$ and $^{138}Ba^+$, were trapped and laser cooled in the experiments of this work, requiring slightly different equipment, both of which are described. N_2^+ was also used as a reactant ion, and the details of its loading into the ion trap for sympathetic cooling by laser cooled $^{40}Ca^+$ ions is discussed.

2.2.1 Source of ions

This work studies the reactions of Rb with three different ions that were generated inside the volume of the ion trap. These ions were $^{40}Ca^+$, $^{138}Ba^+$, and $^{28}N_2^+$. Ca exists as a solid metal at room temperature and atmospheric pressure (RTP). A large solid chunk was ground into powder which was placed into an oven, such that on heating to $\approx 200 - 300$ °C under UHV conditions, an effusive atomic beam was generated. Barium (also a solid metal at RTP) oxidizes in air on the timescale of seconds, and so

the preparation and transportation of the ground powder was done in an inert (Argon) atmosphere. Ba forms an atomic beam in the same way as Ca when heated under UHV conditions.

Fig. 2.1 (a) shows a picture of one of the ovens. It consisted of a small diameter ($2-3$ mm), thin walled (≈ 100 μm) stainless steel tube which was filled with atomic powder, and sealed at one end with a stainless steel cap. It was held in a thermally and electrically insulating macor cylinder, which itself was situated inside an adjustable aluminum frame. The tube was resistively heated using A.C. currents ($\approx 7-10$ A). The resulting effusive beam was collimated by a skimmer (an aluminum plate with a $1-2$ mm hole drilled in) sitting directly in line between the oven orifice and the geometric center of the ion trap. The skimming setup was designed such that the atomic beam passes cleanly through the trap so that no deposits are made on the trap electrodes which could cause unwanted patch potentials. To allow fast (≈ 1 s) switching of the atomic beam, a shutter was implemented at the oven mouth, which could be moved up (into the "beam off" position), or down ("beam on" position) by connection via a "push/pull" UHV feed-through to a computer controlled motor. This feature was useful since the time constant for the oven to warm up to effective effusing temperatures was on the order of 30 s, where as the shutter was closed or opened in 1 s, allowing fast repetition of experiments, whilst maintaining low local background densities at the ion trap center. A photo of the shutter mechanism lying below the chamber is presented in Fig. 2.1(b).

N_2 is a gas at RTP, and so was emitted into the chamber through a leak valve at pressures up to 2×10^{-8} mbar.

Once the neutral precursors of the ions are in the trap volume, they were ionised. This was done in the case of Ca and Ba by non-resonant multiphoton photoionisation by using a focused pulsed 355 nm laser beam from the tripled output of a Nd:YAG laser at $\approx$ 15mJ per pulse at 10 Hz. Ca has a first ionization energy of 6.1 eV, and Ba 5.2 eV, and so both required 2 photons of 355 nm (3.48 eV each) to be ionised. By adjusting the settings of the ovens and the ionising laser beam, loading rates over the range of $0.1-100$ ions s^{-1} were achieved as required. The N_2 was ionized by [2+1] resonance-enhanced multiphoton-ionization (REMPI) via the Q branch of the vibrationless $X\ ^1\Sigma_g^+ \rightarrow a''\ ^1\Sigma_g^+$ transition [91], using 202 nm photons. These photons were generated by a dye laser containing a mixture of Rhodamine-b and Rhodamine-101, pumped by the doubled output of a Nd:YAG laser at 532 nm. Typical loading rates of N_2^+ into the ion trap were ≈ 1 s^{-1}.

2.2.2 The linear Paul ion trap

The theoretical concepts and characteristics of linear quadrupole (Paul) ion traps have been discussed in section 1.4, where it was seen that the "ideal" quadrupole (i.e. that producing a potential which is very closely approximated as harmonic) is created by ensuring that the radius of each rod r is approximately equal to the inscribed radius of the circle on which the rods are distributed r_0. This condition was not fulfilled in the

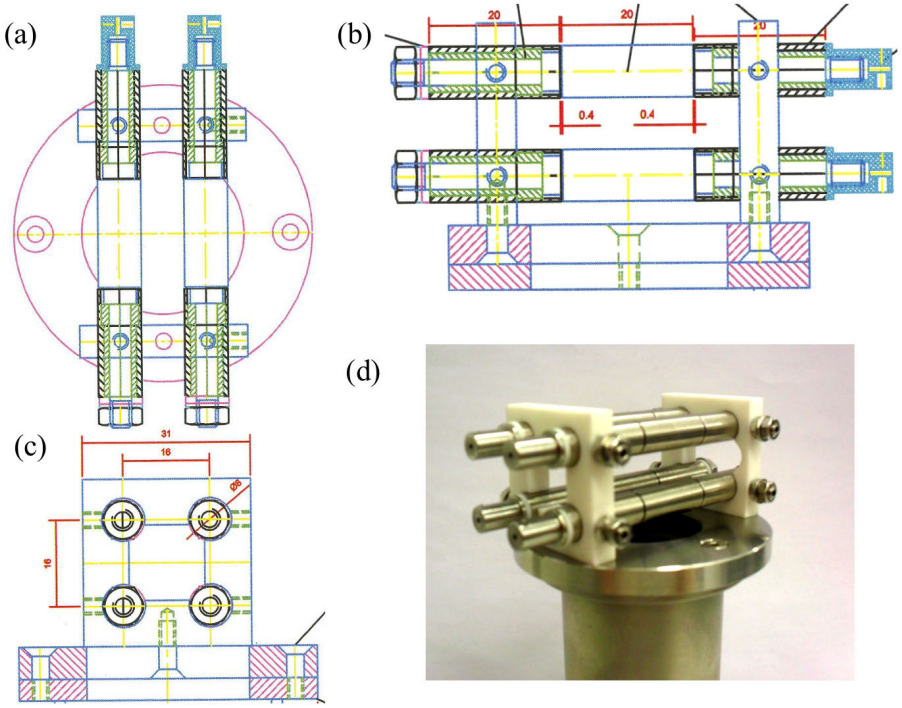

Figure 2.2: Technical drawings by D. Wild: (a) Top view (b) side (radial) view, and (c) side (axial) view of the ion trap and plinth. All measurements are in mm. (d) A photograph of the ion trap mounted on a plinth.

ion trap of this work, since large 3D optical access was needed to permit the operation of a magneto-optical trap (MOT) for atoms (see section 2.3). As a compromise, the ion trap was manufactured with $r = 4.0$ mm, and $r_0 = 7.3$ mm. Numerical simulations showed however that the deviation from an ideal quadrupole potential was only slight, $\approx 6\%$ within 5 mm of the central trap axis [78, 80]. Fig. 2.2 (a)-(c) are *AutoCAD* projections of the ion trap of this work (drawn by D. Wild), while (d) is a photo of the finished ion trap (manufactured by F. Haefeli). The rods were from stainless steel, and insulation was in macor. The trap sat on a hollow plinth to allow optical axes from below. The central electrode of each rod was 20 mm long to enable large axial translation of the ions without significant distortion of the Coulomb crystal, which was useful for overlap with the atom cloud of the MOT.

The rf voltage, which was applied to all electrodes with opposite polarity for adjacent rods, was generated by an rf generator (output = 0-400 V, 3-4 MHz, manufactured by A. Tonin) powered by a DC power supply (0-400 V, 0-100 mA, *Schlumberger IP-17*). The relative voltage in each rf arm could be changed by fine tuning the relative inductance using an iron bar inside a solenoid.

The endcap voltages were generated by a digital-to-analogue-converter (DAC) card of a personal computer (PC) controlled by a *Labview* program (designed by A. Johnson), which allowed each endcap to be individually addressed with a DC voltage of -10 to 10 V. Higher DC voltages of up to 60 V could be applied to the endcaps by sending the output of the DAC card through a voltage addition component (manufactured by G. Holderied).

The rf and DC signals were combined for electric feedthrough into the vacuum chamber by a "rf/DC mixing box" (manufactured by A. Tonin). The mixing box comprised of insulated input and output channels connected via a printed circuit board (PCB) consisting of large capacitive elements designed to mix the DC and rf signals without adding too much extra load on the rf generator. The mixing box also allowed an additional rf voltage to be applied for mass spectrometry (see section 3.4), whereby the excitation configuration could be changed from axial to radial by changing two jumpers inside the mixing box. The mixing box voltages were fed through to the ion trap via kapton-coated wires.

2.2.3 Laser cooling of $^{40}Ca^+$ and $^{138}Ba^+$

As was seen in section 1.4.4, singly charged alkaline-earth cations in ion traps can be efficiently laser cooled to form fluorescing Coulomb crystals. The laser coolable ions used in this work were $^{40}Ca^+$ and $^{138}Ba^+$. The laser cooling schemes showing the energy level structure for each of these ions is shown in Fig. 2.3 (a) and (b) respectively.

For Ca^+, the $(4s)^2S_{1/2} \rightarrow (4p)^2P_{1/2}$ cooling transition at 397 nm is used to remove momentum from the ion. About 6% of spontaneous emission events from the $(4p)^2P_{1/2}$, however, occur to the $(3d)^2D_{3/2}$ level, which has a considerable lifetime ($\tau = 1.2$ s) with respect to the ground state. To avoid population trapping in the $(3d)^2D_{3/2}$ level, a repumper laser at 866 nm is used to return population to the $(4p)^2P_{1/2}$ state, and

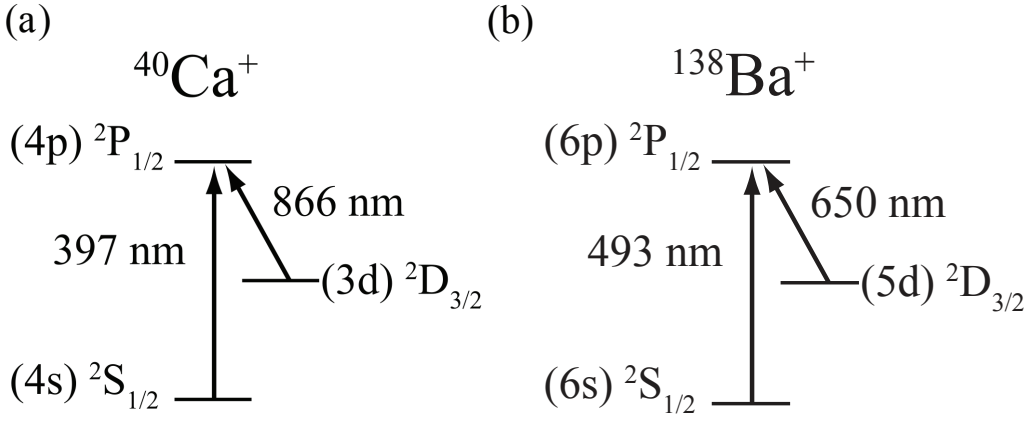

Figure 2.3: Laser cooling schemes for Ca^+ (a) and Ba^+ (b) ions.

hence close the optical cycle required for effective laser cooling.

The situation is very similar for Ba^+, except the cooling is provided on the $(6s)^2S_{1/2} \rightarrow (6p)^2P_{1/2}$ transition at 493 nm, and the repumer on the $(5d)^2D_{3/2} \rightarrow (6p)^2P_{1/2}$ transition at 650 nm.

Fig. 2.4 is an augmented photo of the diode-laser table on which the elements necessary for the production of light for the laser cooling of Ca^+ was located. Light at 397 nm and 866 nm was produced from external cavity stabilized diode lasers (*Toptica Photonics, DL100*) with output powers of around 15 mW and 30 mW respectively. A small portion of this light ($\approx$ 5 %) was coupled to a wavemeter (*HighFinesse, WSU-30*), where the wavelength was determined. A fiber switch allowed the wavelength of up to four lasers to be read sequentially with a total cycle update rate of down to 0.8 s. The wavelength was stabilized to within $\pm$2 fm using a proportional-integral-derivative (PID) feedback loop between the wavemeter and the voltage applied to the piezo-electric element (which tuned the angle of the grating of the laser) via a *Labiew* program and a DAC card. The remaining light of each laser was then split in two with variable relative intensities by half-wave plates ($\lambda/2$) and polarizing-beam-splitter (PBS) cubes for use by two separate experiments. The light was coupled into single mode (SM) fibers where it was directed and collimated onto the experiment with output powers of up to 2 mW for 397 nm and up to 7 mW for the 866 nm light.

Fig. 2.5 is a labeled photo of the setup required to produce the light for effective laser cooling of Ba^+. Light at 493 nm and 650 nm was produced by external cavity stabilized diode lasers *Toptica Photonics, DL100 Pro*. A small portion of the output was sent to the wavemeter for PID stabilization, and the rest was coupled via SM fibers to the experiment. A neutral density (ND) filter was used when necessary as a means to reduce the power of the coupled light in a continuously variable and reproducible way.

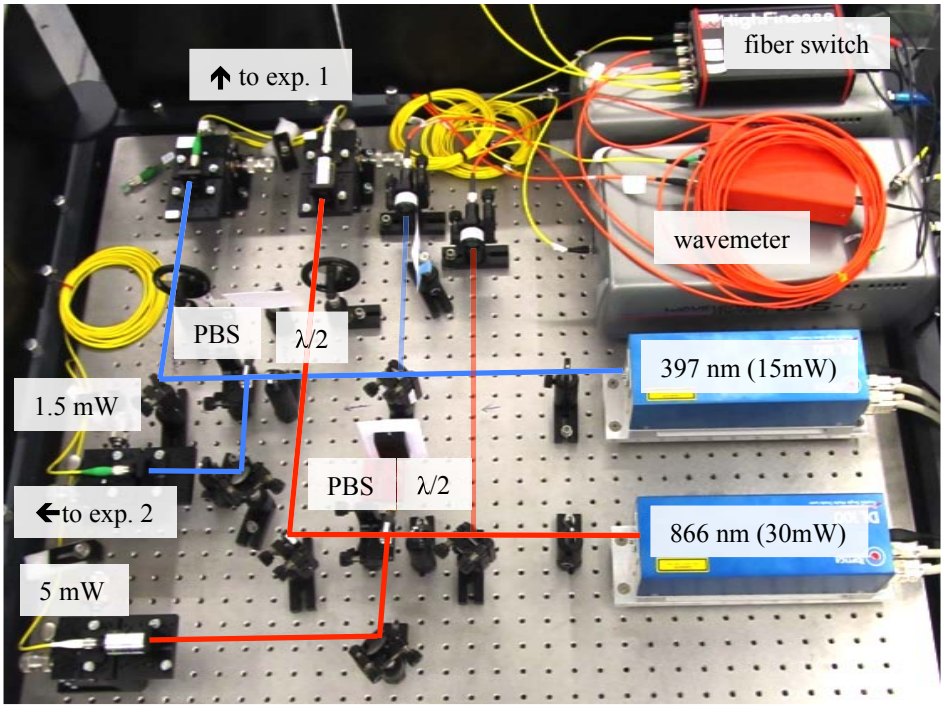

Figure 2.4: An augmented photo of the Ca^+ cooling and repumper laser system. A small portion of the laser output was sent via a fiber coupler and switch to a wavemeter, and the rest was split between two experiments (exp. 1 and 2) using half wave plates ($\lambda/2$) and polarizing beam splitter (PBS) cubes. Also shown are typical laser output powers and fiber in-coupling powers.

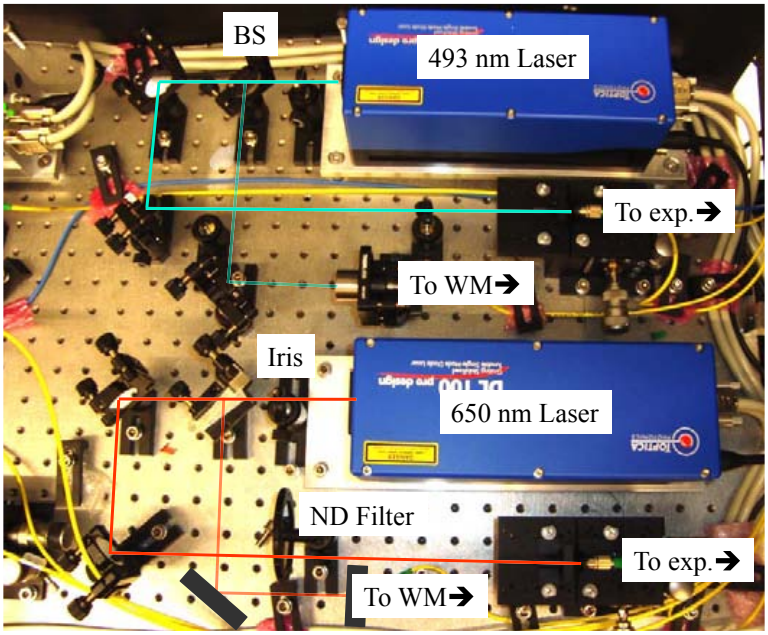

Figure 2.5: (a) An augmented photo of the Ba^+ laser cooling system. A small portion of the laser output is sent via a fiber to a wavemeter (WM), and the remaining beam is coupled via a fiber to the experiment, with the option to attenuate given by a neutral density (ND) filter.

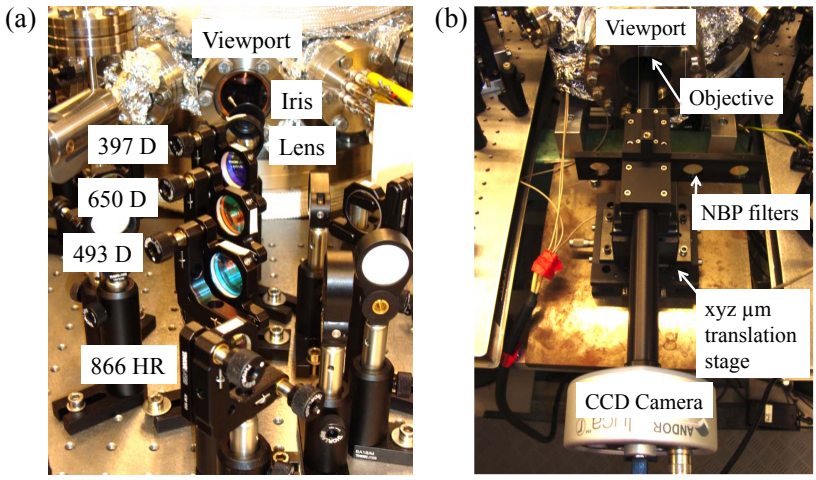

Figure 2.6: (a) A labeled photo of the dichroic mirror setup required to co-axially align cooling and repumping beams for both Ba^+ and Ca^+ ions. D stands for "dichroic", and HR stands for "high reflecting". (b) A labeled picture of the CCD camera, lens and filter system, mounted on an xyz tanslation stage. NBP stands for "narrow band pass" filter. See text for details.

It was often necessary to trap and laser cool Ca^+ and Ba^+ simultaneously. Laser cooling of the ions was implemented along the axis of the ion trap, hence simultaneous cooling (and repumping) of Ca^+ and Ba^+ required the coaxial overlap of a four laser beams, each of a different color. Fig. 2.6 (a) is a labeled photo of the high reflecting (HR) and dichroic (D) mirrors necessary to achieve the coaxial overlap. Also shown is a lens which focused the laser beams down to beam waists of > 120 μm, which allowed for higher intensities at the trap center.

The fluorescing ions are observed by a charge-coupled-device (CCD) camera coupled to a microscope (image system magnification $10\times$). To isolate the photons of different colors from fluorescing Rb, Ba^+ or Ca^+, narrow band pass (NBP) colour filters were implemented in the image path. A labeled photo of the imaging system is presented in Fig. 2.6 (b).

2.2.4 Optical chopping of ion laser cooling beams

As also discussed later in section 2.3.6, photons used for the cooling of Ca^+ and Ba^+ were able to photoionise ^{87}Rb atoms in their 5 $^2P_{3/2}$ state, which were present during MOT operation due to excitation by the MOT cooling beams at 780 nm. To avoid loading Rb^+ ions into the ion trap during experiments via REMPI, the ion and atom cooling lasers were alternately chopped at a frequency of 1000 Hz by a mechanical rotary chopper. Fig. 2.7 (a) shows the effect of simultaneous operation of both the ion and atom traps. Fig.2.7 (a)(i) is a spatially resolved fluorescence image of a Coulomb

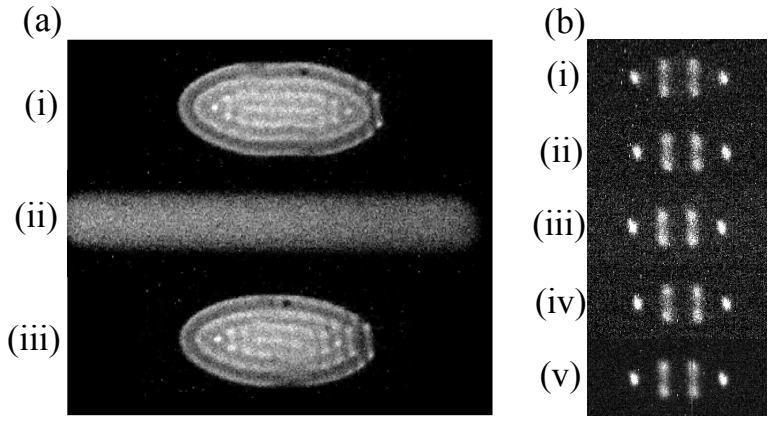

Figure 2.7: (a) Series of fluorescence images of Ca^+ Coulomb crystals, (i) an axialised Coulomb crystal, (ii) Crystal in (i) after ≈ 0.5 s of unchopped simultaneous ion and atom laser cooling, resulting in the efficient loading of Rb^+ ions (which do not fluoresce), which distort the shape of the crystal. (iii) The crystal in (ii) after lowering the rf voltage such that Rb^+ ions are not trapped, and then returning the rf voltage to that in (i) and (ii). (b) A series of fluorescence images of a small Ca^+ Coulomb crystal at varying chopping speeds of the cooling laser: (i) 20 Hz (ii) 80 Hz (iii) 500 Hz (iv) 1000 Hz (v) unchopped.

crystal of Ca^+ ions, (ii) is as in (i) but after ≈ 0.5 s of simultaneous ion and atom laser cooling, showing the efficient loading of non-fluorescing Rb^+ ions, whose presence can be observed by the distortion of the crystal shape, which were then removed by "rf cleaning" (i.e. the lowering of the rf voltage such that heavier ions are no longer trapped, followed by returning to the original rf value) resulting in the pure Ca^+ crystal shown in (iii).

The effect of chopping the cooling laser on a Coulomb crystal of ions was studied by comparing crystal images under different chopping conditions, shown in Fig. 2.7 (b). It can be seen that the average fluorescence level drops for the chopped images as compared to the unchopped image in (v), since the ions were scattering light only 48% of the time when chopped. Apart from this, there was no noticeable change in the images in different chopping conditions, even down to 20 Hz. This is in stark contrast to the situation in the MOT (as will be seen in section 2.3.6). This difference is due to the fact that the cooling lasers also form the trapping force in the MOT, and so when switched off the atoms are no longer trapped and expand ballistically. In the ions' case, they are trapped by the ion trap, and the cooling laser only provides cooling forces. If the heating mechanisms in the ion trap are such that the ions remain Coulomb crystallized in the dark periods, then no significant change in the images are expected in the case of chopping, in line with the experimental observations.

2.3 Technical implementation of a magneto-optical trap

The theoretical concepts behind the interaction of light and matter were introduced in section 1.3, and extended to the operation of a magneto-optical trap (MOT) for neutral atoms in 1.3.10. The characterization of the MOT, including the dependence of atom number and density on various trap parameters is presented in section 4. This section outlines the technical implementation of the MOT in the context of the hybrid ion-neutral trap constructed as part of this work. Also included are descriptions of the hardware, and an outline of the experimental techniques required for the characterisation of the MOT.

2.3.1 Source of atoms

The atomic species used in the MOT for the entirety of this work was ^{87}Rb. A convenient source of non-isotope-selected Rb are commercial "getter" sources. These devices are used in industry for depositing pure metals on surfaces in vacuum. They are also used for maintaining vacuum for example in evacuated cathode-ray tubes due to the reactivity of the deposited metal with gas inside the tube. The getter used in this work was from *SAES Getters*, product code Rb/NF/4.5/12FT10+10. The getter device had the form shown in the schematic in Fig. 2.8 (a), reproduced from a *SAES Getters* catalog. The getter used in this work had the dimension A = 12 mm, and contained 4.5 mg of Rb. The operating principle is that a current (A.C. or D.C.) is passed along the getter by electrical connection to the "FT" tabs, and the getter heats up. The heating starts a reduction reaction of rubiddium chromate by a Zr(84%)-Al(16%) alloy to form Rb, which is then effusively evaporated from gaps on either side of the central bar of the getter.

The current needed for release of Rb from the getter for industrial applications is recommended at 5.3 A. A substantial release of Rb occurred, however, at currents well below this threshold, and indeed release rates suitable for MOT operation were obtained at currents as low as 2.8 A. The getter was placed on a ceramic holder at the height of the MOT trap center with a radial displacement of 80 mm. Fig. 2.8 (b) shows a plot of atom number at steady state operation of the MOT against the A.C. current applied to the getter. It can be seen that the relationship becomes linear past a threshold at about 2.8 A. For getter currents above 4.0 A, the background pressure in the chamber exceeded 5 $\times 10^{-10}$ mbar, which was undesirable for the study of ion-neutral ractions as explained in section 2.1. As a compromise between high atom number and low background pressure, a range of $\approx 3.2 - 3.6$ A was used in the experiments of this work.

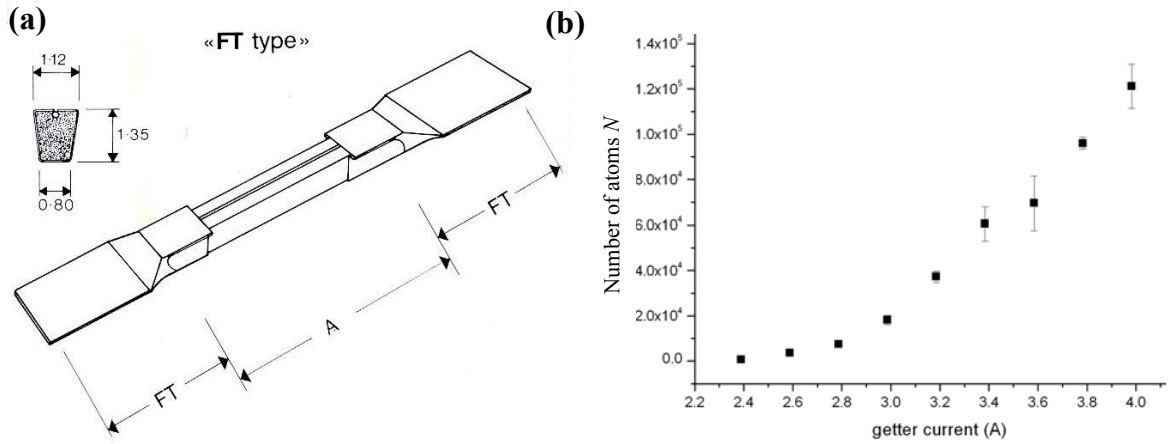

Figure 2.8: (a) Schematic of a Rb getter, reproduced from a catalog of *SAES Getters* (©AMD 920630 Saes Getters S.p.A) where A = 12 mm, and all values shown in mm. (b) Plot of MOT atom number against A.C. current applied to the getter for a given set of MOT operating conditions

2.3.2 Light generation for laser cooling and trapping of ^{87}Rb

As was described in section 1.3.10, ^{87}Rb atoms can be trapped and cooled using light forces in a magneto optical trap (MOT). It was seen that many photons need to scatter from an electronic transition in order for a substantial force to be exerted on the atoms, and hence is a prerequisite for cooling and trapping. In the case of ^{87}Rb, the cycling transition is between hyperfine states of the ground and the first excited electronic level, i.e $5\ ^2S_{1/2}, F = 2 \rightarrow 5\ ^2P_{3/2}, F = 3$, indicated by the thick arrow in Fig. 2.9 (b). The selection rules outlined in section 1.3.8 state that $\Delta F = 0, \pm 1$, and hence spontaneous emission from the excited $5\ ^2P_{3/2}, F = 3$ into the $5\ ^2S_{1/2}, F = 1$ is forbidden by this rule. In reality, the electronic selection rules are not absolute, and in fact about one in every thousand scattering events [92] results in spontaneous emission from the $5\ ^2P_{3/2}, F = 3$ to the $5\ ^2S_{1/2}, F = 1$ level. To close the cycling transition fully, an extra "repumper" frequency was therefore required on the $5\ ^2S_{1/2}, F = 1 \rightarrow 5\ ^2P_{3/2}, F = 2$ transition, indicated by the thin arrow in Fig. 2.9 (b). Repumping to the $5\ ^2P_{3/2}, F = 3$ level is not desirable since this transition is not very efficient as per the F selection rules, and also because the $5\ ^2S_{1/2}, F = 1$ and $F = 2$ states in this case would couple to one another coherently via the $5\ ^2P_{3/2}, F = 3$ state, and population would be pumped into the $5\ ^2S_{1/2}, F = 1$ level.

The scheme for producing appropriate light for the magneto-optical trapping of ^{87}Rb is presented in Fig. 2.9 (a), and is briefly described here. The cooling laser light was provided by a external cavity diode laser (*Toptica Photonics*, *DL100* or *DL100 Pro*), with output power around 120 mW. The wavelength of the light was determined to within ±5 fm by taking a 1 % part of the output of the laser and coupling it through

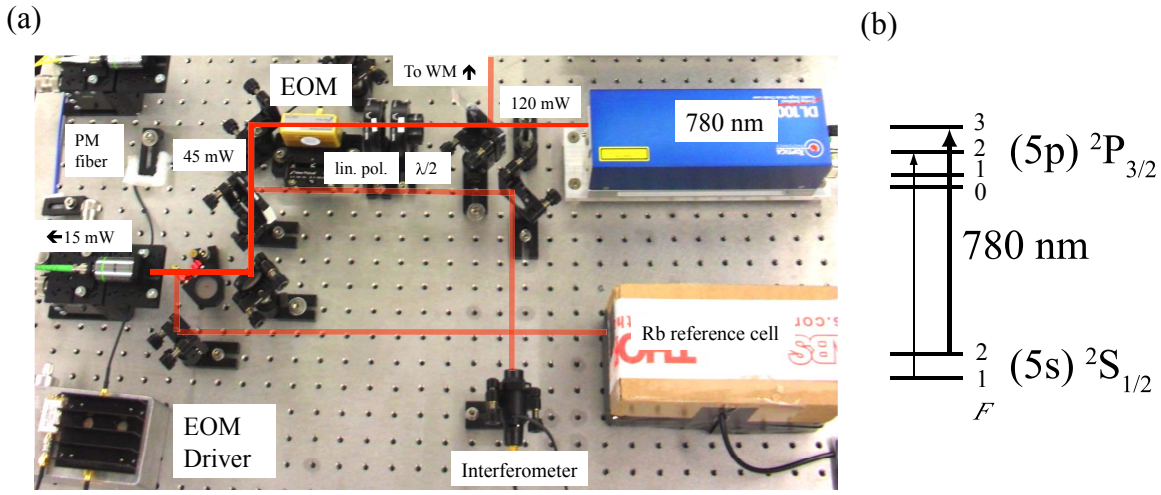

Figure 2.9: (a) A photo of a diode laser table showing the important elements for producing fibre coupled light used for laser cooling of ^{87}Rb. EOM stands for electro-optical modulator, $\lambda/2$ is a half wave plate used for rotating the linear polarisation axis of the light from the laser, PM stands for polarisation maintaining, lin. pol. is a linear polariser, and WM stands for wave meter. Also shown are typical powers of the light at various points along the beam path. (b) Energy level structure with cooling (thick arrow) and repumping (thin arrow) transitions for ^{87}Rb. The frequency of these transitions differ by 6.568 GHz. F is the hyperfine quantum number.

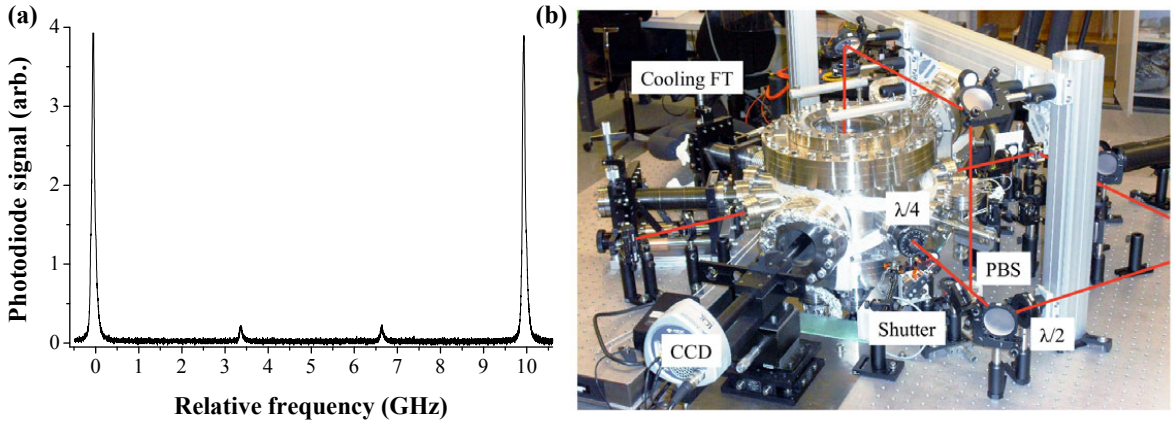

Figure 2.10: (a) An interferometer trace showing the modulation of the ^{87}Rb carrier laser cooling frequency (seen at 0 and 10 GHz) to produce 5 % sidebands at 6.568 GHz for the repumping transition of ^{87}Rb. The free spectral range of the interferometer was 10 GHz. (b) A picture of the chamber with labels of the important parts for MOT operation, and superposed laser beam paths. FT stands for "feed through", $\lambda/4$ are quarter wave plates for creating circularly polarized light, $\lambda/2$ are a half wave plates for adjusting the power ratio in each arm when used in conjunction with a polarizing beam splitter (PBS) cube.

an optical fibre to a wavemeter (*Highfinesse, WSU-30*). The wavelength was stabilized to within ±5 fm by using a proportional-integral-derivative (PID) feedback program implemented in *Labview*. This program adjusted the wavelength of the light read by the wavemeter by varying the voltage applied to the piezo-electric element determining the fine tuning of the grating angle of the external cavity. The remaining 99% of the laser output was sent through a half-wave plate ($\lambda/2$) which rotated the linear polarization axis of the laser output, to a linear polariser to produce a pure horizontal linearly polarized beam.

The repumping transition from $5\ ^2S_{1/2}, F = 1 \rightarrow 5\ ^2P_{3/2}, F = 2$ is shifted by 6.568 GHz from the cooling transition frequency. Rather than use a separate laser for repumping, a portion of the cooling transition light was shifted by 6.568 GHz by an electro-optical (phase) modulator (EOM) (*Newport/Spectra Physics, 495010-01-M)*. About 5% of the cooling laser light was modulated to the repumping frequency. The modulation was observed by coupling a portion of the output of the EOM into a scanning Fabry-Perot interferometer. Such an interferometer (*ThorLabs, SA201*) with a free spectral range (FSR) of 10 GHz was used to observe the frequency shift and modulation depth of the light due to the EOM, and a trace of the photodiode signal against frequency is shown in Fig. 2.10 (a). The large peaks are the carrier frequency (i.e the cooling frequency), and the small peaks are the first sidebands (i.e the repumping frequency). Due to the periodic and relative measurements of the

interferometer there are two large peaks (one for each FSR), and two small peaks. The sideband at 6.568 GHz relates to the carrier at 0 GHz, and the sideband at 3.44 GHz relates to the carrier at 10 GHz, such that the first sidebands of each carrier are always 6.568 GHz away. A 40% power loss occurred at the EOM. A portion ($\approx 5\%$) of the remaining light was sent into a Rb vapor cell with a photodiode attached perpendicular to the beam path. Room temperature zero field spectroscopy of ^{87}Rb was carried out to determine the frequency of the cooling transition, and to optimize the EOM frequency shift for the repumping transition frequency. Doppler laser cooling was achieved by red detuning the cooling frequency in the range of 15 - 30 MHz from the maximum of the zero field transition. The remaining light was coupled into a single-mode polarization-maintaining (SMPM) fiber at a typical efficiency of about 35 %, which was directed to the experiment table.

Once collimated onto the experimental table with typical powers of 12 mW, the light was expanded in an adjustable Galilean beam expander between 2 and 10×. The light was then split into three arms by using two polarising beam splitter (PBS) cubes, and the power in each arm adjusted using two half wave plates. The beams were organized around the chamber as shown by Fig. 2.10 (b). Each arm passed through a quarter wave plate ($\lambda/4$) just before entry to the chamber to create circular polarisations necessary for MOT operation (see section 1.3.10). The three arms were retro-reflected through $\lambda/4$ elements after passing through the chamber, to create the full compliment of six MOT beams. The $1/e^2$ radius of the MOT beams was chosen as a compromise between the maximisation of the MOT capture volume, and the minimization of ion trap anharmonicities (see sections 1.4 and 2.2). A compromise allowing both stable MOT operation, and only a slight deviation from an ideal harmonic potential for the ions ($\approx 6\%$ within 5 mm of the trap axis) was chosen to be $r_{1/e^2} = 2.1$ mm.

2.3.3 Magnetic coils

As was described in section 1.3.10, in order to trap atoms, a conservative, position dependent force must be applied. It was described that scattering forces can be made position dependent in an optical molasses configuration of cooling beams by applying a quadrupolar magnetic field, where the field vanishes at the center of the trap.

The quadrupolar magnetic field was provided in this work by two solenoids in an anti-Helmholtz configuration, i.e. each with current propagating in an opposite direction to the other. The typical field gradients required were on the order of 17 G/cm. Due to the large size of the vacuum chamber necessary for a high flexibility in its applications, if the solenoids had been placed out of vacuum around the chamber, currents of up to 20 A through wire of 1mm diameter would have been necessary to achieve the required field gradients near the trap center. The power dissipation in this case would be in the region of kW requiring significant cooling methods. The experiments of this work required micrometer precision positioning of the atom cloud in 3D space. This can be achieved by using homogeneous magnetic bias fields. As is described in section 3.5.3 however, homogeneous magnetic fields have a large effect

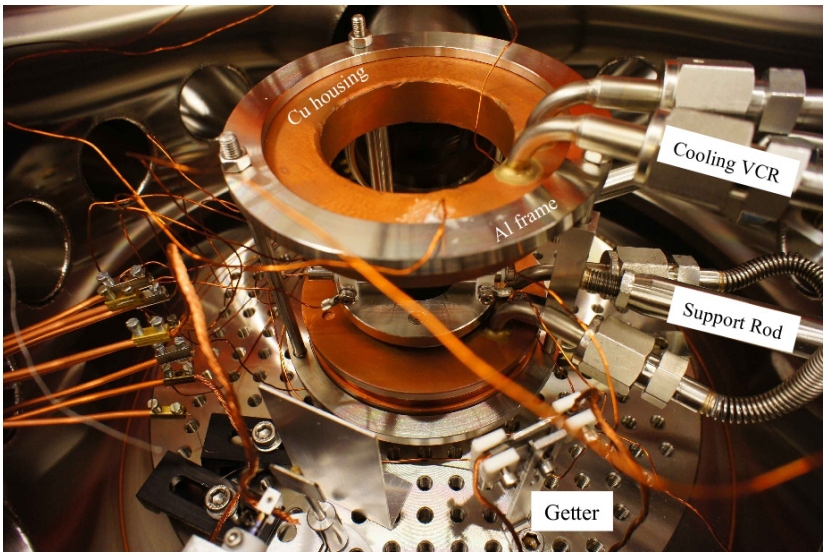

Figure 2.11: A labeled photo of inside the vacuum chamber showing the water cooled solenoids used in MOT operation, and their assembly. "VCR®" is a UHV compatible connection form *Swagelok*. The support rod connects to an xyz micrometer precision translation stage.

on the steady state populations of laser cooled ions. Reproducibility and control over these populations was a key requirement of the experiments, and so magnetic bias fields were avoided. Another way to move the magnetic center of the solenoids, and hence the atom cloud, is to physically move the coils with micrometer precision. The mass of the coils that would have been placed outside of the vacuum chamber would have made this impractical.

To address all the disadvantages of having the magnetic coils outside of the vacuum chamber outlined in the above paragraph, the magnetic coils were placed inside the vacuum, connected to a micrometer xyz manipulation stage. The total mass of the assembly was approximately 2 kg, allowing micrometer manipulation. The smaller coils produced higher field gradients for less current (typically 2 A), and using less wire, resulting in power dissipation of only 16 W. The coils were however in vacuum, and so could not dissipate heat to the environment well, so required water cooling. This was achieved by winding the coils on a copper spool which included an internal water cooling circuit, supplied by pipes connecting via a UHV feedthrough to an external water supply at 11 °C. The specifications of the coils were 0.69 mm Kapton coated wires, wound 121 times each, in a circle of radius 44 mm, in an anti-Helmholtz configuration, separated by 56 mm. A labelled photo of the magnetic coils appears in Fig. 2.11.

2.3.4 Number of MOT atoms and density determination

The number of atoms in the MOT was determined by collecting a portion of the laser induced fluorescence of the atoms from the scattering of photons inherent in magneto-optical trapping. The number of photons collected in a given time was related to the total number of photons scattered in that time by a knowledge of the solid angle of detection, and various loss mechanisms of photons before they were detected. As was seen in section 1.3.5, for a given set of laser parameters, the steady state population of the excited state $5\ ^2P_{3/2}$ can be calculated by equation 1.68. From the knowledge of the natural linewidth of this excited state Γ (in units of Hz), it was then possible to calculate how many photons would be scattered from a single atom in one second R, where

$$R = 2\pi \times \Gamma\rho_{ee} = \frac{\pi\Gamma S_0}{1 + S_0 + \left(\frac{2\delta}{\Gamma}\right)^2}. \tag{2.1}$$

This equation has been verified experimentally where it was shown to be accurate for low saturation parameters where the excited state faction does not exceed 20% [93], as was the case for all experiments of this work. It is noted that in ref. [93], a value of I_S (as related to S_0 through equation 1.67) was found from a fit to experimental measurements of P population in a Rb MOT to be $I_S = 9.2 \pm 1.7$ mW cm^{-2}. The value used for the entirety of this work however was 4.1 mW cm^{-2} calculated using equation 1.65. The total number of atoms in the cloud was then calculated by dividing the total number of photons scattered per second by the calculated number of photons scattered from one atom per second. The photons at the detector from background scattering were subtracted from the photon signal. This was achieved by measuring the fluorescence level when the current in the magnetic coils was turned off, such that there was no atom cloud, but the background scattering from the MOT beams was still present.

The formula for calculating the number of atoms N in a MOT from the number of counts on the CCD chip after background subtraction C_{SUB} in a given exposure time t_{exposure} is given by

$$N = \frac{C_{\text{SUB}}}{R \cdot t_{\text{exposure}} \cdot L \cdot G} \tag{2.2}$$

where G is the electron-multiplying (EM) gain of the gain register of the CCD device, which increases the number of counts compared to the detected photons by a factor of G. Its value did not exceed 200 so that the a linear gain response was guaranteed, and a typical value for experiment was 100. L is the proportion of scattered photons reaching the CCD chip, with

$$L = L_1 \times L_2 \times L_3 \times L_4 \times L_5 \times L_6 \times L_7 \times L_8 \tag{2.3}$$

where

- L_1 is the collection efficiency due to the solid angle of photon collection of the objective. The objective lens has an effective collection radius of 11 mm and is located 63 mm from the atom cloud, and so $L_1 = 7.62 \times 10^{-3}$.

- L_2 is the faction of photons passing through the re-entrant viewport glass, which was measured to be 0.93 ± 0.02.

- L_3 is the fraction of photons passing through the glass plate protecting the CCD chip, which is specified by the manufacturer to be 0.96.

- L_4 is the quantum efficiency of the CCD chip, which for photons of 780 nm was 0.47 (specified by the manufacturer).

- L_5 is the sensitivity of the CCD chip. When EM gain is on, the typical sensitivity (specified by the manufacturer) is 4.6 (photo)electrons per pixel per count, and hence on average L_5 is typically 0.217.

- L_6 is the fraction of photons passing through the narrow-band-pass filter used to isolate the light signal near 780 nm, and was measured to be 0.59 ± 0.02.

- L_7 is the fraction of photons passing through the objective lens, which was measured to be 0.84 ± 0.02.

- L_8 is 1 if there is no chopping, and 0.48 if there is chopping of the Rb cooling lasers, since in this case the atoms are only fluorescing 48% of the collection time.

Considering all the factors, the number of photons scattered in total by the atom cloud was typically 3000× greater than the number of photons registered by the CCD chip after background subtraction for a given time interval. An error analysis was performed by Gaussian error propagation, and a typical systematic uncertainty in atom number was found to be 44%.

The average density of the atomic cloud in the MOT was determined by assuming it had an isotropic Gaussian density distribution $n(r)$ [94] given by

$$n(r) = \frac{N}{\pi^{3/2}\omega^3} e^{-r^2/\omega^2} \tag{2.4}$$

where ω is the $1/e$ radius of the cloud. The average density was calculated by integrating over the product of the probability of an atom being at a distance r, and the density at distance r

$$n_{av} = \int \frac{n(r)}{N} n(r) dV = \frac{N}{2\sqrt{2}\pi^{3/2}\omega^3}. \tag{2.5}$$

The $1/e$ radius of a given atom cloud was obtained by recording fluorescence images. Cuts through the line of maximum intensity were then taken from the images, and Gaussian distributions fitted to the resulting intensity versus position plots. The $1/e$

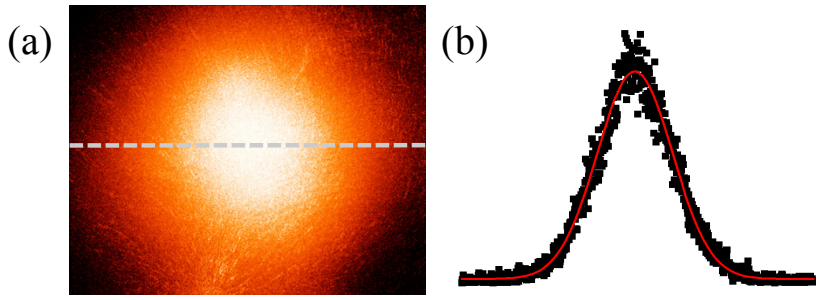

Figure 2.12: (a) False color fluorescence image of a typical atom cloud of ^{87}Rb in a MOT. The width of the image is 800 μm. (b) Pixel counts (black dots) for the row indicated by the dashed line in (a), and a fitted Gaussian distribution (red line).

radius was extracted from these fits. An example of a MOT fluorescence image, along with a Gaussian fitted cut through the horizontal center line of the cloud is presented in Fig. 2.12. During the experiments, vertical and horizontal cuts were taken to ensure the isotropic nature of the distribution.

2.3.5 Measuring the temperature of the ^{87}Rb ensemble in the MOT

The velocity distribution of atoms in the MOT is quasi-thermal, and can be closely approximated by a 1D-Maxwell-Boltzmann distribution in each direction [2]. In this case the temperature can be defined through the width of the velocity distribution, which is centered around zero, i.e. in one dimension $\frac{1}{2}k_BT = \frac{1}{2}mv^2$ where v is the RMS velocity of the distribution.

The temperature of the atoms in the MOT was measured following the techniques of ref. [95]. The technique was roughly based on the method of Ref. [96], which assumes that if the trap is suddenly switched off, the atoms that were held in the trap will expand ballistically at a rate that is characteristic of their initial temperature. The expansion follows

$$\omega^2(t) = \omega^2(0) + \left(\frac{k_BT}{m}\right)t^2 \tag{2.6}$$

where ω is the $1/e$ radius of the atom cloud. Reference [95] showed that instead of turning off the trap completely, it is sufficient to turn off only one dimension (i.e. just one pair of counter-propagating laser beams of the MOT), and to observe the ballistic expansion in this dimension. This makes the observation of expansion easier by virtue of the atoms being constantly illuminated by the four beams beams which remain on. If the x axis is defined as the propagation axis of the beam which is switched off, then

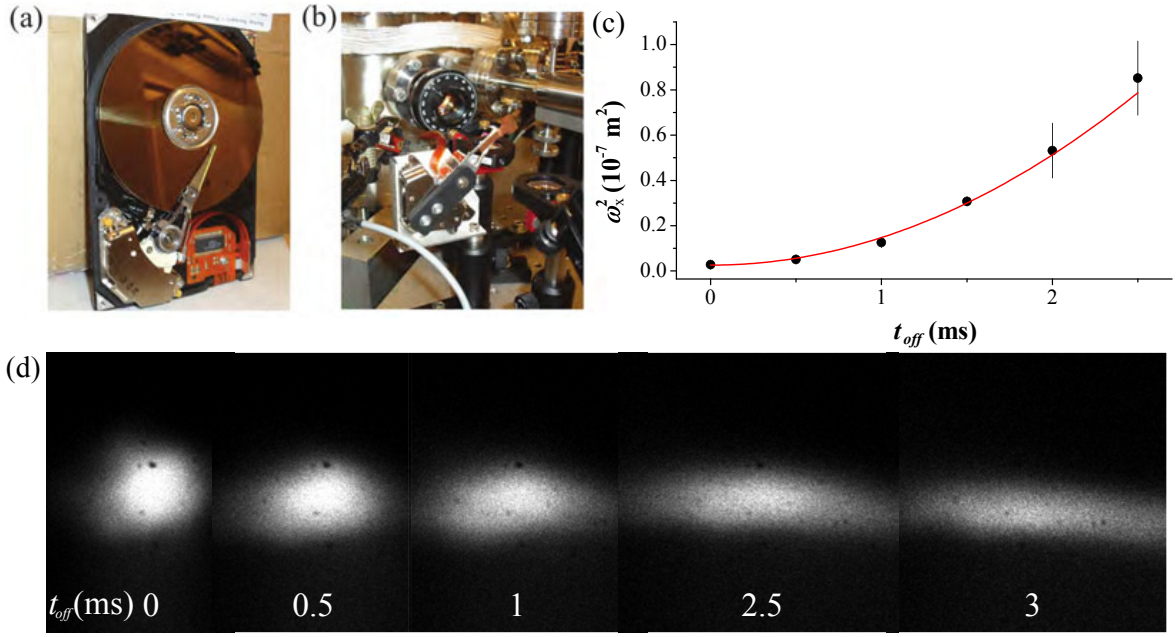

Figure 2.13: (a) A picture of a hard disk of a computer showing needle and voice coil (b) A picture of the fast shutter (made from the hard disk voice coil in (a)) on the experiment. This shutter is used in the temperature measurement of the atoms in the MOT. (c) A Graph of the square of the atom cloud $1/e$ radius in the x direction ω_x against time after the shutter blocks the x direction MOT beams. The line is a fit to equation 2.7. The temperature of the atom cloud in this measurement was found to be 127 $\pm$10 μK. Each data point is an average of three consecutive measurements. (d) A sequence of fluorescence images of a cloud of atoms in the MOT at varying times t after the x direction MOT beams are blocked, showing the ballistic expansion of the cloud in this dimension.

in one dimension equation 2.6 becomes

$$\omega_x^2(t) = \omega_x^2(0) + \left(\frac{k_B T}{m}\right) t^2 \tag{2.7}$$

Since the line of sight of the CCD camera is aligned 45° to the x axis, the observed $1/e$ radius of the cloud on expansion ω_r is related to the $1/e$ radius of the cloud in the expansion direction ω_x by

$$\omega_r^2(t) = (\omega_x^2(t) + \omega_y^2(t))/2 \tag{2.8}$$

where ω_y is the $1/e$ radius of the cloud in the y direction. (Note, x and y define the horizontal plane which does not include the magnetic coils, with z being the remaining orthogonal vertical axis.) There was negligible expansion of the cloud in the y and z directions during the 1D expansion, and hence observation of the atoms in the plane of the CCD chip is sufficient to calculate the temperature of the atoms.

This 1D release and recapture method relies on the fast on/off switching of one of the pairs of laser beams of the MOT. This was achieved by building an optical chopper from the voice-coil actuator of a hard disk drive [97]. The switch time from "beam on" to "beam off" achieved by this shutter was $150 - 200$ μs depending on the drive current used, and the "beam off" time could be varied from 400 μs up to 10 ms. A picture of the shutter (b) and the corresponding hard drive (a) is presented in Fig. 2.13. The shutter was synchronized with the CCD camera using two transistor-transistor-logic (TTL) pulses originating from a DAC card connected to a PC running a control program written in *Labview*. The CCD exposure time was set to 0.6 ms (the minimum allowed value). Fluorescence images were recorded for different "beam off" holding times t_{off}. A series of such images is presented in Fig. 2.13 (d). From fitting cuts of the expansion images to Gaussian distributions, ω_r and hence via equation 2.8 ω_x were determined. ω_x^2 is plotted against expansion time t_{off} in Fig. 2.13 (c). The red line is a best fit to equation 2.7, and yields a temperature of the atoms of $127 \pm 10\mu$K.

2.3.6 Chopping of the MOT

Of the ensemble of ^{87}Rb atoms in a MOT, a certain proportion (typically around 10%) are in the excited 5 $^2P_{3/2}$ level due to laser excitation. The ionization continuum of Rb lies 2.59 eV above this level, and so absorption of a photon with a wavelength below 478 nm results in ionization of Rb. Any Rb^+ generated in this way is then loaded into the ion trap. The successful analysis of ion-neutral reactions requires that any ions present in the ion trap are produced from chemical reactions, and not from other sources. Also, the photoionisation can be so efficient that vast amounts of Rb^+ ions are loaded quickly, and hence distorting and even melting the original ion crystal of interest (see section 2.2.4). It is therefore imperative that no Rb^+ are produced by photoinisation. To ensure this, the ion cooling lasers (at 397 nm for Ca^+ and 493 nm for Ba^+) and the Rb cooling laser (at 780 nm) were alternatively chopped by a mechanical chopper at 1 kHz (see Fig. 2.14 (c)) such that when Rb was being cooled, and hence had some

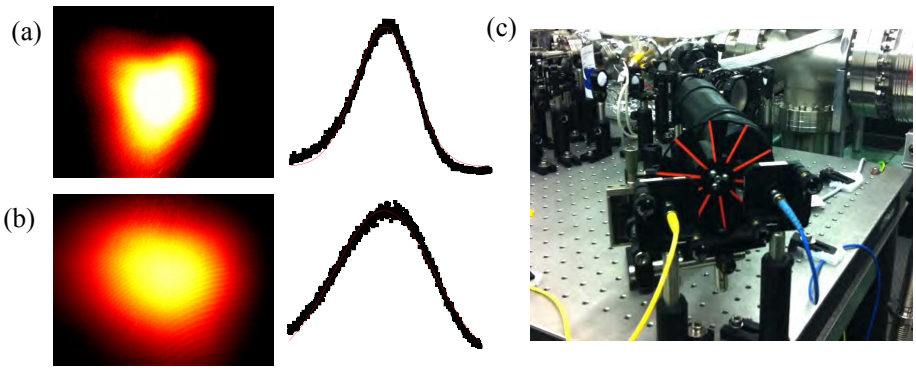

Figure 2.14: (a) Fluorescence image of an unchopped MOT with an intensity plot of a cut through the center row (black dots) and a Gaussian fit (red line) (b) Same as (a) but for optical chopping of all of the MOT beams at 1000 Hz. (c) A picture of the chopping wheel showing fiber out-coupling of the 780 nm (blue fiber) and 397 nm (yellow fiber) beams that are alternately chopped.

population in 5 $^2P_{3/2}$, no intense source of direct (397 nm) or near-direct (493 nm) ionizing photons was present. There was a period of ≈ 50 μs after each on or off cycle where all laser sources are blocked, which was sufficient time for the decay of excited state atoms (excited state lifetime $\tau = 26$ ns for ^{87}Rb), or ions ($\tau = 7$ ns for Ca^+) back to the ground state. Note that the repumping lasers (866 nm for Ca^+ and 650 nm for Ba^+) remained constantly on in experiments to avoid trapping in the long lived $^2D_{3/2}$ states during chopping of the cooling lasers.

When the MOT laser beams were turned off, the atom cloud expanded ballistically in three dimensions, similar to the 1D case as seen in the temperature measurements in section 2.3.5. Once the beams were turned on again, the atoms were forced back towards the trap center. In the 1 kHz optical chopping used in the experiments of this work, the atoms expanded and contracted with a period of 1 ms. The time averaged result was that the atom cloud reduced in atom number, and its width increased, resulting in reduced atom number densities. A comparison is made in Fig. 2.14 between a MOT without (a) and with (b) optical chopping at 1 kHz. Next to each false color fluorescence image is a cut through the center of the cloud with a fit to a Gaussian distribution. The $1/e$ radius of the fitted Gaussian for the chopped MOT was approximately double that of the corresponding unchopped MOT, which in itself implies a reduction of number density by a factor of 8. The number of atoms also reduces due to the loss of atoms on ballistic expansion, resulting in a typical total reduction in density during chopping of a factor of 50, i.e. from $\sim 5 \times 10^{10}$ cm^{-3} to $\sim 1 \times 10^9$ cm^{-3}. Note that the values stated were typical but that under the right conditions, density differences of up to a factor of 200 were possible.

It is interesting to note that this reduction in density upon chopping turned out to be useful for the study of fast reaction processes, since at lower densities, the reaction rate was slower, and hence easier to observe. These low densities also minimized the influence of three-body reactive processes, allowing direct study of the two body processes that were the focus of this work.

2.4 The hybrid trap

The two preceding sections have demonstrated the technical implementations of ion trapping and cooling, and magneto-optical trapping of neutrals. To use these methods to study cold ion-neutral processes, they must be brought together in the same place and operate simultaneously. The resulting setup is referred to as a hybrid trap.

2.4.1 Inter-trap effects

In principle there are five major sources of interference when the ion trap and the MOT operate simultaneously. *Comsol* was used to simulate some of the effects of bringing the two traps together [98], and other effects were determined experimentally. The major sources of interference are listed here:

- The rods of the ion trap may interfere with the magnetic field needed for the MOT. The magnetic susceptibility χ of stainless steel (out of which the ion trap electrodes were made) was assumed to be 0.008, and hence should not effect the magnetic field of the MOT coils. Indeed simulations showed that the magnetic gradients only differed by 0.4% compared to those in vacuum with no rods [98].

- The magnetic field of the MOT coils may interfere with the laser cooling of the ions by Zeeman shifting the relevant energy levels. It was calculated that at 1 mm from the magnetic zero of the MOT coils, the largest Zeeman induced shift in the Ca^+ cooling transition (i.e. for the $(4s)^2S_{1/2}, m = -\frac{1}{2} \rightarrow (4p)^2P_{1/2}, m = +\frac{1}{2}$ transition) was $2\pi \times 3.75$ MHz, which is much smaller than the natural linewidth of the transition of $2\pi \times 22.4$ MHz, and hence had a negligible effect on the laser cooling [98].

- The magnetic field of the MOT coils may exert a Lorentz force on the ions of the ion trap. The Lorentz force on an ion is $F_{Lor} = q(v \times B)$, where q is the charge, v is the ion velocity, and B is the magnetic field strength. It was calculated that at high ion velocities, typical of those associated with the temperature of the atom source (≈ 600 ms^{-1}), at 1 mm from the magnetic zero, the Lorentz force was comparable to the scattering force of laser cooling using typical cooling parameters. The Lorentz force, however, decreases linearly with reducing velocity, but the cooling force increases rapidly with reducing velocity as the Doppler shift of the transition is reduced and brought closer into resonance

with the laser cooling frequency. At typical ion velocities in Coulomb crystals (≈ 30 ms^{-1}) therefore, the Lorentz force is three orders of magnitude lower than the cooling force, hence the effect of the Lorentz force on Coulomb crystallized ions in the hybrid trap is negligible [98].

- The magnetic field from the MOT coils can be approximated as homogeneous over a Coulomb crystal (see section 3.5.3). As can be seen form the results of an 8-level optical Bloch treatment of the laser cooling of Ca^+ and Ba^+ (see section 3.5.3), the laser cooling can be dramatically effected by a homogeneous magnetic field, depending strongly on the angle between the linear polarisation axis of the lasers, and the magnetic field vector. This effect is investigated experimentally and discussed in section 3.5.3. Suffice to say that the conditions can be controlled to allow for optimal laser cooling conditions, and hence negate the interference effects of the MOT magnetic field with the ions.

- Lastly, as has been discussed in the previous two sections, Rb in its $(5p)\ ^2P_{3/2}$ excited state, populated during MOT operation, can be directly photoionised by the Ca^+ cooling laser, and two photon ionized by the Ba^+ cooling laser. To avoid photoionization of Rb (which would interfere with reaction dynamic analysis), the atom and ion cooling lasers are alternately chopped at 1000 Hz, such that no Rb^+ loading is observed. The effect of chopping on the ions and on the MOT has been discussed in detail in sections 2.2.4 and 2.3.6, respectively.

2.4.2 Experimental setup

Fig. 2.15 is a schematic of the experimental setup, where the coils of the MOT and the rods of the ion trap are shown without connections. The laser beam paths for the MOT (780 nm), for cooling and repumping of Ca^+ and/or Ba^+, and for the photoionisation of Ca and/or Ba (355 nm) or N_2 (202 nm) are shown. Also shown is the objective of the imaging system which lies outside of vacuum. The inset shows a typical pair of superposed fluorescence images of two Ca^+ ions (blue) and a cloud of ultracold Rb atoms in the MOT (red).

Fig. 2.16 is an augmented labeled photo of of the open vacuum chamber showing all the important *in vacuo* hardware for hybrid trapping. The leak valve is for the controlled admittance of N_2 for the loading of N_2^+ into the ion trap. Note that for single ion laser cooling, the cooling beams were implemented in a 3D configuration (not shown in the figures) to compensate for the lack of Coulomb coupling between the motional degrees of freedom in this case.

Fig 2.17 is a schematic of the experimental setup, showing the diode and dye laser configurations. Diode lasers are shown in blue boxes on the left. The 493 nm, 650 nm combination is for the cooling and repuming of Ba^+ ions, whereas the 397 nm, 866 nm combination is for that of Ca^+ ions. The 780 nm diode laser is for the cooling and trapping of Rb. The outputs of all the diode lasers are directed to the experiment using

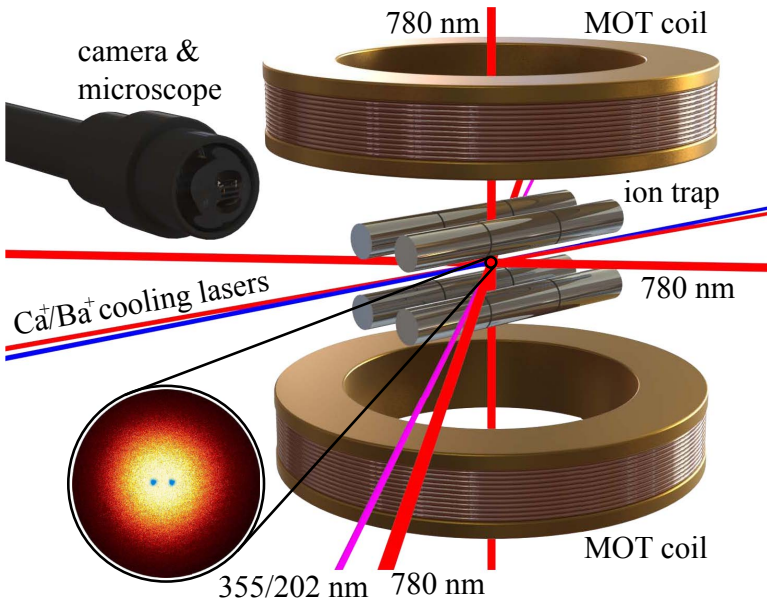

Figure 2.15: A 3D schematic of the hybrid trap (drawn by P. Eberle). For clarity, the holders and connections for the traps are not shown. The 780 nm beams are used for the magneto-optical trapping (MOT) of ^{87}Rb. The 355 nm beam is for the non-resonant ionization of Ca and Ba atoms, and the 202 nm beam is for the [2+1] REMPI of N_2 molecules. The inset shows superposed fluorescence images of a cloud of Rb atoms in the MOT (red) and two calcium ions in the ion trap (blue).

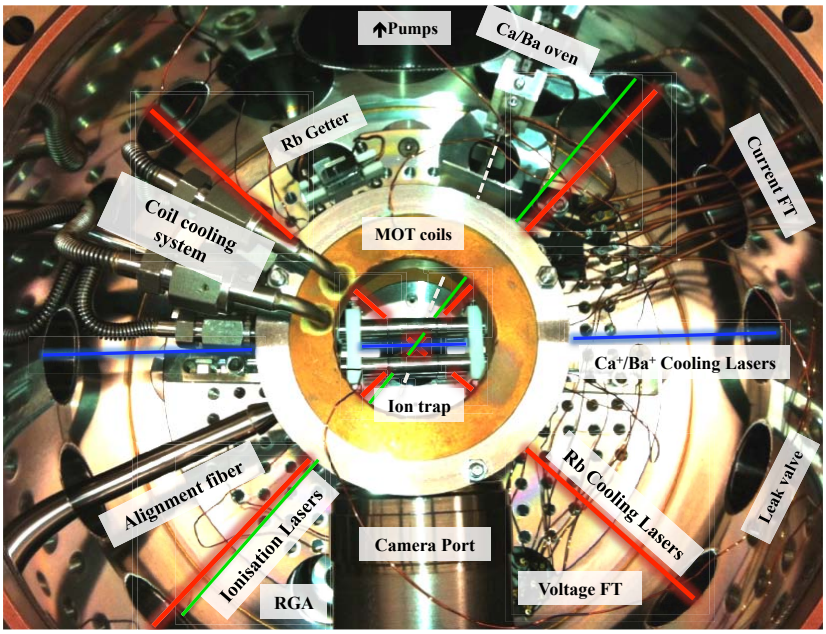

Figure 2.16: An augmented, labeled photo of the top view of the experimental vacuum chamber. RGA = "residual gas analyzer", FT = feed-through. The voltage FT connects to the ion trap voltages, and the current FT connects to the MOT coil and oven currents.

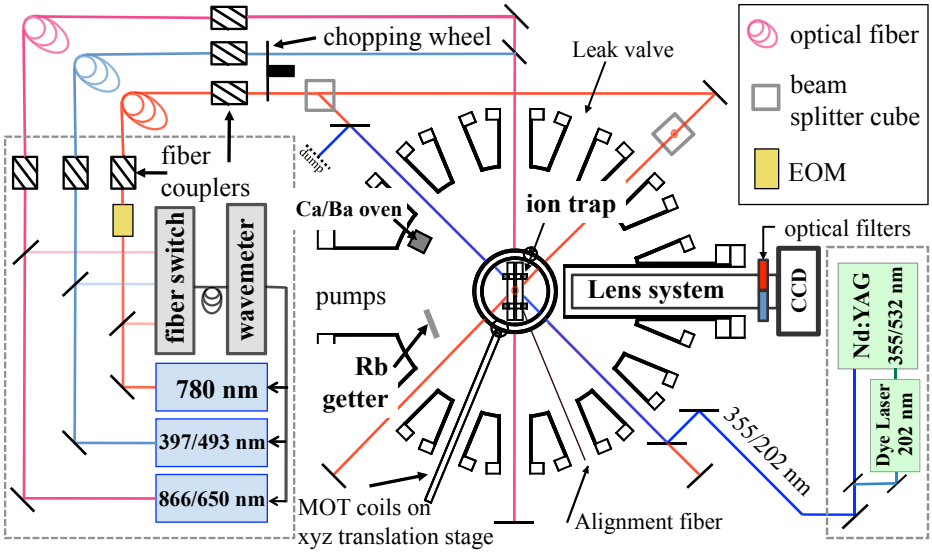

Figure 2.17: A schematic of the experimental setup. The 397 nm and 866 nm configuration corresponds to laser cooling of Ca^+ ions, whereas the 493 nm and 650 nm configuration corresponds to laser cooling of Ba^+ ions. The 780 nm laser is for Rb laser cooling in the MOT. The 355 nm pulsed tripled output of the Nd:YAG is for the ionisation of neutral Ba and Ca, where as the 202 nm output of the 532 nm pumped dye laser is for the [2+1] REMPI of N_2. EOM stands for electro-optic modulator.

single mode optical fibers. The fundamental output of the Nd:YAG laser at 1064 nm was doubled to 532 nm for pumping of a dye laser to produce 202 nm for the REMPI of N_2, and was tripled to 355 nm for the non-resonant ionisation of Ba or Ca. The Nd:YAG and dye laser outputs are too intense to be coupled to fibers, and so were directed to the experiment through free space.

Chapter 3

Experimental and analytic techniques

The previous chapter detailed the technical aspects of the implementation of a hybrid trap. This chapter describes the theory and application of both the experimental techniques used to characterize and investigate the cold ion-neutral reactions of this work, and the techniques used to analyze the experimental data recorded to gain insight into their meaning. The key aspects of the experimental techniques relate to the reproducible initiation and study of the reactions, which requires a well characterized overlap of the ion and neutral distributions, protocols for the definition and determination of reaction rate, procedures for the characterization of the dependence of reaction rate on collision energy, determination of the chemical identity of ions in the ion trap through resonance excitation mass spectrometry, and determination of ion steady state population. The observed chemical dynamics are rationalized using computed potential energy curves, and experimental rates compared to quantum-scattering calculations (both conducted by the Laboratoire Aimé Cotton group) through velocity averaged computed cross sections. To put the comparisons of experiment and theory made in subsequent chapters in context, the methods and implications of such calculations will also be briefly be described.

3.1 Ion-atom overlap

Characterization of the overlap of the density distributions of the ion Coulomb crystal and atom cloud was essential for the determination of rate constants for the reactive processes studied in this work. Positioning inaccuracies and fluctuations of the density distributions will have the least effect on the degree of overlap if the ion and atom distributions have a common center, since this is the position of the 3D Gaussian atom distribution which has the lowest rate of change of local atomic density with respect to displacement. As a consequence, and for experimental simplicity, the ion and atom distributions were made to have a common center in 3D space.

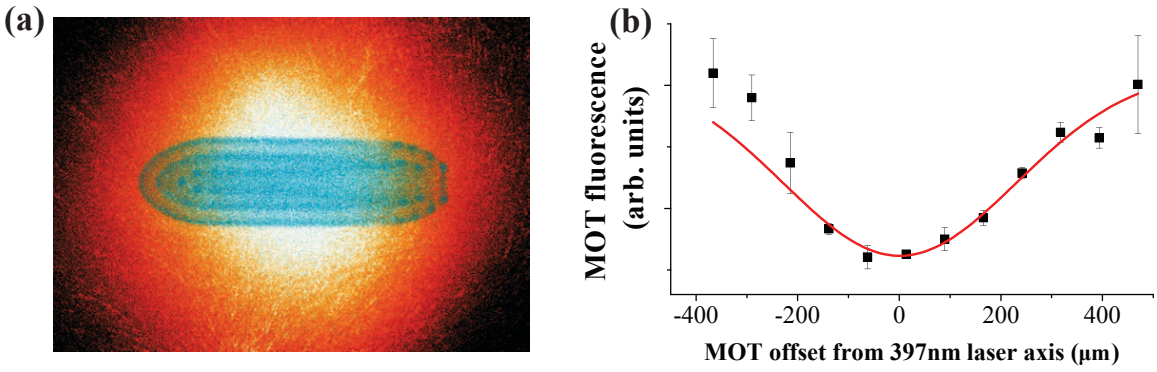

Figure 3.1: (a) Superposed false color fluorescence images of a cloud of Rb atoms (red) and a Coulomb crystal of Ca^+ ions (blue) to determine their overlap in the plane of the camera chip. (b) Depletion of the fluorescence from the MOT as a function of radial displacement of the atom cloud from the central axis of a focused 397 nm laser beam. The fluorescence reaches a minimum when they are perfectly overlapped, corresponding to the maximum photoionisation rate of Rb from the $(5p)\ ^2P_{3/2}$ state by the 397 nm beam. The red line is a Gaussian fit to the data, where the width of the Gaussian has been constrained to be equal to the RMS average of the widths of the 397 nm beam profile and the unperturbed atom cloud in the MOT.

The ions were translated along the ion trap axis using DC fields on the endcaps, without incurring excess micromotion as compared to the geometric trap center, by up to ± 1.5 mm, enabled by the long (20 mm) central electrodes of the rods of the ion trap. The ions could not be positioned in the radial direction using DC fields without incurring excess micromotion, and so were constrained to the axial rf null line in these dimensions.

The atom cloud could be moved in 3D to any position within a radius of ≈ 2 mm of the geometric center of the ion trap. This was possible due to the magnetic coils of the MOT being connected to an xyz micrometer translational stage. This allowed the magnetic center of the MOT to be positioned without needing homogeneous magnetic bias fields (which would interfere with the laser cooling of the ions). When necessary, the MOT laser beams were then re-positioned to the new magnetic center to allow for the most stable and efficient MOT operation.

The determination of the overlap of the ion and atom distributions in the plane of the CCD camera chip was achieved by recording fluorescence images of the distributions. The images were then superposed to ensure common centering in this plane, an example of which is presented in Fig. 3.1 (a). Since the camera only provided a 2D projection, overlap in the line of sight direction of the camera was achieved using a different method. A Ca^+ Coulomb crystal was formed and axialised in the ion trap. The focused Ca^+ cooling laser at 397 nm (which has a near Gaussian beam profile with a waist $1/e^2$ radius of 190 μm) was aligned along the rf axis to within $\approx \pm 10$ μm by

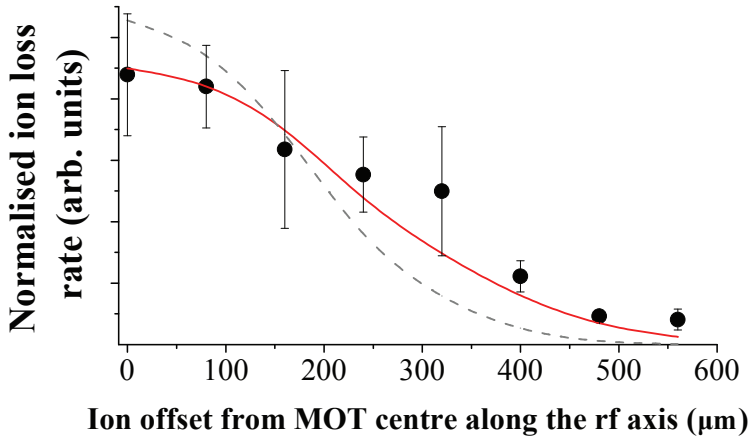

Figure 3.2: Normalized ion loss rate as a function of axial ion distance from the center of a cloud of Rb. The grey dotted line is is the expected distribution according to the overlap factor model. The red line is the best fit of the model to the data, achieved if the offset is scaled by 1.4. See text for details.

maximizing the fluorescence of the Ca^+ ions. The focused 397 nm beam (with typical intensities of 400 mW cm^{-2}) photoionised excited state $(5p)^2P_{3/2}$ Rb present in the MOT. The photoinisation resulted in a reduction of steady state MOT atom number, and hence a reduction in the fluorescence level of the MOT. This change was recorded by the CCD camera as a function of the MOT position in the line of sight direction of the camera. Common center overlap of the ion and atom distributions in this direction was then indicated by the position of maximum depletion of fluorescence of the MOT when the axialised 397 nm beam was emitted. Fig. 3.1 (b) shows a plot of the MOT fluorescence against radial offset from the 397 nm axis (coincident with the rf null axis). A Gaussian distribution is fitted to the data where the width has been constrained to be equal to the RMS average of the 397 nm Gaussian beam width and the unperturbed atom cloud Gaussian width. Using this method, overlap of the ion and atom distribution centers to within ± 80 μm was achieved.

Section 2.3.4 described the method for determining the average atom density in a MOT from fluorescence images. The average density of the atom cloud is a useful metric for MOT characterization, but for rate constant determination, it is more accurate to use the average atomic density inside the Coulomb crystal volume. The average atomic density experienced by ions of a Coulomb crystal was calculated using a model which assumes a 3D Gaussian atomic density distribution with a $1/e$ radius determined form experimental images, and an homogeneous ellipsoidal ion density distribution characterized by the crystal width and length, also determined from experimental images. The atomic density experienced by the ions n can be expressed in terms of the average atom density n_{av} by the use of an "overlap factor" $f_{overlap}$, such that $n = n_{av} f_{overlap}$. A full description of the calculation of the overlap factor, including *matlab* scripts, can be

found in ref. [99]. Briefly, the calculation is the weighted integral of an ellipsoid inside a Gaussian scalar field. The ellipsoid is cut up into many small hollow discs, and the volume of each is multiplied by the local field density. The sum of all these elements is then divided by the volume of the crystal to get the average field density inside the crystal. This is then compared to the average density of the field, to arrive at the overlap factor. Smaller ion Coulomb crystals in larger atomic density distributions produce larger overlap factors, as the ions are experiencing a higher atomic density as compared to average. It is noted that the ion Coulomb crystal radius, and hence the overlap factor, changes as the reaction proceeds, and so a time dependent overlap factor should in principle be required. The effect of this time dependence would however be observable in a departure from linearity in the in pseudo-first order rate constant determination graphs (see next section). This departure, however, is not observed within the error bars for reactions of up to 50% of the initial ion number, and since this is the range used for analysis in the experiments of this work, the calculation of a time dependent overlap factor was not required.

To characterize the importance of the overlap of the atom and ion distributions, and the effectiveness of the overlap model, an experiment was conducted which measured the Ca^+ ion loss rate due to reactions with Rb as a function of the axial displacement of ion and atom distribution centers. In Fig 3.2, the normalized ion loss rate is plotted as a function of axial trap center offset. The dotted grey line is the prediction of the overlap model as informed by static fluorescence images of the atom cloud and ion crystal. The model predicts the loss rate to fall off faster with axial offset than the experiment demonstrated. A better fit is achieved if the MOT radius (or equivalently the displacement) is scaled by a factor of 1.4. This can be explained by the fact that due to small frequency and intensity fluctuations of the MOT laser beams, the atom cloud position and distribution also fluctuates (on the order of 40 μm) and so the effective area the atom cloud samples over the course of the reaction is larger than is suggested by the static fluorescence images. In the case of zero offset, the impact of this fluctuation effect is minimized, and the resulting error in the rate constant, $<$10 %, is much smaller than the dominant error of $\approx$50 % due to the uncertainty in the atom number.

3.2 Rate constant determination

Due to the low densities of the atoms and ions inside the hybrid trap, three body collisions are negligible [40]. As a result, all of the reactive process in the experiments of this work are assumed to be two body. Since no spontaneous decomposition, ionization, or neutralization of any of the reactants are expected, the reaction rates of the atom (Rb) with the various ions (Ca^+ or Ba^+ or N_2^+) are expected to be of second order, i.e. depending linearly on both the densities of the ions and the atoms. For a reaction of the form $A^+ + B \rightarrow products$ the second order rate law for the appearance of ion A^+

can be written

$$-\frac{d[A^+]}{dt} = k[A^+][B] \tag{3.1}$$

where k is the second order rate constant for the process. Equation 3.1 can be simplified by the fact that the density of ions in a Coulomb crystal is approximately constant [100], and so can be replaced by the number of ions in the crystal volume N_{A^+}. Also the concentration of B can be rewritten as the density of B, n_B such that

$$-\frac{dN_{A^+}}{dt} = kN_{A^+}n_B. \tag{3.2}$$

The atoms in the MOT are constantly replenished from background vapor at a rate far exceeding any studied reaction rate (on the order of 10^4 atoms per second), and so n_B can be treated as a constant. The reaction kinetics in this case are pseudo-first order in nature, since the number of ions is the only time dependent factor. Equation 3.2 can be further simplified with the definition of the psudo-first order rate constant $k_{pfo} = kn_B$ to produce

$$-\frac{dN_{A^+}}{dt} = k_{pfo}N_{A^+}. \tag{3.3}$$

Equation 3.3 can be solved by integration, yielding

$$N_{A^+,t} = N_{A^+,0}e^{-k_{pfo}t} \tag{3.4}$$

where $N_{A^+,0}$ is the initial number of ions at reaction time $t = 0$. This equation can be rearranged to give

$$\ln\left(\frac{N_{A^+,t}}{N_{A^+,0}}\right) = -k_{pfo}t \tag{3.5}$$

Due to constant ion density, N_{A^+} is interchangeable with the volume of A^+, V_{A^+} in this equation, and either can be used, depending on the most convenient way to characterize the amount of ions in a given reaction. Plotting a graph of $\ln(N_{A,t}/N_{A,0})$ as a function of t for a reaction yields a straight line with gradient $-k_{pfo}$. The atomic density during the reaction is then used to extract the second order rate constant with $k = k_{pfo}/n_B$. The atom density can be approximated as the average density of atoms inside the ion Coulomb crystal volume, which can be calculated by taking the product of the average atom density in the MOT n_{av} (see section 2.3.4) and an overlap factor $f_{overlap}$(see section 3.1), giving

$$k = \frac{k_{pfo}}{n_{av} \cdot f_{overlap}} \tag{3.6}$$

3.2.1 Pseudo-first-order rate constant determination

As was seen above, given a knowledge of the atom density, calculation of the rate constant of a reaction reduces to determining the pseudo-first order rate constant, k_{pfo}. This can be done by plotting $\ln(N_{A,t}/N_{A,0})$ as a function of reaction time t,

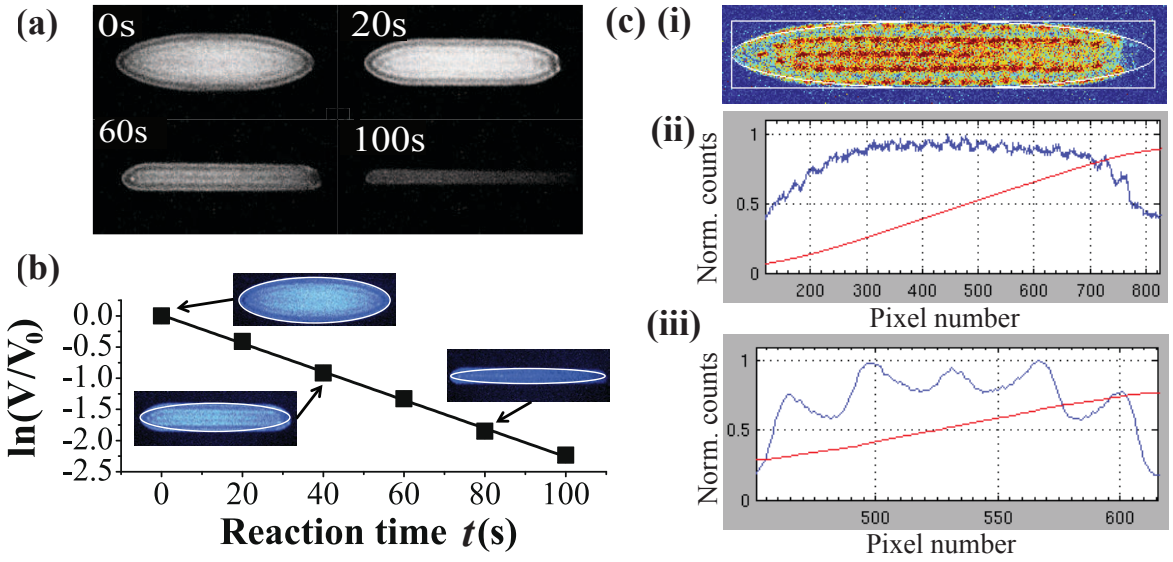

Figure 3.3: (a) Fluorescence images of a Ca^+ Coulomb crystal over the course of a typical reaction with Rb. (b) A plot of the natural logarithm of the volume of the crystal at reaction time t over its initial volume, against reaction time. Also shown are the corresponding crystal fluorescence images. The modulus of the gradient of the black regression line is the pseudo first order rate constant. The error bars are within the data points. (c) Images taken from the *Matlab* program for determining the volume of the crystal from a 2D image. (i) False color fluorescence image of a Ca^+ Coulomb crystal with ellipse fitted. (ii) A plot of the normalized counts against horizontal pixel number tracing a cut along the axis of the image. (iii) Same as for (ii) but for vertical pixel number tracing a cut through the axis of the image. The radial shells of ions are clearly visible as peaks in this trace.

where the gradient of the resulting straight line is $-k_{pfo}$. Instead of ion number N_A, the ion volume V_A can equivalently be used, due to the constant ion density of Coulomb crystals. Axialised crystals are rotationally symmetric about the rf axis, and so 2D projections in a plane perpendicular to the rf axis, recorded as fluorescence images on a CCD camera, were sufficient to calculate the volume of ions in a coulomb crystal.

The determination of k_{pfo} for the Ca^+ + Rb system is now discussed. Fig. 3.3 (a) shows the reaction of Ca^+ ions with ultracold Rb as a function of time. It can be seen that the fluorescing Ca^+ volume reduced as the reaction proceeded, and that all of the products of the reaction were heavier than Ca^+, and so were positioned outside the Ca^+ core in a radially symmetric way. The volume of the Ca^+ for each image was determined using an ellipse fitting method. Fig. 3.3 (c) (i) shows an ellipse fitted around a Ca^+ Coulomb crystal that was reacted with Rb. A *Matlab* program calculated the volume of the corresponding ellipsoid. Slight departure of the

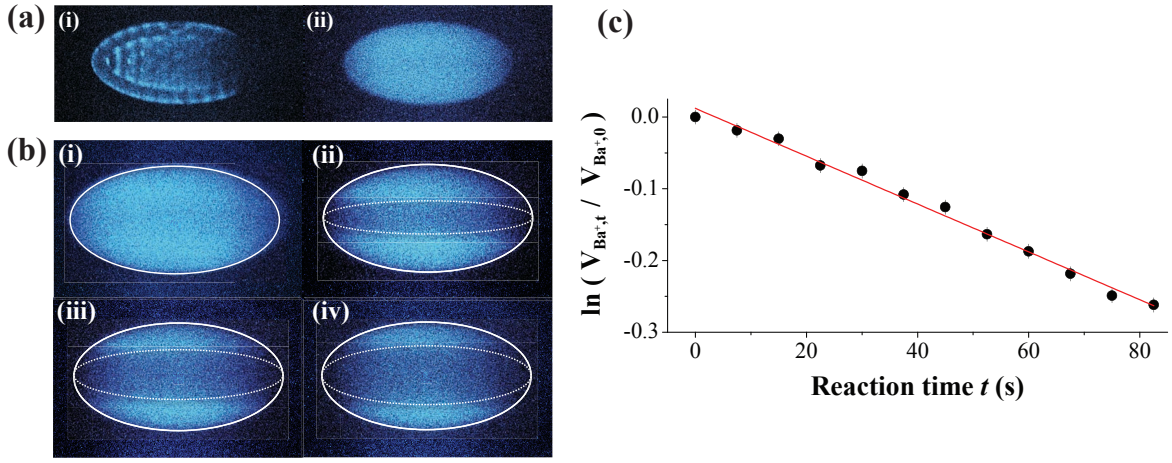

Figure 3.4: (a) Fluorescence images of a Ba^+ Coulomb crystal (i) with cooling from a single axial direction, and (ii) with balanced bi-directional axial cooling. (b) Fluorescence images of a Coulomb crystal of Ba^+ ions during the course of reaction with a Rb MOT. The outer white ellipse of each image marks the total crystal volume, and the inner white ellipse marks the Rb^+ volume. (c) A plot of the natural logarithm of the volume of Ba^+at reaction time t in the crystal divided by the initial volume, against time. The modulus of the gradient of the red regression line is the pseudo first order rate constant.

crystals from ellipsoidal, for example due to the flattening of the crystal edge due to the presence of heavy sympathetically cooled ions, was compensated for by ensuring equal areas inside and outside the area defined by the fitting ellipse. Note that since k_{pfo} depends on a relative measurement of volume, as long as the fitting procedure is consistent for all images, the systematic error in crystal volume will be negated. Fig. 3.3 (c) (ii) and (iii) are cuts through the image in (i) showing the shell structure of a Coulomb crystal. Fig. 3.3 (b) shows a typical plot to determine k_{pfo}, where the error bars are smaller than the data points. Also shown are corresponding reaction images with the fitted ellipse shown in white. The linearity of the data demonstrates that the assumption of pseudo-first order kinetics is justified.

The determination of k_{pfo} for the Ba^+ + Rb system is now discussed. Ba^+ ions were loaded into the ion trap in a non-isotopically-selected way. This resulted in Ba^+ ions being loaded with the natural isotopic abundance of the neutral precursor (^{138}Ba 71.7 %, ^{137}Ba 11.3 %, ^{136}Ba 7.8 %, ^{135}Ba 6.6 %, ^{134}Ba 2.4 %, ^{132}Ba 0.1 %, ^{130}Ba 0.1 %), and hence Coulomb crystal comprised 72 % of the desired $^{138}Ba^+$, and 28 % of lighter isotopes. It is noted that isotope selective loading is possible [101, 102], and will be used in future experiments. Fig. 3.4 (a) (i) shows a non-isotopically-selected crystal which is cooled from only one axial direction. Although the ions in this case had a low secular temperature, and there was near single ion resolution, such

asymmetric crystals did not allow for simple volume determination methods. Full MD simulations would have had to have been conducted for each reaction step which proved impractical. On introducing a counter-propagating cooling laser with equal intensity however, due to their similar masses, the isotopes of Ba^+ mixed in the Coulomb crystal, and the fluorescence images resembled that presented in Fig.3.4 (a) (ii). These radially symmetric crystals were then analyzed using ellipse fitting methods.

In reactions of Ba^+ ions with Rb, the majority of the products (Rb^+ ions) were lighter than Ba^+, and so as the reaction proceeded, a dark core formed about the axis of the crystal (see Fig. 3.4 (b)). The volume of Ba^+ ions at given reaction time $V_{Ba^+,t}$ was therefore calculated by the difference of the total crystal volume V_{tot} and the volume of the dark inner core of Rb^+, V_{Rb^+}. A plot of $\ln(V_{Ba^+,t}/V_{Ba^+,0})$ as a function of reaction time for a typical reaction of Ba^+ with ultracold Rb is presented in Fig.3.4 (c). The gradient of the regression line of this plot is $-k_{pfo}$.

The determination of k_{pfo} for the N_2^+ + Rb system is now discussed. For reactions of N_2^+ with ultracold Rb, the N_2^+ ions were loaded as a string of typically 25 ions into the center of a Ca^+ Coulomb crystal where they were sympathetically cooled [103–105] by their Coulomb interaction with Ca^+, and were observed in the Ca^+ fluorescence images as a dark central core (see Fig. 3.5 (a) (i)). The Ca^+ cooling lasers were made to be slightly imbalanced in the axial direction, such that the radiation pressure force acting on the Ca^+ acted to push them preferentially in one axial direction. As a consequence, the sympathetically cooled N_2^+ ions were displaced in the opposite direction to the Ca^+ ions. The reactions were initiated with a string of N_2^+ just filling the core of the Ca^+ Coulomb crystal. As each N_2^+ ion reacted away with Rb, the chain got shorter, which, due to the effect of the radiation pressure, happened in such a way that the dark core shrank to one side. This can be seen in Fig. 3.5 (a) (i)-(iii), where the chain shrinks away to the left.

Due to the constant density of ions in Coulomb crystals, the length of the dark core is proportional to the number of N_2^+ ions remaining. To accurately observe such changes however, fluorescence images must be taken. Due to the low fluorescence levels, the total time needed for the CCD camera to acquire, average, record and store sufficiently clear images was approximately 1 s. The reaction of N_2^+ with Rb at low temperatures however is very fast, such that typically the entire string was reacted away within $\approx$ 4 s. For such fast reactions, the definition of the start of the reaction needs to be accurate enough to enable consistent and meaningful analysis. For these reasons a different method than image capture and analysis was needed to determine k_{pfo} for N_2^+ + Rb reactions.

Fig. 3.5 (a) includes two boxes for each image which correspond to user defined regions of integrated fluorescence capture on the CCD camera software. F_1 is for the dark core region where N_2^+ ions are located, and F_2 is to monitor the fluorescence of the Ca^+ ions. The integrated fluorescence from each box was recorded as a function of time, a typical example of which is shown in Fig. 3.5 (b). The ions were inserted to the MOT region (where the F boxes were also located) at time $t = 1.8$ s, at which

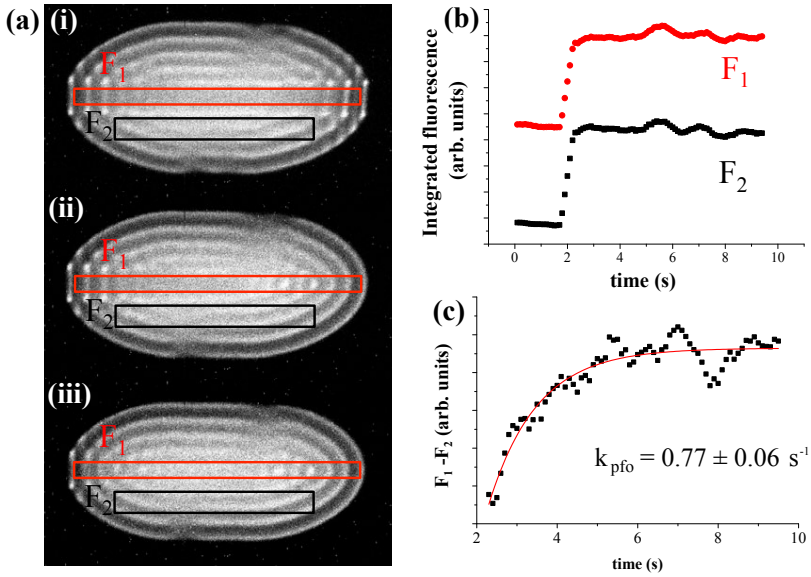

Figure 3.5: (a) (i)-(iii) Fluorescence images of a Ca^+ Coulomb crystal loaded with a central string of ≈ 25 sympathetically cooled N_2^+ ions as the reaction with ultracold Rb atoms proceeds. The dark core of N_2^+ reacts away (from right to left due to unbalanced axial radiation pressure forces on the Ca^+). F_1 counts the integrated fluorescence signal from the N_2^+ dark core area, whereas F_2 is that for a region of fluorescing Ca^+ ions. (b) A plot of integrated fluorescence F_1 and F_2 as function of time. The crystal is inserted into the atom cloud region at 1.8 s (where the regions of interest (ROIs) F_1 and F_2 are also set up) and so F_1 and F_2 increase at this time over five points due to the five frame moving averaging of the CCD software. (c) A graph of the difference of F_1 and F_2 starting from the full crystal insertion time, showing the time dependence of the disappearance of the dark core of N_2^+ ions due to reactions with Rb. The red line is an exponential fit to the data, characterized by k_{pfo}. See text for details.

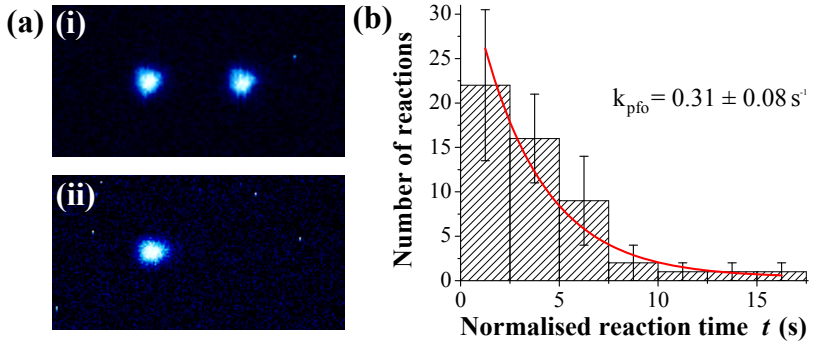

Figure 3.6: (a) (i) False colour fluoresence image of two Ca^+ ions before reaction. (ii) same as in (i) but after overlap with the ultracold Rb cloud, showing one fluorescing Ca^+ ion, and one dark product ion. (b) Histogram of reactions of a single Ca^+ ion with ultracold Rb against normalized reaction time bin. The red line is an exponential fit to the data yielding k_{pfo}.

point the integrated fluorescence signal from both boxes increased. The integration time was 0.1 s, and the insertion was instantaneous on this time scale. The gradual increase of fluorescence at 1.8 s over five data points is due to the five frame moving averaging applied by the CCD software to average out noise. The fifth data point in this rise defines the start of the reaction. After this point, it can be seen that the F_1 and F_2 signals fluctuate in a correlated way due to slight fluctuation in the laser cooling frequencies and intensities. On this scale no apparent increase in F_1 relative to F_2 due to reactions of N_2^+ is observed. The fluorescence fluctuations however are correlated, and have the same amplitude up to a time independent scaling factor. Since the level of F_2 will not change due to reaction of N_2^+, by taking the difference of F_1 and F_2 as a function of time, the time dependence of the relative increase of fluorescence in F_1, and hence the time dependence of the disappearance of N_2^+ can be revealed. This difference as a function of time is shown in Fig. 3.5 (c), with the first data point shown corresponding to that of the start of the reaction as defined above. The increase in fluorescence (and hence the decrease in N_2^+ number) showed an exponential dependence (as expected from equation 3.4), to which an exponential function was fitted, characterized by the time constant k_{pfo}. It should be noted that analysis using F_1/F_2 instead of F_1-F_2 yielded identical k_{pfo} values within the error bars of the parameter fit.

The determination of k_{pfo} for reactions of a single Ca^+ ion is now discussed. In all of the examples above, the smooth exponential decay of the reactant ion was observed due to the statistical averaging over a sufficient number of the individual stochastic reactions. To enable the lowest possible collision energies, experiments were conducted using reactions of a single Ca^+ ion. Two ions were loaded into the ion trap (as in Fig. 3.6 (a) (i)). Upon insertion of the ions into the atom cloud, the time until one of

the Ca^+ ions reacted away was recorded, at which time the reaction was immediately stopped. The result was one unreacted laser cooled Ca^+ ion, and one sympathetically cooled product ion, as in Fig. 3.6 (a) (ii). This process was repeated 49 times to build up a statistically significant picture of the individually stochastic reactions (see also Ref. [106]). Fig. 3.6 (b) is a histogram of the number of reaction events, binned by the normalized time until reaction. Each reaction time is normalized to an atom density of 4×10^9 cm^{-3}. The error bars are determined by the change in bin occupation when the bin center is shifted half a bin size. An error weighted exponential fit to the histogram yielded the characteristic decay rate k_{pfo}. This value was divided by the overlap corrected atom density used for normalization of the reaction times to determine the second order rate constant.

3.3 Ion kinetic energy variation and determination

An important aspect of the study of low collision energy ion-neutral reactions is the dependence of the rate constants of the various processes on collision energy. The translational energy of Rb atoms in the MOT followed a quasi-thermal distribution, corresponding to typical temperatures of 100 μK. The translational energy of laser- and sympathetically cooled ions in an ion trap, however, was highly non-thermal. The kinetic energy distribution of ions in this case follows a distribution which is dependent on the shape and position of ions in the Coulomb crystal, as well as specific laser cooling and trapping conditions. As was seen in section 1.4, the motion of the ions can be decomposed into the slow, thermal motion within the pseudopotential (which for laser cooled Ca^+ ions in this work is typically 12 mK) and a fast oscillatory micromotion associated with ions displaced from the rf null line. This micromotion was the dominant contribution to the collision energy for all the reactions of this work. For a string of ions, as will be discussed below, the axialistaion techniques used in this work put a lower bound on the micromotion kinetic energy of $k_B \cdot 17$ mK. For larger crystals of this work, the high energy tail of the ion energy distribution (with kinetic energy $E_{K.E.}/k_B$ in units of K) had spreads up to 70 K. Since the kinetic energy of the atoms in this work was always at least two orders of magnitude lower than for the of the ions, the atoms are considered to be a stationary target. In this case the ion-neutral collision energy E_{coll}/k_B is defined through $E_{coll}/k_B = \frac{1}{2}\mu v^2$ where μ is the reduced mass of the collision partners, and v is the velocity of the ion. The average collision energy $\langle E_{coll} \rangle /k_B$ (K) for a given crystal is then defined as the weighted average of the collision energy distribution, which is determined by comparison of experimental crystal images to images from MD simulations (see section 1.5).

It should be noted that the thin kinetic energy distribution of a string of axialised ions in ion traps cannot be shifted to higher kinetic energies as with, say, crossed or merged beam techniques for neutrals [13, 107], but rather can only be broadened so that the distribution samples higher energies. As such, the collision energy resolution using this technique is intrinsically poor. A full characterization of the collision energy

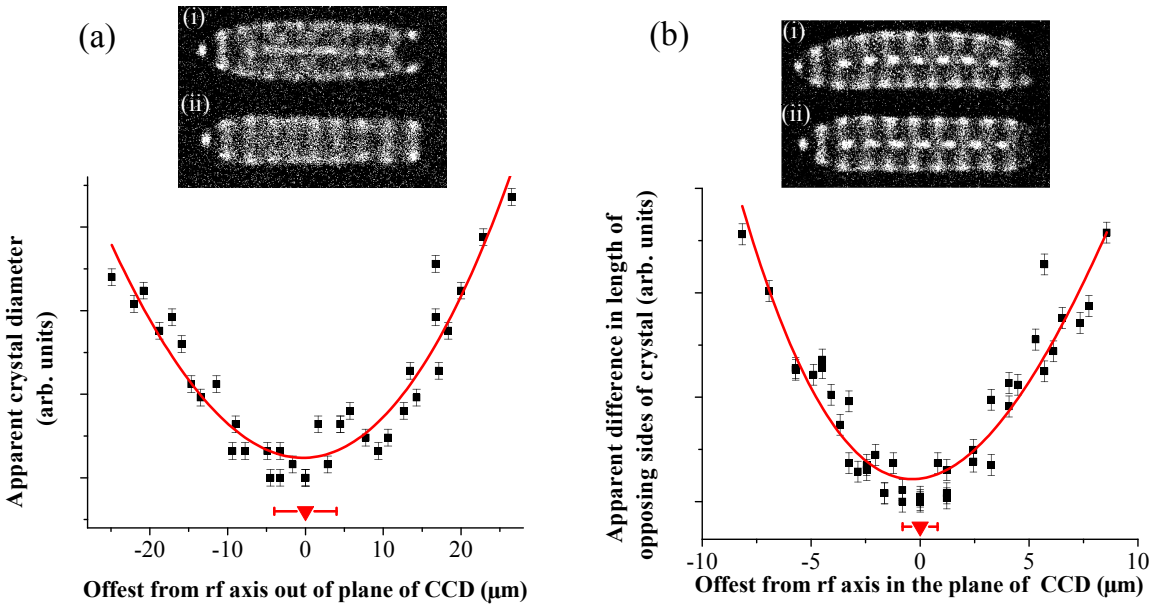

Figure 3.7: Techniques for axialisation of Coulomb crystals. (a) Axialisation in the line of sight direction of the CCD camera. The crystal is translated by DC fields such that heavy ions form symmetric shells around the laser cooled ions, and the fluorescing crystal diameter is minimized (compare (ii) (axialised) against (i) (off axis)). (b) axialisation in the plane of the CCD chip. The crystal is axialised when the length difference of the upper and lower flat portions of the fluorescing ion crystal is minimised (compare (ii) (axialised) against (i) (off axis)). Axialisation accuracies were ≈ 4 μm and 1 μm, respectively, indicated by the red error bar in each plot. See text for details.

distribution resulting from using Coulomb crystals was essential for comparison of experimental results to those of theory, which was achieved using MD simulations (see section 1.5).

The technique of axialistaion of Coulomb crystals to minimize excess micromotion in this work is now described. Crystals centered exactly on the rf null line (the "axis") arrange in rotationally symmetric shells, with ions of greater mass in outer shells due to the mass dependence of the trapping potential. Such a situation is displayed in Fig. 3.7 (a) (ii), and (b) (ii), where the fluorescing core is Ca^+ ions, and dark non fluorescing ions are arranged symmetrically around the core. In the line of sight direction of the CCD camera, an offset of the ions from the axis results in the heavy ions collecting either in front or behind the lighter fluorescing Ca^+ ions. When this happens, the heavy ions no longer exert a force on the Ca^+ ions in the plane of the CCD, an so there is a disappearance of the characteristic flattening of the edge of the Ca^+ crystal (see Fig. 3.7 (a) (ii)$\rightarrow$(i)). A figure of merit for axialisation in this direction is the apparent crystal diameter, which is plotted as a function of offset from the rf axis

in Fig. 3.7 (a). The precision of axialisation in this direction was ± 4 μm, which for typical trapping conditions imposes a lower bound on the collision energy due to excess micromotion of $k_B \cdot 17$ mK. The red line is a polynomial fit to the data. If the ions are displaced in the plane of the CCD camera, the heavy ions collect either above or below the lighter fluorescing Ca^+ ions (see Fig. 3.7 (b) (ii)$\rightarrow$(i)). A figure of merit of axialisation in this direction is the apparent difference in length of flat regions due to heavy ions on opposing sides of the crystal (where an axialised crystal has the same flat length on both sides), which is plotted against offset from the rf axis in Fig. 3.7 (b). The precision of axialisation in this direction is ± 1 μm, corresponding to a lower bound of excess micromotion energy of $k_B \cdot 1$ mK.

Molecular dynamics (MD) simulations were used to determine the kinetic energy, and hence collision energy distribution, for different ion crystals with ultracold Rb. Simulated fluorescence images were generated from the MD simulations. The methodology is that the parameters of the simulation, which when possible are informed from experimental conditions, are optimized until the resulting simulated image correlates to the corresponding experimental image as close as possible. The collision energy distributions can then be extracted from the MD simulations (see section 1.5), and are treated as an accurate representation of the experimental collision energy distributions. Fig. 3.8 (a) and (b) shows experimental and simulated images of coulomb crystals of different shapes and sizes for Ca^+ and Ba^+ ions, respectively. The corresponding collision energy distributions calculated from MD simulations for collisions with ultracold Rb are shown for Ba^+ (c) and Ca^+ (d). The thinnest collision energy distribution is achieved for two axialised Ca^+ ions, where the distribution peaks at 9 mK and goes to zero by 140 mK, with a weighted average (i.e. $\langle E_{coll} \rangle / k_B$) of 21 mK. The shell structure of the Coulomb crystals is visible in 3.8 (c), as bumps in the probability density.

For reactions involving a string of sympathetically cooled N_2^+ ions with Rb, the kinetic energy distribution were varied by offsetting the ions from the rf axis, and in doing so inducing excess micromotion. This was achieved by applying additional positive DC voltages to all six electrodes of the lower two rods, which effected a vertical upwards translation of the ions away from the rf axis. Fig. 3.9 (a) shows crystals of laser cooled Ca^+ with a dark core of a string of ≈ 25 N_2^+ ions for different offset conditions: (i) is axialised, (ii) is slightly displaced from axis, and (iii) is severely displaced from axis. Note that due to the mass dependence of the pseudopotential, the heavier Ca^+ ions were offset further from the rf axis than the lighter N_2^+ ions for a given DC offset voltage, and so an asymmetry arises in the crystal which can clearly be seen in Fig. 3.9 (a) (iii). This offset was also implemented in the MD simulations (see sec. 1.5). Fig. 3.9 (b) shows the collision energy distributions for strings of N_2^+ with ultracold Rb for an axialised crystal (black trace) and a radially offset crystal (grey trace). The insets are simulated images corresponding to the indicated distributions. Due to the radial asymmetry, the limit of offset for the N_2^+ ions was set by the highest offset for which the sympathetically cooled ion string remained in the laser cooled crystal volume.

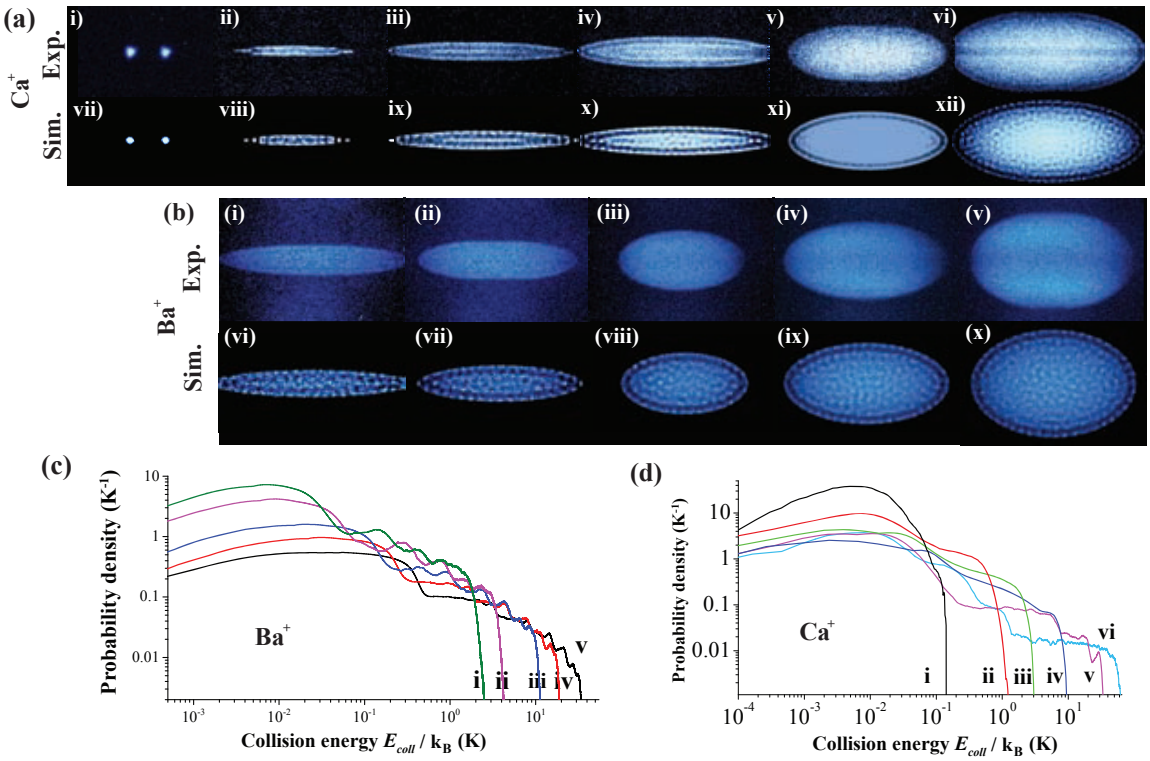

Figure 3.8: (a) Experimental and simulated fluorescence images of Ca^+ Coulomb crystals of different shapes and sizes. The corresponding collision energy distributions of these crystals for collisions with ultracold Rb atoms are plotted in (d). (b) Same as in (a) but for Coulomb crystals of Ba^+ ions, where the corresponding collision energy distributions for collisions with ultracold Rb atoms are plotted in (c). The ion numbers N and average collision energies for collisions with ultracold Rb $\langle E_{coll} \rangle / k_B$ denoted with (N, $\langle E_{coll} \rangle / k_B(K)$) are for Ca^+ (i)-(vi): (2, 0.021), (25, 0.21), (100, 0.69), (300, 2.12), (800, 7.76), and (2000, 16.13) respectively; and for Ba^+ (i)-(v): (150, 0.57), (205, 1.00), (400, 2.61), (850, 4.36), (1500, 7.76) respectively. See text for details.

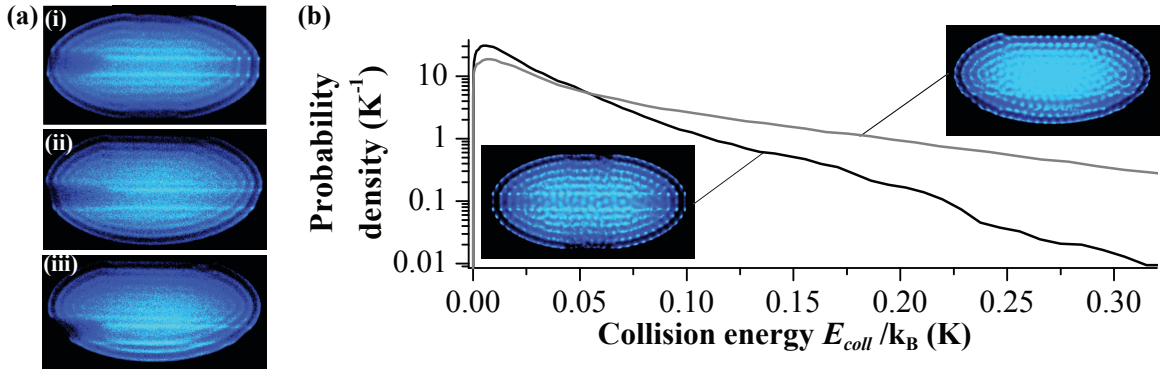

Figure 3.9: (a) False color experimental fluorescence images of Ca^+ Coulomb crystals loaded with a string of ≈ 25 N_2^+ ions (visible as the dark core), where (i) is on axis, (ii) is slightly off axis, and (iii) is far offset from the axis. (b) Is a plot of the collision energy distribution for the string of N_2^+ for collisions with ultracold Rb atoms, for an axialised crystal (black trace, 25 N_2^+ ions, $\langle E_{coll} \rangle / k_B = 23$ mK) and a radially offset crystal (grey trace, 25 N_2^+ ions, $\langle E_{coll} \rangle / k_B = 54$ mK). The insets are simulated images corresponding to the indicated collision energy distributions.

3.4 Resonance-excitation mass spectrometry

A convenient way to determine the chemical identity of ions present in the ion trap was to use resonance-excitation mass spectrometry (REMS). As discussed in section 1.4, the ion trap potential is mass dependent, and hence the radial and axial trap frequencies change for different ion masses. Indeed, it was shown that the trap frequencies ω_i for a single ion in the harmonic approximation can be expressed in terms of the Mathieu a_i and q_i parameters with $\omega_i = \frac{1}{2}\Omega\sqrt{a_i + \frac{1}{2}q_i^2}$, where $i = x, y, z$. In this work, x and y correspond to the two radial axes, and z the axial.

To excite motion of the ions at the trap frequencies, a small additional rf voltage was applied to portions of the rods of the ion trap. The frequency of the voltage was then swept, and the crystal monitored. When the drive frequency matched a trap frequency, the ion's motion was excited such that a visible change in the fluorescence images was observed. A *Matlab* program was implemented, interfacing the CCD camera and a function generator, such that the integrated fluorescence in a user defined region of interest was recorded as a function of drive voltage frequency for preset step sizes, and in such a way a spectrum recorded. Typical step sizes were 0.3 kHz, with typical scan times ≈ 60 s. The observed resonance frequencies were compared to the calculated single ion frequencies for different mass-to-charge ratios of ions, and hence chemical identity inferred.

To excite only radial motion, the drive voltages were applied in an axially symmetric way, e.g. equally to electrodes 1,2 and 3 in Fig. 1.19. Conversely, to excite only axial motion, the drive voltages were applied in a radially symmetric way, e.g. equally to

electrodes 1,4,7, and 10 in Fig. 1.19.

There were two methods used in this work to observe an increase in ion motion due to a resonance condition being met, and hence enable the plotting of mass spectra for ions in the trap.

- The first relied on the spatial displacement of the ions on resonance, causing a reduction of the integrated fluorescence of the crystal. Fig. 3.10 (a) shows an example of a mass scan resulting from this method for a string of 8 Ca^+ ions. The integration box was placed directly around the ions in their off-resonance configuration. The two dips in the spectrum correspond to the slightly different radial trap frequencies in the x and y directions, due to slight imperfections in the trap construction, and in the application of rf voltages to the different rods. The calculated radial single Ca^+-ion frequency for these trap conditions was 112 KHz, which matched well with the observed resonances.

- For large Coulomb crystals, the fluorescence decrease method outlined above was often not useful, since large drive amplitudes were needed to effect a marked difference in the ion fluorescence, which often lead to melting of the crystal when precisely on resonance. Melting of the crystal is not desirable in crystals which have many sympathetically cooled ions, since in melting, these ions can be lost, or at least require significant time for recooling back into the crystal. This could lead to distorted, inaccurate, and unreproducible mass spectra, highly dependent on the fluctuations of the laser cooling conditions. In this case, a method which only slightly disturbs the crystal was more appropriate. This second method relied on the fact that when ions motion is excited due to a resonance condition being met, there is a decrease of the efficiency of laser cooling to localize the ions, and hence an apparent decrease in the strength of the asymmetric radiation pressure. At high oven temperatures, when a Ca^+ crystal was being loaded, a few light ions were often also loaded into the trap from background. When cooled from one axial direction only, the radiation pressure acting on the Ca^+ ions (but not on the light ions) caused an axially asymmetric ion distribution (see left hand inset of Fig. 3.10 (b)). The integration box was placed in the position of the light ions. Agitation of the crystal due to a resonance condition being met for a component of the Coulomb crystal caused the radiation pressure to be less effective, and the crystal resumed its symmetric ellipsoidal shape. In the integration box, therefore, an increased fluorescence level is recorded (see right hand inset of Fig. 3.10 (b)), and so a peak is observed in the spectrum, as presented in Fig. 3.10 (b). This technique was made to be very sensitive by tuning the radiation pressure such that only a slight agitation of the ions results in a fluorescence signal detectable in the integration box. This sensitivity was crucial in observing peaks for product ions formed in low numbers and with high masses (i.e such that they have a reduced back-action on the laser cooled ions), such as the $CaRb^+$ and $BaRb^+$ molecular ions.

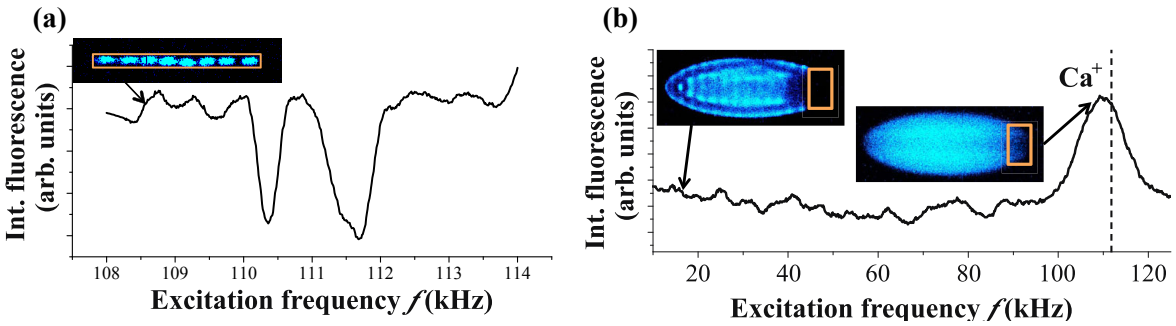

Figure 3.10: (a) Resonance-excitation mass spectrum (REMS) of a string of 8 Ca^+ ions in the region near the calculated single ion radial trap frequency (112 kHz). A dip indicates the reduction of fluorescence inside the orange box due to delocalization of the ions when a resonance condition is met. The two dips indicate the slightly different trap frequencies in the radial x and y directions, due to imperfections in the ion trap. The inset is a false-color fluorescence image of the string of ions far from resonance. (b) A REMS for a crystal of Ca^+ ions with a few ($\approx$ 10) light ions present from ionization of background gas during Ca^+ loading, cooled from one axial direction only. The orange box represents the region of integration of fluorescence. Off resonance, the box is dark due to the asymmetry of the crystal induced by the radiation pressure of single direction cooling. On resonance, the heating reduces the effectiveness of the radiation pressure, and the Ca^+ fills the ellipse, resulting in an increased fluorescence signal inside the orange box, and hence a peak in the REMS. This technique requires only a very gentle excitation of the ion motion.

For large Coulomb crystals, and especially multi-component crystals, there are a number of effects which caused a deviation of the observed resonance frequencies from those calculated for the single ion case in the harmonic pseudopotential. These effects are discussed in detail in ref. [108], which include: scan direction, excitation amplitude, coupling (damping) between species of different masses, crystal asymmetry and crystal size. Molecular dynamics simulations were used to produce simulated mass spectra, and to aid investigation into these effects [109]. In the simulations, crystals were offset from the rf axis, released, and left to oscillate in the ion trap potential. The total kinetic energy of the ions in free oscillation was recorded as a function of time, and then Fourier transformed to get a plot of oscillation amplitude against frequency. The oscillation amplitude was not a direct representation of the experimental observable (i.e. fluorescence intensity), but gave an indication of the relative peak intensities expected in the experimental scan for different crystal compositions. The frequency of oscillation in the simulations may be compared more directly to the experiment, and indeed reproduced observed shifts in the resonant frequencies as compared to those calculated for a single ion in a pseudo potential [109] (see also Fig. 5.2). To minimize computing time, the simulations were performed using the pseudopotential approximation for the trap with an isotropic friction force for laser cooling. Also, an empirical background subtraction function of the form $I = a(1-\exp(-f/b))^c$ (where I is the signal intensity, f the motional frequency and a, b and c are adjustable parameters) was applied to remove spurious low-frequency components from the spectra resulting from chaotic ion motions during the relaxation of the Coulomb crystal in the simulation.

For experiments using strings of two ions, the axial motion of the ions was strongly coupled and the ions no longer exhibit individual resonance trap frequencies, but rather a single center of mass mode related to their mass ratio [110]. It should be noted that in principle two modes can be excited in this case, an in phase center of mass (COM) mode, and an out of phase breathing mode (BR). The symmetry of the excitation voltages used in this experiment however precluded the excitation of the breathing mode, and so only the COM mode will be considered further. If the axial frequency of one of the two ions, v_1, is known, then given the mass ratio of this known ion with the second ion, i.e $\mu = m_1/m_2$, the COM frequency of the two ions v_{COM} is given by [111]

$$v_{COM}^2 = \left[1 + \mu - \sqrt{1 - \mu + \mu^2}\right] v_1^2. \tag{3.7}$$

Fig. 3.11 shows an axial REMS for two Ca^+ ions (upper trace), and one Ca^+ ion and one product ion of the reaction of one Ca^+ ion with an ultracold Rb atom (lower trace). Notice that the two spectra were taken at different scan amplitudes (6 V upper, and 2 V lower). This was due to the fact that at 6 V, bi-component 2 ion strings as in the lower trace melt due to instability induced by sympathetic cooling, but at 2 V (where the bi-component crystal doesn't melt), the peak for 2 Ca^+ ions as in the upper trace was not sufficiently above background. As a result, two different scan amplitudes were required as mentioned above, which is not desirable since scan amplitude can

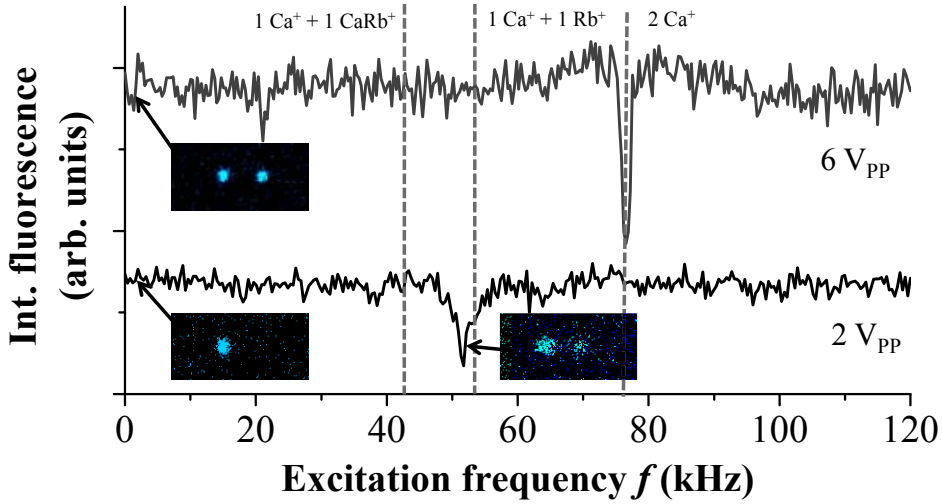

Figure 3.11: Axial resonance excitation mass spectra (REMS) of 2 Ca^+ ions (upper trace), and of $1Ca^+ + 1Rb^+$ ion. The insets are false color fluorescence images of the strings at different excitation frequencies. The dashed line marked 2 Ca^+ is centered on the peak of the upper trace, since the identity of both ions is known from the fluorescence images. The drive amplitude corrected calculated frequencies (from equation 3.7) for the lower trace are given for the cases 1 Ca^+ + 1 Rb^+ ion, and 1 Ca^+ + 1 $CaRb^+$ ion. The measured frequency matches with the 1 Ca^+ + 1 Rb^+ calculated frequency, and hence the identity of the dark ion in the lower trace is assigned Rb^+. The peak-to-peak drive voltages are given in each case.

effect the resonance positions, but however can be corrected for [108]. The insets on the left hand side are false color fluorescence images of the two cases far from resonance. Note that a single dark ion was known to be next to the single Ca^+ ion in the lower left inset, due to the symmetric arrangement of ions about the trap center, and that the radiation pressure was set such that the Ca^+ ions were always at the left most position of the chain. The dashed line marked 2 Ca^+ is set at the peak of the resonance in the upper trace and defines v_1 for use in equation 3.7. The dashed lines marked $1Ca^+$ + $1Rb^+$ and $1Ca^+$ + $1CaRb^+$ are at the scan amplitude corrected frequencies given out by equation 3.7 for the corresponding masses of the unknown ion. The resonance of the lower trace overlaps with the calculated $1Ca^+$ + $1Rb^+$ frequency, and hence the dark ion in this case was identified as Rb^+. For reference, the lower right hand inset shows a false color fluorescence image of the $1Ca^+$ + $1Rb^+$ crystal on resonance, where the axial displacement of the Ca^+ ion is clearly visible in the spreading out of the fluorescence along the axis.

3.5 Ion steady state population determination

A key aspect of this work was the state-to-state rate constant determination for the possible combinations of reactant states within each reaction system. To allow a state specific analysis, the steady state population of all relevant states must be known during a reaction. By varying the distributions of populations whilst monitoring the reaction rate, each channel's contribution to the observed rate can be determined. There are various experimental and theoretical methods for determining steady state population in systems of three electronic states with various magnetic sublevels (as per the Ca^+ and Ba^+ ions used in this work). As will be seen in section 3.5.3, the most accurate of which combines a theoretical method which includes a description for all of the important phenomenology, but is able to be informed by and checked against a plethora of experimental observables (i.e the 8-level optical Bloch model). The different techniques used in this work to determine the $^2P_{1/2}$, $^2D_{3/2}$, and $^2S_{1/2}$ populations in Ca^+ and Ba^+ will now be described and compared.

3.5.1 Fluorescence measurement

A straightforward and model-independent way to determine the steady state population of the $^2P_{1/2}$ state in Ca^+ or Ba^+ during laser cooling was to measure the time averaged fluorescence of a single ion. The lifetime with respect to spontaneous decay to the $^2S_{1/2}$ ground state is well known, and so a comparison of the experimentally observed scattering rate to the expected scattering rate for 100% $^2P_{1/2}$ population was used to determine the steady state population for a given set of laser cooling conditions. This was then mapped out for a variety of cooling and repumper laser detunings and intensities, such that $^2P_{1/2}$ population could be be inferred for reactions of larger crystals at the same laser cooling parameters. To set the scale, the maximum Ca^+

$^2P_{1/2}$ population observed in the survey was 19.5 ± 2 % with the following conditions: 397 nm power P_{397}= 454 μW, 397 nm beam $1/e^2$ radius at the ions $w_{1/e^2,397}$ =192 μm, 397 nm frequency detuning Δ_{397} = 11 MHz; 866 nm power P_{866}= 726 μW, 866 nm beam $1/e^2$ radius at the ions $w_{1/e^2,866}$ =277 μm, 866 nm frequency detuning Δ_{866} = "0"MHz (the 866 nm detuning was set to maximize fluorescence, which typically is actually blue detuned from the unperturbed transition frequency by ≈ 15 MHz (see Fig 3.13 (b)). The measured Ca^+ $^2P_{1/2}$ populations over a wide variety of laser parameters are presented as black data points in Figs. 3.13, 3.14, and 3.15, and provide a test for the 8 level optical Bloch equation (OBE) model described in section 3.5.3.

There were however, three states populated in laser cooling of Ca^+ and Ba^+, and the fluorescence measurement says nothing about the individual population in the $^2S_{1/2}$ and the $^2D_{3/2}$ states. The system was therefore modeled to gain access to these populations.

3.5.2 Einstein rate equations

In section 1.3.5, the steady state populations were derived for a two level system in a near resonant laser field, which included the effects of absorption, stimulated emission, and spontaneous emission, including their coherences, as discussed in section 1.3.4. The extension of this approach to three (or indeed eight) levels is more involved, and is discussed in section 3.5.3. As a first approximation, however, it is convenient to consider these three levels as coupled by the aforementioned processes, but whose populations are governed simply by the Einstein rate equations [112]. It is important to notice that this treatment does not include coherences, and so cannot reproduce the coherent population trapping observed experimentally for both Ca^+ and Ba^+ (see section 3.5.3). It also does not include magnetic field effects, which play a role in Ca^+ and Ba^+ due to hyperfine structure of the levels involved in laser cooling. The Einstein model is easily implemented however, and is sufficient for gaining a rough understanding of the behavior of the populations under different light fields. Fig. 3.12 shows a schematic energy level diagram showing the competing processes in a generic three level system (i.e. common to Ca^+ and Ba^+). The lifetime of the $^2D_{3/2}$ state with respect to the $^2S_{1/2}$ state is long ($\tau = 1.2$ s) and so spontaneous emission in this case is ignored.

The rate of spontaneous emission is characterized by the Einstein A coefficient A_{ij} (equivalent to the natural linewidth of the transition) from state i to j. The rate of stimulated absorption or emission is characterized by the product of the Einstein B coefficient B_{ij} from state i to j, and the spectral density $\rho(\nu_0)$ of the coupling field at frequency ν_0. Plank's law (which gives the spectral density), and the Maxwell Boltzmann distribution (which gives relative thermal state populations) are combined in the conditions of thermal equilibrium to arrive at the following equations

$$\frac{A_{21}}{B_{21}} = \frac{8\pi h\nu_0^3}{c^3} \tag{3.8}$$

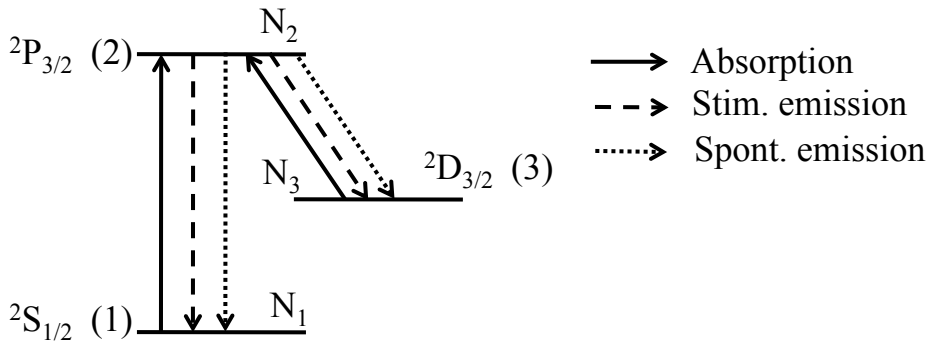

Figure 3.12: Schematic energy level diagram for the generic three level system showing processes considered in the Einstein rate model, including nominal state numbers and corresponding populations N_i.

$$g_2 B_{21} = g_1 B_{12} \tag{3.9}$$

where g_i is the degeneracy of state i.

The rate equations for population of each state can then be written to include all of the processes shown schematically in Fig. 3.12:

$$\frac{dN_1}{dt} = -B_{12}N_1\rho(\nu_0) + A_{21}N_2 + B_{21}N_2\rho(\nu_0) \tag{3.10}$$

$$\frac{dN_2}{dt} = +B_{12}N_1\rho(\nu_0) - A_{21}N_2 - B_{21}N_2\rho(\nu_0) - A_{23}N_2 - B_{23}N_2\rho(\nu_0) + B_{32}N_3\rho(\nu_0) \tag{3.11}$$

$$\frac{dN_3}{dt} = -B_{32}N_3\rho(\nu_0) + A_{23}N_2 + B_{23}N_2\rho(\nu_0) \tag{3.12}$$

In the steady state, these equations can be set to zero, and solved for N_1, N_2, and N_3, by using the additional information that $N_1 + N_2 + N_3 = 1$, i.e conservation of population. This was done using a program written in *Matlab*. The model works well for conditions where coherent and magnetic field effects are negligible. The output of this model for the Ca^+ $^2P_{1/2}$ population against repumper laser detuning is given by the grey curve in Fig. 3.15 (a), where it is found, however, to not agree well with the experimentally determined values (black data points).

3.5.3 Eight-level optical Bloch model

In section 1.3.4, the optical Bloch equations were derived for a two level system. Ca^+ and Ba^+ may be approximated as three level systems (see Fig. 2.3). In this case the Hamiltonian of equation 1.59 must be extended for the three level system to include relevant coupling radiation detuning and Rabi frequencies between the three levels,

and can be written [113, 114]

$$H = \hbar \begin{pmatrix} \delta_c & \frac{\Omega_{12}}{2} & 0 \\ \frac{\Omega_{12}}{2} & 0 & \frac{\Omega_{23}}{2} \\ 0 & \frac{\Omega_{23}}{2} & \delta_r \end{pmatrix} \tag{3.13}$$

where δ_c and δ_r are the frequency detunings of the cooling and repumping lasers respectively, and Ω_{12} and Ω_{23} are the Rabi frequencies of the $S \rightarrow P$ and $D \rightarrow P$ transitions respectively (computed in practice via equation 1.67). The Heisenberg equation of motion of equation 1.57 can be extended to describe the dynamics of the density matrix including damping terms, and is presented as the Liouville equation [113]

$$\frac{d}{dt}\rho = -\frac{i}{\hbar}[\rho, H] + L(\rho) \tag{3.14}$$

where $L(\rho)$ is the Lindblad operator which describes dissipative processes such as spontaneous emission, and includes effects such as the finite laser linewidths for couplings between the three levels. These equations can be solved in the steady state (i.e., $\dot{\rho} = 0$), and the steady state S, P, and D populations recovered for a given set of laser conditions [99, 113, 114].

As described in section 1.3.4, this treatment includes the effects of coherence between the levels, unlike the Einstein model described above. As a result, the phenomena of coherent population transfer [115] is reproduced. This effect happens when the detunings of the cooling and repumper lasers are set equal, such that a coherent superposition of S and D states is created via a virtual state, and thus avoiding the P state altogether. The experimental signature of the corresponding reduction in P steady state population is a reduction in the observed fluorescence from the ion corresponding to spontaneous emission from the P to the S state. This effect can be observed in an experiment where the cooling laser frequency is held constant, and the repumper frequency is swept over the resonance while the fluorescence is recorded. Such a spectrum is plotted as the black data points in Fig. 3.13 (b), where the dip in fluorescence at equal detunings is visible at $\Delta_{866} \approx 12$ MHz.

In the presence of an external magnetic field, as described in section 1.3.8, the three levels of the Ca^+ and Ba^+ ions split into their Zeeman sublevels. The S and the P states have $J = 1/2$ and so split into two sublevels with $m = \pm 1/2$. The D state, however, has $J = 3/2$, and so splits into four sublevels with $m = \pm 3/2, \pm 1/2$. In this case there are a total of eight magnetic sublevels to consider to fully describe the state dynamics in the presence of near resonant laser fields. The increased number of levels, and dependence of the dynamics on magnetic field strength and orientation, result in a increased complexity in forming and solving the 8 level optical Bloch equations over the two and three level case. This topic has been described in detail for Ba^+ [113] and Ca^+ [114, 116], where the references include *matlab* scripts for calculating the steady state solutions to the 8 level OBE, and so the reader is referred to these references for

further details. The 8 level OBE model code used in this work was kindly provided by A. Gingell.

As described in section 1.3.8, an external magnetic field shifts the Zeeman sublevels in energy $\Delta E \propto mB$ where B is the magnetic field strength. The resulting shift changes the effective detuning conditions of the coupling lasers, and so effects the populations, but this effect is small under the experimental conditions of this work as demonstrated in section 2.4.1. An external magnetic field plays another role however in defining a quantisation axis in the system. The ion cooling and repumping lasers used in this experiment were linearly polarized. From section 1.3.8 however, the selection rules state that linearly polarised light can only promote transitions of $\Delta m = 0$. Given sufficient laser intensities, this is of no consequence for the cooling (i.e., $S \rightarrow P$) transition, since both states have $m = \pm 1/2$. The repumping transition however must couple the D state with $m = \pm 3/2, \pm 1/2$ to the P state with $m = \pm 1/2$. From the selection rules oulined in section 1.3.8, linear polarized light cannot address the $m = \pm 3/2 \rightarrow m' = \pm 1/2$ transitions, and so population will be pumped into the $m = 3/2$ and $m = -3/2$ levels, and the laser cooling fluorescence from the ion will drop dramatically. When the quantisation axis is defined by the magnetic field as opposed to the light polarization, however, there is now an angle α between the main quantisation axis of the system and the laser polarisation axis. If this angle is zero and the axes are parallel, then the system acts no differently compared to if the light polarization was the main quantisation axis, and indeed population is pumped into the $m = 3/2$ and $m = -3/2$ levels of the D state, and the laser cooling fluorescence level drops. This is observed experimentally for angles close to 0° (and equivalently 180°), and is presented in Fig. 3.15 (b). If this angle is close to 90° so the axes are perpendicular however, the electric filed oscillation of the linearly polarized light can impart angular momentum to an electron about the principle (magnetic) quantisation axis, and hence $\Delta m = \pm 1$ transitions are induced [117], the population is no longer trapped in the $m = \pm 3/2$ sublevels of the D state, and the laser cooling fluorescence level is unaffected. This is indeed observed at angles close to 90° as can be seen in Fig. 3.15 (b).

The output of the 8-level optical Bloch model was tested against the results of the experimental fluorescence measurements for a large set of experimental parameters by inferring from both the steady state Ca^+ $^2P_{1/2}$ population, and plotting them together. The results are displayed in Figs. 3.13, 3.14, and 3.15, where the black data points are from experimental fluoresence measurements as described in sec. 3.5.1, and the red curves are the P population outputs of the 8 level OBE model with input parameters corresponding to those of each experiment. The magnetic field is assumed to be homogeneous over the ion distribution. This is because although the magnetic field vanishes at the geometric center of the MOT coils, the position of the atom cloud is determined by the balance of radiation pressure from all six cooling beams. The three retro-reflected beams have less intensity than the three incoming beams due to additional losses at the windows, mirrors and quarter wave plates, and therefore the atom cloud sits offset from the geometrical center of the MOT coils, and so the magnetic

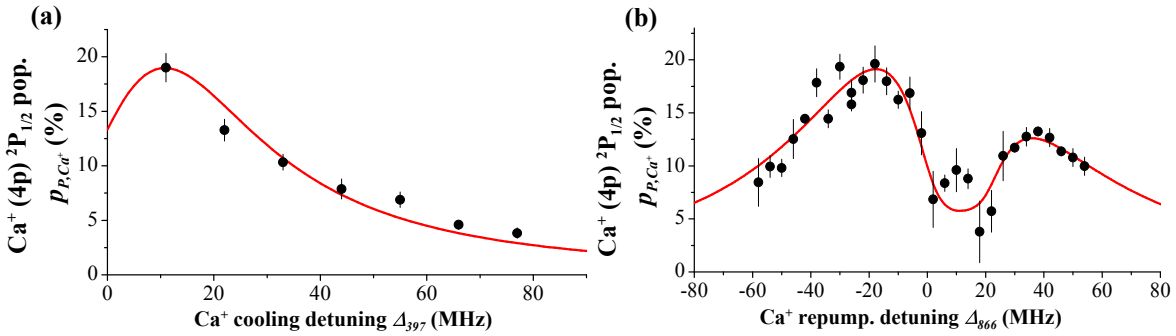

Figure 3.13: Experimental Ca^+ $^2P_{1/2}$ steady state population obtained via calibrated fluorescence measurements (black points) against 397 nm cooling laser frequency detuning (a), and 866 nm repumper laser frequency detuning (b). The red curves are outputs of the 8 level optical Bloch model. The parameters used in the model are experimentally determined (P_{866}=719 μW, $w_{1/e^2,866}$ = 0.277 mm, P_{397}=457 μW, $w_{1/e^2,397}$ = 0.192 mm (a):Δ_{866}=-15 MHz (b):Δ_{397}=11 MHz), except for the magnitude of the magnetic field, and the angle between the polarization axis of the lasers and the magnetic field vector, which were found to best reproduce the data in (b) when set to 2.3 G and $\pi/2$ respectively.

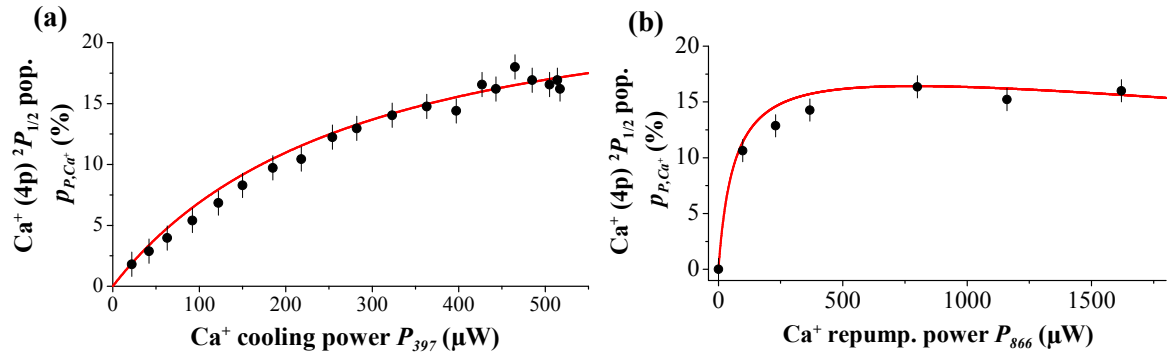

Figure 3.14: Experimental Ca^+ $^2P_{1/2}$ steady state population obtained via calibrated fluorescence measurements (black points) against 397 nm cooling laser power (a), and 866 nm repumper laser power (b). The red curves are outputs of the 8 level optical Bloch model. The parameters used in the model are experimentally determined (Δ_{866}=-15 MHz, $w_{1/e^2,866}$ = 0.277 mm, Δ_{397}=20 MHz, $w_{1/e^2,397}$ = 0.192 mm (a):P_{866}=719 μW (b):P_{397}=457 μW), except for the magnitude of the magnetic field, and the angle between the polarization axis of the lasers and the magnetic field vector, which were found to best reproduce the data in Fig. 3.13 (b) when set to 2.3 G and $\pi/2$ respectively. See text for details.

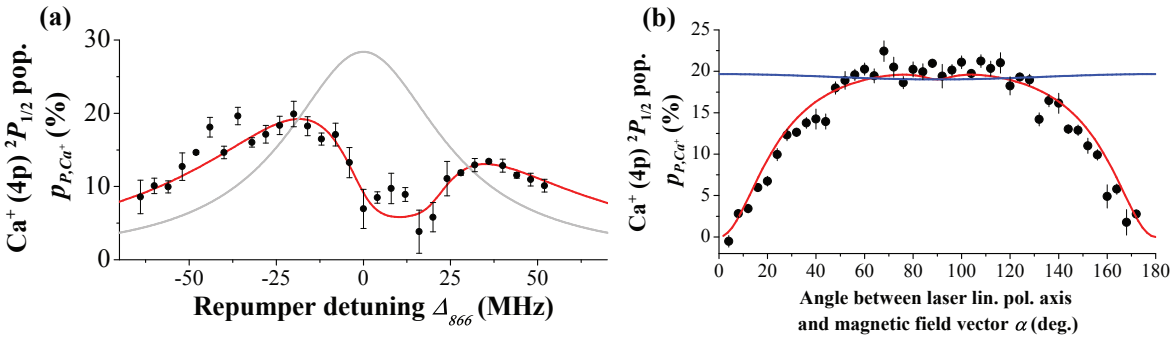

Figure 3.15: Experimental Ca^+ $^2P_{1/2}$ steady state population obtained via calibrated fluorescence measurements (black points) against 866 nm repumper detuning (a), and the angle between the linear polarisation axis of the 866 nm laser beam and the magnetic field vector (b). In (a) the red curve is the output of the 8 level optical Bloch model (OBM), whereas the grey curve is that of the Einstein model. (See Fig. 3.13 for input parameters). In (b) the red and blue curves are the output of the OBM for varying the 866 nm and 397 nm lin. pol. angle with respect to magnetic field vector respectively.

field at the ions (which are overlapped with the atom cloud) will be approximately constant. Another reason is due to the stray homogeneous magnetic fields from other sources due, for example, to the earths magnetic field and permanent magnets in the turbo-molecular pumps, which, however, are constant over all experiments. The effective magnetic field is a sum of all the magnetic fields present, and is approximately constant over the ion distribution. This assumption is justified by the excellent agreement between the 8-level optical Bloch model and experiment demonstrated below. The strength and orientation with respect to the polarization axis of the lasers of the effective magnetic field is determined by fitting the output of the 8-level model to reproduce the depth and width of the observed dark resonance as in Fig. 3.13 (b). All other parameters in the model were experimentally determined. The specific parameters for each figure are given in the corresponding caption. Fig. 3.13 (a) shows the P population dependence on cooling laser frequency detuning, and (b) the dependence on repumper laser detuning. Fig. 3.14 (a) shows the P population dependence on cooling laser power, and (b) on repumper laser power, demonstrating the saturation effects at large intensities. Fig. 3.15 (a) is the same as for Fig. 3.13 (a), but also shows the result from the Einstein model as the grey curve. It can be seen that the Einstein model fails in the region of the dark resonance, but reproduces the experimental observations within a factor of two at larger detunings. Fig. 3.15 (b) shows the the P population dependence on the angle α between external magnetic field and laser polarization axes. The black data points and red curve are for the repumper laser, whereas the blue curve is for the cooling laser, which as rationalized above, shows almost no angular dependence.

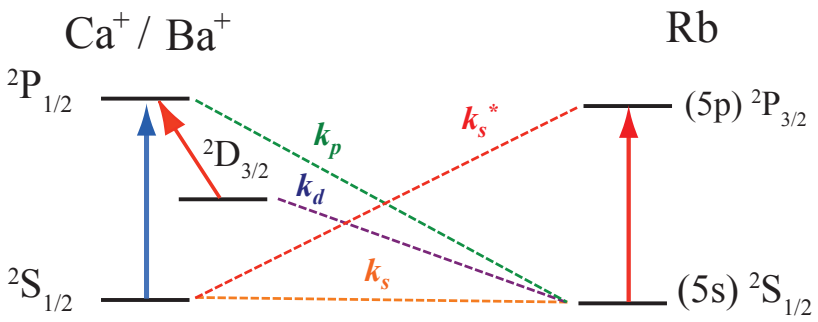

Figure 3.16: Possible entrance channels (indicated by dashed lines) in the Ca^+/Ba^+ + Rb system under conditions of alternate chopping of the cooling laser beams. The k_i indicate the label of the rate constant associated with each entrance channel.

It can be seen from these figures that the agreement between experiment and the 8 level OBE model is extraordinary, and demonstrates how comprehensively the steady state populations can be accounted for by the model. This model was therefore the one used for the calculation of atomic ion population for the determination of state specific rate constants in this work.

3.6 State specific rate constants

The previous section described methods of determining the steady state population of the electronic states of the ion. The method of determining the steady state population of atoms in the MOT was described in section 1.3.5. There is a significant probability that in an atom-ion collision in the hybrid trap one of the reaction partners is electronically excited. Due to the alternate chopping of the ion and atom cooling lasers as described in section 2.3.6, however, simultaneous excitation is prohibited. Within this framework, there are several entrance channels available, which are presented schematically in Fig. 3.16, where k_i is the rate constant associated with reactions from the corresponding entrance channel (indicated by the dashed lines).

The observed reaction rate constant is a weighted average over all of the entrance channels, where the weight is provided by the population of the corresponding levels. Note that during chopping, the laser which repumps ion population from the $^2D_{3/2}$ state is permanently on. This fact coupled with the nanosecond scale lifetimes of the Ca^+, Ba^+, and Rb excited P states means that during alternate chopping, when one partner is being laser cooled, the other has 100% population in its ground state. As a result, during alternate cooling laser chopping, all excited state entrance channels (k_d, k_p, and k_s^*) can only participate 50 % of the total reaction time, whereas the ground state entrance channel (k_s) can participate for the whole reaction time. With the above information, and with reference to Fig. 3.16, the total observed rate constant k can be

formulated as

$$k = \frac{1}{2}\left[(p_{S,ion} + p_{S,Rb})k_s + p_{P,ion}k_p + p_{D,ion}k_d + p_{P,Rb}k_s^*\right], \tag{3.15}$$

where $p_{i,ion}$ is the ion steady state population of state i, and $p_{i,Rb}$ is the Rb steady state population of state i. This formula can be adjusted for the case of insignificant population or negligible state rate constant by omitting the related terms as will be seen in subsequent chapters. The populations can be varied by changing the laser cooling intensities and frequency detunings. If the total rate constant is monitored as a function of varying populations, then for a sufficient number of simultaneous equations of the form of equation 3.15, the state specific rate constants k_i can be deduced by a multi-dimensional least squares fit. For this purpose, a *Matlab* script was used, adapted from a script developed by X. Tong. The script involves a function definition and a executable part, and both are given in the appendix B.2 for reference. It is worth noting that to obtain the most meaningful fits, rank deficiency in the simultaneous equations should be as widely avoided as possible, i.e. that as large a range of each state population as possible should be explored whilst monitoring the reaction rate, with other steady state populations remaining constant.

3.7 Potential energy curve and quantum scattering calculations

While the focus of this work is on the experimental realization and study of cold collisions in a hybrid trap, a close collaboration was maintained with a theory group whose study focuses on ab initio potential energy curve and quantum scattering calculations for radiative processes in cold atomic neutral and ion-neutral collisions. The principle investigator of this group is Olivier Dulieu, and members of the group who contributed to the calculations relevant for this work were Nadia Bouloufa-Maafa, Mireille Aymar and Maurice Raoult. The group is based at Laboratoire Aimé Cotton at the Université Paris-Sud XI in France. The potential energy curves generated by them (as will be seen in further sections) are key in rationalizing the observed experimental state dependent rate constants. The scattering calculations performed with these curves are also key in rationalizing the observation of molecular ion formation by radiative association in the ground state channels, the observed product branching ratios, and the collision energy dependence of the rate constants. Indeed, much of the success of this work and the resulting publications has been in the detailed comparison of experiment and theory, with the resulting understanding of the chemical dynamics in the systems studied being much greater than if the experiment and theory had been conducted separately without discussion. For these reasons the discussions with and input from Olivier Dulieu and members of his group is here again most gratefully acknowledged, and the fruitful collaboration highlighted.

While members of the Basel group played no role in performing the calculations, due to their importance in rationalizing the experimental observations, the methods are very briefly introduced here, relying heavily on the descriptions as presented in Refs. [42], [41], and [36], and references therein to more detailed descriptions in other publications.

3.7.1 Potential energy curve calculation

The potential energy curves (PECs) for the energy regions of the experimentally accessible entrance channels in the Ca^+ + Rb system are displayed in Fig. 5.3. A zoom of the region of the ground state entrance channel for this system is shown in Fig. 5.4. The PECs were calculated inline with the methods of Ref. [118,119] using effective core potentials (ECP) [120–122] representing the Rb^+ and the Ca^{2+} ionic cores including the core-polarization potentials (CPP) [123] to simulate the correlation between core and valence electrons. As a result, it is only necessary to treat the two valence electrons of Rb and Ca^+ explicitly. In this case, a full configuration interaction (FCI) calculation can be performed in the configuration space generated by the large Gaussian basis sets reported in Refs. [119,122,124]. The fine structure (spin-orbit correction) of the calcium ion and of the rubidium atom are neglected. This is justified in the Ca^+ + Rb system since even for the smallest calculated energy difference between asymptotic states (the Rb^++Ca($4s4p,^3P$) asymptote is located 352 cm^{-1} below the Rb(5s)+Ca^+(4s) ground state entrance channel, see Fig. 5.3 (a)), the energy spread of the Ca($4s4p,^3P$) fine structure manifold (158 cm^{-1}) is smaller and hence does not modify the order of the dissociation limits [42]. Spin-orbit coupling is key to non-radiative mechanisms, and has been studied in the ground state entrance channel by Gianturco and co-workers [29,47]. The accuracy of the FCI calculation is typically a few hundred wave numbers [36], and so in the congested region around the Rb($5s$)+Ca^+($4p$) asymptote (Figure 5.3 (c)), the order of several asymptotic limits is changed. The calculations in these highly excited regions therefore aim to provide a qualitative understanding of the observed dynamics.

The PECs for the energy regions up to the second highest experimentally accessible entrance channel in the Ba^+ + Rb system are displayed in Fig. 6.4. Similarly to $CaRb^+$, the $BaRb^+$ complex has the same valence electronic structure as for two external electrons moving in the field of Rb^+ and Ba^{2+} ionic cores, and so the energies can be calculated using a full configuration interaction approach performed in a configuration space generated by the large Gaussian basis sets reported in Refs. [118, 125, 126]. The corresponding two-electron Hamiltonian then involves an effective core potential for the Ba^{2+} [127, 128] and Rb^+ [118] ions, and core-polarization potentials [121, 123] to account for the core-valence electron correlation. As for the $CaRb^+$ system, the fine structure and spin-orbit coupling was not included, as justified above.

3.7.2 Quantum-scattering calculations

Quantum-scattering calculations aim to calculate cross sections for predefined processes given a set of PEC's and asymptotic wave functions. The methods presented here are for calculation of the cross sections of radiative charge transfer and radiative association. Calculations for the cross section of non-radiative processes are possible and have been presented e.g. for the $CaRb^+$ system in ref. [29].

For ground state collisions of Ca^+ and Rb species, the entrance channel correlates with a single adiabatic Born-Oppenheimer (ABO) state. This state is not the absolute ground state of the $CaRb^+$ molecular ion, and in fact represents the second excited state (see Fig 5.3). Emission of a photon can therefore occur from the ground state entrance channel to the absolute ground state, whose ABO correlates at long distance with the lowest Ca + Rb^+ asymptote. As described in section 1.2.5, in this case two radiative processes can occur, either decay into the dissociation continuum of the absolute ground state forming Ca and Rb^+ in their respective ground states (RCT), or decay into a bound rovibrational level of the absolute ground state forming the $CaRb^+$ molecular ion (RA). The radiative cross-section can therefore be formed as the sum of two contributions [17, 42, 129]:

$$\begin{aligned}\sigma^{RCT}(\epsilon_i) &= p \quad \frac{8\pi^2}{3c^3}\frac{1}{k_i^2}\sum_{J=0}^{\infty}\int_0^{\epsilon_f^{max}} \omega_{i,f}^3 \Big(J|\langle J-1,\epsilon_f|D(R)|\epsilon_i,J\rangle|^2 \\ &\quad +(J+1)|\langle J+1,\epsilon_f|D(R)|\epsilon_i,J\rangle|^2\Big)\, d\epsilon_f \end{aligned} \tag{3.16}$$

and

$$\begin{aligned}\sigma^{RA}(\epsilon_i) &= p \quad \frac{8\pi^2}{3c^3}\frac{1}{k_i^2}\sum_{J=0}^{\infty}\sum_{v=0}^{v_{max}} \Big(\omega_{iJ,v(J-1)}^3 J|\langle J-1,v|D(R)|\epsilon_i,J\rangle|^2 \\ &\quad +\omega_{iJ,v(J+1)}^3 (J+1)|\langle J+1,v|D(R)|\epsilon_i,J\rangle|^2\Big) \end{aligned} \tag{3.17}$$

in atomic units, where p is the statistical probability of entrance channel population, J is the collisional angular momentum or "partial wave" quantum number, ω is the angular frequency of the emitted photon and the ket $|\epsilon, J\rangle$ is the partial wave component of an energy-normalized continuum wave function of the two nuclei corresponding to an energy ϵ at infinite internuclear separation. ϵ_i is the kinetic energy in the incoming (or entrance) channel $\epsilon_i = E - V_i(\infty)$, $k_i = \sqrt{2\mu\epsilon_i}$ is the associated wave number, μ is the reduced mass of the system and ϵ_f represents the kinetic energy in the exit channel $\epsilon_f = E - V_f(\infty) - \hbar\omega_{i,f}$. Due to the selection rules outlined in section 1.3.8, if J is the total angular momentum in the entrance channel, then $J' = J \pm 1$ are the two possible allowed total angular momenta in the exit channel. In Eq. (3.16), $\langle J', \epsilon_f|D(R)|\epsilon_i, J\rangle$ is the transition dipole moment (TDM) between two energy-normalized continuum wave functions, where

$$\langle J',\epsilon_f|D(R)|\epsilon_i,J\rangle = \int_0^{\infty} F_{J'}^f(\epsilon_f,R)D(R)F_J^i(\epsilon_i,R)\; dR \tag{3.18}$$

where $D(R)$ is the electronic dipole moment function. The continuum wave functions behave like

$$F_\ell(\epsilon, R) \sim \sqrt{\frac{2\mu}{\pi k}} \sin(kR - \ell\frac{\pi}{2} + \delta_\ell) \tag{3.19}$$

at large internuclear distances, where $\ell\pi/2$ and δ_ℓ are the phase shifts due to the centrifugal barrier and the interaction potential respectively. In Eq. (3.17), the final state $|v, J\rangle$ is a discrete, bound rovibrational level of the absolute ground state of the $CaRb^+$ molecular ion. Accordingly, the transition dipole moment becomes

$$\langle J', v|D(R)|\epsilon_i, J\rangle = \int_0^\infty \chi^f_{vJ'}(R) D(R) F^i_J(\epsilon_i, R)\ dR. \tag{3.20}$$

Here, $\chi_{v,J}$ is a rovibrational wave function of the molecule normalized to unity.

For useful comparison between experiment and theory, the calculations for the $CaRb^+$ system covered the energy range spanned by the experiment (10^{-5} cm^{-1} - 50 cm^{-1}). As a result, up to 200 partial waves had to be taken into account in the calculations to obtain converged cross sections [42]. In order to ensure long range behavior was captured in the calculations, the continuum wave function was propagated to large values of internuclear distance $R \approx 20000$ a.u.. Moreover, in the integral over the exit-channel energy appearing in Eq. (3.16), an upper limit ϵ_f^{max}=1000 cm^{-1} and an integration step size $d\epsilon_f$= 1cm^{-1} were used to ensure convergence. In order to simplify the calculations and decrease the computation time, it was assumed that the J to $J\pm1$ TDMs are equal in both Eqs.(3.16) and (3.17) [42]. In order to reliably locate narrow ($\geq 10^{-4}$ cm^{-1}) shape resonances in the radiative cross sections (as described in sec. 1.2.4), a very small energy-step size would have to be used in the calculations, which due the broad energy range considered would have required a prohibitive amount of computing time. Instead, the Milne phase-amplitude method was employed which yields a good estimation of resonance energies [42, 130, 131]. The RA and RCT cross sections from the ground state entrance channel in the Ca^+ + Rb system are displayed in Fig. 5.5.

The cross sections for RA and RCT for the Ba^+ + Rb system are computed using the same method as in the Ca^++Rb system [41], and are presented in Fig. 6.5.

As described in section 1.2, the rate constant k can be derived from the cross section σ via the collision velocity v with $k = \sigma v$. A plot of the calculated rate constant for the radiative processes from the ground state entrance channel of the Ca^+ + Rb system is shown in Fig. 5.6 (b).

3.8 Velocity-averaged theoretical rate constants

To compare the rate constants obtained from the theoretical treatments outlined above with those observed in the experiment, the theoretical rate constant must be averaged over the distribution of collision energies available in the experiment. As described in sections 1.5 and 3.3, MD simulations can be used to calculate the collision velocity

distribution $\rho(v)$ (i.e. probability density against velocity) which closely resembles that of a specific experiment, and which is normalized such that the area under the distribution equals unity. The calculated cross sections $\sigma(v)$ can then be combined with $\rho(v)$ to get the velocity averaged theoretical rate constant using the relationship [79]

$$k = \int_0^\infty \sigma(v) v \rho(v) dv. \tag{3.21}$$

The output of the cross section calculations is discrete, and the fitting of an analytic function over the entire energy range is prohibitively complicated. The collision velocity histograms as described in 1.5, however, can be fitted sufficiently well with up to a 25^{th} order polynomial, generating an analytic form of $\rho(v)$. The product $\sigma(v)v\rho(v)$ can therefore be calculated for every discrete v present in the output of the cross section calculations. The integral of equation 3.21 is therefore executed as a Riemann sum where the integral is replaced by a sum over all discrete v_i, and dv is replaced with the cross section calculation step size δv:

$$k \approx \sum_{i=0}^{\infty} \sigma(v_i) v_i \rho(v_i) \delta v. \tag{3.22}$$

This procedure is only accurate for sufficiently small δv. It is worth noting that to ensure the accuracy of the result, $\rho(v)$ must still be normalized in the Riemann sum, i.e. $\sum_{i=0}^{\infty} \rho(v_i)\delta v = 1$.

Due to the small effect of resonances on the velocity averaged theoretical rate constants (e.g see Fig. 5.6 (c)), the theoretical cross sections can be approximated by power function $\sigma \approx av^b$ where a and b are constants determined by fitting. Due to the close approximation of the baseline of the calculated cross-sections to a power function over a wide range of collision energies, it is assumed that the cross sections can also be approximated at collision energies outside the range of scattering calculation by extrapolation of the fitted power function. This was the case for the calculation of velocity averaged theoretical rate constants in the $BaRb^+$ system due to the prohibitively expensive scattering calculations up to the high collision energies reached in the experiment.

This chapter has given a detailed description of the experimental and analytic techniques essential for the study of cold ion-neutral collisions in this work, and tools for the comparison of the experimental observations to theoretical predictions. The next chapters describe the results obtained as a consequence of this work, and are presented system by system for clarity.

Chapter 4

Characterisation of the magneto-optical trap

As discussed in section 1.3.10, the magneto-optical trap has been the workhorse of ultracold atomic physics since its first demonstration in 1987 for Na atoms [62]. Since then, this method of cooling and confining atoms has been developed (e.g. implementation on a silicon chip [132]), and successfully applied to most of the rare earths (Li [133], Rb [134], K [135], Cs [136]), alkaline earths (Mg [137], Ca [138], Sr [139], Ba [140]), and some transition metal elements (Cr [94], Yb [141]). The MOT has found itself to be the starting point for many important experiments within the ultracold collisions field, including Bose Einstein condensation [9, 142], ultracold molecular formation and collisions [143], and cold ion-atom collisions [33, 36–39, 41, 42, 44]. The general behavior of the characteristics of these MOTs (e.g. temperature, atom number, and density) upon variation of important parameters (e.g. laser frequency detuning, laser power, and magnetic field gradient) have been well studied, and semi-empirical models developed [144, 145], although to date there still exists no universal model describing a MOT.

As discussed in section 2.3, the MOT must work as part of a hybrid trap, and to avoid scattering of the MOT laser beams as they pass in between the rods of the Paul trap, the beam $1/e^2$ radius was constrained to 2.1 mm.

Much of the experimental effort and analysis of MOTs has been directed towards their optimization for high phase space densities, and high atom numbers, which are needed for efficient subsequent magnetic trapping [9], and for better absorption imaging contrast [146]. However, in the limit of high density, three body processes become important [40], which are not desirable for the study of two body processes as in this work. Also for the study of fast reaction rates, it is helpful to reduce the density of the reactants, such that more time is afforded to follow the reaction to completion. The behavior at high densities follows the characteristics of the so called "multiple scattering" regime, where photons from the cooling lasers are scattered on average more than once in the atom cloud volume, and the density is independent of atom number [145]. With small atom numbers, the so-called "temperature limited regime

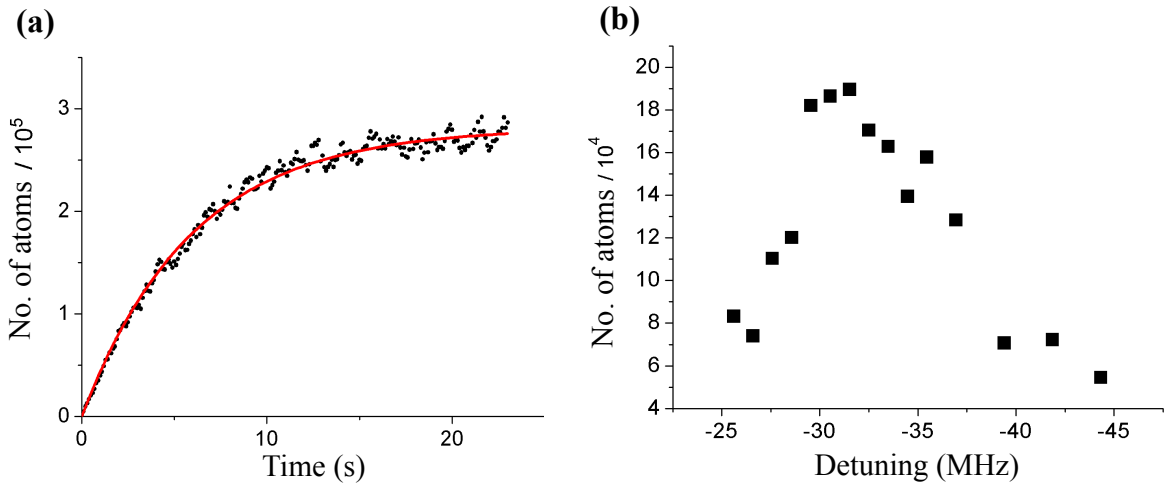

Figure 4.1: (a) A typical loading curve for the MOT. Black circles are experimental data, and the curve is a fit based on equation 4.1. Time zero indicates the switching on of the magnetic fields. (b) Atom number against detuning of the cooling laser frequency from zero field resonance, with a magnetic field gradient of 27 G/cm, and a total laser power of 10.0 mW. The error bars are contained within the points.

(TLR)" [145] is reached, where the density has been shown to increase proportionally with atom number, and hence can be easily controlled.

The theory and technical details of the ^{87}Rb MOT operation of this work can be found in sections 1.3.10 and 2.3, respectively, which include the analytic techniques for determining such quantities as atom number, density, and temperature. The results of the characterization of the MOT used in the experiments of this work are now presented.

The loading characteristics of the MOT were studied. Initiating the trap by turning on the magnetic fields leads to the loading of atoms into the trap. By monitoring the number of atoms as a function of time, a loading curve was recorded, an example of which is shown in Fig. 4.1 (a). The steady state population of the MOT ($N(0)$), and the trap time constant τ can be derived from these measurements using the simple expression [92]

$$N(t) = N(0)e^{1-\frac{t}{\tau}}. \tag{4.1}$$

For the particular case shown in Fig. 4.1 (a), $N(0) = 2.9 \times 10^5$ and $\tau = 6.1$ s, meaning that on average, an atom spends 6.1 s inside the MOT volume [92].

The dependence of atom number on detuning of the cooling laser frequency was investigated. Fig. 4.1 (b) illustrates the behavior for a magnetic field gradient of 27 G/cm, showing a maximum in atom number at a detuning of 32 MHz. The detuning of the cooling laser frequency for a given measurement is determined by subtracting the frequency that maximizes the fluorescence from an Rb vapor reference cell, from

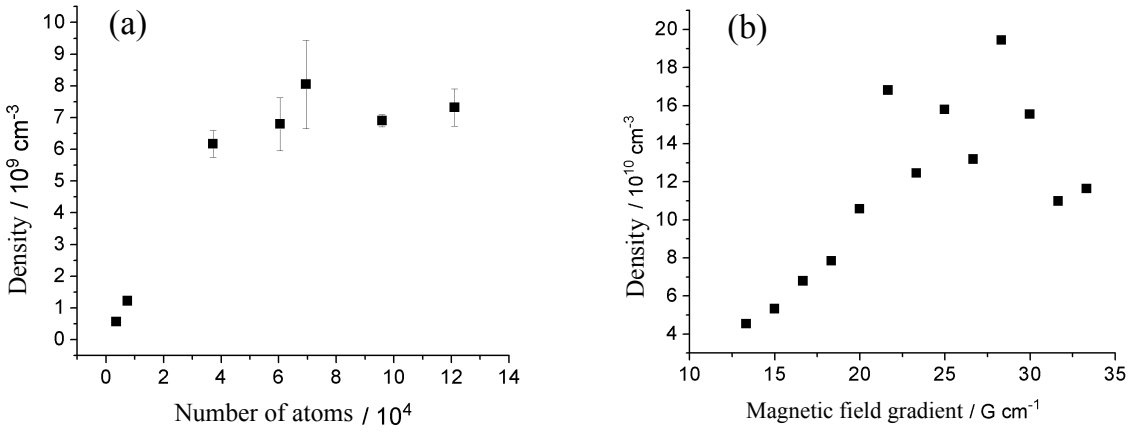

Figure 4.2: (a) The variation of atomic density with atom number in the small beam MOT at a magnetic field gradient of 20 G/cm, and a cooling laser power of 10.8 mW. (b) The variation of atomic density with magnetic field gradient at a background Rb density of 3.5×10^7 cm^{-3}, and a laser cooling power of 11.2 mW. A total range of densities of nearly three orders of magnitude is observed.

the frequency recorded by the wavemeter during the experiment cycle. The expected shape, observed and described in other reports (e.g. [147]), is indeed reproduced, which confirms normal MOT operation for this system, even when using small beams.

The average atomic density n_{av} (see section 2.3.4 for n_{av} determination) was determined for a range of atom numbers (varied by changing the current applied to the getter and hence background Rb pressures) at constant magnetic field gradient (Fig. 4.2 (a)); and over a range of magnetic field gradients at a constant background Rb pressure (Fig 4.2 (b)). In these figures it can be seen that a range spanning nearly three orders of magnitude of average density was achieved, from 5×10^8 cm^{-3} to 2×10^{11} cm^{-3}.

The atomic density has an upper limit because fluorescent light emitted by some trapped atoms is absorbed by others, leading to a repulsive radiation pressure force, which limits how close atoms can get to one another (multiple scattering regime) [148]. As the magnetic field gradient is increased, the effective potential becomes tighter, and with appropriate readjustment of the cooling laser detuning, the trap volume becomes smaller. Since the atom number decreases only slightly when the magnetic field is increased, an overall increase in the atomic density is expected, and indeed observed, as shown in Fig. 4.2 (b). The lower limit on density in this setup is set by the lowest detectable level of fluorescence at low atom numbers, and atom clouds with much fewer atoms than 10^4 cannot be observed.

The observed dependence of density on atom number in Fig. 4.2 (a) can be described by a transition between two regimes of operation, each with a slightly different spatial distribution of atomic density [145]. In the first "temperature limited" regime (TLR), the atom numbers are low, and the volume, and hence the density of the

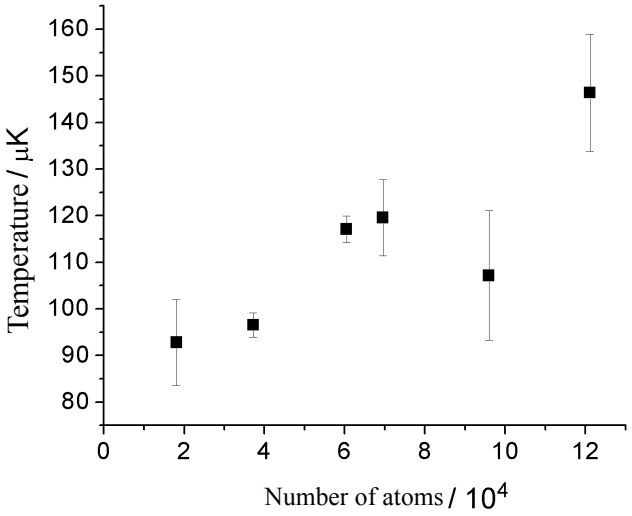

Figure 4.3: The variation of temperature of the atom cloud, determined by the 1D ballistic expansion technique, with atom number.

trapped cloud, depends on its temperature. In this case, the density distribution is Gaussian, and the average density is proportional to the atom number, and this behavior can be seen in Fig. 4.2 (a) at atom numbers below 4×10^4. In the "multiple scattering" regime, re-absorption of scattered photons in the MOT becomes important, and in this case, density distribution departs slightly from Gaussian, becoming more uniform, and the average density becomes independent of atom number. This can be seen in Fig. 4.2(a) for atom numbers above 4×10^4. It is interesting to note that this transition is also observed at $\approx 10^4$ atoms in a Cs MOT in [145], which points towards a possible system independence of the observed transition in MOT systems.

The variation of temperature (the determination of which is discussed in section 2.3.5) with atom number is shown in Fig. 4.3. Another signature of the transition from "temperature limited" to "multiple scattering" regimes is the change from independence of temperature on atom number, to a $T \approx (N)^{1/3}$ dependence [145]. Fig. 4.3 does not convincingly reproduce this theoretical transition. The figure does firmly indicate however that above $\approx 4 \times 10^4$ atoms, the temperature of the atoms increases with increasing atom number, which demonstrates that above this atom number the cloud is no longer in the "temperature limited" regime. Measurements of temperature at atom numbers lower than $\approx 2 \times 10^4$ were not possible due to the low level of fluorescence from these clouds during the expansion necessary for the temperature measurement.

In conclusion a MOT with an imposed beam $1/e^2$ radius of 2.1 mm was studied and a range of atomic density of 5×10^8 cm^{-3} to 2×10^{11} cm^{-3}, and temperatures of 90 to 150 μK have been observed. These ranges are well suited to the application of the overlap of the MOT with a linear Paul ion trap to study ion-atom reactions. Two signatures of the transition between the "temperature limited" and "multiple scattering"

regimes of MOT operation at an atom number of $\approx 4 \times 10^4$ atoms were observed.

Chapter 5

The $Ca^+ + Rb$ system

5.1 Introduction

Despite the breadth of both experimental and theoretical investigations into cold ion-neutral collisions so far [33–36, 38, 39, 41, 44, 149], key aspects relating to the dynamics of these processes are still unresolved. An important question pertains to what extent cold barrierless reactive processes are solely governed by long-range intermolecular forces [15,18,150–152], such that they can be described within the framework of capture models (see section 1.2). In cold ion-neutral reactions however, few attempts have been made to directly compare the results of experiment and theory [36,41,42,44,153]. Such comparisons are necessary to validate reactive-scattering models and gain a more in-depth understanding of the dynamics observed in cold ion-neutral systems.

Another key question pertains to the types of chemical processes which can occur in cold atomic-ion atom collisions. As described in section 1.2.5, non-adiabatic couplings can lead to charge transfer, and radiative processes can lead to charge transfer and radiative association. So far, either fast near-resonant homonuclear charge exchange (in Yb-Yb^+ [33]) or a slow loss of the atomic ions from the trap were observed (in Rb-Yb^+ [34] and Rb-Ba^+ [35]), rationalized for the latter in terms of radiative and non-radiative charge exchange [154]. Molecular-ion formation has also been considered as a result of a three body process in Rb-Rb^+ [40], and evidence for a radiative mechanism has been found in the Ca-Yb^+ system [44]. However, a general understanding of these reactive processes and in particular the role of light remains to be established.

To address the above issues, a combined experimental and theoretical investigation of cold reactive collisions between Ca^+ ions and Rb atoms in a hybrid trap was undertaken, and the results are presented in this chapter. Reaction rate constants were determined in the range of collision energies $\langle E_{\mathrm{coll}} \rangle / k_{\mathrm{B}} = 20$ mK - 20 K. The lowest energies were achieved in experiments using single localized Ca^+ ions. Rich chemical dynamics were observed and interpreted in terms of non-adiabatic and radiative charge exchange as well as radiative molecule formation using high-level electronic structure and quantum-scattering calculations. Light-assisted processes were investigated, and

enhancement of the efficiency of the dominant chemical pathways in excited reaction channels was observed. Ionic reaction products were identified, and branching ratios studied using resonant-excitation mass spectrometry. The energy dependence of the reaction rate constants was studied and compared to theoretical predictions, and were found to be governed by long-range interactions in line with classical capture models, but whose magnitude was determined by short-range couplings which only weakly depend on the asymptotic energy. The results highlight both universal and system-specific phenomena in cold ion-neutral reactive collisions.

5.2 Methods

The experimental apparatus for the simultaneous trapping of laser-cooled Ca^+ ions and ultracold Rb atoms has been described in detail in chapter 2. A Ca^+ Coulomb crystal was axialised (sec. 3.3) and overlapped in space with an ultracold Rb cloud (sec. 3.1). Upon overlap, the volume of Ca^+ ions reduced as a result of reactions with Rb (see Fig. 3.3). The pseudo-first order rate constant (sec. 3.2) for this process was determined by recording spatially resolved Ca^+ laser cooling fluorescence images as a function of reaction time (sec. 3.2.1). Laser cooling fluorescence images of the Rb cloud were taken to determine the average atom density (sec. 2.3.4), which, combined with an overlap factor (sec. 3.1) and the pseudo-first order rate constant, gave the second order rate constant (sec. 3.2) for the observed processes.

As seen in section 3.6, when both species are laser cooled, the populations are distributed over the $(4s)\ ^2S_{1/2}$, $(4p)\ ^2P_{1/2}$ and $(3d)\ ^2D_{3/2}$ states of Ca^+ and the $(5s)\ ^2S_{1/2}$ and $(5p)\ ^2P_{3/2}$ states of Rb. Reactive collisions occur in excited states of the Rb-Ca^+ system and the observed reaction rates represent an average over all possible channels. Note that simultaneous excitation of both species does not occur because of the alternate chopping of the cooling laser beams. The populations of the ionic states were determined using an 8-level optical Bloch model (sec. 3.5.3), and that of the atoms by a 2-level optical Bloch model (sec. 1.3.5). The populations were varied by changing laser cooling detuning and intensities, and the state specific rate constants (as defined in sec. 3.6) determined using a multi-dimensional least squares fitting procedure (sec. 3.6).

The observed rate constants were rationalized using high level ab initio electronic structure calculations of the potential energy curves (sec. 3.7).

The ionic products of the reaction remained in the ion trap and were identified using resonance excitation mass spectrometry, and their abundances qualitatively indicated by comparison to simulated spectra (sec. 3.4). The experimental branching ratios were compared to the results of quantum scattering calculations (sec. 3.7).

The energy dependence of the rate constants were studied. The temperature of the atoms was measured to be $T = 90 - 150\ \mu$K (sec. 2.3.5). This was at least two orders of magnitude lower than the average ion kinetic energy (determined by comparison of experimental ion fluorescence images to those of MD simulations (sec. 3.3) which was

dominated by the micromotion of the ions), and hence had a negligable contribution to the collision energy. The average collision energy was therefore varied by changing the size and shape of the Coulomb crystals, resulting in different ion kinetic energy distributions (sec. 3.3). The experimental energy dependence was compared to the results of classical capture models (sec. 1.2), and to the results of quantum scattering calculations which were velocity averaged with results of MD simulations (sec. 3.7) for a more accurate comparison to the experimental results.

5.3 Results and discussion

5.3.1 State specific rate constants

For the reaction measurements displayed earlier in Fig. 3.3 (a) and (b), the rate coefficient was established to be $k = 2.5(9) \times 10^{-11}$ cm^3 s^{-1}, two orders of magnitude smaller than the collisional (Langevin) rate coefficient ($k_{\mathrm{L}} = 3 \times 10^{-9}$ cm^3 s^{-1} [47]).

For reactions in which the Ca^+ cooling lasers were switched off, a rate constant of $k_s = 2 \times 10^{-12}$ cm^3 s^{-1} was obtained. This value was insensitive to the excited-state population of Rb which was varied in the range from 2% to 5% compatible with a stable operation of the MOT. As the ions were not laser cooled over the course of the reaction in these particular "cooling laser off" measurements, no fluorescence images could be obtained during reaction, and the rate constant relies on a succession of "before and after" reaction fluorescence images. It is possible that the Coulomb crystal melted during that period and the reaction occurred with a diffuse ion cloud for which the overlap with the ensemble of ultracold atoms and the ion kinetic energies were not well defined. Given the uncertainty of the experimental conditions, this particular rate constant is to be regarded as an order-of-magnitude estimate for the rate constant in the lowest channel.

Reactions were then studied with the Ca^+ cooling laser on. The contribution of the excited Ca^+ channels to the observed rate constant was investigated by varying the populations in the Ca^+ states by changing the frequency detuning of the 397 nm and 866 nm lasers in the range 20-100 MHz and 0-70 MHz, respectively. In these measurements, it was ensured that the ion cloud always remained Coulomb-crystallized so that the effect of the detuning on the average ion energies was negligible. Figure 5.1 shows the resulting rate constants which were seen to correlate with the population in the $Ca^+(4p)\ ^2P_{1/2}$ state, whereas no correlation with the populations in the $(4s)\ ^2S_{1/2}$ and $(3d)\ ^2D_{3/2}$ levels was observed.

The data in Fig. 5.1 was fitted to a kinetic model (see sec. 3.6) accounting for the relevant reaction channels. Taking into account the chopping of the Ca^+ cooling laser beam, and the independence of the reaction rate on the Rb electronic state, the measured rate coefficient can be expressed as $k = \frac{1}{2}\Big[k_s(p_s + 1) + k_p p_p + k_d p_d\Big]$. Here, k_s, k_p, k_d and p_s, p_p, p_d stand for the rate constants and populations in the $Ca^+(4s), (4p)$ and $(3d)$ levels. The result of the fit was $k_p = 1.5(6) \times 10^{-10}$ cm^3 s^{-1} and $k_{s,d} \leq$

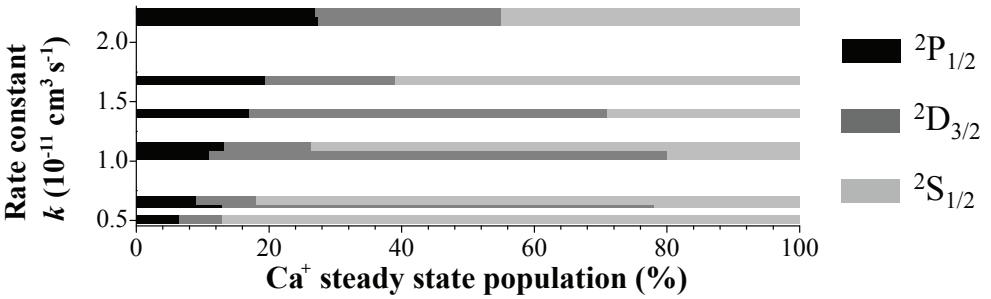

Figure 5.1: Variation of reaction rate constants k with Ca^+ level populations. The bars indicate the relative level populations obtained by varying the detunings of the cooling-laser beams, their intercepts with the y axis give the values of the corresponding rate constants. Each data point corresponds to an average of three consecutive measurements (average statistical uncertainty (2σ) $\Delta k = 3 \times 10^{-12}$ cm^3 s^{-1}).

3×10^{-12} cm^3 s^{-1}, indicating that the rate constant is enhanced by a factor >50 in the Ca^+ $^2P_{1/2}$ state as compared to from the $^2D_{3/2}$ and $^2S_{1/2}$ states.

5.3.2 Ionic products of reaction

The deep potential of the ion trap (3-4 eV), enabled the ionic reaction products to remain trapped and to be sympathetically cooled into the Coulomb crystal. The chemical identity of the product ions was established using resonant-excitation (RE) mass spectrometry [108, 155] (sec. 3.4). As discussed in Ref. [108] and in sec. 3.4, a quantitative analysis of the RE mass spectra is not available owing to the strong dependence on experimental parameters such as drive amplitude, scan direction, scan speed, and the crystal size and composition. The intensities of the peaks in the spectra therefore only serve as a qualitative guide to the abundance of different ion species in the Coulomb crystal. The mass spectra were simulated using MD methods (see sec. 3.4) by Fourier-transforming the time-dependent ion kinetic energies after displacing the Coulomb crystals from the trap axis in the radial direction and relaxing their positions. The result is a frequency spectrum of the ion crystal, which qualitatively reproduces the intensities of the peaks observed in the spectra [108], and quantitatively reproduces the observed resonance positions [109].

Fig. 5.2 (c) shows a RE mass spectrum of a pure Ca^+ crystal before overlap with Rb. One resonance is observed in the spectrum and its position matches well to the radial frequency for a single Ca^+ ion in the trap given by the grey dashed line at 112 kHz. As discussed above, the observed resonance differs in position slightly from the calculated single ion frequency, but is still clearly assignable to Ca^+ ions. To investigate the product branching ratios in different reaction channels, RE mass spectra were recorded under different Ca^+ laser-cooling conditions, resulting in varying contributions of the excited $Ca^+[(4p)\ ^2P_{1/2}]/[(3d)\ ^2D_{3/2}]$ + $Rb[(5s)\ ^2S_{1/2}]$ reaction channels.

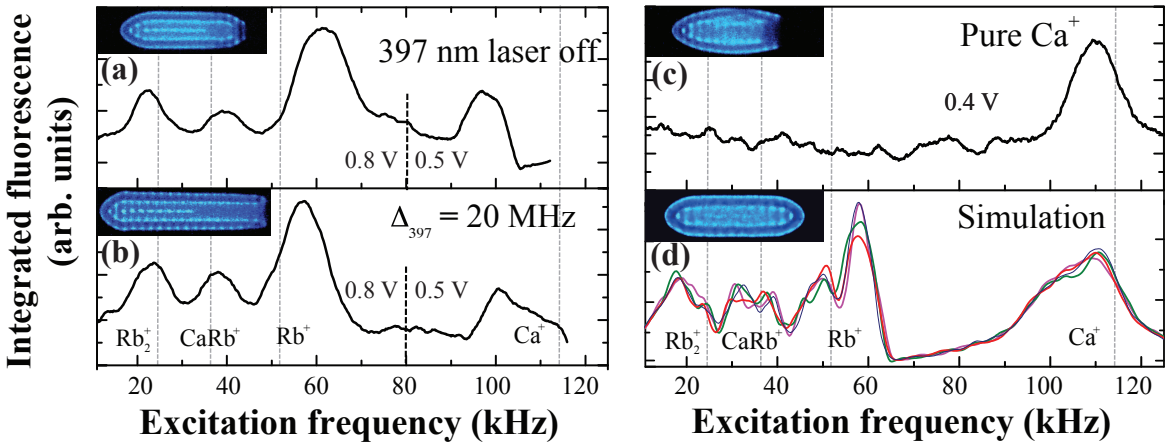

Figure 5.2: Resonant-excitation mass spectra of Coulomb crystals: (a) after reaction without laser cooling of Ca^+, (b) after reaction with laser cooling both species, (c) pure Ca^+ crystal before reaction, (d) molecular-dynamics simulation (produced by G. Hegi) of the spectrum in (b). The coloured traces represent different simulations performed with slightly varying initial conditions. See text for details.

Fig. 5.2 (a) shows a RE mass spectrum recorded after a reaction in which the 397 nm cooling laser was switched off for the duration of the reaction with Rb, and hence had its population in the ground state. As mentioned above, the Coulomb crystal's overlap with the Rb cloud and the ion kinetic energies are not well defined in this situation. However, after reaction, four resonances can be distinguished in the spectrum in Fig. 5.2 (a). Three of them correspond to the product ions Rb_2^+, $CaRb^+$, Rb^+, and one of them to the remaining Ca^+ ions in the crystal. Note that the excitation amplitude has been reduced from 0.8 V to 0.5 V in the region of the strong Ca^+ resonance in order to prevent a melting of the crystal during the scan. Whereas the Rb^+ is a result of either non-radiative charge transfer (NRCT) or radiative charge transfer (RCT) between Ca^+ and Rb, $CaRb^+$ can only be formed in an association reaction whereby the collision complex is stabilized either collisionally or by the spontaneous emission of a photon (radiative association, RA). Collisional stabilization is negligible at the low Rb densities in the MOT [40], so the formation of $CaRb^+$ ions is assigned as a product of RA. The Rb_2^+ is only observed in the presence of $CaRb^+$ indicating that this product results from the reaction $CaRb^+ + Rb \rightarrow Rb_2^+ + Ca$ which is exothermic by $\approx$0.4 eV. In principle, the generation of Rb_2^+ by photoionization or charge transfer with Rb_2 formed by photoassociation of Rb by the 780 nm cooling lasers is possible as well. However, Gabbanini et al. [156] showed that the formation of $^{87}Rb_2$ molecules in a MOT is inefficient and governed by three-body recombination processes which can be neglected at the low Rb number densities used in the present experiment. Another possible route leading to Rb_2^+ is RA of Rb^+ product ions with excited Rb atoms in the MOT. Further studies are needed to determine the exact origin, or indeed combination

of origins, of the Rb_2^+ product.

Fig. 5.2 (b) shows a spectrum obtained at a 397 nm-laser detuning of 20 MHz, corresponding to Ca^+ excited-state populations of $p_p = 12\%$ and $p_d = 13\%$ where p_p and p_d denote the populations in the $(4p)\ ^2P_{1/2}$ and $(3d)\ ^2D_{3/2}$ states, respectively. While subtle differences can be observed, the similarity between the spectra in Figs. 5.2 (a) and (b) suggests that the product branching ratios are similar in both excited and ground state channels.

The contribution of the ground and excited reaction channels to the observed reaction rate, and hence the product distribution, can be estimated from a combination of the state specific rate constants determined above, and the state populations during the experiment. The contribution from the $Ca^+(3d)$ channel is at least an order of magnitude smaller than for the other two channels, and so its contribution is neglected. From the kinetic model given above, the effective rate constants for the $Ca^+(4s)$ and $(4p)$ channels can be written $k'_s = \frac{1}{2}(1 + p_s)k_s$ and $k'_p = \frac{1}{2}p_p k_p$, respectively. For the conditions corresponding to Fig. 5.2 (b), $k'_s \approx 1.8{\times}10^{-12}$ cm^{3}s^{-1} and $k'_p = 9.0{\times}10^{-12}$ cm^{3}s^{-1}, indicating that the $Ca^+(4s)$ and $(4p)$ channels contribute with a ratio of $\approx$ 1:5 to the product yields observed in the RE spectra. Considering that all of the three processes NRCT, RCT and RA are also expected to occur in the excited $Ca^+(4p)$ channel with significant efficiencies as explained below, the similarity between the spectra in Figs. 5.2 (a) and (b) is therefore not necessarily surprising.

The RE spectra were compared to the results of MD simulations shown in panel (d). A crystal composition of 170 Ca^+, 120 Rb^+, 39 $CaRb^+$ and 52 Rb_2^+ ions was found to best reproduce the experimental peak intensities. The different simulations shown in panel (d) were performed using slightly different initial conditions to check the robustness of the procedure. The approximations inherent in the simulation procedure and the sensitivity of the experimental spectra to the specific experimental conditions (sec. 3.4), however, limit the direct comparison between experiment and simulation, which can only be expected to provide a rough estimate of the relative numbers of the ion species in the crystal.

5.3.3 Potential energy curves

Figure 5.3 shows the $RbCa^+$ non-relativistic potential energy curves (i.e., without spin-orbit interaction) up to the twenty-second dissociation threshold $Rb(5s)$+$Ca^+(4p)$ which is the highest-energy entrance channel accessed in the experiments. These were calculated as described in section 3.7 by the Dulieu group.

Over the energy range of about 41000 cm^{-1}, two kinds of asymptotic channels are present: a Rb ($5s$ or $5p$) atom colliding with a Ca^+ ($4s$, $3d$, or $4p$) ion (4 channels), and a Rb^+ ion colliding with a Ca atom (18 channels). As described in section 3.7, the energies of the effective two-electron Ca atom are obtained through a FCI calculation, with a typical accuracy of a few hundred wave numbers, and as a result, in the congested region around the $Rb(5s)$+$Ca^+(4p)$ asymptote (Figure 5.3 (c)), the order of several asymptotic limits is altered, preventing a detailed state-to-state modeling

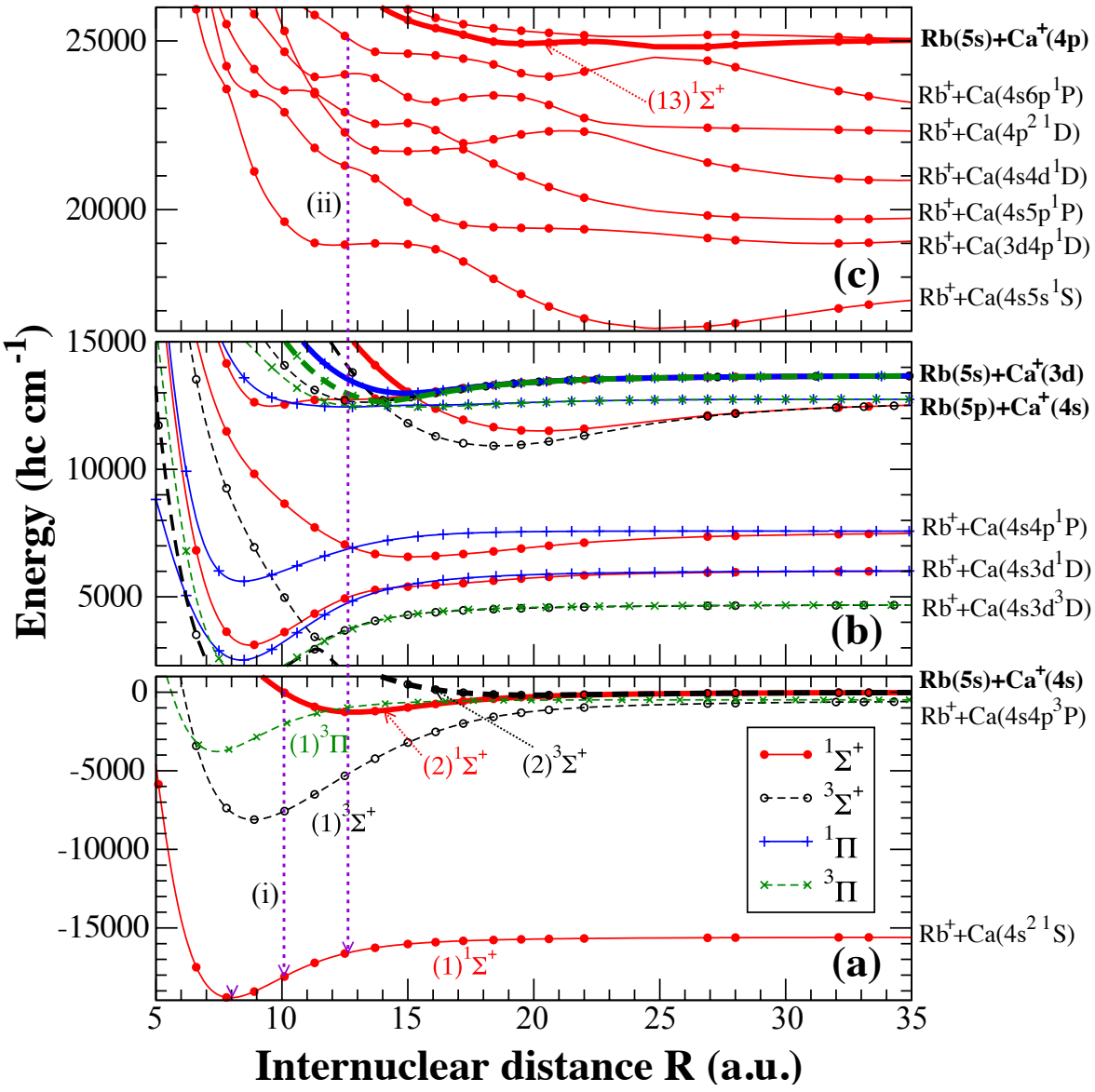

Figure 5.3: Computed $RbCa^+$ potential energy curves (PECs) (Produced by N. Bouloufa-Maafa, M. Aymar and O. Dulieu) in the regions of (a) Rb($5s$)+Ca^+($4s$), (b) Rb($5s$)+Ca^+($3d$), (c) Rb($5s$)+Ca^+($4p$). The PECs of the relevant entrance channels of the reaction are highlighted with thick lines. PECs for $^1\Delta$ and $^3\Delta$ symmetries are omitted for clarity. Downward arrows suggest possible pathways for formation of ground-state $RbCa^+$ ions by radiative association. In (c), only PECs of $^1\Sigma^+$ symmetry are displayed for clarity.

of the dynamics from this entrance channel. The calculations still provide however, a useful guide to a qualitative understanding of the underlying reaction mechanisms.

Figure 5.3 (a) shows the region already studied theoretically in Ref. [47], where the $Rb(5s)+Ca^+(4s)$ entrance channel (indicated in bold) is not the lowest dissociation limit. NRCT induced by non-adiabatic couplings can occur around the crossings with the $(1)^3\Pi$ state correlating with the $Rb^+ + Ca(4s4p\ ^3P)$ asymptote [47] (see sec. 1.2.5). The emission of a photon from the $(2)^1\Sigma^+$ entrance channel to the $(1)^1\Sigma^+$ curve can lead to either RCT or RA forming molecular ions provided sufficient Franck-Condon (FC) factors (see sec. 1.2.5). The dashed arrow (i) in Figure 5.3 (a) indicates a transition for which favorable FC overlap for RA can be expected. This result is compatible with the observation of both RA and CT products in this channel. It should be noted that the upper limit for the experimental rate coefficient $k_s \leq 3 \times 10^{-12}$ cm^3 s^{-1} determined above is close to value of $\approx 1 \times 10^{-12}$ cm^3 s^{-1} estimated from theoretical NRCT cross sections reported in Ref. [47].

In the energy vicinity of the $Rb(5s)+Ca^+(3d)$ entrance channel, there are no exit channels which would enable efficient NRCT (Figure 5.3 (b)). This is in agreement with the experimental finding of a small reaction rate for this channel ($k_d \leq 3 \times 10^{-12}$ cm^3 s^{-1}). RCT and RA connecting to lower-lying states are in principle possible in various symmetries, but the shape of the entrance curves indicates that the FC factors to the ground state curve are small. As discussed above, adjusting the Rb population in the (5p) state did not have any measurable effect on the reaction rate. This result can be simmilarly rationalized by the isolation of the molecular curves connecting to the $Rb(5p)+Ca^+(4s)$ asymptote which do not cross with any charge-transfer curves hence precluding NRCT, and by their repulsive character at short range which lead to small Franck-Condon factors and hence a small radiative transition probability to the lower-lying molecular states.

Figure 5.3 (c) shows the dense network of the PECs of $^1\Sigma^+$ symmetry in the region around the $Rb(5s)+Ca^+(4p)$ entrance channel. The situation is comparable for the other symmetries which are not shown for clarity. Inspection of Fig. 5.3 (c) reveals the mechanism leading to the large reaction rate observed from this entrance channel. At large distances, the $Rb(5s)+Ca^+(4p)$ entrance curve is attractive (varying with $-R^{-4}$). The PECs of the states correlating with the $Rb^+ + Ca^*$ asymptotes are also attractive at long range, but soon turn repulsive due to their Rydberg state character converging to the $Rb^+ + Ca^+$ ionization limit. As a consequence, the entrance channel curve ($(13)^1\Sigma^+$) encounters many avoided crossings with curves correlating to charge-transfer asymptotes. Non-adiabatic transitions at these crossings result in a large rate for NRCT leading to the formation of Rb^+. Through consecutive non-adiabatic transitions, there are also many possibilities for the system to reach short internuclear distances, and so the likelihood of favorable FC factors for radiation to lower lying states is increased. A possible radiative pathway to the ground state is indicated by the downward arrow (ii). Apart from FC factor considerations, radiative transition probability scales with the cube of the frequency of the emitted photon, and hence emission to the ground state is possibly a significant pathway. Additionally, radiative

emission at long range can also contribute to the observed RCT and RA processes. The increased density of charge transfer states at high excitation energy is a common feature of mixed alkaline-atom alkaline-earth-ion molecular systems and so it can be expected that the enhancement of the reaction rate constant in these channels, as well as RA and RCT mechanisms, are generally important phenomena in their reactive dynamics.

5.3.4 Scattering calculations for the ground state entrance channel

Using the PECs calculated for the ground state entrance channel ($Ca^+(4s)$+$Rb(5s)$) and curves below, quantum scattering calculations were conducted by the Dulieu group to obtain the cross sections for radiative processes from this channel (see sec. 3.7).

For clarity, further to Fig. 5.3, the potential energy curves correlating with the three lowest asymptotes of the $(CaRb)^+$ complex are presented in Fig. 5.4 (a). The transition dipole moments (TDMs) between the indicated electronic states are presented in Fig. 5.4 (b). Collisions in the ground state entrance channel proceed through two statistically populated states: (i) The repulsive $(2)^3\Sigma^+$ state (with a statistical weight $p = 3/4$) in which the system is prevented from undergoing inelastic collisions, and from which the TDMs suggest radiative processes are negligable (see Fig. 5.4 (b)); and (ii), the attractive $(2)^1\Sigma^+$ state (with a statistical weight $p = 1/4$) which represents the main channel for inelastic collisions, and from which significant radiative emission is expected via RA or RCT.

The two circles in Fig. 5.4(a) indicate the positions of avoided crossings resulting from spin-orbit coupling of the $(2)^1\Sigma^+$ and $(1)^3\Pi$ states leading to non-radiative charge transfer (NRCT). As discussed in section 1.2.5 and in refs. [29, 47], this process has a significant cross section at low energies, and so will compete with the radiative processes, and a comparison is given in a subsequent section. In principle, RA is possible from the $(1)^3\Pi$ state towards the $(1)^3\Sigma^+$ state due to the large TDM (dashed-dotted blue line in Fig. 5.4 (b)), but because of the small energy difference between these states the relevant cross section is small in comparison to the singlet states.

The calculated cross sections for the radiative processes between the lowest $^1\Sigma^+$ states are displayed in Fig. 5.5. The RA cross sections are seen to be $\approx 2.5\times$ larger than the RCT cross sections over the energy interval shown. The RA and RCT cross sections both show shape resonances reflecting the dynamic trapping of the wavefunction behind the centrifugal barrier at well-defined collision energies (see sec. 1.2.4). The positions and intensities of the features in both the RA and RCT channels are identical, highlighting that the resonances are primarily governed by the long-range and centrifugal potentials and not the details of the short-range dynamics (see sec. 1.2.5). The pattern of shape resonances appears similar to the one found for the NRCT process in the same entrance channel in Ref. [29].

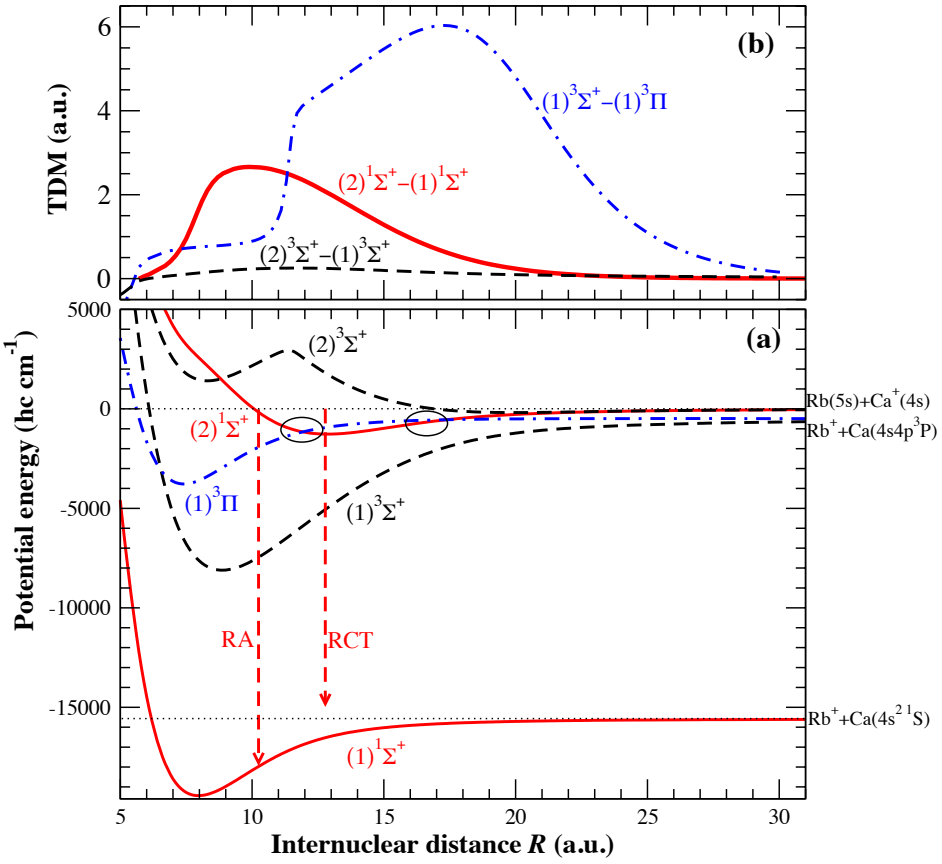

Figure 5.4: (Produced by M. Aymar and O. Dulieu) (a) Computed non-relativistic potential energy curves (PECs) and (b) transition dipole moments (TDMs) relevant for the present study. Downwards arrows illustrate the radiative association (RA) and the radiative charge transfer (RCT) processes between the lowest singlet states. Circles indicate the crossing points between the $(2)^1\Sigma^+$ PEC associated with the lowest accessible collision channel Rb($5s$)+Ca$^+$($4s$) and the $(1)^3\Pi$ PEC around which strong non-adiabatic interactions caused by spin-orbit coupling lead to non-radiative charge transfer (NRCT) [47].

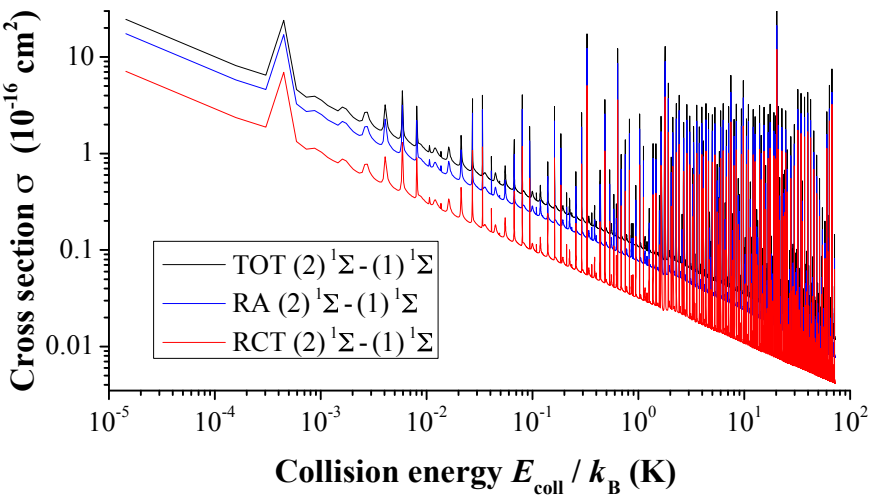

Figure 5.5: (Produced by M. Raoult and O. Dulieu) Theoretical cross sections for radiative charge transfer (RCT) and radiative association (RA) from the $(2)^1\Sigma^+$ molecular state associated with the $Ca^+(4s)$+Rb($5s$) entrance channel. TOT denotes the sum of both processes.

5.3.5 Collision-energy dependence of reaction rates and reaction mechanism

The dependence of the rate constant on the collision energy represents an important dynamical characteristic of collision systems. As described in section 3.3, the energies of collisions between Ca^+ and Rb were varied using two different approaches. Rate constants at medium to high average collision energies in the range $\langle E_{\rm coll}\rangle/k_{\rm B} \approx 200$ mK - 20 K were obtained by reacting Coulomb crystals of varying size and shape as shown in Figs. 3.8 (a) (ii)-(vi). The lowest collision energies $\langle E_{\rm coll}\rangle/k_{\rm B} \approx 20$ mK were achieved in a series of experiments in which single Ca^+ ions were reacted from a string of two Ca^+ ions localized on the central trap axis, as shown in 3.8 (a) (i). As described in section 3.2.1, the rate constant at this collision energy was obtained from a pseudo-first order fit of the time to reaction observed in a total of 49 single-ion reaction experiments as shown in Fig. 3.6. (see also Ref. [106]). As described in section 3.3, the collision energy distributions were obtained from MD simulations, which are each characterized by an average collision energy $\langle E_{\rm coll}\rangle$.

The experimental rate constants as a function of average collision energy (corresponding to distributions (i)-(vi) in Fig. 3.8 (d)) are presented in Fig. 5.6 (a). The rate constant was found to be essentially constant within the error boundaries in the interval $\langle E_{\rm coll}\rangle/k_{\rm B}$ =20 mK - 20 K. As described in section 1.2.4, the predicted shape resonances in the rate constant are not resolved in the experiments due to the much larger width of the experimental collision energy distributions.

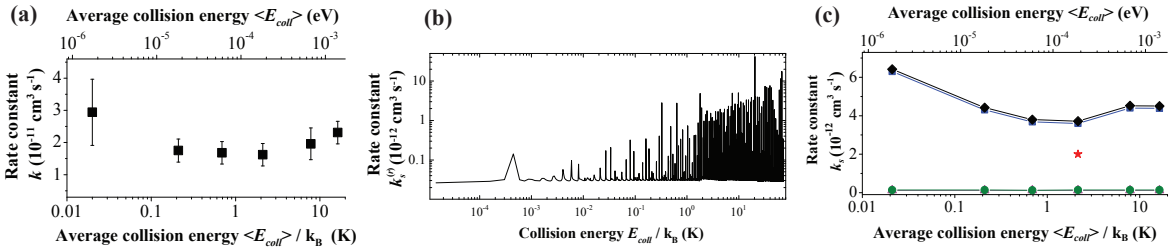

Figure 5.6: (a) Channel-averaged rate constant k as a function of the average collision energy for Coulomb crystals exhibiting the shapes displayed in Fig. 3.8 (a). (b) Theoretical total radiative rate constant $k_s^{(r)}$ for the ground state entrance channel. (Produced by M. Raoult and O. Dulieu) (c) Theoretical rate constant k_s for the $Ca^+(4s)$+Rb$(5s)$ channel as a function of the collision energy. Green circles: total radiative rate constants, violet triangles: total radiative rate constants without resonances, blue squares: non-radiative rate constants calculated from the cross sections reported in Ref. [47], black diamonds: summed radiative and non-radiative rate constants, red star: experimental result at $\langle E_{\rm coll}\rangle/k_{\rm B}$ =2 K.

Fig. 5.6 (b) shows a double-logarithmic plot of the total theoretical radiative rate constant $k_s^{(r)}$ from the ground state entrance channel in the energy interval 10 μK - 70 K obtained by multiplying the total radiative cross sections (Fig. 5.5) by the velocity of the collision partners. Apart from the narrow shape resonances, the calculated rate constant is also essentially constant with collision energy.

The observed and predicted energy dependence can be understood in terms of a classical model as described in section 1.2.3. Since the Rb $^2P_{3/2}$ state does not appear to play a significant role, the dominant long range interaction can be considered as charge induced-dipole, which leads to the Langevin expression for the collision rate constant which is independent of energy. The observed rate constant, and indeed the baseline of the computed rate constants, can be reproduced with the product of this collision rate with a constant opacity function to describe the short range reaction efficiency. The fact that the energy dependence of the cross sections can be recovered with a classical model is not surprising considering the large number of partial waves which contribute to the collisions even at the low energies reached in the present study (from $J \leq 23$ at $E_{\rm coll}/k_B \approx 20$ mK to $J \leq 200$ at $E_{\rm coll}/k_B \approx 50$ K).

This form of energy dependence can however also be recovered from the quantum-mechanical theory described in section 3.7. The transition-dipole moment function $D(R)$ in Eqs. (3.16) and (3.17) is significant only at short internuclear distances R (see Fig. 5.4 (b)). At these distances, the wave function amplitude is nearly independent of the collision energy (ϵ_i in the equations) which is small compared to the well depth of the entrance channel. The matrix element in Eq. (3.18) is thus nearly constant with collision energy. Ignoring the shape resonances, it is found that the TDMs in Eq. (3.16) and (3.17) are also nearly independent of the total angular momentum J as long as

$J < J_{\max}$, where $J_{\max}$ is the maximum value of J for which the collision energy exceeds the height of the centrifugal barrier, and J is large. As a result, the collision partners can approach to short internuclear distances to react only if the incident energy is large enough to surmount the centrifugal barrier, which corresponds to the classical capture description given in section 1.2. The TDM can therefore be factored out of the sums in Eqs. (3.16) and (3.17), and the energy dependence of the cross section only results from the summation over J up to the maximum allowed value $J_{\max}$ yielding $\sigma \propto J_{\max}^2/k_i^2 \equiv b_{\max}^2$, which, as seen in section 1.2.3, for a charge induced-dipole long range interaction potential leads to a rate constant independent of energy.

The same arguments are expected to hold for the NRCT processes, and indeed is approximately reproduced in the NRCT cross sections reported in Ref. [47]. The dynamics of the ion-neutral reactive collisions can therefore indeed be framed in terms of two separable contributions: long-range classical capture which governs the energy dependence of the rate constants, and the short-range dynamics of the different channels which determines their magnitudes.

Fig. 5.6 (c) shows the predicted rate constants k_s from the ground state entrance channel for collision energy conditions as shown in Fig 3.8 (a) (ii)-(vi). As described in section 3.8, the rate constants were calculated by velocity averaging the calculated cross sections with velocity distributions from MD simulations. The green circles and violet triangles represent the total radiative rate constants including and excluding shape resonances, respectively, and indicate that the contribution of resonances to the averaged rate constant is small. The blue squares indicate the rate constants calculated from the NRCT cross sections for the lowest reaction channel taken from Ref. [47]. The black diamonds represent the summed radiative and non-radiative rate constants, and the red star indicates the experimental estimate for the lowest reaction channel at $\langle E_{\text{coll}} \rangle / k_{\text{B}}$=2 K. The data in Fig. 5.6 (a) are rate constants averaged over all reaction channels under conditions as described above where the the entrance channels $Ca^+(4s)$+Rb($5s$) and $Ca^+(4p)$+Rb($5s$) contribute with a ratio of $\approx 1:5$. The calculated rate constants in Fig. 5.6 (c), however, are for the ground state entrance channel only, and hence their magnitude is reduced as compared to those in (a). There is a close resemblance, however, between the shape of the energy dependence in (a) and (c), suggesting that the energy dependence must be similar for reactions in the ground and excited entrance channels. This is expected since the long range interaction potential is independent of the electronic state of the ion, and hence it is only the magnitude of the reaction rate constant, and not its energy dependence that is affected by changing the ion electronic state, in line with the separable long and short range reactivity arguments given above.

From the results displayed in Fig. 5.6 (c), at $\langle E_{\text{coll}} \rangle / k_{\text{B}}$=2 K, the relative predicted rate constants for the radiative and non-radiative processes differ by a factor of ≈ 40. This is in contrast to the experimental estimate of the branching ratio of molecule-formation to charge-transfer informed by mass spectra and MD simulations of $\approx 1:4$. Whether this difference is significant is difficult to ascertain, considering that different potential curves and numerical approximations were used for the calculation of the

radiative processes by the Dulieu group, and NRCT by Gianturco and co-workers in Ref. [47]. A future unified theoretical treatment of the radiative and non-radiative processes is required to address this question conclusively, and forms part of the further work being currently undertaken.

5.4 Summary and conclusions

This chapter has characterized the dynamics of chemical reactions between laser-cooled Ca^+ ions and Rb atoms in an ion-atom hybrid trap in the ground and excited entrance channels. The state specific reaction rate constants were rationalized in terms of couplings between computed potential energy curves, and highlighted the dominant role light assisted processes can play in hybrid traps. Three reactive processes were found to be competing from the ground state entrance channel, namely non-radiative charge transfer, radiative charge transfer, and radiative association. Signatures of the formation of $CaRb^+$ molecular ions were observed through mass spectrometry, and product branching ratios informed by comparison to MD simulations. The observed branching ratios and ground state rate constant were compared to results of quantum scattering calculations for both radiative and non-radiative mechanisms. An order-of-magnitude agreement between experiment and theory was established, with the aim for further improvements by a unified theoretical treatment of all reactive processes and more accurate experiments for the lowest reaction channel. The collision energy dependence of the rate constants was found to be consistent with predictions of a classical capture model. The observed reactivity was explained in terms of the product of a long range charge induced-dipole interaction influencing the collision rate, and an opacity factor describing the short range non-adiabatic and radiative couplings of potential energy curves leading to chemical change. This framework is expected to be applicable to other cold ion-atom collisions for which an intermediate number of partial waves contribute. As was discussed in section 1.2, a key aspect of these experiments was to address the issue of the universal nature of cold ion-neutral reactions [15, 16, 18, 20]. It has been shown in this system that while the energy dependence of the reaction rate constant is independent of the entrance channel or indeed the type of reactive process and depends only on the long range form of the interaction potential, its magnitude is not capture limited, and depends strongly on the specific interactions of the PECs at short range. This long-range dependence is in line with the predictions of universal behavior from a "quantum Langevin" model as described in ref. [15]. This effect was able to be observed experimentally by relying on the fact that changing the electronic state of the ion does not change the form of the long-range interaction potential (charge induced-dipole), but dramatically changes the types of processes and the interactions between PECs available at short range. The quantum character of the collisions was predicted to manifest itself in the occurrence of narrow shape resonances at well-defined collision energies. The similarities of the calculated shape resonance spectrum for RA and RCT from the ground state entrance channel of the Ca^+ + Rb system, i.e., their

identical energy position and intensity, showed more evidence for the universality of the energy dependence of cold ion-neutral reactions, since these features only depend on the long range form of the interaction potential. Again, inline with refs. [15, 20], whilst the energy dependence is the same, the magnitude of the reaction rate constant depends on the specific processes and interactions between the PECs at short range. The predicted shape resonances, however, had little impact on the velocity averaged rate constants for the studied system and conditions, and so could not be observed. Further work is presently being undertaken to resolve these issues. For collision systems such as B^{5+}+H and N_3^++H which are considerably lighter the Ca^+ + Rb system, the width of the resonances are considerably increased, and occur at higher collision energies, so that a classical treatment of the collision process is inappropriate, and resonances may be more readily observed [157, 158]. The results highlight the complexity and richness of chemical dynamics in even the simplest possible (i.e. atomic) cold ion neutral collisions, and demonstrate the need for close collaboration of theory and experiment to achieve a comprehensive understanding of their chemistry.

Chapter 6

The Ba^+ + Rb system

6.1 Introduction

In light of the previous chapter concerning the Ca^+ + Rb system, it is important to see to what extent the conclusions drawn about the universal nature of cold ion-neutral reactions (that is the extent to which the dynamics are governed by the long-range interaction potential) can be extended to other systems. Changing the ionic reaction partner from Ca^+ to Ba^+ changes the reduced mass of the system, and so effects the scale (but not the form) of the long-range charge induced-dipole interaction potential. It is interesting to see what effect this has on the reaction rate constant, and whether the results support or contradict the predictions of a universal behavior of cold ion-neutral reactions. It is also very instructive to compare behaviors observed in the Ca^+ + Rb system (such as rate constants which are not capture limited but depend strongly on the specific electronic state of the collision partners and can be rationalized through short-range PEC interactions, the flatness of the collision energy dependence of the rate constant due to the universal long-range charge induced-dipole interaction, and the production of molecular ions by RA) to the corresponding behaviors in the Ba^+ + Rb system to gain a deeper understanding of the underlying mechanisms of these effects.

There have been previous studies on cold collisions of Ba^+ + Rb. A theoretical study [159] focused on the calculation of the short range part of the low lying electronic states, where the $BaRb^+$ ground state is found to form a partially covelant bond with partial charge transfer from Ba to Rb^+, which sits in the long ranging charge induced-dipole potential. This suggests that the formation of stable molecular ions in the experiments should be possible. It was postulated that the occurrence of a hump in the short range ground state entrance channel PEC (see also section 6.3.3) due to non-adiabatic interactions with an excited state could play an important role in the processes occurring from this curve. One of the important aspects of the current study is to determine what role this hump plays, especially as compared to Ca^+ + Rb where no such hump is observed in the ground state entrance channel PECs (see section 5.3.4).

A further theoretical paper [23] analyzed the prospects for sympathetic cooling of a Ba^+ ion by ultracold Rb, by computing relativistic potential energy curves for the low lying molecular states, and computing elastic and inelastic cross sections from them. It was found that the elastic processes are a few orders of magnitude more favorable than the inelastic ones, suggesting that the ground state rate constant in this system is not capture limited. An experimental study was carried out to investigate ground state collisions between single Ba^+ ions in an ion trap and Rb atoms held in an optical dipole trap [35]. It was found that the dominant inelastic process was charge transfer with a cross section in the range 10^{-19} to 10^{-18} m^2, which was postulated to be dominantly from radiative processes. There was no observation of molecular ions, although more recent investigations [40] have shown that at the high atomic densities used in these experiments, three body processes can play an important role, and complicate the observation of two body dynamics. The work presented in this chapter is aimed at complementing the study of ref. [35] by providing experimental information on the role of electronically excited states, investigating the collision energy dependence using large Coulomb crystals, and directly comparing experiments with the results of quantum scattering calculations.

In this chapter, the results of a study of light-assisted reactive collisions between laser-cooled Ba^+ ions and ultracold Rb atoms in the ion-atom hybrid trap are presented. The reaction rate was found to depend strongly on the electronic state of both the reaction partners, where the largest rate constant ($7(2) \times 10^{-11}$ cm^3 s^{-1}) was obtained for the excited $Ba^+(6s)$+$Rb(5p)$ entrance channel. Both charge transfer and radiative association were found to be important reactive processes, indicated by the direct observation of Rb^+ and $BaRb^+$ as reaction products. Potential energy curves were calculated by the Dulieu group up to the $Ba^+(6s)$+$Rb(5p)$ asymptote as a means of rationalizing the observed reactivity. Reactive-scattering cross sections for the radiative processes were also calculated and used to rationalize the observation of significant $BaRb^+$ formation. The theoretical rate constant obtained from these calculations for the ground state reaction channel ($Ba^+(6s)$+$Rb(5s)$) is compatible with the experimental estimates obtained in this study, and a study conducted by Schmid et al. [35]

In this study, average collision energies $\langle E_{\text{coll}} \rangle / k_B \geq 600$ mK were achieved by using elongated Coulomb crystals of down to ≈ 150 Ba^+ ions. By varying laser cooling conditions, significant enhancement of the rates in electronically excited channels was observed, which is rationalised with reference to computed potential energy curves and transition dipole moments, calculated by Mirelle Aymar and Maurice Raoult in the group of Olivier Dulieu at Laboratoire Aimé Cotton at University Paris-Sud. Quantum-scattering calculations also performed by the group in Paris, predict that of the reactive collisions occurring in the ground-state channel, radiative association (RA) of molecular ions dominates, supported by the experimental observation of significant $BaRb^+$ ion formation. The dependence of the observed rate constant on average collision energy is studied and compared with theoretical predictions.

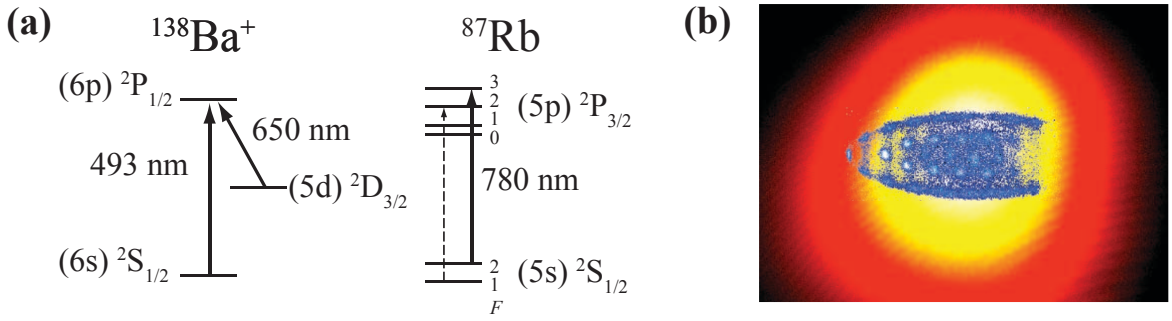

Figure 6.1: (a) Laser cooling schemes for $^{138}Ba^+$ and ^{87}Rb. (b) Superposed false-colour fluorescence images of a Coulomb crystal of $^{138}Ba^+$ ions (blue) and a cloud of ultracold ^{87}Rb atoms (yellow-red) in the hybrid trap. The asymmetric shape of the $^{138}Ba^+$ Coulomb crystal is caused by non-fluorescing sympathetically-cooled Ba^+ isotopes, see text for details.

6.2 Methods

The experimental setup used for the simultaneous trapping of atomic ions and neutral atoms has been described in section 2. Details of other experimental and theoretical techniques can be found in previous sections: Ion-atom overlap sec. 3.1, crystal axialisation sec. 3.3, rate constant detrmination sec. 3.2, steady state population determination sec. 3.5, state specific rate constant determination sec. 3.6, resonance excitation mass spectrometry sec. 3.4, molecular dynamics simulations sec. 1.5, potential energy curves and scattering calculations sec. 3.7, collision energy dependence and variation sec. 3.3, velocity averaged theoretical rate constants sec. 3.8.

For reference, Fig. 6.1 (a) shows the laser cooling schemes for Ba^+ and Rb, and the relevant states involved in these experiments. Fig. 6.1 (b) shows superposed false-colour fluorescence images of a Coulomb crystal of $^{138}Ba^+$ (blue) and a cloud of ultracold Rb atoms (red). The asymmetry of the crystal results from a combination of the presence of heavier isotopes of Ba^+ and single direction cooling, as described in section 3.2.

6.3 Results and discussion

6.3.1 Reaction channels and channel-specific rate constants

Upon overlap of the Ba^+ Coulomb crystal with the cloud of Rb atoms, the formation of a dark core about the central axis of the crystals was observed. This core consisted of sympathetically-cooled product ions (Fig. 3.4(b)(ii-iv)). As outlined in section 3.2, the Ba^+ Coulomb crystals are not isotopically pure with only 72% of each crystal being the laser cooled $^{138}Ba^+$. In principle, all Ba^+ isotopes can participate in the

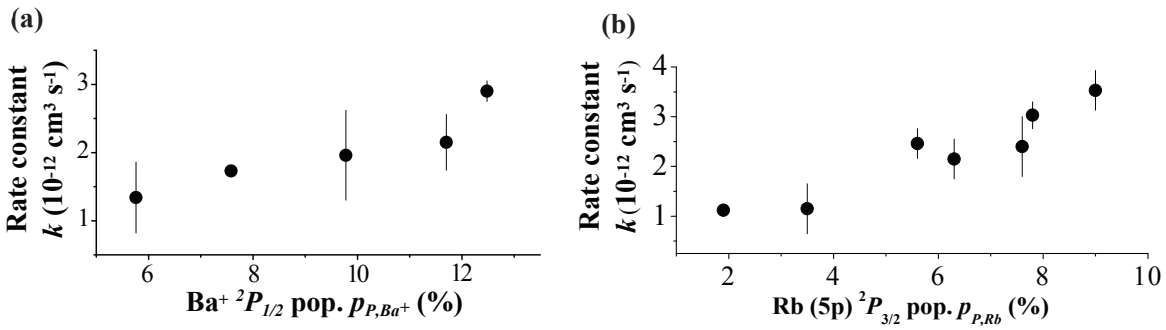

Figure 6.2: Effective rate constant k as a function of (a) the population of the Ba^+ $^2P_{1/2}$ state, and (b) the population in the excited Rb($5p$) $^2P_{3/2}$ state.

reactions. However, the laser-cooled $^{138}Ba^+$ species react faster as a result of the electronic excitation as outlined below.

By inspection of the energy level diagram Fig. 6.1(a), it can be expected that the following channels contribute to the observed reactions: (i) Ba^+(6s)+Rb(5s), (ii) Ba^+(5d)+Rb(5s), (iii) Ba^+(6p)+Rb(5s) and (iv) Ba^+(6s)+Rb(5p). Because of the alternate blocking of the Ba^+ and Rb cooling laser beams (see section 3.6), reactions with simultaneously excited collision partners were precluded. The rate constants for the processes (i)-(iv) are labeled k_s, k_d, k_p, and k_s^*. The experimentally observed rate constant k is a weighted average over the contributions from all possible channels and is formulated as [36]:

$$k = \frac{1}{2}[(p_{S,Ba^+} + p_{S,Rb})k_s + p_{P,Ba^+}k_p + p_{D,Ba^+}k_d + p_{P,Rb}k_s^*], \tag{6.1}$$

where $p_{i,j}$ are the steady state populations of the electronic state i of the reaction partner j (see section 3.6). A strong dependence of k on the populations in the $Ba^+(6p)$ and Rb($5p$) states is observed (see Fig. 6.2 (a) and (b) respectively). To quantify the contributions from the individual reaction channels, k was measured as a function of channel population for a set of 19 different laser intensities and detunings, from which the channel-specific rate constants k_i were determined in a multi-dimensional least-squares fit of the data to Eq. (6.1) (see section 3.6 for details on the fitting procedure). Some k_i were found to be consistent with zero in the fit, in which case their value was associated with an upper bound given by their 1σ uncertainty in the fitting procedure. The fit yielded $k_s \leq 5 \times 10^{-13}$ cm^3 s^{-1}, $k_p = 2(1) \times 10^{-11}$ cm^3 s^{-1}, $k_d \leq 1 \times 10^{-12}$ cm^3 s^{-1}, $k_s^* = 7(2) \times 10^{-11}$ cm^3 s^{-1}. The numbers in parentheses denote the 1σ statistical uncertainty of the fitted values. Note that the rate constants are subject to an additional systematic error of $\approx 50\%$ resulting from the uncertainty in the determination of the Rb number density in the MOT. These rate constants indicate that reactions from the Ba^+(6p)+Rb(5s) and Ba^+(6s)+Rb(5p) entrance channels are over $20\times$ faster than from the Ba^+(6s)+Rb(5s) and Ba^+(5d)+Rb(5s) entrance channels.

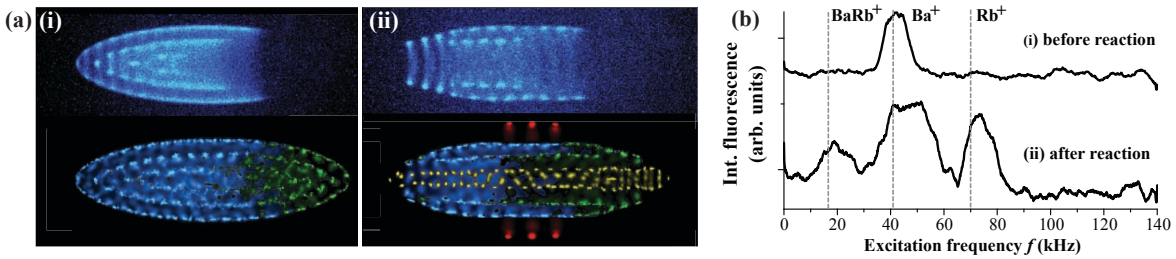

Figure 6.3: (a) Experimental false-colour fluorescence images of Ba^+ Coulomb crystals (upper panels) and their molecular-dynamics (MD) simulations (lower panels) (i) before and (ii) after reaction with ultracold Rb atoms. Sympathetically-cooled ions have been made visible in the MD simulations for clarity. Colour code: blue: $^{138}Ba^+$, green: lighter Ba^+ isotopes, yellow: ^{87}Rb, red: $BaRb^+$ molecular ions. (b) Resonance-excitation mass spectra of crystals (i) before and (ii) after reaction. See text for details.

6.3.2 Reaction products

Fig. 6.3 (a) shows fluorescence images of a Coulomb crystal (i) before and (ii) after reaction together with their respective MD simulations. In order to enable an accurate determination of the composition from the MD simulations, a uni-directional laser-cooling configuration of the Ba^+ ions was used in the experiments. In this case, a nearly single ion resolution in the experimental images was achieved.

In order to prove the identity of the ionic products of the reaction, resonance excitation mass spectrometry was used, as described in detail in section 3.4. Fig. 6.3(b) shows two resonance-excitation mass spectra of crystals recorded (i) before and (ii) after reaction. In the spectrum before reaction, only one feature was observed, corresponding to the Ba^+ reactant ions. After reaction with ultracold Rb atoms, a total of three peaks were observed, corresponding to the remainder of the Ba^+ reactant ions, and the Rb^+, and $BaRb^+$ product ions. The dashed lines in Fig. 6.3 (b) indicate the theoretical single-ion radial excitation frequencies of the different ion species.

In the MD simulations of Fig. 6.3(a), the non fluorescing Ba^+ isotopes as well as the product ions have been made visible to indicate their abundance. The best reproduction of the experimental fluorescence image in (ii) was obtained by using a composition of 170 $^{138}Ba^+$ (blue), 116 lighter isotopes of Ba^+ in their relative natural abundances (green), 90 $^{87}Rb^+$ (yellow), and 40 $BaRb^+$ (red). From the relative product ion yields, the $BaRb^+$: Rb^+ branching ratio (representing an average over all reaction channels) was estimated to be $\approx 1 : 2.25$.

In the previous chapter concerning Ca^++Rb collisions (see also [36,42]), the formation of Rb_2^+ ions was observed. Their presence in the Coulomb crystals after reaction with Rb was conjectured to be from consecutive reactions of $CaRb^+$ with Rb. Another mechanism leading to their generation could be radiative association of the Rb^+ product ions with Rb atoms from the MOT. In the present Ba^+ + Rb system, how-

ever, no clear feature corresponding to Rb_2^+ (which would be located in between the broad $BaRb^+$ and Ba^+ resonances in Fig. 6.3 (b) (ii)) was observed in the mass spectra. It is therefore concluded that the formation of Rb_2^+ was only a minor process in these experiments and was therefore neglected in the modeling of the Coulomb-crystal composition after reaction.

6.3.3 Potential energy curves and reaction mechanisms

In order to rationalize the observed behavior in this system, it is extremely useful to consult computed potential energy curves and results from quantum-scattering calculations which were performed by the Dulieu group. Fig. 6.4 shows computed non-relativistic potential energy curves for the lowest electronic states of $BaRb^+$ up to the $Ba^+(6s)$+$Rb(5p)$ asymptote. The PECs for the lowest electronic states show a qualitative agreement with those reported in Refs. [23, 159]. A key feature in these curves is the double-minimum structure for the $A\ ^1\Sigma^+$ PEC which arises as a result of an avoided crossing with the $C\ ^1\Sigma^+$ state. This feature was also found in the calculations of Refs. [23, 159]. A difference as compared to the results of Knecht et al. [159] is that according to their results, the top of the barrier is located slightly above the dissociation limit of this state both in the non-relativistic and relativistic calculations, whereas for the curves presented here, the barrier height is slightly smaller than the dissociation energy. Krych et al. [23] have, however, demonstrated that the height of this barrier dramatically depends on the configuration space size used for the calculations. This feature is particularly important as slight changes can have a dramatic effect on the rate of RA in the ground state entrance channel.

The entrance channels accessible under the current experimental conditions are indicated in bold in Fig. 6.4. The lowest channel $Ba^+(6s)$+$Rb(5s)$ correlates with the $A\ ^1\Sigma^+$ and $a\ ^3\Sigma^+$ first excited electronic states of the $BaRb^+$ molecule. Dipole-allowed radiative transitions from the $A\ ^1\Sigma^+$ to the $X\ ^1\Sigma^+$ ground electronic state can occur, leading to RCT forming Rb^+ ions and Ba atoms in the case of transition to the dissociation continuum, or RA of $BaRb^+$ molecular ions in the case of transition to a bound state within the potential well of the $X\ ^1\Sigma^+$ state.

In contrast to the Ca^+ + Rb system of the preceding chapter, there are no accessible pathways for non-radiative charge transfer from the ground state entrance channel. There are expected to be non-adiabatic transitions induced by the spin-orbit interaction around the curve crossings with the b, B and c states visible in Fig. 6.4, however the $Ba(6s5d)$+Rb^+ charge transfer asymptotes lie far higher in energy than the entrance channel, (recall 1 K corresponds to ≈ 0.7 cm^{-1}), and so are energetically inaccessible. A consequence is that all observed reactivity in the ground state entrance channel is predicted to be purely radiative, as compared to the Ca^+ + Rb system where NRCT was found to dominate [36, 42, 47].

The low reaction rate constant $k_d \leq 1\times10^{-12}$ cm^3 s^{-1} observed for the $Ba^+(5d)$+$Rb(5s)$ entrance channel can qualitatively be explained by the repulsive character of the relevant PECs. It should be noted that NRCT is energetically possible in this channel

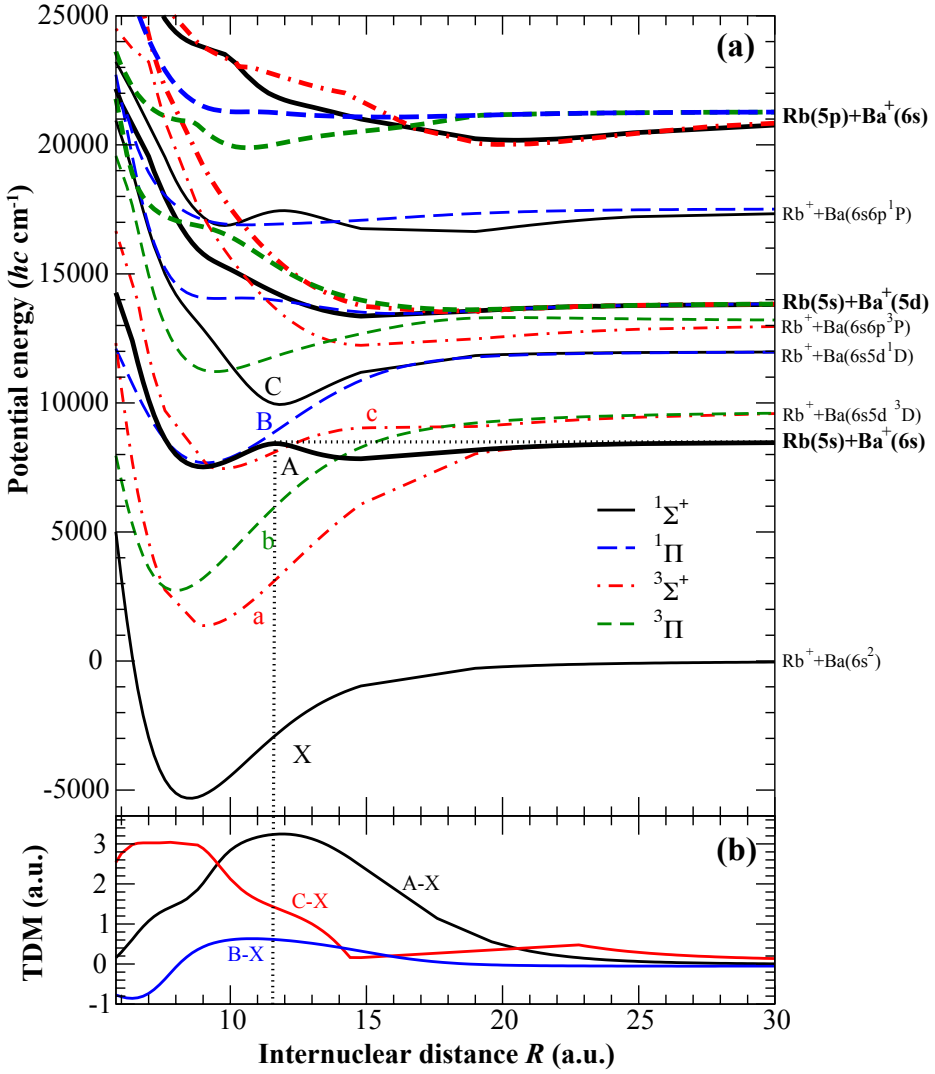

Figure 6.4: (Produced by M. Aymar and O. Dulieu) (a) Computed non-relativistic potential energy curves (PECs) of the $BaRb^+$ molecule. The lowest states have been labeled using standard spectroscopic notation. Collision channels relevant for the experiments have been indicated in bold. States with Δ symmetry are not shown. (b) Computed transition dipole moments (TDMs) between the ground (X) and the two lowest $^1\Sigma^+$ states (A and C) as well as the lowest $^1\Pi$ state (B). The horizontal dotted line represents the energy of the initial collisional state in the lowest channel, while the vertical dotted line locates the position of the top of the barrier in the A state.

due to an avoided crossing with a charge transfer state at ≈ 18 a.u. of $^3\Pi$ symmetries. So far, no calculations have been made to estimate the efficiency of this pathway, but the experiments suggest that this pathway is relatively inefficient.

The $Ba^+(6s)$+$Rb(5p)$ entrance channel has the largest experimental rate constant among the channels observed ($k_s^* = 7(2) \times 10^{-11}$ cm^3 s^{-1}). The fast rate in this channel is likely caused by radiative processes connecting to any of the many lower-lying electronic states. Quantum-scattering calculations were prohibitively complex for this channel, so no quantitative comparison to theory can be made. The fast rate observed in this channel can be rationalised qualitatively, however, by noticing that the radiative transition strength scales with the cube of the emitted photon energy, and hence ignoring FCFs and TDMs, transitions to lower lying molecular states have an enhanced likelihood. Also, crucially, as discussed in sections 1.2.3 and 7, the collision rate in this channel is expected to be about 4-5 times larger than in all other entrance channels because of the strongly attractive interaction of the charge of Ba^+ with the permanent quadrupole moment and the increased dipole polarisability of Rb in the $^2P_{3/2}$ state [39]. It is therefore likely that this entrance channel should exhibit an enhanced rate constant, which is in line with the experimental observations.

It is noted that the mechanism for the suppression of reaction channels involving excited neutral atoms as presented in Ref. [37] does not seem to play an important role in the present study. In the present system, the Condon point for excitation to the $Ba^+(6s)$+$Rb(5p)$ curve is at $R \approx 1000$ a$_0$, whereas at collision energies typical of these experiments ($E_{\rm coll}/k_{\rm B} \approx 1$ K), the collision system can travel over 9000 a$_0$ within the 26 ns natural lifetime of the $Rb(5p)$ state, and hence collisions in the excited channel can readily occur.

A large rate constant ($k_p = 2(1) \times 10^{-11}$ cm^3 s^{-1}) was also obtained for the reaction channel with the highest electronic excitation of the ion accessible by the present laser-cooling scheme, ($Ba^+(6p)$+$Rb(5s)$). It is noted that the corresponding channel in the Ca^+ + Rb system showed the highest rate constant studied in that system. The PECs of this asymptote, however, could not be reliably extracted from the present set of calculations because their pattern was found to be too complex to follow them adiabatically from large to small internuclear distances. The picture for the $BaRb^+$ system is likely to be similar to that of $CaRb^+$, however, which exhibits a high density of electronic states correlating asymptotically with excited electronic states of neutral Ca. The high density of states provides opportunities for NRCT mediated by a multitude of curve crossings. Also, RA and RCT are expected to be important from this entrance channel due to the ω^3 dependence of the rate of photon emission. It is noted that similar effects have also recently been used to explain the dynamics in electronically excited channels in the $BaCa^+$ system [37]. Indeed, the high density of electronic states occurring at higher excitation energies should be a common feature of mixed alkaline-earth-ion alkali-atom systems [160] and it appears that the fast kinetics which has been observed in electronically excited channels across several systems [36, 37, 45] is a direct consequence of the associated enhanced radiative and non-adiabatic dynamics.

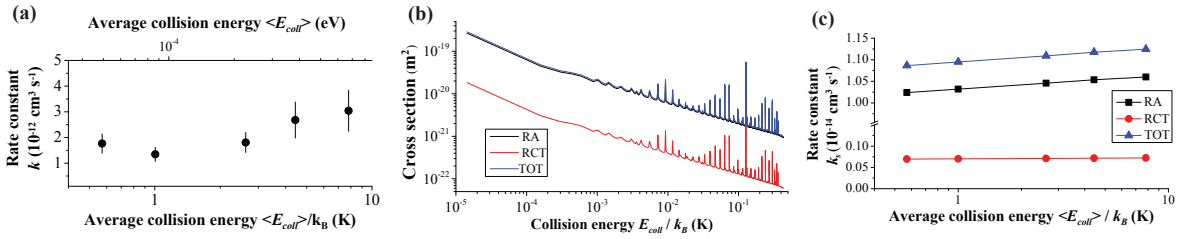

Figure 6.5: (a) Dependence of the observed rate constant k on the average collision energy $\langle E_{\rm coll}\rangle$. Error bars denote the 2σ statistical uncertainty of at least three consecutive measurements. (b) (Produced by M. Raoult and O. Dulieu) Theoretical cross sections for radiative association (RA) and radiative charge transfer (RCT) for the lowest entrance channel $Ba^+(6s)$+Rb$(5s)$. (c) Velocity averaged theoretical rate constant k_s for the lowest channel $Ba^+(6s)$+Rb$(5s)$ obtained by integrating the total radiative cross section over the relative velocity distributions. See text for details.

6.3.4 Radiative cross sections and collision-energy dependence

Fig. 6.5 (a) shows the experimentally observed rate constants k plotted against average collision energy, achieved by varying the size and shape of the Coulomb crystals as described in section 3.3. The rate constant was found to be nearly invariant with average collision energy within the uncertainty limits, with a slight increase observable at the highest energies. Note that a similarly flat dependence of k on $E_{\rm coll}$ was also observed in the Ca^+ + Rb system [36, 42] (see previous chapter).

Fig. 6.5 (b) shows the theoretical cross sections σ for RA (black) and RCT (red) in the $Ba^+(6s)$+Rb$(5s)$ entrance channel, as well as their sum (TOT) in blue. The cross sections for RA from the $A\ ^1\Sigma^+$ to the $X\ ^1\Sigma^+$ state are calculated to be an order of magnitude larger than for RCT. This is due to the more favorable Franck-Condon factors for transitions to bound vibrational levels of the X state arising from the double-well structure of the $A\ ^1\Sigma^+$ PEC. Note that in Ca^++Rb, the non-relativistic $^1\Sigma^+$ PECs associated with the lowest entrance channel exhibit no such feature [42] (see previous chapter). As discussed in section 1.2.4, a series of shape resonances can be observed in the calculations, arising from the dynamical trapping of the incoming wave function behind centrifugal barriers associated with successively larger collisional angular momentum. As discussed in section 1.2.4, however, these resonances cannot be observed in the present experiments due to the order of magnitude wider ion velocity distributions. It is noted that the calculated values for the total radiative cross section in the energy interval between 1 and 100 mK ($\sigma \approx 10^{-19} - 10^{-20}$ m^{-2}) are slightly lower than the experimental estimate from Ref. [35] ($\sigma \approx 10^{-18} - 10^{-19}$ m^{-2}).

In Fig. 6.5 (c), theoretical rate constants k_s for the lowest entrance channel $Ba^+(6s)$+Rb$(5s)$ are shown which were obtained by integrating the total radiative (i.e., RA+RCT) cross sections over the velocity distributions of the Coulomb crystals as described in section 3.8. Because of convergence problems arising from the double-

minimum structure of the A state PEC, the radiative cross sections for high-angular-momentum collisions arising at energies $E_{\mathrm{coll}}/k_{\mathrm{B}} > 400$ mK were not calculated. The findings of the previous chapter, however, showed that the radiative cross sections show a smooth and monotonous energy dependence across a large energy range [42]. In this instance, in order to obtain a theoretical estimate of the rate constants, the base line of the total cross section curve (black in Fig. 6.5 (d)) was extrapolated over the entire energy range relevant for the present study ($E_{\mathrm{coll}} \leq 40$ K) (see also section 3.8). Also shown in the previous chapter was that the narrow shape resonances only insignificantly contribute to the integrated cross section and were therefore neglected. As can be seen in Fig. 6.5 (c), the predicted rate constant k_s slightly increases with energy over the interval studied. The theoretical values are compatible with the experimental upper bound $k_s \leq 5 \times 10^{-13}$ cm^3 s^{-1}. The resemblance of the energy dependence for the experimental rate constant (Fig 6.5 (a)) and the calculated ground state rate constant (Fig. 6.5 (c)) implies that the energy dependence of the processes occurring across all entrance channels must be similar, which indeed, as has been discussed in the previous chapter, is expected.

6.4 Summary and conclusions

Cold reactive collisions between laser-cooled Ba^+ ions and Rb atoms show features similar to other mixed ion-atom systems detailed in this thesis (Ca^++Rb [36, 42]), as well as in other studies (Yb^++Ca [44], Ba^++Ca [37] and Yb^++Rb [45]). These features include a dependence of the reaction rate on the electronic state of the reaction partners, the significant role of radiative processes, and the formation of molecular ions by RA. In the present system, molecular ions were observed by their sympathetic cooling into the Coulomb crystals, and so their abundance could be determined, and a channel averaged branching ratio could be calculated.

The entrance channel reactivity has been found to depend on both the very system specific nature of the PECs (demonstrated for example by the sensitive dependence of the ground state reactivity in Ba^++Rb on the double well structure), and also more general phenomena (like the high density of charge transfer states in the vicinity of the entrance channels with highest electronic excitation), which seem to play a more universal role. Its clear that a wealth of detail is still to be obtained in such systems, not least the observation of the predicted shape resonances in the ground state channel, and further experimental and theoretical studies are in progress to characterize these phenomena in more detail.

As discussed in sections 1.2 and 5 the universal nature of cold ion-neutral reactions, that is the extent to which the collision energy dependence and resonance spectrum of the rate constant only depend on the long-range form of the interaction potential, is a key topic in these experiments. By changing from Ca^+ + Rb to Ba^+ + Rb, the reduced mass of the system was changed, and so the scale (but not the form) of the long-range potential was changed. In line with universal behavior predictions [15, 18], the energy

dependence of the reaction rate constant has been indicated to be independent of the electronic state of the ion, but the magnitude strongly dependent on the electronic state. This is expected within the universal behavior predictions since the electronic state of the ion does not change the long-range charge induced-dipole potential, but does dramatically change the specific PEC interactions at short-range. The observed collision energy dependence also has the same flat form as the $Ca^+ + Rb$ system (see previous chapter) due to both systems having the same dominant charge induced-dipole long-range interaction potential. This observation provides experimental evidence for the predicted universal behavior of cold ion-neutral reactions.

Since no reactions in either atomic-ion neutral system of this work are capture limited, it is not possible to tell whether the differing magnitude of the rate constants between the systems are due to the reduced mass change in the long-range potential, or due to the change in the short-range interaction of the PECs. Since the reduction in the Langevin collision rate due to the the increased reduced mass of the $Ba^+ + Rb$ system compared to $Ca^+ + Rb$ is only a factor of 1.4, it can be expected that the large observed differences between the two system's state specific rate constants are due to short-range effects.

Similar to the $Ca^+ + Rb$ system, the computed shape resonances for RA and RCT from the ground state entrance channel in $Ba^+ + Rb$ occur at the same energy and have the same intensity, further reinforcing that the spectrum is only dependent on the long-range potential. The effect of the specifics of the short-range potential is demonstrated for example by the fact that RA from the ground state entrance channel is expected to be more efficient in the $Ba^+ + Rb$ system than $Ca^+ + Rb$ system as compared to RCT by a factor of ≈ 5 (which is in line with the experimental observation of a relatively large amount of product $BaRb^+$ in the crystals), but the combined rate of radiative processes for both systems is predicted to be similar ($\approx 1 \times 10^{-14}$ cm^3 s^{-1}).

An important difference between the $Ca^+ + Rb$ and $Ba^+ + Rb$ systems was the response of the rate constant to electronic excitation of the Rb. In both cases the form of the long-range potential in this channel included the additional charge permanent-quadrupole interaction, which acts to increase the collision rate (see section 1.2). While this may have manifested itself in the large observed reaction rate from the Ba^+ (6s) + Rb (5p) entrance channel, it was not manifested in the $Ca^+ + Rb$ system due to the isolation of the corresponding potential energy curves. Hence, whilst the *collision* rates from the entrance channels involving Rb (5p) in these systems may have been similar, the *reaction* rates were substantially different. This highlights the dominant role the interactions of the PECs at short-range can have on the magnitude of the reaction rate constants.

Further to the above comparison of the $Ca^+ + Rb$ and $Ba^+ + Rb$ systems, it is useful to compare experimental results of other cold atomic-ion atomic-neutral systems in detail. In the $Yb^+ + Yb$ system [33], it was found that the rate constant for charge transfer agreed well with half that of the collision rate calculated by Langevin theory over two decades of collision energy. This was rationalized by the probability of

resonant charge exchange during a collision between otherwise identical species being 1/2. It was also postulated that the effect of the P state polarizability of the neutral Yb could contribute to the observed rate constant, but its contribution could not be determined accurately due to the experimental uncertainty of the reaction rate constants. Similar to the atomic-ion atom systems of this work, the collision energy dependence of the reaction rate constant was approximately flat, providing further evidence for the universal description of cold ion-neutral reactions.

In purely ground state collisions of the Yb^+ + Rb system [34] a flat energy dependence of the reaction rate constant was observed, indicating universal behavior. The rate constants were, however, five orders of magnitude lower than the Langevin value, suggesting a low reaction efficiency at short-range. This is similar to the ground state reactions in this work where the ground state rate constants are at least three orders of magnitude slower than the calculated collision rate. Both radiative and non-radiative charge transfer were postulated to play a role in the ground state Yb^+ +Yb system indicated by the observation of Rb^+ product ions, but no observation of molecular ions from RA was reported from these experiments. This can be compared to the systems of this work since the large majority of reaction products in each case were from charge transfer processes. The products of RA could be observed, however, in the experiments of this work due to a large trap depth ($\approx$ 3 eV) and a high sympathetic cooling power of the large ensemble of laser cooled ions. The effect of electronic excitation was also studied in the Yb^+ + Rb system [45], where it was found that ion loss events from the excited Yb^+ $^2D_{3/2}$ + Rb (5s) are significantly enhanced as compared to the ground state entrance channel, and a reaction efficiency from this excited entrance channel of unity was implied. This can be compared to the results of the systems of this work in that electronic excitation of the ion can lead to enhanced rate constants, due to the increased efficiency of processes connecting different PECs.

In the Yb^+ + Ca system [44] it was also found that the rate constant was approximately independent of collision energy, and was rationalized in terms of purely radiative processes occurring from the ground state entrance channel. This reinforces the independence of the form of the collision energy to the type of reactive process, and is similar to the observations made in this work, where in the ground state entrance channel of Ba^+ + Rb, only radiative processes are possible. Signatures for the formation of molecular ions were also found in the Yb^+ + Ca system, similar to the observation of molecular ions in both the atomic-ion atom systems of this work.

In the Ba^+ + Ca system [37], the role of electronic excitation of both of the reaction partners was investigated. In this system, ground state reactions are energetically forbidden. It was found that the most significant excited reaction pathway was from the Ba^+ $^2P_{1/2}$ + Ca ^1S entrance channel. This is similar to the results of this work since the corresponding entrance channel in Ca^+ + Rb (i.e., electronic excitation of the Ca^+ P state) also produced the highest state specific rate constant observed in that system, and the second highest in the corresponding entrance channel of the Ba^+ + Rb system. These observations were rationalized by an increased density of charge transfer states at these high excitation energies, which is likely to be extendable to explain the result

in the Ba^+ + Ca system. It was also found in the Ba^+ + Ca system [37] that electronic excitation of the Rb had no significant effect, which is similar to the result of the Ca^+ + Rb system, but dissimilar to the Ba^+ + Rb system of this work. This highlights the dominant effect the system and state specific interaction of PECs at short-range can have on these cold ion-neutral reaction systems.

Chapter 7

The N_2^+ + Rb system

7.1 Introduction

Molecular-ion neutral and ion molecule reactions have been previously studied at temperatures between 1 and 200 K using for example guided ion beams, drift tubes, and free jet expansions (see e.g. review [161]) where reactive processes such as charge transfer and ternary molecular association have been observed. At the lowest temperatures ($\approx$ 1 K), measurements of the reaction rate constant for the charge transfer reaction of $Ar^+ + O_2$ [161] for example were found to converge to a value consistent with Langevin theory. The development of laser-cooling and trapping technologies for ions, coupled with velocity selection of neutrals led to the study of the $Ca^+ + CH_3F$ reaction at collision energies down to $\approx k_B \cdot 2$ K with single particle sensitivity [43]. In these experiments, a slight inverse dependence of the rate constant on the collision energy was observed in line with ion-molecule adiabatic capture theories [162]. The molecular-anion molecule reaction $NH_2^- + H_2 \rightarrow NH_3 + H^-$ was studied down to temperatures of 8 K in a 22-pole ion trap using buffer gas cooling with He [163]. A stark increase of the probability of proton transfer was observed with decreasing temperature, in line with a longer intermediate complex lifetime at lower temperatures. At the lowest temperatures, a maximum in the rate constant was observed and was attributed to a small long range barrier or resonance feature. More recently, reactions of trapped OH^- anions with ultracold Rb atoms in a MOT were studied, which, however, due to the high temperature of the anions were restricted to high (200 K) relative temperatures [164]. With the hybrid trapping technology outlined in the present work, it is possible to extend the range of collision energies for molecular-ion neutral reactions down to $\approx k_B \cdot$ 20 mK, two orders of magnitude lower than realized in previous studies. Particularly in the light of the results of the previous two chapters for atomic-ion atom systems, and of the results outlined above, it is interesting to see how the universal nature of cold ion-neutral reactions, that is the extent to which the dynamics can be described by the long-range form of the potential, extends to systems involving molecular ions at unprecedentedly low collision energies. This study aims at addressing these questions

and to compare the results of the molecular-ion neutral system to those of the atomic-ion neutral systems studied so far to see whether the the general picture of universal behavior found previously is strengthened or weakened as a result.

At the time of writing, studies of ion-neutral reactive processes in hybrid traps have been constrained to systems of atomic ions and neutral atoms [33–36, 38, 44, 45]. Even in these chemically simplistic systems, a diverse wealth of phenomena has been observed. These effects have ranged from the important role of light-assisted processes in radiative association of molecular ions and the enhancement of the rate of charge exchange in Ca^+ + Rb [36] (as seen in chapter 5) and Ba^+ + Rb [41] (as seen in chapter 6), the observation of fast reaction rates in Yb^+ + Ca [44], and the dominant role of the hyperfine state of the ion on reactivity in Yb^++Rb [45]. It is natural however to extend these studies to molecular ions in order to fully explore the diversity of reactive effects important at low energies, and also for the extension of knowledge towards more chemically relevant systems, for example of astro-chemical significance.

This chapter details a study of cold reactive collisions between sympathetically-cooled N_2^+ molecular ions and laser-cooled Rb atoms in the ion-atom hybrid trap. Chemical reactions were studied at average collision energies $\langle E_{\text{coll}} \rangle / k_{\text{B}} \geq 23$ mK, which, as outlined above, is two orders of magnitude lower than has been achieved in previous experiments with molecular ions [43, 161, 163]. The experiments revealed that the reaction rate is independent of the collision energy in the region studied, but strongly dependent on the electronic state of Rb. Collisions between ground state N_2^+ and Rb in its electronically excited $(5p)\ ^2P_{3/2}$ state resulted in efficient charge transfer four times faster than the Langevin rate (i.e. the charge induced-dipole collision rate). This observation was rationalized using a classical capture model which includes the effects of the strong charge permanent-quadrupole interaction at long range, as well as a near resonance between the entrance and exit channels of the reaction at short range. Reactive collisions in the ground state of this system were found to be at least two orders of magnitude slower. This opposing behavior is rationalized by a slower collision rate due to the absence of a charge permanent-quadrupole interaction and a smaller static atomic polarizability of the Rb atom in this channel at long range, coupled with an inefficient charge transfer mechanism at short range. The results provide a test of classical capture models for reactions of molecular ions at the lowest energies reached to date, and provide evidence for distinctly molecular effects in the high efficiency of charge transfer in the excited channel.

7.2 Methods

The methods used for loading, sympathetically cooling, and characterizing the number and velocity distributions of the N_2^+ ions in a Coulomb crystal of Ca^+ ions, as well as the determination of the pseudo-first-order and second-order reaction rate constants with Rb have been outlined in sections 3.2.1 and 3.2 respectively.

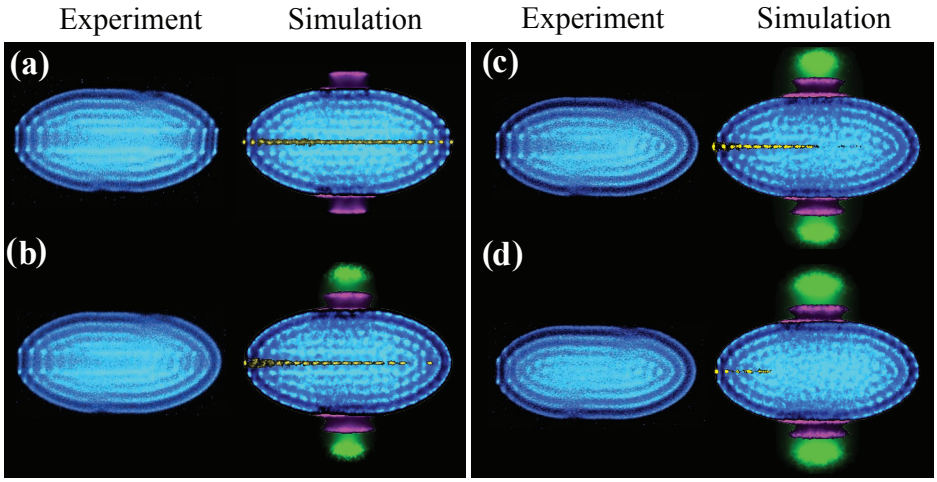

Figure 7.1: Experimental false-color laser-cooling fluorescence images of Coulomb crystals recorded over the course of reaction with ultracold Rb atoms. Sympathetically-cooled ions are made visible in molecular dynamics simulations. Color code: blue: laser-cooled Ca^+ ions; yellow: N_2^+ reactant ions; green: Rb^+ product ions; magenta: CaH^+, $CaOH^+$. See text for details.

After loading a Coulomb crystal of ≈ 1000 Ca^+ ions, a string of ≈ 25 N_2^+ ions were sympathetically cooled into the crystal. The N_2^+ ions were produced by [2+1] REMPI of N_2, and thermalised with background N_2 gas for 30 seconds to ensure a room-temperature rotational state-distribution. The Coulomb crystal was then translated along the axis of the linear RF trap for overlap with the cloud of ultracold atoms by applying a static electric potential of 2 V to four axially similar endcap electrodes. Clouds of ultracold Rb atoms at typical average densities $n_{\rm av} = 4 \times 10^8$ cm^{-3} were generated by laser-cooling in the MOT, which was overlapped with the ion trap as demonstrated in section 3.1. Both the sympathetically cooled N_2^+ and the laser cooled Ca^+ ions react with Rb. However, the channel averaged rate constant for Ca^++Rb for typical optimal laser cooling parameters was $\approx 2 \times 10^{-11}$ cm^3 s^{-1} (see chapter 5), whereas that for N_2^+ + Rb was $\approx 2 \times 10^{-9}$ cm^3 s^{-1} as demonstrated below. In this case the change of the Coulomb crystal due to loss of Ca^+ could be neglected on the time scale of the typical N_2^+ + Rb reaction experiment (≈ 5 s), and the measurement of the reactivity of the two systems separated.

7.3 Results and discussion

7.3.1 Reaction products

Fig. 7.1 (a)-(d) shows a sequence of false-color laser-cooling Coulomb crystal images with their corresponding MD simulations recorded over the course of a typical reaction.

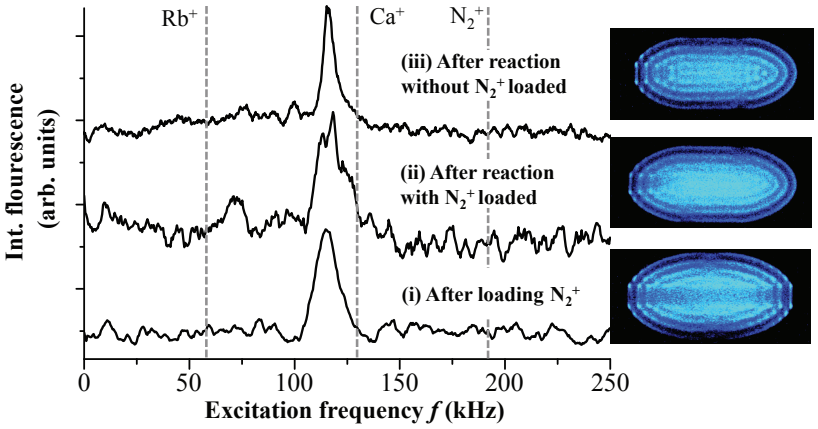

Figure 7.2: Resonant-excitation mass spectra of Coulomb crystals (insets) loaded with sympathetically-cooled N_2^+ ions (i) before reaction with ultracold Rb atoms and (ii) after reaction of the N_2^+ ions with Rb. The dashed vertical lines indicate the single-ion resonance frequencies of the relevant ion species. The weak feature around 70 kHz in (ii) is identified with the Rb^+ product ions generated by charge exchange of N_2^+ with Rb. (iii) Spectrum of a crystal prepared without N_2^+ ions recorded after the same time of reaction with Rb as in (ii) illustrating the effect of the background reaction $Ca^+ + Rb \rightarrow Ca + Rb^+$. See text for explanation.

A color filter blocked the laser-cooling fluorescence of the Rb atoms, so that only the Ca^+ fluorescence (blue) is visible in the images. The N_2^+ ions were observed as a dark non-fluorescing core in the center of the crystals, but have been made visible in yellow in the simulations. Fig. 7.1 (a) shows the Coulomb crystal of Ca^+ and N_2^+ before insertion into the Rb cloud. Once overlapped with the Rb cloud, the N_2^+ ions were removed from the crystal by charge-exchange collisions resulting in a reduction of the crystal's dark core (Figs. 7.1 (b)-(d)). The Rb^+ product ions (green in the simulations) remained trapped and were sympathetically cooled by the Ca^+ ions. The magenta-colored ions in the simulated images represent CaH^+ and $CaOH^+$ which are impurities formed by reactions of excited state Ca^+ with background H_2 [90] and H_2O [89] gas, present during the loading and thermalisation of N_2^+ ions, where the background gas pressure was held at 2×10^{-8} mbar for ≈ 60 s. For simplicity of the MD simulations, these ions are assumed not to undergo further reactions in the presence of the Rb cloud. The total number of ions in each simulation is conserved, and the Rb^+ present from reactions of Rb with Ca^+ was calculated based on the observed channel averaged rate constant from previous studies (as in chapter 5). Typical contributions to the number of Rb^+ at the end of a reaction were ≈ 35 from $Ca^+ + Rb$, and ≈ 25 from $N_2^+ + Rb$, which could be discriminated by REMS (see below).

Evidence for the chemical identity of the reaction products was provided by resonant-excitation mass spectra of the Coulomb crystals [108] (see section 3.4). Fig. 7.2 shows

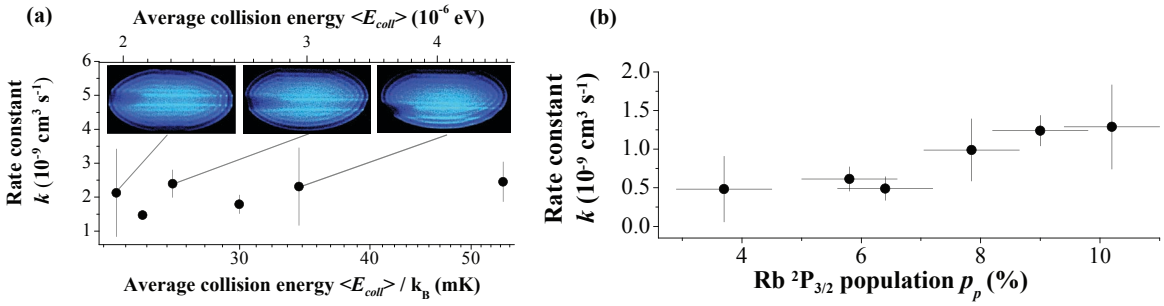

Figure 7.3: (a) Rate constants for N_2^+ + Rb as a function of the collision energy. Each data point represents an average over three independent measurements, the error bars indicate the statistical uncertainty (2σ). The insets show the images of the Coulomb crystals corresponding to the three data points indicated. (b) Rate constant as a function of the population in the Rb $(5p)$ $^2P_{3/2}$ state.

mass spectra of Coulomb crystals (i) before and (ii) after reaction. Additionally, a pure Ca^+ crystal (iii) was reacted for the same duration as in (ii) to illustrate the effect of the background reaction Ca^+ + Rb. The insets are images of the corresponding crystals and the vertical lines indicate the theoretical single-ion resonance frequencies of the indicated species.

The spectrum recorded before reaction only shows a single resonance corresponding to the excitation of the Ca^+ ions. There is no peak corresponding to N_2^+ ions which are indeed present in the crystal during this scan. The absence of the peak was due firstly to the low number of N_2^+ ions in the trap, and secondly, and most importantly, to the increased stiffness of the radial trapping potential for the lighter N_2^+ ions prohibiting any significant back action of the excited motion of the N_2^+ onto the Ca^+ ions at the excitation voltages used in this experiment. Larger excitation voltages would have resulted in the broadening of the peak to such an extent that it would have overlapped with the peak corresponding to Ca^+, and also would have melted the crystal at the position of the Ca^+ resonance, so could not be used. Resonances for the $CaOH^+$, CaH^+ ions could not be clearly observed due to their low numbers. The spectrum after reaction in (ii) shows an additional weak feature around 70 kHz assigned to the sympathetically-cooled Rb^+ product ions. Note that the positions of the resonances are slightly shifted from the single-ion frequencies because of coupling effects in multi-component coulomb crystals [108]. The spectrum in (iii) shows that the number of Rb^+ ions after reaction without N_2^+ loaded was too small to give rise to a clear feature in the spectrum under the conditions used (which were the same for all spectra in Fig. 7.2). This demonstrates the sensitivity of the REMS technique to discriminate between differing ion numbers, since the expected Rb^+ numbers in (ii) as explained above is 60 (where a peak is observed), but in (iii) is 35 (where no peak is observed).

7.3.2 Collision-energy dependence of reaction rate constant

Fig. 7.3 (a) shows the dependence of the rate constant on average collision energy. In the experiments, the Rb kinetic energies ($\langle E_{\text{kin}}\rangle/k_{\text{B}} \approx 200\ \mu$K) were much smaller than the ion energies ($\gtrsim 20$ mK) so that the collision energies were entirely dominated by the contribution of the ions. Strings of N_2^+ ions were used such that all ions in the string possessed approximately the same velocity distribution, increasing the resolution of the experiments as compared to using multiple ion shells. As described in section 3.3, the ion kinetic-energy distributions and hence average collision energies were obtained using ion trajectory outputs from MD simulations of experimental images. The secular energies were determined to be $\langle E_{\text{sec}}\rangle/k_{\text{B}} \approx 12$ mK for Ca^+ and 14 mK for N_2^+. The lowest collision energies were limited by the precision with which the N_2^+ ions could be localized on the axis. The axialization procedures as described in section 3.3 allowed for a micromotion energy limit corresponding to $k_B \cdot 17$ mK. As discussed in section 3.3, the average collision energies were varied by displacing the N_2^+ ions radially from the axis using static electric fields (see insets of Fig. 7.3 (a)), such that they acquire an increased micromotion energy which scales with the square of the displacement from the rf axis. The displaced crystals exhibit an asymmetric ion distribution because of the mass dependence of the trapping potential (see section 1.4). Fig. 7.3 (a), shows that within the uncertainty limits the rate constant is independent of the collision energy in the interval studied.

7.3.3 Channel-specific rate constants and reaction mechanisms

The ultracold atoms are electronically excited during laser cooling, and so a fraction of the reactions occur with Rb atoms in the $(5p)\ ^2P_{3/2}$ state. The population in the excited state was modulated by varying the intensity of the Rb cooling laser (see section 1.3.5). The rate constant shows a near linear increase with the $(5p)\ ^2P_{3/2}$ population (Fig. 7.3 (b)). The y error bars indicate 2σ statistical uncertainty from atleast three consecutive measurements. The x error bars represent the uncertainty in the population dominated by the uncertainty in the determination of the detuning of the Rb cooling laser. As introduced in section 3.6, a kinetic model of the form $k = \frac{1}{2}\Big[k_s(1+p_s) + k_p p_p\Big]$ was constructed, where $k_{s,p}$ and $p_{s,p}$ are the rate constants and populations in the Rb $(5s, 5p)$ states, respectively, and fitted to the data. The fit yielded $k_p = 2.4(13) \times 10^{-8}$ cm^{3}s^{-1} and an upper bound $k_s \leq 2 \times 10^{-10}$ cm^{3}s^{-1}. The uncertainty of k_p is dominated by a systematic error of $\approx 50\%$ in the Rb density.

The observation of the large difference in reaction rates from the Rb $(5s)\ ^2P_{1/2}$ and $(5p)\ ^2P_{3/2}$ states is rationalized in terms of both short and long range effects. The short range character is examined by comparing the asymptotic energy of the relevant entrance channels and the possible product channels for reaction as presented in Fig. 7.4, where the majority of electronic states of N_2 are taken from Ref. [165]. It can be seen that a minimum of 11.4 eV of energy is released upon charge transfer, which dominates the other energy scales of the reaction (N_2^+ room temperature rovibrational

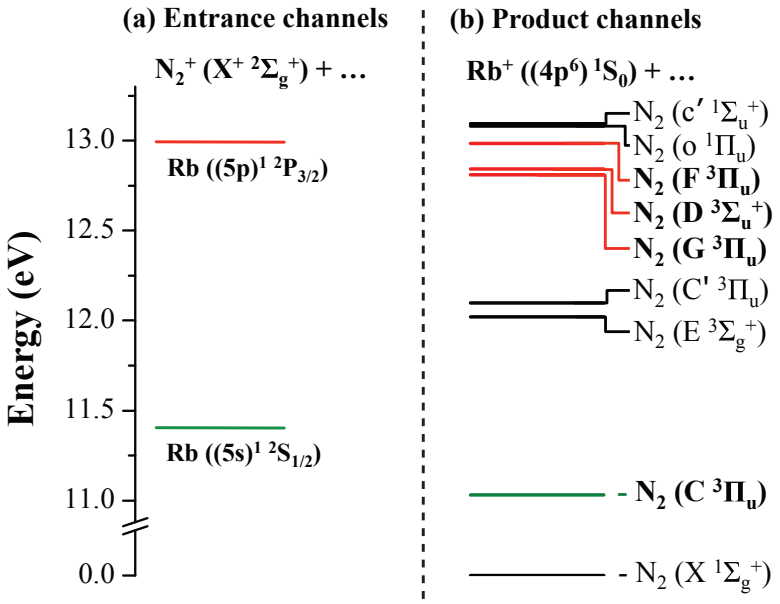

Figure 7.4: Total electronic energies of (a) the possible entrance N_2^+ + Rb channels with Rb in its ground $^2S_{1/2}$ (green) or electronically excited $^2P_{3/2}$ state (red), and (b) possible product Rb^+ + N_2 channels in the energy region of the relevant entrance channels. See text for details.

energy ≈ 0.025 eV, collision energy $\approx 10^{-6}$ eV).

Fig. 7.4 shows that the $N_2^+(X^+)$ + Rb($5s$) entrance channel is closest in energy to a product channel forming N_2 in the C $^3\Pi_u$ electronic state (shown in green) with a relatively large energy mismatch of $\Delta E = 372$ meV . This process also entails a significant rearrangement of the core electronic configuration from $N_2^+(X^+)$ $((2\sigma_g)^2(2\sigma_u)^2(1\pi_u)^4(3\sigma_g)^1)$ to form N_2 in the C state $((2\sigma_g)^2(2\sigma_u)^1(1\pi_u)^4(3\sigma_g)^2(1\pi_g)^1)$. Studies of keV N_2^+ ion beams impinging on neutral Cs atoms in a collision cell [166] have shown that charge transfer is most efficient for entrance and product channels with a minimized energy mismatch and which involve minimal rearrangement of the core electronic configuration. Charge transfer in the ground state of the present system is therefore expected to be inefficient, in line with the observation of a low rate constant in the experiments for this channel. The excited $N_2^+(X^+)$ + Rb($5p$) entrance channel, however, is near resonant with product channels forming N_2 in the the close-lying G $^3\Pi_u$, D $^3\Sigma_u^+$ and F $^3\Pi_u$ states with energy mismatches ΔE=183 meV, 151 meV and 8 meV respectively (shown in red). These states are among the lowest Rydberg states of N_2 built on the N_2^+ X^+ $^2\Sigma_g^+$ (in case of the G, D states) and A^+ $^2\Pi_u$ (in case of the F state) ion cores. The F state is heavily mixed with the G state and therefore also contains X^+ core character [167]. As a result, charge transfer into all three product channels is expected to be efficient, in agreement with the large rate constant observed in the excited channel. Further to these effects, the increased density of states

at higher excitation energies (see Fig. 7.4) as well as their short lifetime (and therefore large resonance width) [167] are also expected to contribute to the observed enhancement of the reaction probability. The Rydberg molecules subsequently predissociate into the atomic fragments $N(^4S)+N(^2D)$ [166] which, however, cannot be detected in the present experiment. It is worth noting that the efficiency of charge transfer into these states, and hence the large observed rate constant, is enhanced in this molecular system as opposed to an otherwise equivalent atomic ion system by the high density of vibronic states available in the N_2^* molecule, and the large resonance widths which arise due to the short lifetime of these states with respect to predissociation.

The quantitative rationalization of the large rate from the $N_2^+(X^+)$ + Rb($5p$) entrance channel is set in terms of long range interactions. In previous studies on cold atomic ion-neutral collisions in hybrid traps [33, 45], rate constants were found to be limited by the value according to Langevin theory [168] (see also discussion in chapters 5 and 6). As discussed in section 1.2.3, Langevin theory assumes that only the charge induced-dipole intermolecular force is acting, and returns a classical collisional rate constant independent of collision energy. The rate constant for the excited channel determined above ($k_p = 2.4(13) \times 10^{-8}$ cm^3 s^{-1}), however, is about four times larger than the value for the collision rate constant predicted by Langevin theory ($k^{(L)} = 6.6 \times 10^{-9}$ cm^3 s^{-1}) for this system. This underestimation indicates that additional long-range intermolecular forces are responsible for the large rate constant in this channel. As discussed in section 1.2.3, the ($5p$) $^2P_{3/2}$ state of Rb has a permanent electric quadrupole moment, generated by its anisotropic charge distribution [169]. The quadrupole moment of Rb ($5p$) $^2P_{3/2}$ was calculated within the single-electron approximation following Ref. [170]. As detailed in section 1.2.3, the collisional rate constant in the excited state using an extended interaction potential [23] incorporating the charge induced-dipole and charge permanent-quadrupole interactions was calculated at $E_{\mathrm{coll}}/k_{\mathrm{B}} = 23$ mK to be $k_p^{(c)} = 1.7 \times 10^{-8}$ cm^3 s^{-1} which is within the uncertainty limits of the measured rate constant for this channel. The agreement of the measured reaction rate constant with the calculated collision rate constant in this channel implies that once at short range, charge transfer occurs with near unit probability, which is supported by the short-range efficiency arguments given above.

As shown in Fig. 7.5, the charge permanent-quadrupole interaction leads to a rate constant scaling with $E_{\mathrm{coll}}^{-1/6}$, whereas the Langevin interaction results in a rate constant that is independent of collision energy. The inset compares the extended model to the experimental results of Fig. 7.3 (a) scaled to 100 % Rb ($5p$) $^2P_{3/2}$ population. The inset demonstrates that in the range of collision energy studied, the energy dependence predicted by the extended model would not be observable within the uncertainty limits of the present experiments.

Even given the approximations inherent in the classical capture model, which ignores quantum as well as molecular effects, its agreement with the observed rate constants demonstrates the need for the extension of Langevin theory to explain the dynamics in this system. The agreement also indicates that for this system, a purely classical capture model gives a satifactory description of the dynamics in this low col-

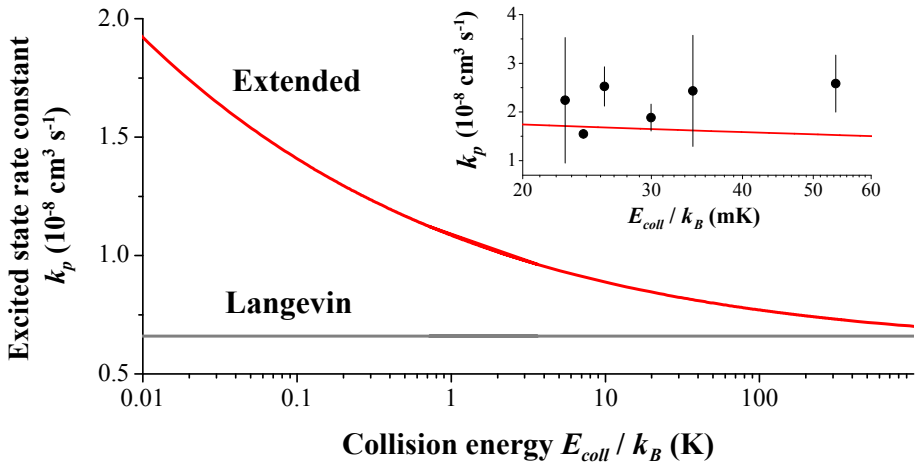

Figure 7.5: A plot of the collisional rate constant in the N_2^+ + Rb $(5p)\ ^2P_{3/2}$ channel as calculated by a model including charge induced-dipole interactions only i.e. Langevn theory (grey), and an extended model also including charge permanent-quadrupole interactions (red). The inset shows the extended model as compared to the experimental results of Fig. 7.3 scaled to 100% Rb $(5p)\ ^2P_{3/2}$ population.

lision energy regime. This is consistent with the theoretical results of Refs. [15, 150] which predict a satisfactory performance of classical capture models for ion-neutral reactions down to ultracold (<mK) temperatures for all but the lowest mass systems. This behavior has been rationalized in Ref. [150] by a cancellation of tunneling and reflection effects at the centrifugal barrier.

7.4 Summary and conclusions

The results highlight the importance of resonant electronic effects in charge transfer processes in ultracold alkali atom - cold molecular ion collisions. It is worth noting, as discussed above, that opportunities for resonant charge transfer may be significantly enhanced by the dense structure of rotational-vibrational levels in such molecular systems [166,167], in contrast to the atomic species studied in hybrid traps so far [36,44,45].

As discussed in sections 1.2, 5, and 6, the question of the universal nature of ion-neutral collisions, i.e., to what extent the dynamics are governed solely by long-range interactions, is an important topic. The enhanced short-range charge transfer efficiency in the excited entrance channel of the N_2^+ + Rb system suggested a short-range reaction probability of unity. This implied that the dynamics in this channel are capture limited, and so according to the predictions of universal behavior of cold ion-neutral reactions [15, 18], the reaction rate should only depend only the long-range part of the interaction potential. In this excited entrance channel therefore, there is the possibility

to study a process where the energy dependence *and* the magnitude of the reaction rate constant depends solely on the long-range part of the potential, and so can be *quantitatively* compared to universal models such as a classical capture model. This is in contrast to the other atomic-ion atom systems in this work, since in no channel studied were the reactions capture limited. Since the dominant contributions in to the long range potential in this excited entrance channel were charge induced-dipole and charge permanent-quadrupole, this study also provided a quantitative test for the ability of classical capture models to accurately incorporate the charge permanent-quadrupole potential. The agreement between the observed reaction rate constant and the result of the extended classical capture model indicates that these universal models are indeed sufficient to quantitatively describe the dynamics of cold ion-neutral processes where the reaction probability is unity. The results of this system suggest that cold atomic ion-neutral systems and cold molecular-ion atomic-neutral systems are both described by the same reaction mechanisms of universal long-range classical capture, followed by a chemical change at short-range due to interactions of PECs which influence the magnitude of the reaction rate, but have no effect on its collision energy dependence.

The enhanced reaction rate constant in the excited entrance channel in this system due in part to the additional attractive long-range interaction should be compared to the observation of a fast rate constant from the Ba^+ (6s) + Rb (5p) channel, where it was postulated the additional interaction also played an important role. The importance of the charge permanent-quadrupole interaction for enhancing collision rates that has been directly observed in this molecular-ion atom system gives weight to the arguments rationalizing the corresponding large rate constant in the Ba^+ + Rb (5p) system. The contrast in the corresponding entrance channel for the Ca^+ + Rb system, where a low rate constant was observed rationalized by the isolation of the corresponding short-range PECs, highlights again the dominant role the specific interactions of the PECs at short-range can play.

Short-range effects such as the rotational-vibrational state of the molecular ion which are not accounted for in the present capture picture could in principle influence the charge transfer efficiencies, indeed the present experiments were performed with room temperature rotationally thermalized ions in their vibrational ground state and were therefore not sensitive to these effects. To assess their possible role in the present system, further experiments are planned with rotationally and vibrationally state-selected nitrogen ions [12] as well as other molecular ion reactants including O_2^+.

Chapter 8

Conclusions and outlook

The main goal of this project was to construct an experiment to study ion-neutral reactions at unprecedentedly low collision energies, and provide tests for the classical and quantum theories predicting chemical behavior in this domain. This goal has been achieved. Through a close collaboration with a theory group, not only does this work provide experimental information, but by studying and discussing the experiment and theory for different systems in parallel, provides a picture of the current general understanding of cold light-assisted ion-neutral reactions.

The atomic ion-neutral systems $Ca^+ + Rb$ and $Ba^+ + Rb$ showed similar characteristics in that electronic excitation of the ion led to higher observed reaction rates. This was rationalized by the high density of charge transfer states in high energy regions leading to an increased number of non-adiabatic interactions leading to charge transfer. Radiative mechanisms were also postulated to have an enhanced efficiency in these excited channels due to the cubic dependence of the emission rate on the photon energy. Both systems also showed a similar collision energy dependence of rate constants. This was compared in detail to theoretical predictions, and the observed behavior was found to be in line with both classical and quantum scattering models. These results for both systems were analyzed in the context of universal behavior of cold ion-neutral reactions, where the energy dependence and the resonance spectrum of the reaction rate constants are predicted to depend only on the long-range interaction potential, but where the magnitude depends on the types of processes and the specific details of the short-range PECs. Both systems were found to conform to these predictions in their flat nature of the collision energy dependence of the reaction rate constants due to the long-range charge induced-dipole potential. This dependence was indicated to be independent of the ion electronic state, which is in line with universal behavior since the long-range potential is not effected by the ion's internal electronic state. The magnitude of the reaction rate constant was, however, dramatically effected due to the differences of the short-range PEC interactions. In both systems, molecular ions formed by radiative association were observed, but in line with predictions of quantum scattering calculations were formed with different product branching ratios as compared to Rb^+ formation by charge transfer mechanisms. The two systems responded

very differently to electronic excitation of the Rb, where the Ca^+ + Rb system showed no measurable effect, and where the Ba^+ + Rb system showed a significantly enhanced reaction rate. This was rationalized through the isolation and repulsive nature of the entrance channel in the Ca^+ + Rb case, and a large postulated radiative efficiency, and the effect of the permanent quadrupole moment of the Rb (5p) state enhancing the collision rate in the Ba^+ + Rb case. In both systems, the quantum mechanical nature of the collision was predicted to manifest itself as shape resonances in the rate constant, which, however, due to the collision energy distribution widths of the current experiments, could not be observed. The calculation of the shape resonances in both the systems however gave evidence for the universal nature of cold ion-neutral reactions since within each system, the resonance positions and intensities were identical (due to the identical nature of the long-range interaction potential) but their magnitude was governed by the specifics of the interactions between PECs at short-range.

The molecular ion-neutral system N_2^+ + Rb, represented the lowest collision energy experiments with molecular ions to date. A fast rate constant was observed from the excited Rb $^2P_{3/2}$ state, which was faster than the Langevin collision rate. A classical model including the charge-permanent quadrupole intermolecular force present in the $N_2^+(X^+)$ + Rb $^2P_{3/2}$ entrance channel reproduced the observed rate constant. This observation demonstrated the need to go beyond the Langevin model in describing light assisted cold ion-neutral collisions. The high short range reaction efficiency was rationalized by a near resonance of the entrance channel with exit channels correlating with Rydberg states of the neutral N_2 with the same core electronic configuration, hence allowing efficient charge transfer. The efficiency of energy transfer in this channel was also rationalized as a distinctly molecular effect due to the high density of product vibronic states available with large resonance widths due to the short lifetimes of the the states with respect to predissociation of N_2^* to 2N. The unit reaction probability from the excited entrance channel allowed a quantitative comparison to the predictions of universal models such as a classical capture model, and provided a test of the ability of such models to incorporate the charge permanent-quadrupole interaction. The agreement implied that such universal models are indeed sufficient to quantitatively describe cold ion-neutral dynamics for processes with reaction probabilities of unity. The results of this work therefore suggest that cold atomic ion-neutral systems and cold molecular-ion atomic-neutral systems are both described by the same reaction mechanisms of universal long-range classical capture, followed by a chemical change at short-range due to interactions of PECs which influence the magnitude of the reaction rate, but have no effect on its collision energy dependence. In such a way this work has provided an insight into the seemingly very general nature of cold ion-neutral reactions.

A clear direction of further work in the atomic ion-neutral systems is to manipulate the collision energy distribution such that the predicted shape resonances in the reaction rate can be observed experimentally. Current work in this direction is being undertaken, where two ions are very well axialised using techniques superior to those outlined in this work [77]. The resulting collision energy spread with Rb atoms in a MOT can then be $\approx$ 1 mK. The atoms, which have an $\approx$ 100 μK kinetic energy

distribution can be swept across the ions with differing sweep velocities, and hence result in different collision energies. In such a way a high resolution collision energy dependence of the reaction rate constant could be obtained, which in a certain energy range, should show the predicted shape resonances. The comparison of the experimental result to theory would then provide detailed information about the relevant potential energy surfaces, as it has done recently for the He^*+H_2 system in merged beam experiments [13]. The molecular ions formed by radiative association in these systems could be interesting targets for further studies, either in their spectroscopy or in further reactions with other species. Also, schemes for their controlled production through photo-association [63] could be explored, with a view to providing another degree of control in such experiments.

A clear direction for further work in molecular ion-neutral systems is to investigate the extent to which specific rovibrational states play a role, using the state selection techniques already developed in our group [12]. Systems which are more likely to be sensitive to this effect have already been identified. For example, the ordering of the energy levels in the O_2^+ + Rb system are such that reactions should be energetically forbidden in the ground rovibrational state, but become possible on rovibrational excitation. This experiment would demonstrate another interesting level of complexity and control in cold ion-neutral collisions, and could have implications in fields as far as quantum computing with molecular ions [171].

With the wealth of effects already uncovered so far by the community, and on the back of the complexity revealed in this work for even the simplest systems, it is clear that the field of cold chemistry has much to offer in the future, and has a significant role to play in the understanding of reactivity at the most fundamental level.

Bibliography

[1] P. W. Atkins, *Physical Chemistry* (Oxford University Press, 1994), 5th ed.

[2] H. J. Metcalf and P. van der Straten, *Laser Cooling and Trapping* (Springer, New York, 1999).

[3] S. Y. T. van de Meerakker, H. Bethlem, and G. Meijer, Chem. Rev. **112**, 4828 (2012).

[4] P. Dawson and N. Whetten, Naturwissenschaften **56**, 109 (1969).

[5] D. J. Wineland, R. E. Drullinger, and F. L. Walls, Phys. Rev. Lett. **40**, 1639 (1978).

[6] W. Neuhauser, M. Hohenstatt, P. Toschek, and H. Dehmelt, Phys. Rev. Lett. **41**, 233 (1978).

[7] W. Phillips, J. Prodan, and H. Metcalf, J. Opt. Soc. Am. B **2**, 1751 (1985).

[8] C. Adams, O. Carnal, and J. Mlynek, Adv. At. Mol. Opt. Phys. **34**, 1 (1994).

[9] M. H. Anderson, J. R. Ensher, M. R. Matthews, C. E. Wieman, and E. A. Cornell, Science **269**, 5221 (1995).

[10] H. Häffner, C. F. Roos, and R. Blatt, Phys. Rev. **469**, 155 (2008).

[11] K.-K. Ni, S. Ospelkaus, D. Wang, G. Quéméner, B. Neyenhuis, M. H. G. de Miranda, J. L. Bohn, J. Ye, and D. S. Jin, Nature **464**, 1324 (2010).

[12] X. Tong, A. H. Winney, and S. Willitsch, Phys. Rev. Lett. **105**, 143001 (2010).

[13] A. Henson, S. Gersten, Y. Shagam, J. Narevicius, and E. Narevicius, Science **338**, 234 (2012).

[14] P. Langevin, Ann. Chim. Phys. **5**, 245 (1905).

[15] B. Gao, Phys. Rev. A **83**, 062712 (2011).

[16] R. Côté and A. Dalgarno, Phys. Rev. A **62**, 012709 (2000).

[17] B. Zygelman and A. Dalgarno, Phys. Rev. A **38**, 1877 (1988).

[18] B. Gao, Phys. Rev. Lett. **104**, 213201 (2010).

[19] Z. Idziaszek, A. Simoni, T. Calarco, and P. S. Julienne, New J. Phys. **13**, 083005 (2011).

[20] M. Li and B. Gao, Phys. Rev. A **86**, 012707 (2012).

[21] R. D. Levine, *Molecular Reaction Dynamics* (Cambridge University Press, 2005).

[22] B. Jeziorski, R. Moszynski, and K. Szalewicz, Chem. Rev. **94**, 1887 (1994).

[23] M. Krych, W. Skomorowski, F. Pawłowski, R. Moszynski, and Z. Idziaszek, Phys. Rev. A **83**, 032723 (2011).

[24] A. Stone, Theory of Intermolecular Forces, Oxford University Press (1997).

[25] R. Zare, Angular Momentum, Wiley, New York (1988).

[26] V. Aquilanti, G. Liuti, F. Pirani, and F. Vecchiocattivi, J. Chem. Soc., Faraday Trans. 2 **85**, 955 (1989).

[27] P. Atkins and R. Friedman, Molecular Quantum Mechanics, OUP, New York (2005).

[28] C. Champenois, M. Houssin, C. Lisowski, M. Knoop, G. Hagel, M. Vedel, and F. Vedel, Phys. Lett. A **331**, 298 (2004).

[29] A. K. Belyaev, S. A. Yakovleva, M. Tacconi, and F. A. Gianturco, Phys. Rev. A **85**, 042716 (2012).

[30] P. Zhang, A. Dalgarno, R. Côté, and E. Bodo, Phys. Chem. Chem. Phys. **13**, 19026 (2011).

[31] A. Rakshit and B. Deb, Phys. Rev. A **83**, 022703 (2011).

[32] B. Zygelman, A. Dalgarno, M. Kimura, and N. Lane, Phys. Rev. A **40**, 2340 (1989).

[33] A. T. Grier, M. Cetina, F. Oručević, and V. Vuletić, Phys. Rev. Lett. **102**, 223201 (2009).

[34] C. Zipkes, S. Palzer, C. Sias, and M. Köhl, Nature **464**, 388 (2010).

[35] S. Schmid, A. Härter, and J. Hecker Denschlag, Phys. Rev. Lett. **105**, 133202 (2010).

[36] F. H. J. Hall, M. Aymar, N. Bouloufa-Maafa, O. Dulieu, and S. Willitsch, Phys. Rev. Lett. **107**, 243202 (2011).

[37] S. Sullivan, W. Rellergert, S. Kotochigova, and E. Hudson, Phys. Rev. Lett. **109**, 223002 (2012).

[38] K. Ravi, S. Lee, A. Sharma, G. Werth, and S. A. Rangwala, Nat. Commun. 3 : 1126, doi:10.1038/ncomms2131 (2012).

[39] F. H. J. Hall and S. Willitsch, Phys. Rev. Lett. **109**, 233202 (2012).

[40] A. Härter, A. Krükow, A. Brunner, W. Schnitzler, S. Schmid, and J. H. Denschlag, Phys. Rev. Lett. **109**, 123201 (2012).

[41] F. H. J. Hall, M. Aymar, M. Raoult, O. Dulieu, and S. Willitsch, accepted by Mol. Phys. (2013).

[42] F. H. J. Hall, P. Eberle, G. Hegi, M. Raoult, O. Dulieu, and S. Willitsch, accepted by Mol. Phys. (2013).

[43] S. Willitsch, M. T. Bell, A. D. Gingell, S. R. Procter, and T. P. Softley, Phys. Rev. Lett. **100**, 043203 (2008).

[44] W. G. Rellergert, S. T. Sullivan, S. Kotochigova, A. Petrov, K. Chen, S. J. Schowalter, and E. R. Hudson, Phys. Rev. Lett. **107**, 243201 (2011).

[45] L. Ratschbacher, C. Zipkes, C. Sias, and M. Köhl, Nat. Phys. 8 pp. 649, doi:10.1038/nphys2373 (2012).

[46] C. Wittig, J. Phys. Chem B **109**, 8428 (2005).

[47] M. Tacconi, F. A. Gianturco, and A. K. Belyaev, Phys. Chem. Chem. Phys. **13**, 19156 (2011).

[48] M. Kimura, N. Lane, A. Dalgarno, and R. Dixson, Astrophys. J. **405**, 801 (1993).

[49] B. Zygelman and A. Dalgarno, Astrophys. J. **365**, 239 (1990).

[50] P. Stancil, J. Babb, and A. Dalgarno, Astrophys. J. **414**, 672 (1993).

[51] S. Butler, S. Guberman, and A. Dalgarno, Phys. Rev. A. **16**, 500 (1977).

[52] A. Dalgarno, M. Du, and J. You, Astrophys. J. **349**, 675 (1990).

[53] G. Barinovs and M. van Hemert, Astrophys. J. **636**, 923 (2006).

[54] D. Gerlich and S. Horning, Chem. Rev. **92**, 1509 (1992).

[55] S. Barlow, G. Dunn, and M. Schauer, Phys. Rev. Lett. **52**, 902 (1984).

[56] D. Smith and N. Adams, Adv. At. Mol. Phys. **24**, 1 (1988).

[57] V. Weisskopf and E. Wigner, Zeit. f. Phys. **63**, 54 (1930).

[58] J. Miller, R. Cline, and D. Heinzen, Phys. Rev. A **47**, 4567 (1993).

[59] R. Grimm, M. Weidermüller, and Y. Ovchinnikov, Adv. At. Mo. Opt. Phys. **42**, 95 (2000).

[60] T. Hänsch and A. Schawlow, Opt. Commun. **13**, 68 (1975).

[61] S. Chu, L. Hollberg, J. E. Bjorkholm, A. Cable, and A. Ashkin, Phys. Rev. Lett. **55**, 48 (1985).

[62] E. L. Raab, M. Prentiss, A. Cable, S. Chu, and D. E. Pritchard, Phys. Rev. Lett. **59**, 2631 (1987).

[63] P. Lett, P. Julienne, and W. Phillips, Annu. Rev. Phys. Chem. **46**, 423 (1995).

[64] F. G. Major, V. N. Gheorghe, and G. Werth, *Charged Particle Traps* (Springer, Berlin and Heidelberg, 2005).

[65] H. Friedburg and W. Paul, Naturwissenshaft **38**, 159 (1951).

[66] H. Benewitz and W. Paul, Z. Physik **139**, 489 (1954).

[67] E. Courant, M. Livingstone, and H. Snyder, Phys. Rev. **88**, 1190 (1952).

[68] W. Paul and H. Steinwedel, Z. Naturforschung **8a**, 448 (1953).

[69] W. Paul and M. Raether, Z. Physik **140**, 262 (1955).

[70] W. Paul, O. Osberghaus, and E. Fischer, Forsch. Berichte des Wirtschaftsministeriums Nordhein-Westfalen **415** (1958).

[71] M. Drewsen, C. Brodersen, L. Hornekaer, J. Hangst, and J. Schiffer, Phys. Rev. Lett. **81**, 14 (1998).

[72] J. D. Prestage, G. J. Dick, and L. Maleki, J. Appl. Phys. **66**, 1013 (1989).

[73] G. Gräff, F. Major, R. Roeder, and G. Werth, Phys. Rev. Lett. **21**, 340 (1968).

[74] S. R. Jefferts, C. Monroe, E. W. Bell, and D. Wineland, Phys. Rev. A **51**, 3112 (1995).

[75] M. Drewsen and A. Brøner, Phys. Rev. A **62**, 045401 (2000).

[76] W. Paul, Rev. Mod. Phys. **62**, 531 (1990).

[77] D. J. Berkeland, J. D. Miller, J. C. Bergquist, W. M. Itano, and D. J. Wineland, J. Appl. Phys. **83**, 5025 (1998).

[78] A. Buck, Masters Thesis, University of Basel (2011).

[79] D. Gerlich, Adv. Chem. Phys. **82**, 1 (1992).

[80] A. Mokhberi, 8 mm Ion Trap Simulation Report, University of Basel (2011).

[81] E. L. Pollock and J. P. Hansen, Phys. Rev. A **8**, 3110 (1973).

[82] J. P. Schiffer, Phys. Rev. Lett. **88**, 205003 (2002).

[83] D. Leibfried, R. Blatt, C. Monroe, and D. Wineland, Rev. Mod. Phys. **75**, 281 (2003).

[84] J. P. Schiffer, M. Drewsen, J. S. Hangst, and L. Hornekaer, Proc. Natl. Acad. Sci. **97**, 10697 (2001).

[85] C. B. Zhang, D. Offenberg, B. Roth, M. A. Wilson, and S. Schiller, Phys. Rev. A **76**, 012719 (2007).

[86] J. P. Schiffer, J. Phys. B: At. Mol. Opt. Phys. **36**, 511 (2003).

[87] T. Matthey, T. Cickovski, S. S. Hampton, A. Ko, Q. Ma, M. Nyerges, T. Raeder, T. Slabach, and J. A. Izaguirre, ACM Trans. Math. Softw. **30(3)**, 237265 (2004).

[88] A. Winney, Project Report, Group of S. Willitsch, University of Basel (2010).

[89] K. Okada, M. Wada, L. Boesten, T. Nakamura, I. Katayama, and S. Ohtani, J. Phys. B: At. Mol. Opt. Phys. **36**, 33 (2003).

[90] N. Kimura, K. Okada, T. Takayanagi, M. Wada, S. Ohtani, and H. A. Schuessler, Phys. Rev. A **83**, 033422 (2011).

[91] X. Tong, D. Wild, and S. Willitsch, Phys. Rev. A **83**, 023415 (2011).

[92] C. Wieman, G. Flowers, and S. Gilbert, Am. J. Phys. **63**, 317 (1995).

[93] M. H. Shah, H. A. Camp, M. L. Trachy, G. Veshapidze, M. A. Gearba, and B. D. DePaola, Phys. Rev. A **75**, 053418 (2007).

[94] C. C. Bradley, J. McClelland, W. Anderson, and R. Celotta, Phys. Rev. A **61**, 53407 (2000).

[95] S. Pradhan and B. N. Jagatap, Rev. Sci. Instrum. **79**, 013101 (2008).

[96] D. Guéry-Odelin, J. Söding, P. Desbiolles, and J. Dalibard, Opt. Express **2**, 323 (1998).

[97] L. Maguire, S. Szilagyi, and R. Scholten, Rev. Sci. Instrum. **75**, 3077 (2004).

[98] A. Bünzli, Project Report, University of Basel (2010).

[99] P. Eberle, Masters Thesis, University of Basel (2012).

[100] J. Schiffer, Phys. Rev. Lett. **61**, 1843 (1988).

[101] B. Wang, J. Zhang, C. Gao, and L. Wang, Opt. Expr. **19**, 16438 (2011).

[102] A. Steele, L. Churchill, P. Griffin, and M. Chapman, Phys. Rev. A **75**, 053404 (2007).

[103] D. J. Larson, J. C. Bergquist, J. J. Bollinger, W. M. Itano, and D. J. Wineland, Phys. Rev. Lett. **57**, 70 (1986).

[104] P. Bowe, L. Hornekaer, C. Brodersen, M. Drewsen, J. S. Hangst, and J. P. Schiffer, Phys. Rev. Lett. **82**, 2071 (1999).

[105] A. Ostendorf, C. B. Zhang, M. A. Wilson, D. Offenberg, B. Roth, and S. Schiller, Phys. Rev. Lett. **97**, 243005 (2006).

[106] P. F. Staanum, K. Højbjerre, R. Wester, and M. Drewsen, Phys. Rev. Lett. **100**, 243003 (2008).

[107] K. Liu, J. Chem. Phys. **125**, 132307 (2006).

[108] B. Roth, P. Blythe, and S. Schiller, Phys. Rev. A **75**, 023402 (2007).

[109] G. Hegi, Wahlpraktikum Report, University of Basel (2012).

[110] P. F. Staanum, K. Højbjerre, and M. Drewsen, in *Practical Aspects of Trapped Ion Mass Spectrometry* (CRC Press, Boca Raton, 2010), vol. 5, p. 291.

[111] G. Morigi and H. Walther, Eur. Phys. J. D **13**, 261 (2001).

[112] W. Demtröder, *Laser Spectroscopy* (Springer, Berlin, 2008), 4th ed.

[113] H. Oberst, Diploma Thesis, University of Innsbruck (1999).

[114] A. D. Gingell, M. T. Bell, J. M. Oldham, T. P. Softley, and J. M. Harvey, J. Chem. Phys. **133**, 194302 (2010).

[115] E. Arimondo, in E. Wolf, ed., *Progress in Optics* (Elsevier, 1996), vol. 35, p. 257.

[116] A. Gingell, PhD Thesis, University of Oxford, Oxford (2010).

[117] P. F. Bernath, *Spectra of Atoms and Molecules* (Oxford University Press, Oxford, 2005), 2nd ed.

[118] M. Aymar and O. Dulieu, J. Chem. Phys. **122**, 204302 (2005).

[119] M. Aymar, R. Guérout, and O. Dulieu, J. Chem. Phys. **135**, 064305 (2011).

[120] P. Durand and J. Barthelat, Chem. Phys. Lett. **27**, 191 (1974).

[121] R. Guérout and M. Aymar, Phys. Rev. A **82**, 042508 (2010).

[122] R. Guérout, M. Aymar, and O. Dulieu, J. Chem. Phys. **135**, 064305 (2011).

[123] W. Müller, J. Flesch, and W. Meyer, J. Chem. Phys. **80**, 3297 (1984).

[124] T. Bouissou, G. Durand, M.-C. Heitz, and F. Spegelman, J. Chem. Phys. **133**, 164317 (2010).

[125] M. Aymar and O. Dulieu, J. Chem. Phys. **125**, 047101 (2006).

[126] M. Aymar and O. Dulieu, J. Phys. B **45**, 215103 (2012).

[127] P. Fuentealba, L. von Szentpaly, H. Preuss, and H. Stoll, J. Phys. B **18**, 1287 (1985).

[128] P. Fuentealba and O. Reyes, Mol. Phys. **62**, 1291 (1987).

[129] F. Gianturco and P. G. Giorgi, Astrophys. J. **479**, 560 (1997).

[130] W. Milne, Phys. Rev. **35**, 863 (1930).

[131] H. Korsch and H. Laurent, J. Phys. B **14**, 4213 (1981).

[132] S. Pollock, J. Cotter, A. Laliotis, and E. Hinds, Optics Express **17**, 14109 (2009).

[133] U. Schünemann, H. Engler, M. Zielonkowski, M. Weidemuller, and R. Grimm, Opt. Commun. **158**, 263 (1998).

[134] C. D. Wallace, T. Dinneen, K. Tan, T. Grove, and P. Gould, Phys. Rev. Lett. **69**, 897 (1992).

[135] W. McAlexander, E. Abraham, N. Ritchie, C. Williams, H. Stoof, and R. Hulet, Phys. Rev. A **51**, 871 (1995).

[136] A. M. Steane and C. Foot, Europhys. Lett. **14**, 231 (1991).

[137] F. Y. Loo, A. Brusch, S. Sauge, M. Allegrini, E. Arimondo, N. Andersen, and J. Thomsen, J. Opt. B **6**, 81 (2004).

[138] J. Grünert, S. Ritter, and A. Hemmerich, Phys. Rev. A **65**, 41401 (2002).

[139] H. Katori, , T. Ido, Y. Isoya, and M. Kuwata-Gonokami, Phys. Rev. Lett. **82**, 1116 (1999).

[140] S. Dee, U. Dammalapati, K. Jungmann, and L. Willmann, Phys. Rev. A **79**, 41402 (2009).

[141] K. Honda, Y. Takahashi, T. Kuwamoto, K. Ishikawa, and T. Yasuzaki, Phys. Rev. A **59**, R934 (1999).

[142] S. Chu and et al., Rev. Mod. Phys. **70**, 685 (1998).

[143] S. Ospelkaus, K.-K. Ni, G. Quemener, B. Neyenhuis, D. Wang, M. H. G. de Miranda, J. L. Bohn, J. Ye, and D. S. Jin, Phys. Rev. Lett. **104**, 030402 (2010).

[144] M. Drewsen, P. Laurent, A. Nadir, G. Santarelli, A. Clairon, Y. Castin, D. Grison, and C. Salomon, Appl. Phys. B **59**, 286 (1994).

[145] C. G. Townsend, N. H. Edwards, C. J. Cooper, K. P. Zetie, C. J. Foot, A. M. Steane, P. Szriftgiser, H. Perrin, and J. Dalibard, Phys. Rev. A **52**, 1423 (1995).

[146] P. D. Lett, R. N. Watts, C. I. Westbrook, W. D. Phillips, P. L. Gould, and H. J. Metcalf, Phys. Rev. Lett. **61**, 169 (1998).

[147] K. Lindquist, M. Stephens, and C. Wieman, Phys. Rev. A **46**, 4082 (1992).

[148] T. Walker, D. Sesko, and C. Wieman, Phys. Rev. Lett. **64**, 408 (1990).

[149] S. Willitsch, Int. Rev. Phys. Chem. **31**, 175 (2012).

[150] E. I. Dashevskaya, A. I. Maergoiz, J. Troe, I. Litvin, and E. E. Nikitin, J. Chem. Phys. **118**, 7313 (2003).

[151] E. E. Nikitin and J. Troe, Phys. Chem. Chem. Phys. **7**, 1540 (2005).

[152] B. Gao, Phys. Rev. Lett. **105**, 263203 (2010).

[153] P. Zhang, A. Dalgarno, and R. Côté, Phys. Rev. A **80**, 030703 (2009).

[154] C. Zipkes, S. Palzer, L. Ratschbacher, C. Sias, and M. Köhl, Phys. Rev. Lett. **105**, 133201 (2010).

[155] M. Drewsen, A. Mortensen, R. Martinussen, P. Staanum, and J. L. Sorensen, Phys. Rev. Lett. **93**, 243201 (2004).

[156] C. Gabbanini, A. Fioretti, A. Lucchesini, S. Gozzini, and M. Mazzoni, Phys. Rev. Lett. **84**, 2814 (2000).

[157] P. Barragán, L. Errea, F. Guzmán, L. Méndez, I. Rabadán, and I. Ben-Itzhak, Phys. Rev. A **81**, 062712 (2010).

[158] M. Roudjane, R. McCarroll, and D. Rabli, J. Phys. B **40**, 2491 (2007).

[159] S. Knecht, L. Sorensen, H. A. Jensen, and C. Marian, J. Phys. B **43**, 055101 (2010).

[160] O. Dulieu, M. Aymar, N. Bouloufa-Maafa, and M. Raoult, in preparation (2013).

[161] M. A. Smith, Int. Rev. Phys. Chem. **17**, 35 (1998).

[162] D. C. Clary, Chem. Phys. Lett. **232**, 267 (1995).

[163] R. Otto, J. Mikosch, S. Trippel, M. Weidemüller, and R. Wester, Phys. Rev. Lett. **101**, 063201 (2008).

[164] J. Deiglmayr, A. Göritz, T. Best, M. Weidemüller, and R. Wester, Phys. Rev. Lett. **86**, 043438 (2012).

[165] A. Lofthus and P. H. Krupenie, J. Phys. Chem. Ref. Data **6**, 113 (1977).

[166] A. B. van der Kamp, P. C. Cosby, and W. J. van der Zande, Chem. Phys. **184**, 319 (1994).

[167] B. R. Lewis, A. N. Heays, S. T. Gibson, H. Lefebvre-Brion, and R. Lefebvre, J. Chem. Phys. **129**, 164306 (2008).

[168] G. Gioumousis and D. P. Stevenson, J. Chem. Phys. **29**, 294 (1958).

[169] F. Pirani, G. S. Maciel, D. Cappelletti, and V. Aquilanti, Int. Rev. Phys. Chem. **25**, 165 (2006).

[170] I. I. Sobelman, *Atomic Spectra and Radiative Transitions* (Springer, Berlin, 1979).

[171] J. Mur-Petit, J. Pérez-Ríos, J. Campos-Martínez, M. I. Hernández, S. Willitsch, and J. J. García-Ripoll, Phys. Rev. A **85**, 022308 (2012).

Appendix A

Publications

"Light-Assisted Ion-Neutral Reactive Processes in the Cold Regime: Radiative Molecule Formation versus Charge Exchange"
Felix H.J. Hall, Mireille Aymar, Nadia Bouloufa-Maafa, Olivier Dulieu, and Stefan Willitsch.
Physical Review Letters **107**, 243202 (2011).

"Millikelvin Reactive Collisions between Sympathetically Cooled Molecular Ions and Laser-Cooled Atoms in an Ion-Atom Hybrid Trap"
Felix H.J. Hall and Stefan Willitsch.
Physical Review Letters **109**, 233202 (2012).

"Light-Assisted Cold Chemical Reactions of Barium Ions with Rubidium Atoms"
Felix H.J. Hall, Mireille Aymar, Maurice Raoult, Olivier Dulieu, and Stefan Willitsch.
Accepted by *Molecular Physics* (2013).

"Ion-neutral chemistry at ultralow energies: Dynamics of reactive collisions between laser-cooled Ca^+ ions and Rb atoms in an ion-atom hybrid trap"
Felix H.J. Hall, Pascal Eberle, Gregor Hegi, Maurice Raoult, Mireille Aymar, Olivier Dulieu, and Stefan Willitsch.
Accepted by *Molecular Physics* (2013).

Appendix B

Codes and script

B.1 Collisional rate constant determination script

In section 1.2, a classical capture model was derived for calculating the collisional rate constant for collisions experiencing an inter-species potential $V(R)$. As was seen in section 1.2.3, the form of $V(R)$ may be such that an analytic form of the rate constant is not possible. Instead, equation 1.10 must be solved for each collision energy to give plot of collision energy against rate constant. Equation 1.10 may be formulated in terms of collision energy E and b_{max} (which is referred to in the script below as x) all in SI units. The following *matlab* script can then be used to solve this equation for a specified range of E in specified step sizes of E, and it outputs a vector whose rows contain E in J and a rate constant in $\mathrm{cm}^3\mathrm{s}^{-1}$. The symbol `%` is intended to indicate a comment which is not part of the script, and the "..." signify the continuation of a line.

```
clear
abc=[1E-23:1E-23:2E-23]; %start energy : step size : end energy, all in J.
mysize=size(abc);
mysize2=mysize(1,2);
myans=zeros(mysize,2);
mycount=1;
for E = abc
E;
syms x
solve(****insert the left hand side of equation referred to in the text...
...above with "x" instead of "b_max" in SI units****);
myans(mycount,1)=E;
myans(mycount,2)=(((ans(1,1))^2)*3.1415*(((2*E)/(3.52E-26))^(0.5)))*(1E6);...
...%insert appropriate reduced mass
mycount=mycount+1;
end
myans
```

B.2 State specific rate constant solver

This is a *matlab* script developed by X. Tong to perform a multi-dimensional least squares fit to a set of simultaneous equations with the form of equation 3.15, where parameter uncertainties are returned even if the parameters are constrained. It is made of two parts, the first a function definition which should be saved as `solver_rate_constant.m`, and the second an executable script which returns the parameter values and errors. The symbol `%` is intended to indicate a comment which is not part of the script. "N" is the number of simultaneous equations to solve for. The function file is presented here:

```
function keff = solver_rate_constant(k,t)    %function definition

%relabeling of the state rate constants, where k_s^* is written ks1 here:

ks=k(1);
kp=k(2);
kd=k(3);
ks1=k(4);

%insert the populations derived from experiment for each,
%but leave k1 as "k1" etc here

k1 = (0.5)*(ks*(psion+psrb)+kp*(ppion)+kd*(pdion+ks1*(pprb));
k2 = (0.5)*(ks*(psion+psrb)+kp*(ppion)+kd*(pdion+ks1*(pprb));
.
.
.
kN = (0.5)*(ks*(psion+psrb)+kp*(ppion)+kd*(pdion+ks1*(pprb));

%also leave here k1 as "k1" etc as obove

keff = [k1,k2,...,kN];


end
```

The second, executable part is presented here:

```
clear;clc;

%insert the observed rate constants in order as they
%appear in the function file here:
```

```
expdata = [k1,k2,...kN];

%initial guess of state rate constants, in order as defined
%in function file here:

k = [1,1,1,1];

%constrain lower bound of state rate constants

lb = [-100,-100,-100,-100];

%constrain upper bound of state rate constants here

ub = [100,100,100,100]; %constrain upper bound of state rate constants

%see normal "lsqcurvefit" for details here, "..." indicates
%it should be one line:

t=0;
options = optimset('TolFun', 1e-15, 'TolX', 1e-15, 'MaxFunEvals', 2000,...
... 'Algorithm', 'trust-region-reflective', 'Display', 'iter');
[fitted_K, resnorm_N, residual_N, exitflag, output, lambda,...
...jacobian_vector]=lsqcurvefit(@solver_rate_constant, k, t, expdata,...
... lb, ub, options);
fitted_K

%calculation of covariance matrix, change as
%appropriate for N and number of parameters:

covariance_matrix = resnorm_N/(19-4)*inv(jacobian_vector'*jacobian_vector);

%lists the uncertainties in each state rate constant:

Uncertainties= sqrt(diag(covariance_matrix))

residual_N

%change for N used:

Standard_deviation=sqrt(resnorm_N/19) %change for N used
```

Felix H.J. **Hall**

Klingelbergstrasse 80 • Basel 4056 • Switzerland
PHONE (+41) 0612673827 • **E-MAIL** felix.hall@unibas.ch

Education

Doctor of Philosophy in Science (Chemical Physics), summa cum laude
Sept. 2009 – Apr. 2013. University of Basel, Switzerland
Thesis title: *Cold ion-neutral reactions*. Supervisor: Prof. Dr. Stefan Willitsch. Selected courses: *"Ultracold atoms", "Frontiers of Physical Chemistry", "Effective scientific article writing".*

Master in Science (Chemical Physics), 1st class Honors
Sept. 2005 – July 2009. University College London, U.K.
Thesis title: *The Stark effect in autoionising and predissociating Rydberg states of NO*. Supervisor: Prof. Dr. Helen Fielding. Selected courses: *"Literature project: Bose-Einstein Condensates", "Electricity and Magnetism", "Chemical dynamics", "Lasers and Modern optics".*

A levels: **Maths** (A), **Physics** (A), **Chemistry** (A), **Fine Art** (A)
Sept. 1998 – July 2005. Truro School, U.K.

Publications

"Light-Assisted Ion-Neutral Reactive Processes in the Cold Regime: Radiative Molecule Formation versus Charge Exchange." F.H.J. Hall, N. Bouloufa-Maafa, O. Dulieu and S. Willitsch. *Phys. Rev. Lett.* **107**, 243202 (2011)

"Millikelvin Reactive Collisions between Sympathetically Cooled Molecular Ions and Laser-Cooled Atoms in an Ion-Atom Hybrid Trap." F.H.J. Hall and S. Willitsch. *Phys. Rev. Lett.* **109**, 233202 (2012)

"Light-Assisted Cold Chemical Reactions of Barium Ions with Rubidium Atoms." F.H.J. Hall, M. Aymar, M. Raoult, O. Dulieu and S. Willitsch. Accepted by *Mol. Phys.* (2013)

"Ion-neutral chemistry at ultralow energies: Dynamics of reactive collisions between laser-cooled Ca^+ ions and Rb atoms in an ion-atom hybrid trap." F.H.J. Hall, P. Eberle, G. Hegi, M. Raoult, M. Aymar, O. Dulieu and S. Willitsch. Accepted by *Mol. Phys.* (2013).

Awards

Christopher Ingold Prize, University College London, U.K. Sept. 2007

Physics Prize, Truro School, U.K. July 2005

Conferences

Attended: CUSO Frontiers in mass spectrometry, Villars, Switzerland, 2009.
Attended: European Conference on Trapped Ions (ECTI), Darlington, U.K., 2010.
Poster: Swiss Physical Society (SPS) meeting, Basel, Switzerland, 2010.
Poster: Swiss Chemical Society (SCS) meeting, Zürich, Switzerland, 2010.
Talk: SCS meeting, Lausanne, Switzerland, 2011.
Poster: Cold and controlled molecular collisions, Ringberg, Germany, 2011.
Talk & Poster: IOTA-COST cold molecular ions workshop, Sandbjerg, Denmark, 2011.
Poster: Coherence and decoherence at ultracold temps., Munich, Germany, 2011.
Poster: Faraday Disc. Frontiers in Spectroscopy, Basel, 2011.
Poster: SPS, Zürich, 2012.
Poster: ECTI, Obergurgl, Austria, 2012.
Talk: Ion trap group meeting, Zürich, 2012.
Talk: Cold chemistry meeting, Diavolezza, Switzerland, 2012.
Talk: RSC Spectroscopy and Dynamics meeting, Durham, U.K., 2013.

Teaching

Physical Chemistry Laboratory Demonstrator
Sept. 2009 – Dec. 2012. University of Basel, Switzerland.
Demonstrated two undergraduate lab experiments over six semesters successfully supervising and marking reports of over 180 students.

Master and Project Student Research Supervisor
Sept. 2009 – Dec. 2012. University of Basel, Switzerland.
Successfully supervised the research lab work of two Masters students and four project students.

Teaching Assistant
June – July 2007. Penair School, U.K.
Teaching assistant in Maths, Physics, and Chemistry to G.C.S.E. students

References

References are available on request

Contact

Office phone: (+41) 0612673827
Office Email: felix.hall@unibas.ch
Office address: Klingelbergstrasse 80, Basel 4056, Switzerland.